The University Of Sheffield.

High Resolution Atomic Force Microscopy Imaging of Living Bacterial Surfaces

By:

Jonathan Matthew Burns

A thesis submitted in partial fulfilment of the requirements for the degree of

Doctor of Philosophy

The University of Sheffield

Faculty of Science

Department of Physics and Astronomy

September 2017

Abstract

The study of bacteria is important for understanding disease, the development of drugs and understanding bacterial ecosystems. Bacterial cells have a cell wall which is made of a biopolymer called peptidoglycan. In Gram positive species of bacteria like *S. aureus* and *B. subtilis* the peptidoglycan cell wall layer is ~25 nm thick.

AFM is a powerful tool for understanding biological structures and processes. By immobilising the *S. aureus* cells in a silicon wafer etched with holes, AFM can be performed on living bacteria in a liquid environment. In this work small amplitude tapping mode AFM, combined with optimisation of imaging buffers has allowed for high resolution images of living *S. aureus* cells to be taken at different time points in the cell cycle revealing the architecture of the cell wall peptidoglycan with molecular resolution on living bacteria. Different structures have been seen on the cells that range from the freshly formed tightly spaced concentric rings to the mature loose mesh which are a result of the remodelling of the cell wall. Cells that are seen to be undergoing a division event have also been imaged revealing how the splitting process develops in *S. aureus* as two halves of the dividing cell separate into the two daughter cells. A set of experiments have been performed to study the architecture of the cell wall in mutants and under the influence of disruptive chemicals including detergent and lysostaphin. The experiments showed two distinct peptidoglycan architectures in *S. aureus*, the young rings and the mature mesh like structure. Comparing the organisation of the peptidoglycan in the mutants and the wild type cells showed that the features seen are made of peptidoglycan.

A series of quantitative analyses have been performed on the high resolution images of ringed architecture including measuring the concentricity of the rings and comparing this concentricity in the dense and less dense ringed structures which shows that the rings at both densities have a common centre that they orbit. A bearing analysis technique has been developed for the analysis of the holes that are seen within the mature architecture that allows the depths, densities and areas of holes to be quantified at different depths in the cell wall layer. This analysis shows that some of the holes are as deep as the thickness of the whole cell wall layer and up to 50% of the cell wall material can lay in the deepest 10 nm of the cell wall thickness that was imaged. An analysis of the diameter of the peptidoglycan fibres seen in the mesh architecture was performed to

measure the distribution of the fibre widths which was then used to calculate an estimate for the average number of glycan chains within a fibre.

Imaging of another Gram positive bacterial species, *B. subtilis*, has been performed using the same small amplitude tapping technique. A method of physical immobilisation using etched silicon wafers was developed for the rod shaped cells then a protein immobilisation process (Cell-Tak) was tested. Using Cell-Tak allowed high resolution images to be taken of the cell wall structure of *B. subtilis* revealing a previously unreported mesh like disordered organisation, similar to the mature architecture in *S. aureus*. The same analysis techniques that had been developed for the mature architecture in *S. aureus* were performed on the images from *B. subtilis* revealing holes that measure over 20 nm deep into the cell wall thickness as had been measured in *S. aureus*.

The first stages in developing a protocol for imaging outer membrane proteins *in situ* in Gram negative bacteria were made. BtuB is a protein that is responsible for the transport of vitamin B12 in *E. coli*. The BtuB proteins were overexpressed and reconstituted into lipid vesicles then imaged on a mica surface using small amplitude tapping mode. Partially deflated vesicles showed evidence of thousands of proteins on the surface with some proteins forming ringed structures.

The work aims to develop understanding of the cell wall architecture at molecular scale and how it changes over the cell cycle which could aid in understanding how these antibiotics that target the cell wall synthesis work.

Acknowledgements

First and foremost I would like to thank my parents and my sister, Imi, who have all supported me through the PhD and in every aspect of my life. Your help, love and homemade biscuits have seen me through.

I would like to thank Dr David Brockwell and his lab members, especially Dr Sam Hickman who showed me how to make the BtuB protein samples.

I would like to thank Professor Simon Foster for his guidance and all of the members of his ginormous research group for being so welcoming to the invaders from physics. Thank you to all of you for answering all of my basic microbiology questions and showing me where stuff is in the lab. I would particularly like to thank Dr Victoria Lund and Dr Bob Turner who were my go-to people to quiz on microbiology and AFM.

The person I am most grateful to during the course of my PhD is my primary supervisor Professor Jamie Hobbs. I would like to thank you for giving me the opportunity to do the PhD and then for your guidance and support throughout. It has been a pleasure to work in your research group. I would also like to thank the many members of the Hobbs group over the years that I have been working in Sheffield. In roughly chronological order I would like to thank Dr Nic Mullin, Dr Becc Savage, Dr Ross Carter, Dr Jake Albon, Dr Rik Bailey, Dr Paul Chapman, Lamiaa Alharbe, Stephen Jackson, Raveen Tank, Nick Jenkins, David Owen, Dr Sandip Kumar, Spyros Sovatzoglou, Dr Xinyue Chen and Laia Pasquina. You have all made it a friendly working environment, been great company and I have enjoyed collaborating with you all. I will miss being in the office with you all too. I would also like to thank my fellow soft matter and AFM users who are like an extended Hobbs family, in particular Dr Ana Lorena Morales-Garcia, Tom Kennelly and Amy Moores who I have enjoyed working alongside and socialising with as well as all of the other friends I have made in the department during the PhD.

I would finally like to thank my housemates during the four years of the PhD. In the top room Ben, Martin and Tom, thank you all for making the house a great place to live. I would also like to thank the two permanent fixtures alongside me, Dave and Rob who have put up with me or I have had to put up with, I'm not sure which. You have all made this time fly past and I'm sure I will miss living with some of my best mates.

Cheers!

Contents

List of figures

List of abbreviations

%	Percentage
~	Approximately
°	Degree
°C	Degree Celsius
β-OG	n-octyl-β-D-glucopyranoside
µg	Microgram
µl	Microlitre
µM	Micromolar
µm	Micrometre
2D	Two Dimensional
3D	Three Dimensional
A_{SP}	Set point Amplitude
A_0	Free Amplitude
Å	Angstrom
AFM	Atomic Force Microscopy/ Atomic Force Microscope
AMR	Antimicrobial Resistance
Atl	Autolysin
BHI	Brain Heart Infusion
BtuB	Cyanocobalamin
cm	Centimetre
CDM	Chemically Defined Media
Cryo EM	Cryo Electron Microscopy
Da	Dalton
D-ala	D-alanine
DEAE	Diethylaminoethanol
DNA	Deoxyribonucleic Acid
EDTA	Ethylenediaminetetraacetic acid
EM	Electron Microscopy
EPS	Extracellular Polymeric Substances
FTS	Tip-Sample Force
FtsZ	Filamenting temperature-sensitive mutant Z
$\delta F'_{min}$	Minimum Force Gradient
g	Grams
GlcNAc	N-acetyl glucosamine
h	Hour
HCl	Hydrochloric Acid
HDMS	Hexamethyldisilazane
HPLC	High Performance Liquid Chromatography
HS-AFM	High Speed Atomic Force Microscopy
Hz	Hertz
ICP	Inductively Coupled Plasma
JPK	JPK Instruments (AFM Manufacturer)
k	Spring Constant
KCl	Potassium Chloride
kDa	Kilodalton

kHz	Kilohertz
l	Litre
LB	Lysogeny Broth
LiCl	Lithium Chloride
LPS	Lipopolysaccharides
M	Molar
mg	Milligram
$MgCl_2$	Magnesium Chloride
min	Minute
ml	Millilitre
mM	Millimolar
MRSA	Methicillin Resistant *Staphylococcus aureus*
MurNAc	N-acetyl muramic acid
N	Newton
N	Number of samples
NaCl	Sodium Chloride
$NaHCO_3$	Sodium Bicarbonate
NaOH	Sodium Hydroxide
NB	Nutrient Broth
NH_2	Amino group
nm	Nanometre
NMR	Nuclear Magnetic Resonance
nN	Nanonewton
OD	Optical Density
PECVD	Plasma Enhanced Chemical Vapour Deposition
PBP	Penicillin Binding Protein
PBS	Phosphate Buffered Saline
PCTE	Polycarbonate Tracked Etched
PDMS	Polydimethylsiloxane
pH	Potential of Hydrogen
pN	Piconewton
Q	Quality Factor
QI mode	Quantitative Imaging mode
QNM	Quantitative Nanomechanical Mapping
R	Radius
RMS	Root mean squared
RNA	Ribonucleic acid
rpm	Revolutions per Minute
S-layer	Surface Layer
SIM	Structured Illumination Microscopy
SMD	Steered Molecular Dynamics
SDS	Sodium Dodecyl Sulphate
SDS PAGE	Sodium Dodecyl Sulphate Polyacrylamide Gel Electrophoresis
SPM	Scanning Probe Microscopy
STM	Scanning Tunnelling Microscopy
STORM	Stochastic Optical Reconstruction Microscopy

TBDT	TonB Dependent Transporter
TEM	Transmission Electron Microscopy
TLM	Time Lapse Media
Tris	Tris (hydroxylmethyl) aminomethane
TSB	Tryptone Soya Broth
UV	Ultra-violet
vs	Versus
v/v	Volume for Volume
w/v	Weight for volume
WTA	Wall Teichoic Acids
x	Multiplication

Chapter 1- Introduction and project aims

The field of microscopy has grown out of the interest in understanding objects that are too small to see with the naked eye. Variations of devices that use water or glass lenses to magnify objects have been developed for hundreds of years but it was not until the 17th century that a Dutch scientist, Antonie van Leeuwenhoek, developed a single lens microscope which he used to study what he called "animalcules". Some of these organisms were later determined to be the bacteria from the genus *Selenomonas* [(Cruz et al., 2015)]. The ensuing development of optical microscopes focussed on the development of better lenses and improved sample illumination to allow for the collection of better resolution information of a range of samples. In the field of biology microscopes were revolutionary.

There is a fundamental limit to the potential resolution that is possible with optical microscope systems which is known as the diffraction limit. It is due to the properties of light when it goes through a slit. Conventional optical microscopes cannot resolve features below this length scale (~200 nm). To circumvent this limit a range of techniques have been developed. Fluorescence microscopy is a technique that can be used to label specific parts of a cell and can be enhanced using super-resolution techniques that allow for resolution below the diffraction limit. Electron microscopy can also be used to image below the optical diffraction limit by utilising a beam of electrons to illuminate the sample instead of a beam of visible light. This can result in images with a resolution on the order of Ångstroms, however, the technique requires samples to be heavily processed and can cause damage to the samples. The other major branch of microscopy is Scanning Probe Microscopy (SPM) which includes the technique that will be focussed on in this thesis project. Atomic Force Microscopy (which will be fully discussed in Chapter 2) is a powerful technique, capable of obtaining images on the scale of nanometres. It can be used on a wide variety of samples including living biological cells. It is the most recently invented of the three major branches of microscopy with its development happening in the 1980s. Since this time the technique has been adapted for a wide range of uses including its use in studying bacteria (fully discussed in Chapter 2).

In the first part of Chapter 2 the experimental set-up of AFM will be detailed before an introduction to a selection of modes of operation that were important in this study. The concept behind charge screening by ions in the imaging buffer will be explained before the errors and artefacts that can arise from AFM imaging will be discussed.

Bacteria were first observed using one of the early versions of the optical microscope in the 17th Century and since then their study has become an important part of the study of microbiology. Bacteria are important to study because of the great influence they have on human life. Humans are host to many species of bacteria with some working to help maintain a healthy gut and some that can be pathogenic and can cause diseases. Outside of the human body bacteria are used in food processing, filtration and the production of proteins on an industrial scale. To further understand bacteria genetic manipulation and microscopy are often employed. Genetic techniques allow for specific properties of bacteria to be added or removed and then these new strains of the bacteria can be compared to a control strain. There are countless different variations of bacteria so some species have been chosen as model organisms so that there can be collective study on the same species. *Escherichia coli* is a well-known model bacterium that can cause infection in humans. It is a Gram negative species which means it does not hold the purple Gram stain. Gram positive model bacterial species include *Staphylococcus aureus* and *Bacillus subtilis.* The differences between the two classifications will be explained further in Chapter 2.

Chapter 2 will also explore the importance of bacteria. There are thousands of species so they have been classified into two main groups based on their cell wall and cell membrane properties: Gram positive and Gram negative. Details will be given on what determine which of these classifications a species of bacteria is in. The cell wall of bacteria is made of a biopolymer that there is no homolog to in eukaryotic cells. This molecule peptidoglycan will be explained as well as how it is formed and how it is inserted into the cell wall. The model bacteria that have been chosen to study in the main section of this thesis are both Gram positive. *Bacillus subtilis* and *Staphylococcus aureus* come from the same genetic class of bacteria so they do share many characteristics. Their similarities and differences will be explained as well as other characteristics to these bacteria like their division processes and previously published data will be reviewed. For both of these species of bacteria the peptidoglycan architecture has been studied using various techniques. This previous data will be presented before the current model for the peptidoglycan structure for each species will be outlined as well as how individual strands are organised together based on NMR data.

Antibiotics are used across the globe every day to save lives from diseases and in the prevention of disease. Even routine operations rely on the use of antibiotics but the rise of antimicrobial resistance in bacteria may jeopardise the ability to perform these

procedures in the future. The history of antibiotic development and the rise of resistant strains will be explained as part of Chapter 2.

AFM is a relatively new technique in terms of the history of microscopy of bacteria and it has many applications that it can be used to help the understanding of bacteria. The ability to image samples at resolution below the diffraction limit in a liquid and potentially physiological environment makes the AFM well suited to the study of bacteria. Established microscopy techniques must be adapted to allow the cells to be imaged using the AFM as there must be access to the cells from above the sample and there must be measures to ensure the cells do not get displaced by the scanning AFM probe. The results of AFM being used to study bacterial samples have so far provided great insight into the cell wall peptidoglycan structure, protein organisation and it has been used effectively as a force sensing tool to measure the physical properties of bacterial surfaces and proteins associated with them,

AFM of bacterial samples can be problematic due to the relatively topographic nature of the cells and the fact that some of them are motile. Some of the sample preparation techniques that have been used in other bacterial AFM studies will be outlined before some of the results of important AFM studies of bacterial samples will be discussed.

The third chapter in the thesis is the materials and methods chapter. It is in three main sections: microbiology methods, sample surface preparation methods and then methods for preparing the samples for imaging. The microbiological methods include all of the techniques that were needed to culture and process the bacterial samples. The sample surface techniques includes the method of producing the etched silicon wafers via photolithography and the trapping of the *B. subtilis* cells in upright columns and on a Cell-Tak coated surface.

The aims of the part of the project relating to the imaging of *S. aureus* are to better understand the structure of the cell wall peptidoglycan at the scale of single molecules so that a new model for the development of the cell wall architecture over time can be built. Much of the previous work has been performed on broken apart fragments of cells which can deliver useful information about the cell wall architecture, however, this cannot provide information about a dynamic process and there can be doubt about the relevance to the living bacteria. Having a reliable and repeatable method for the imaging of the cells is important to be able to collect enough data to have a comprehensive picture of the maturation process of the peptidoglycan so optimising the experimental

method is one of the aims of the project. The major aim of the project is to develop the imaging method to allow for high resolution images of the living cells. The models of how antibiotics work are on a whole cell basis so understanding their effect at a single molecule scale would greatly improve the understanding of their effect. Another key aim of the project is to develop effective methods of analysing AFM images that make them more quantitative. To be able to measure these quantitative parameters the resolution of the images needs to be consistently good enough to be able to compare the images. Imaging of dynamic processes such as peptidoglycan maturation and cell division at this higher level resolution would provide new information on how the organisation of the polymers within the cell wall are reorganised and may provide information on the function of some of the architecture that is seen.

Chapter 4 is the first results chapter and will cover the development of the small amplitude tapping mode for imaging of living *S. aureus* cells. The experiments that were performed trialling different AFM modes to determine the best experimental set-up will be described then the results from imaging the wild type *S. aureus* cells will be shown and discussed. The results of the mutant experiments will also be discussed.

The young ringed architecture that is seen in the *S. aureus* cells will be presented in Chapter 5, showing the different densities of ringed structures before focussing on some of the features and measurements that can be made from high resolution images of the recently inserted peptidoglycan. A concentricity analysis has been performed on the images of the rings which will be explained and the results will be presented and discussed.

The 6th chapter will concentrate on the mature architecture that is seen in the *S. aureus* cells. These mesh structures will be shown before the analysis of the mesh is presented including a bearing analysis and a fibre width analysis that were both performed on the mesh images.

Many cells during the imaging sessions were seen to be at different stages of a division cycle of *S. aureus.* Images that show cells that undergoing division events will be shown in Chapter 6 along with some experiments that investigate the effect of detergent and lysostaphin are presented. The data from Chapters 5 and 6 will be used to assemble an effective peptidoglycan remodelling timeline which starts with the dense rings progressing through to the disordered mesh.

For *B. subtilis* there is no reliable and repeatable method of trapping living cells for imaging with AFM that might allow them to grow and divide, as there is for *S. aureus.* The major aim of the work with *B. subtilis* is to create an experimental system that can trap the rod shaped cells for AFM imaging as effectively as the silicon holes do for spherical cells. High resolution imaging of the surface of *B. subtilis* would provide information about the outer cell wall which did not have as good resolution as the inner cell wall in the previous sacculi AFM studies which will be explained in Chapter 2. Combining the high resolution imaging with a trapping system that allows the growth and division of the cell would allow for a series of images showing how the peptidoglycan is remodelled during these processes. Chapter 7 details the development process of the silicon trapping system for *B. subtilis* through different iterations of the silicon pattern and the different imaging modes that were used to trap the rod shaped bacteria. Images will be presented of the cells that are trapped in the silicon channels. An alternative protein trapping method was tested in combination with high resolution small amplitude tapping mode. The optimisation of this technique will be explained and then the resulting images are presented. Due to the similarity in the structure that is seen in the *B. subtilis* and the mature architecture in *S. aureus*, a similar set of bearing analysis and fibre width analysis will be performed and then used to compare the results with the similar data in *S. aureus.*

BtuB is the protein in *E. coli* that is responsible for the transport of vitamin B12 into the cell. It has a plug that undergoes a conformational change when bound to the vitamin which opens a channel that allows the vitamin to pass through the outer cell membrane. The aim of the work with BtuB is to try to image the proteins in the lipid vesicles and study how they are organised with respect to each other. Another aim with the work is to try to push the resolution to possibly be able to resolve the different domains in the proteins. A final experiment could involve imaging the whole *E. coli* cells with the AFM using a rod shaped trapping technique like the one being developed for *B. subtilis* to then be able to image native proteins in a living cell.

In Chapter 8 this process and an explanation of some of the results from force spectroscopy experiment that have been obtained by the group of one of the supervisors of the project (Dr David Brockwell, FBS, University of Leeds) will be explained. The method of the extraction of the protein from *E. coli* cells, its transfer into the lipid vesicles and the sample preparation will be outlined. The results from imaging the lipid vesicles filled with proteins will be presented and discussed.

The final chapter of the thesis, Chapter 9, will summarise all of the work that has been done during the PhD project and discuss the outcomes and conclusions that can be drawn from the work before potential future work relating to the experiments and results will be discussed and explained.

Chapter 2- Background

2.1- Atomic Force Microscopy

Atomic Force Microscopy (AFM) is a powerful and widely used imaging technique that has been developed without the need to use lenses or illumination beams, therefore avoiding the problem of diffraction limited systems. AFM can achieve spatial resolutions far smaller (on the scale of nanometres) than some of the optical based techniques and also has an advantage over electron beam imaging techniques in being able to image samples in their natural state or at least without applying a conductive coating to the sample or using chemical fixation. Use of AFM is growing in the biological fields as it can be used in aqueous environments to track live processes and can also be used to measure physical properties of samples at single molecule scales. In this chapter the basic technique of AFM will be explained with some of the different modes of operation outlined. The modes that have been used in this project will be presented as well as some of the issues that can cause artefacts while using AFM imaging.

2.1.1- AFM configuration and principles

The Scanning Probe Microscopy (SPM) field includes a varied range of instrumentation that are based on the original Scanning Tunnelling Microscope (STM) which was first developed in Switzerland by Gerd Binnig and Heinrich Rohrer at the start of the 1980s [(Binnig et al., 1982)]. Their Nobel Prize winning design involves a sharp metal tip being scanned close to a conducting sample surface, while a voltage bias is applied between the tip and the sample. The system utilises the phenomenon of electron tunnelling, when there is a small distance between the conducting tip and sample surface, to be able to accurately measure the tip-sample separation. The set-up included a feedback system that used piezoelectric materials that kept the tip- sample separation at the desired value.

AFM was born out of the development of STM as modifications were made that would allow non-conducting samples to be imaged. Binnig, alongside Calvin Quate and Cristoph Gerber created the first AFM system that was able to image a wider range of samples [(G Binnig, CF Quate, 1986)]. A major component of the modern AFM was introduced in 1988 by Gerhard Meyer and Nabil Amer who developed the optical lever detection system that is widely used in AFM systems [(Meyer and Amer, 1988)]. The original AFM used an STM

to detect the deflection of the cantilever, while the optical lever detector introduced the use of a laser being reflected off the back of the cantilever and into a split photodiode to measure the deflection of the cantilever.

With these important breakthroughs in the development of AFM, a common set-up can be described.

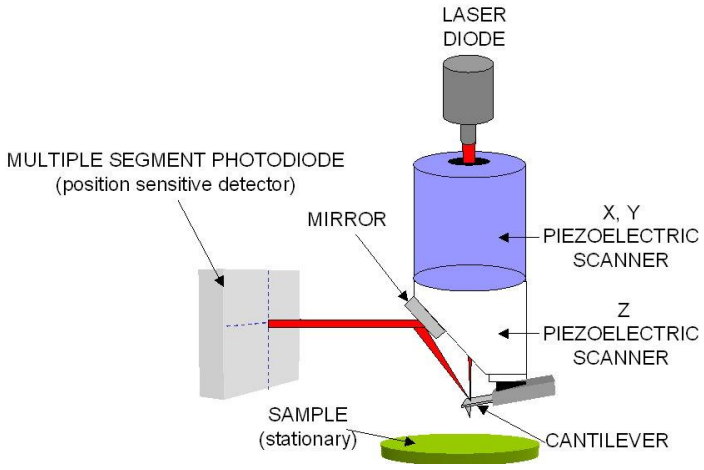

Figure 2.1- A schematic of a common AFM e.g. Veeco Dimension 3100. Reproduced from [(Varbel and Leilani, 2000)]

A cantilever is mounted into a cantilever holder which is positioned at the base of a piezoelectric Z scanner which is responsible for the fine positional control of the height of the cantilever. A laser diode shines a beam onto the reflective surface on the back of the cantilever, then into an adjustable mirror and then finally into a multi-segment photodiode (commonly 4) which is part of the detection system. There are two common configurations for how the tip is moved across the sample surface; tip scanning AFMs have the x,y and z piezos above the tip and scan the tip across the stationary sample or alternatively there are sample scanning AFMs which move the sample in x and y and z using piezoelectric scanners while the tip remains stationary.

Cantilevers are commonly made out of silicon or silicon nitride and often have a reflective material deposited on the top side of the cantilever like gold or aluminium to increase the amount of the laser light that is reflected into the mirror. The spring-like nature of the cantilever means the deflection of the cantilever can be used to measure interaction forces using Hooke's law for small deflections:

$$F = kx \qquad \text{Equation 2.1}$$

where F is the force applied to the tip, x is the cantilever deflection and k is the spring constant of the cantilever [(Cappella and Dietler, 1999)].

The cantilever's height is controlled by the Z piezo which constantly monitors the position of the laser spot in the photodetector and adjusts the height of the cantilever accordingly, to maintain a user defined setpoint value of the chosen feedback parameter.

Common parameters in AFM imaging that need to be adjusted by the user are the feedback gains: proportional gain and integral gain. These settings control how fast the feedback loop will adjust to a perturbation from the setpoint value. The proportional gain controls the instantaneous error in the feedback parameter, this error value is multiplied by a user controlled value for the proportional gain with a higher gain value adjusting for an error faster. The integral gain calculates the integral of the feedback error over time and then multiplies that by the user controlled value. The integral gain takes into account changes in the topography over a larger area rather than smaller point deviations in the sample surface that are adjusted for by the proportional gain. Together the gains must be optimised for every sample type, cantilever model and imaging environment. If the values for the gains are set too low the feedback loop will not track the surface well and there is a chance of damage to the tip if there is a tall feature that the cantilever does not climb over. Conversely, gains that are too high can introduce noise into the images as the cantilever lifts off the surface for small features leading to the surface not being tracked well and the potential of high frequency oscillations appearing in the images. The gains are dimensionless constants with values that are not the same for each model of AFM.

2.1.2- Interactions between the tip and the surface

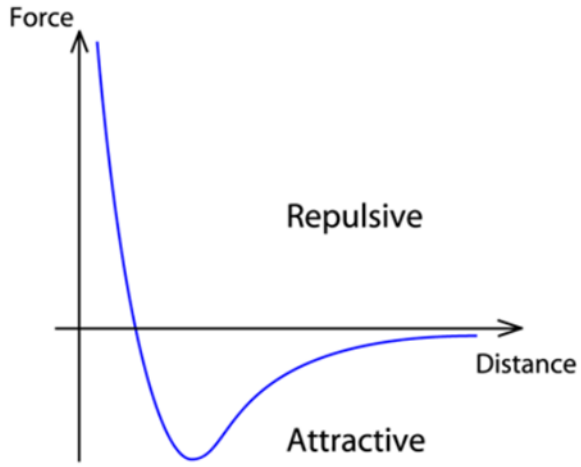

Figure 2.2 - A model force vs displacement curve showing the interactions between the tip and the sample as the tip sample separation changes. Reproduced from [(JPK Instruments, 2011)]

Force vs distance curves can be used to illustrate the balance of attractive and repulsive interactions between the tip and the sample with changing separation [(Cappella and Dietler, 1999)]. At large separations there is no interaction force felt between the tip and sample. As the cantilever is brought close to the sample surface it begins to feel a combination of different interaction forces. In general, the tip and sample will feel a weak attractive force at longer range distances due to van der Waals forces which get stronger as the two objects are brought closer together, resulting in a stronger attractive force (more negative in Figure 2.2). When imaging in liquid van der Waals and electrostatic forces can work over several nanometres but in air, these forces are several orders of magnitude smaller than the capillary forces between the water layer and the tip [Engel 1997]. These forces also dictate the adsorption of the sample to the surface. At short range there is a repulsive force due to the two objects touching. The two objects repel each other as they cannot occupy the same space. The strength of the repulsion increases as the tip is pressed harder into the surface. [(JPK Instruments, 2011)][(Paulo and García, 2001)][(Butt, 1991)][(Weisenhorn et al., 1989)]

2.1.3- AFM modes

There are a wide variety of AFM operating modes that use a variation on the set up outlined in Figure 2.2. One common difference between these modes is the choice of

which parameter is used as the parameter that the feedback loop will correct for. There are some other techniques that are more suited to different sample types or conditions [(Barth et al., 2011)].

2.1.3.1- Contact mode

Contact mode AFM involves the tip being held on the surface at all times while it is scanned across the sample surface. In the example force vs distance curve in Figure 2.2 contact mode operates in the repulsive region of the graph. It can either be used in constant height mode where there is no feedback loop used or constant deflection mode where the deflection of the cantilever is used as the parameter that is corrected for by keeping the deflection setpoint constant. In constant deflection mode the height of the sample at a given point on the surface is measured from the value of the height of the Z piezo. A deflection image can also be built which is calculated as the average deviation of the cantilever deflection from the deflection setpoint, giving an error associated with the imaging at a given point on the image.

Contact mode is a versatile imaging mode and can achieve molecular resolution [Kostic 2009]. It also does not create oscillations in the imaging liquid which can displace the sample, however, due to the tip being constantly in contact with the surface as it scans there are large lateral forces applied to the sample surface which can cause damage to soft samples like biological samples [(Zhong et al., 1993)].

2.1.3.2- Tapping mode

To overcome the issues of sample and tip damage in contact mode due to lateral forces, tapping mode AFM was developed [Zhong 1993]. In this mode the cantilever is oscillated at close to its resonant frequency with the tip tapping the surface each time it oscillates. In the force vs distance graph in Figure 2.2, tapping mode operates by oscillating between the attractive and repulsive regime. It was developed to use large oscillation amplitudes that allow the tip to overcome the adhesion forces between the tip and the sample. The feedback parameter that is used for the imaging is the amplitude of the oscillations with the root mean squared (RMS) value of the amplitude being calculated from the photodiode signal. In many models of AFMs, the cantilever oscillation is performed by a piezoelectric oscillator in the cantilever holder which can be oscillated at a range of different drive amplitudes and frequencies, while some AFMs will oscillate the whole Z piezo up and down to achieve the tapping motion. Each type of AFM cantilever has

different resonance properties and even two cantilevers of the same model will have slight variations in their resonant frequencies so it is important to tune the cantilever oscillation to its resonant frequency before imaging. To tune, the RMS amplitude of the oscillations of the cantilever is monitored as the piezo sweeps through a range of drive frequencies. Typically a frequency that gives a high amplitude response is chosen as the drive frequency. The actual frequency that is chosen for the cantilever oscillation is just below the peak of the resonance to allow for directional sensitivity in measurements, i.e. if the cantilever were tuned to the peak of the resonance curve, an interaction will result in a negative change in amplitude as the frequency of oscillation is shifted, however, if the cantilever is tuned to a frequency that is just to one side of the peak then it is known that an increase in frequency corresponds to an increase in amplitude and vice versa [(Rodríguez and García, 2002; Zhong et al., 1993)]. The drive voltage of the piezo can be changed during the tuning process to select a desired free amplitude.

Above the sample surface the tip will oscillate at its free amplitude. A parameter called the amplitude setpoint is controlled by the user and dictates the amplitude that the AFM will maintain the amplitude of oscillation at. If the amplitude setpoint is higher than the free amplitude then the tip will never engage with the surface. As the tip is brought closer to the sample surface interaction forces between the tip and the surface will start to affect the oscillation of the cantilever, reducing the amplitude. Once the amplitude of the oscillations reaches the amplitude setpoint the AFM will start scanning the surface, altering the height of the tip to maintain a constant amplitude. If the amplitude setpoint is decreased the tip will be brought closer to the sample surface and will exert higher force on the sample. During imaging a height image is created of the topography of the sample as the tip scans the surface. An amplitude image can also be created which maps the error in the amplitude at any point in the scan. The phase image can also be built from the difference in phase between the driven oscillation and the oscillation of the cantilever. When the cantilever is tuned a graph of how the phase differs between the drive signal and the recorded signal is formed. This difference in phase is known when the tip is not feeling any interaction with the surface but when the tip is brought closer to the surface the amplitude of the oscillation changes and so does the phase difference. These phase images can often show information or structure that is difficult to resolve in the height images. The phase can also show features in contrast when imaging a heterogeneous sample as the phase lag can be affected by the viscoelastic properties of a material [(Tamayo and Garcia, 1996)].

Tapping mode has been widely used in AFM measurements with modifications made since its initial use to improve its resolution and suitability for a wider range of samples. For soft biological samples that are loosely immobilised on a surface there is a difficulty in finding a suitable imaging mode that achieves high resolution without displacing the sample. Some AFMs have the capability of performing small amplitude tapping mode if changes are made to the experimental set-up. Small cantilevers used in liquid mode provide some advantages in having higher resonant frequencies than typical liquid cantilevers and are able to perform at lower amplitudes. The AFMs that can be used with these smaller cantilevers need to have high speed electronics that allow the piezos in the feedback loop to react fast enough and a smaller laser size that is compatible with the smaller cantilevers. Combining these improvements and the small cantilevers results in higher control over the amplitude of the cantilever with a lower noise measurement in the amplitude and also noise associated with the system is lower and spread across a larger range of frequencies.

Overall this enables finer control over the forces applied to the sample surface and a reduction in the acoustic waves that are formed in the imaging liquid which can be responsible for displacing the sample. The cantilevers that are used for the small amplitude tapping have a spoon shaped end that creates a larger reflective area. The amplitudes that can be used in this mode are below 1 nm of oscillation compared to typical values in conventional tapping mode of 20 – 100 nm [(Zhong et al., 1993)]. The tip length of these cantilevers is shorter (~3 µm) than regular TESPAv2 tapping cantilevers (16 µm) or the cantilevers used in liquid tapping, MLCT (8 µm), which means that for extremely topographic samples, the tip may not be able to reach the bottom of the features [(Bruker, 2017a, 2017b, 2017c)]. This technique has previously successfully been used to image proteins on the surface of self-supporting vesicles that are found in light harvesting bacteria [(Kumar et al., 2017a)].

Tapping mode is most commonly performed with the oscillations occurring flexurally or on the long axis of the cantilever. A technique has been developed that uses the torsional oscillation of the cantilever instead which allows for smaller amplitudes to be used which can obtain greater sensitivities. Special T-shaped cantilevers are used for the mode [(Mullin and Hobbs, 2008, 2011; Mullin et al., 2009)].

2.1.3.3- Force spectroscopy

The AFM is not only a powerful imaging tool but can also be used for measuring the physical properties of samples with only minor changes to the experimental method using the same equipment.

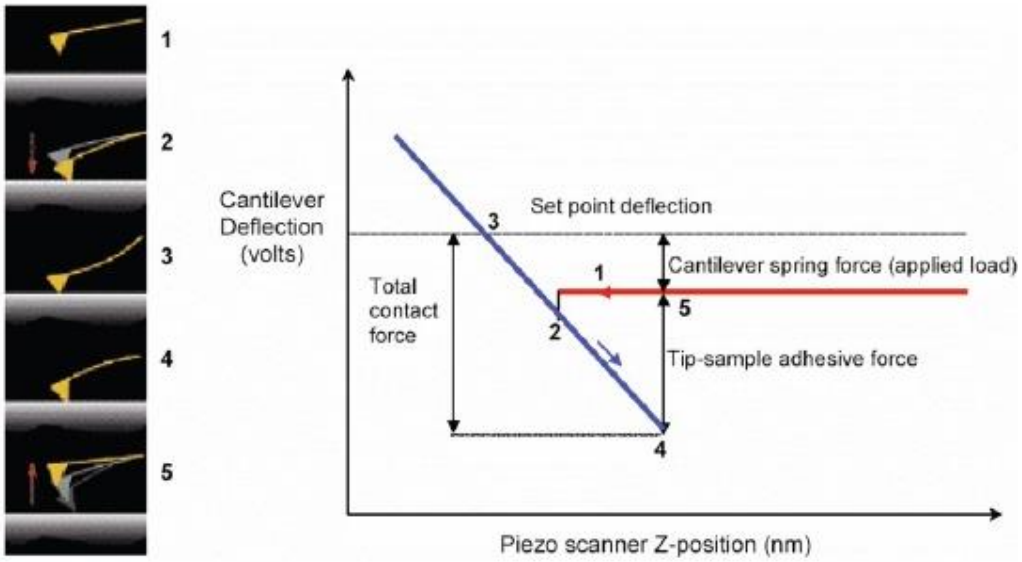

Figure 2.3- A typical force curve graph where the height of the Z piezo is plotted against the vertical deflection of the cantilever with representative cartoon of the cantilever deflection. The approach is shown in red and the retraction is shown in blue [(Kaemmer, 2011)].

The vertical deflection can be equated to the force applied to the cantilever due to Hooke's law (Equation 1). The tip is initially positioned well above the sample surface and has no vertical deflection as can be seen in Figure 2.3 (Point 1), the Z piezo is then lowered so the height of the tip above the surface decreases. When the tip comes close to the surface the tip can "snap" in to the surface (Point 2) due to attractive forces acting between the surface and the tip, deflecting the cantilever down. The cantilever begins to be deflected up and as the piezo is lowered further the tip is deflected (Point 3) until a trigger deflection is reached due to the tip pressing into the sample. This trigger deflection is controlled by the user and is set as the maximum force the user wants the tip to exert on the sample. At this deflection the piezo movement is reversed and the cantilever is retracted from the surface. The deflection of the cantilever is reduced up to and past the normal deflection of the cantilever (towards Point 4) and is then deflected down towards the surface so it has a negative deflection compared to the deflection at Point 1 when the tip is not interacting with the surface. This is due to the adhesive forces

between the tip and the surface that hold the tip on the surface, acting against the force of the retraction of the Z-piezo. When the force of the retraction of the piezo crystal becomes greater than the adhesive forces the cantilever will "snap" off the surface (Point 4 to Point 5) which causes the cantilever to return to its normal deflection where it remains for the rest of the retraction to the top of the Z length of the force curve. When the height of the piezo reaches the initial value (Point 1) the force curve is complete and the next force curve is ready to be taken.

Force curves can then be used to calculate stiffness and adhesion values which can then be converted into units that are commonly used in material property measurements like Young's modulus if the cantilever has been calibrated. Calibration is a two-step process which allows for the measurements that are taken in units of Volts to be converted into forces in units of Newtons. The tip must first be indented into a hard material like mica or glass to measure the deflection sensitivity of the cantilever which comes from calculating the gradient of the indentation curve in air. Secondly, a thermal tune of the cantilever must be performed to accurately calculate the spring constant of the cantilever. The most common technique requires measuring a power spectral density for the cantilever while it is in the environment that the experiment will take place in. The cantilever is held at one end and the fluctuations due to Brownian motion and other noise sources are recorded before plotting the amplitude of oscillation against frequency. By modelling the peak of the thermal noise spectrum as a simple harmonic oscillator, the peak can be fitted and a value for the spring constant can be calculated [(Butt and Jaschke, 1995; Hutter and Bechhoefer, 1993)]. The calibration process is often performed within and corrections are automatically applied by the AFM manufacturer's software [(JPK Instruments, 2012)]. From these two steps the force curves that are taken with the AFM can be plotted as Force in Newtons vs Distance in nanometres or micrometres and physical quantities can be calculated from them. An alternative method of cantilever calibration that is non-destructive can be performed. The Sader method of cantilever calibration only requires a measurement of the resonant frequency of the cantilever, a quality factor measurement and knowledge of the dimensions of the cantilever [(Sader et al., 1995, 1999)]. Force spectroscopy is a widely used technique on biological samples and allows for the ability to measure single molecule forces [(Bailey et al., 2014; Hickman et al., 2017; Pfreundschuh et al., 2014), (Dufrêne, 2015; Hugel and Seitz, 2001; Merkel et al., 1999; Pen et al., 2015; Rief et al., 1997)].

2.1.3.4- Force mapping

Single force curves can be used to measure the physical properties of a single position on a sample surface but on some samples there can be a heterogeneous nature to the physical properties. Force mapping or force volume mode involves a systematic approach to force spectroscopy where force curves are taken at chosen positions in a desired area to form an image where the values of the pixels represent a chosen physical property like stiffness or adhesion. The height of the sample surface can also be measured. Force mapping allows for a spatial representation of the physical properties like adhesion or stiffness which can be useful for locating specific binding points [(Hinterdorfer and Dufrêne, 2006)]. The tip does not undergo any movement in x or y while the force ramp takes place, only once the entire force ramp cycle is complete does the tip move to the next pixel location to take the next force curve [(Dufrêne, 2003; Müller and Dufrêne, 2008; Müller and Ziegler, 2013; Radotić et al., 2012; Roduit et al., 2009)].

2.1.3.5- Quantitative Imaging mode

Quantitative Imaging (QI) mode is an AFM mode developed by AFM manufacturer JPK that works like a faster version of force volume mode, allowing for higher pixel density scans while maintaining useable force curves that can give physical properties of a sample. It can measure the surface at a faster scan rate than force spectroscopy due to the deceleration procedure it undergoes at the top of the tip's travel as this stops the ringing in the force data that would be caused if normal force spectroscopy were used at this imaging rate. The speed of the imaging is not controlled by the scan rate but rather the ramp speed which is user defined and other parameters like Z length and the rate of deceleration when moving the tip to the next pixel location are also user controlled. This ability to customise the speed of imaging lets the user optimise the parameters for a given sample. On tall samples the Z length needs to be increased or there may need to be a larger lift height on sticky samples to ensure that the tip detaches from the sample surface. If these parameters are not optimised for each imaging session, noise from ringing of the cantilever as it moves between each pixel can cause false values to be recorded.

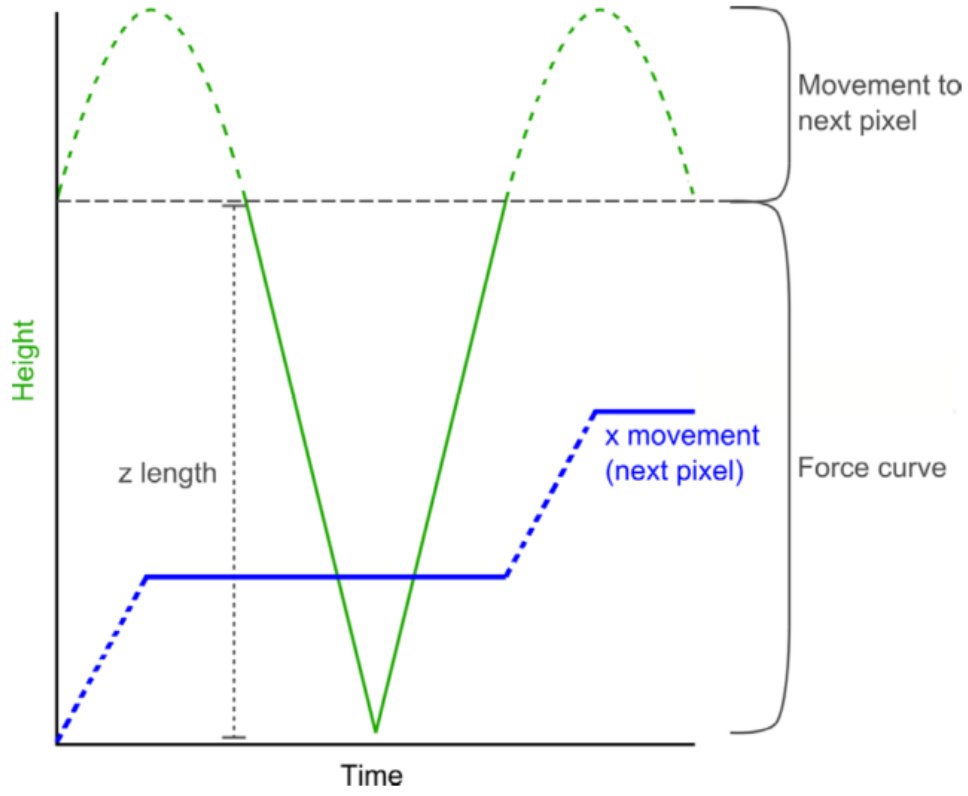

Figure 2.4- A schematic view of the tip movement algorithm in QI. The green line displays the Z movement of the cantilever, whereas the blue line symbolises the x movement. A complete force curve is recorded while there is no xy movement of the tip. Reproduced from [(JPK Instruments, 2011)].

QI can be used solely for imaging of samples without collecting the force data and holds an advantage over contact and tapping modes in practice as the force applied to the sample can be controlled better by using the force set-point feature of QI mode, so the surface of the soft bacterial samples could be imaged at a desired force. QI mode also does not exert lateral forces on the surface unlike contact mode so there was less chance of the cells being dragged out of the holes by the tip during imaging and fewer streaks were seen. QI mode is not designed to take high resolution images of samples but to allow for more detailed and faster force mapping capabilities so it was not suitable for obtaining images that match the highest resolution by contact or tapping modes [(Chopinet et al., 2013; JPK Instruments, 2011)].

2.1.3.6- PeakForce tapping

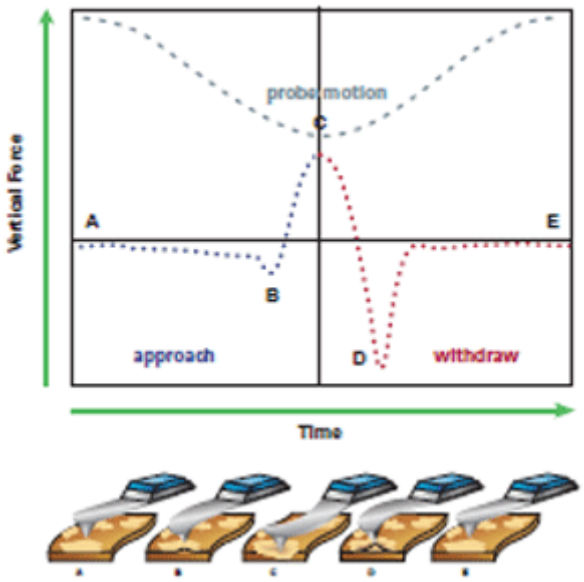

Figure 2.5- A schematic showing the PeakForce Tapping probe motion, the force vs time profile of each oscillation of the cantilever and a diagram of the probe interaction with the surface for each PeakForce oscillation. Reproduced from [(Kaemmer, 2011)].

An alternative approach is provided by PeakForce Tapping, developed by Bruker for their FastScan AFM head. It comes from a similar idea to QI mode as it is a fast force data taking method that allows for force control. The cantilever is oscillated at a frequency of 2-8 kHz which is not the resonant frequency of the cantilever and the acceleration of the cantilever is sinusoidal as shown in Figure 2.5. It uses feedback controls to maintain a constant set force by adjusting the height of the Z piezo. Unlike QI mode, PeakForce mode moves the tip in the xy plane at the same time as in Z. Physical properties can be calculated from these force curves in the PeakForce QNM mode (Quantitative Nanomechanical Mapping) if the tip is calibrated properly. The fast force curve modes allow for either higher spatial or temporal resolution force mapping of sample surfaces, the latter of which can be useful for imaging dynamic systems. PeakForce mode can struggle to image some topographic samples due to the small number of force curves that are taken per pixel. PeakForce imaging has been used to map the adhesion and deformation properties of a sample surface on a wide range of samples from inorganic materials [(Trtik et al., 2012)] to living cancer cells [(Heu et al., 2012)].

2.1.3.7- Small amplitude tapping mode

The Fast Scan D probe is designed for high resolution tapping mode imaging in liquid as it is physically smaller than a typical cantilever like a Bruker TESPA v2 or Bruker MLCT.

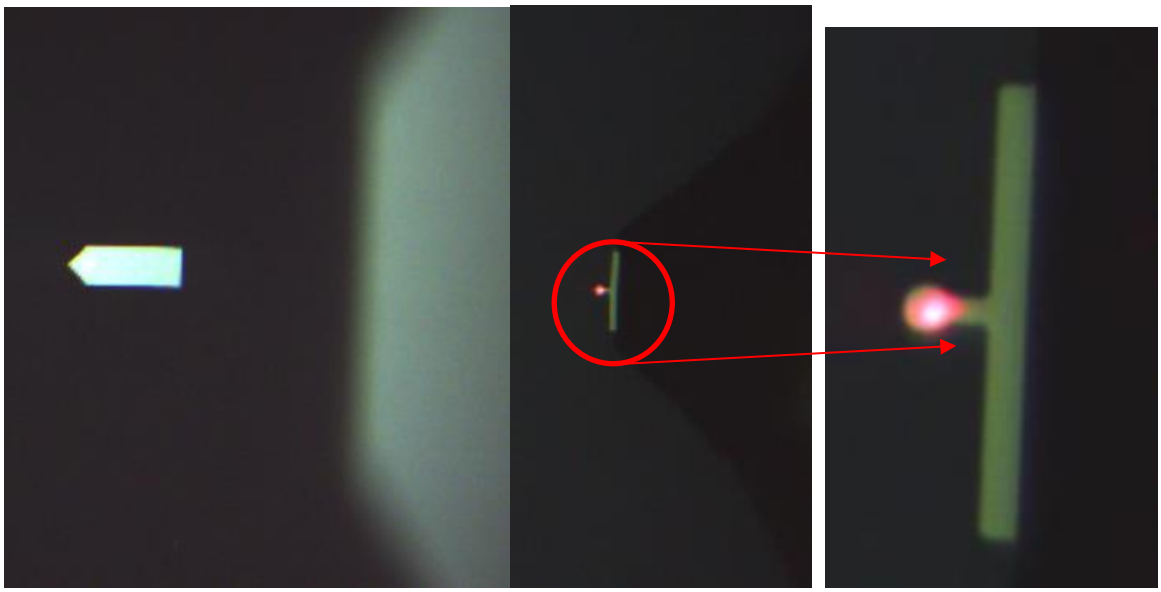

Figure 2.6- Optical images showing TESPA v2 cantilever at x1 zoom, FastScan-D cantilever at 1x zoom and FastScan-D at 3x zoom. The TESPA v2 is nominally 120 µm long and the FastScan-D is nominally 16 µm long.

Its size allows for smaller amplitudes which leads to better force sensitivity (higher signal to noise) meaning the force applied to a sample surface is more accurately controlled.

$$\langle F_{TS} \rangle = \frac{k}{2Q}\sqrt{\left({A_0}^2 - {A_{SP}}^2\right)} \qquad \text{Equation 2.2}$$

where F_{TS} is the force between the tip and the sample, k is the spring constant of the cantilever, Q is the Q Factor of the cantilever, A_0 is the free amplitude of the cantilever and A_{SP} is the setpoint amplitude. [(Rodríguez and García, 2003)]

During imaging it is important to keep the imaging forces low to avoid damaging the sample. To do this the setpoint amplitude should be as close to the free amplitude as possible to keep F_{TS} from Equation 2.2 to a minimum. Using the FastScan-D probes free amplitudes of ~1-2 nm are used with an ideal setpoint amplitude being 90% of the free amplitude as this keeps the imaging force low, ~10s pN.

By reducing the size of the cantilevers, probes with higher resonant frequencies can be produced. This gives the benefit of reducing the minimum change in force that is detectable and also helps the feedback system adjust to features faster.

$$\delta F'_{min} = \left(\frac{2k_1 k_B T B}{\omega_0 Q \langle {z_{osc}}^2 \rangle}\right)^{\frac{1}{2}} \qquad \text{Equation 2.3}$$

where $\delta F'_{min}$ is the minimum force gradient detectable, k_1 is the cantilever's spring constant, k_B is the Boltzmann constant, T is the temperature, B is the bandwidth of the measurement, ω_0 is the resonant frequency of the cantilever, Q is the Quality Factor of the oscillator and $\langle z_{osc}^2 \rangle$ is the mean squared amplitude of the oscillations[(Mullin, 2009)][(Martin et al., 1987)].

From Equation 2.3 by using the smaller cantilevers the resonant frequency is increased and a smaller amplitude of oscillation can be used which both result in a reduced minimum detectable force gradient.

Experiments performed by a fellow group member Dr Nic Mullin, shown in Figure 2.7, measured the deflection of a normal cantilever and a small cantilever as they were oscillated sinusoidally with an amplitude of 1 nm.

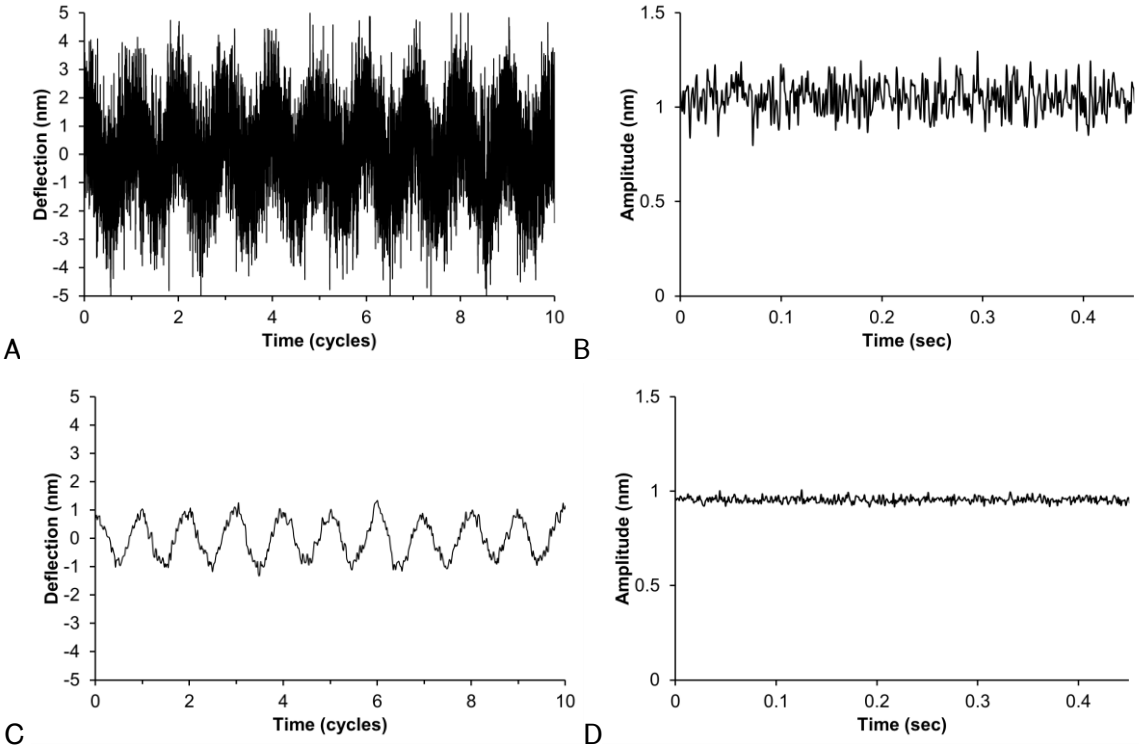

Figure 2.7- Graphs reproduced from (Kumar et al., 2017b) showing deflection of a large and a small cantilever changing over time as they are oscillated at a 1 nm amplitude in water. The large cantilever (Bruker DNP-B cantilever with a nominal length of 205 µm (A) & (B)) and The small (Bruker FastScan-D with a nominal length of 16 µm (C) & (D)) cantilever were driven sinusoidally. (A) & (C) show the raw signal while (B) & (D) show the demodulated amplitude signal using a lock in amplifier.

From the graphs in Figure 2.7 there is clearly higher noise in the larger cantilever than the smaller cantilever due to their improved lever sensitivity which means the small tip will be more accurate in maintaining a desired amplitude so the force applied to the surface can be controlled better [(Viani et al., 1999)]. The short cantilevers have also been shown to suffer less noise due to thermal motion [(Walters et al., 1996)][(Leung et al., 2012)]. From the graphs in Figure 2.7 the signal to noise ratio was calculated for the two cantilevers to be approximately 8 for the long cantilever and approximately 47 for the small cantilever [(Kumar et al., 2017b)].

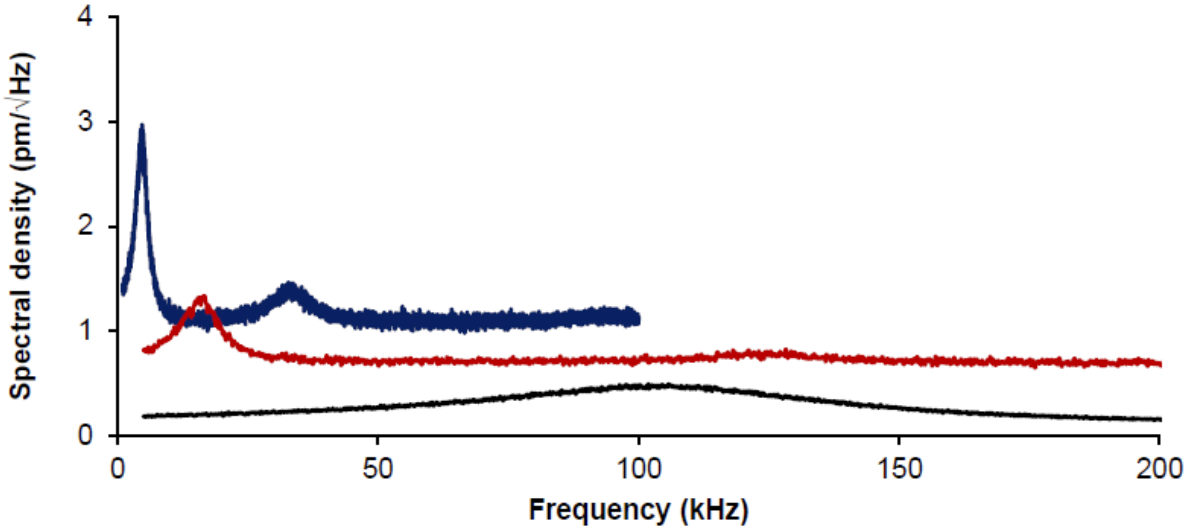

Figure 2.8- Reproduced from (Kumar et al., 2017b) shows the spectral noise densities over a range of frequencies of three cantilevers with similar spring constant values. The small cantilever is a Bruker FastScan-D with a nominal length of 16 µm (black), the medium cantilever is a Bruker DNP-C with a nominal length of 120 µm (red) and the large cantilever is a DNP-B with a nominal length of 205 µm (blue).

The noise of the small cantilever is also spread over a greater range of frequencies so it has a lower noise peak and the spread of noise allows a lock in amplifier to be used to filter out any frequencies of noise outside the resonance peak so overall there is a drop in the noise in the system [(Kumar et al., 2017b)].

2.1.4- Charge screening

Adding electrolytic salts to the imaging buffer can affect the interactions between the sample and the tip. Only short range forces carry high resolution information. Imaging a flat protein surface (OmpF protein and Aquaporins) under a high and a low concentration of the monovalent salt KCl showed 6 nm height difference [(Müller and Engel, 1997)]. The salt ions are attracted to the tip and the sample so they form a layer around each surface which reduces the repulsion force between the sample and the tip [(Butt, 1991)][(Engel et al., 1997)]. With a high enough salt concentration the electrostatic repulsion can be screened out which results in the correct sample surface height measurements when height measurements in low salt conditions can measure increased sample feature heights. $MgCl_2$ is a divalent salt and can be used instead of or together with the monovalent electrolytes. Divalent ions reduce the double layer thickness

measured by a factor of two when the height of the protein layers was measured in increasing divalent ion concentration [(Müller and Engel, 1997)]. Addition of these electrolytes screens charge between the tip and the sample surface, reducing the repulsive forces but has the undesired effect of also reducing the repulsive forces between the tip and other dirt in the sample. The concentrations of the monovalent and divalent salts must be tuned to suit the sample, optimising for resolution and preservation of the tip.

Another factor that can affect the tip-sample separation is pH. Experiments were performed where force vs distance curves were taken on purple membrane samples at a range of pHs from 3.2 to 10.3 showing best results between 6.1 and 8.2 [(Butt, 1992)]. Similar experiments have been performed that measured the height of the purple membrane suggested an optimal pH of between 7 and 8 [(Müller and Engel, 1997)].

2.1.5- AFM imaging artefacts

As the AFM tip scans the sample surface the image that is built can differ from the actual sample topography due to irregular interactions between the tip and the surface. These artefacts can manifest themselves in different ways on the image including streaks, smears and broadening of features.

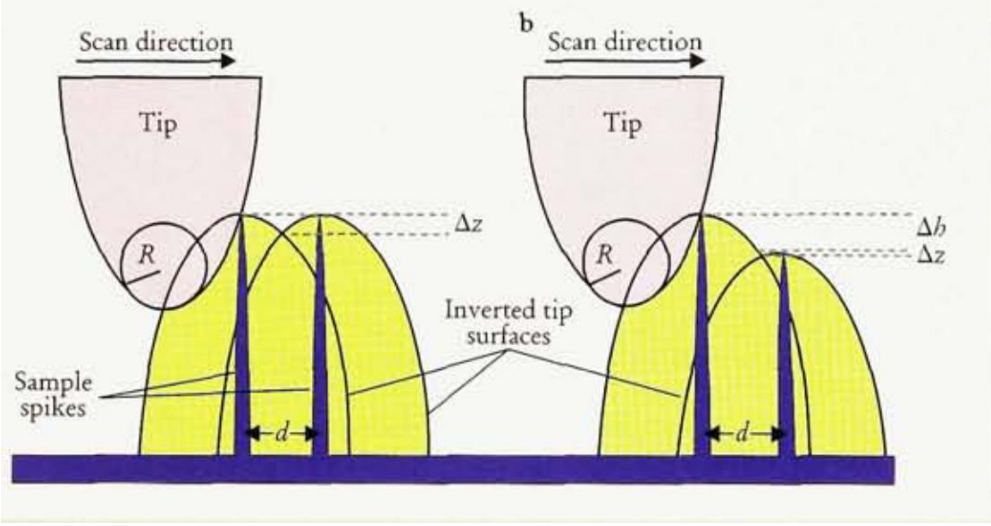

Figure 2.9- A diagram showing how scanning of small or narrow features with the tip can cause broadening of features in AFM imaging. The blue spikes are the sample features and the yellow area shows the topography that the tip measures. Reproduced from (Bustamante and Keller, 1995).

Tip broadening can occur on features that are narrow, often with a smaller diameter or separation than the tip radius. The tip will be scanning the sample and the sharp feature will interact with the side of the tip instead of the end of the tip, as shown in Figure 2.9. This will cause the feedback loop to react to the change in height of the surface, lifting the tip height up. As the side of the tip may still be triggering the set point value before the end of the tip is in contact with the surface the topography of the feature that is measured in the image is broadened. In Figure 2.9 the dark narrow features are measured to have the profiles of the broad yellow features due to this effect. This tip convolution can also have an effect on the height of some of the features that are measured with AFM due to the side of the tip interacting with nearby taller features. The diagram gives a good example of how the resolution of the image can be limited by the shape of the tip or the interactions between the tip and the surface. A surface feature will only be resolved if the tip can differentiate between one broad feature and two features that are close together. This type of artefact is extremely important in high resolution imaging as the small features on the surface are on down to 1 - 2 nm which is often smaller than the tip radius. It is difficult to know how much the broadening is contributing to the image that is being taken. The balance between the salt concentration and the tip shape is important in these artefacts as the buffer strength affects the charge screening between the tip and the sample, which can allow the tip to get closer to the surface, but it also affects the likelihood of dirt attaching to the end of the tip, which changes the shape of the tip and can cause this type of tip convolution and loss of resolution.

Imaging large objects such as whole bacteria with AFM has proven difficult and requires various trapping techniques. One of the reasons for this is the fact that whole bacteria are tall (>1 μm diameter) and have steep sides. The steep sides can cause convolution on a larger scale than in Figure 2.9 with a whole cell broadening effect. The tip may be scanning a flat surface when it comes to a cell that has a large height if cannot adjust the piezo fast enough, either dislodging the cell or causing these large broadening artefacts. This also happens as the tip has passed over the cell and the end of the tip is over a flat surface, the image that is built can show a shadow or streak artefact due to the side of the tip still hitting the cell. One way that can negate this effect is by trapping the cells in holes which allows the tip to only scan the top of the cell without having to scan the whole height of the cell. This also allows for the Z length of the imaging to be reduced which can lead to higher Z sensitivity in the measurements [(Alsteens et al., 2008; Bustamante and Keller, 1995; Velegol et al., 2003)].

2.2- Bacteria

Bacteria are important to study as they are the cause of many common diseases, play a role in maintaining human gut health, are used in the development of medicines and are vital in the nutrient cycle that enables all life to thrive on Earth. This section will outline some of the basic structural properties of different types of bacteria before discussing the different cell wall architectures that are seen in bacteria and our model for how antibiotics affect the cell wall architecture. Techniques for studying bacteria require methods of trapping the cells so that new information can be learned about bacteria so some methods of trapping them will be discussed before some of the findings from using AFM to study a range of bacteria and their proteins will be reviewed.

2.2.1- Overview

Bacteria are unicellular prokaryotic life forms which means that they do not have a nucleus containing their genetic information. The single cells are small, on the order of microns in size, but can exist in large colonies in biofilms [(Arciola et al., 2012; Toole et al., 2000)]. They are descended from the earliest life on Earth over 3 billion years ago and have evolved to fill niches in every given environment including those classed as extremophiles that can live in conditions like high temperature and high salt conditions [(Christner et al., 2003; Hoffmann et al., 2013; Rothschild and Mancinelli, 2001; Takami et al., 1997)]. Some genetic information is common to all bacteria, but through genetic mutations over billions of years the different species have evolved, though some have more similar genetic sequences. Bacteria are vital in maintaining gut health in humans as they help to digest food but they can also be responsible for many fatal diseases in humans including tuberculosis (caused by *Mycobacterium tuberculosis* [(Barkan et al., 2012; Smith, 2003)) and cholera (caused by *Vibrio cholerea* [(Heidelberg et al., 2000)]). [(Alberts, 2002)]

2.2.2- Gram negative vs Gram positive

Bacteria can be put into two major classifications which are called Gram positive and Gram negative. This classification mainly separates bacteria with two distinct types of cell wall. Gram positive bacteria have a thick cell wall made of peptidoglycan strands and a single cell membrane. The Gram stain tests whether the cell holds the colour stain so Gram positive bacteria hold the purple stain while Gram negative bacteria do not as they have a thinner peptidoglycan layer [(Ben-Yehuda and Losick, 2002)]. *Bacillus subtilis* is

used as a model Gram positive bacterium and *Escherichia coli* is used as a model Gram negative bacterium so there is a wealth of scientific knowledge on them from which example bacterial behaviour and mechanisms can be theorised and then these theoretical characteristics and properties can be tested in other bacteria to determine whether the models apply for all bacteria.

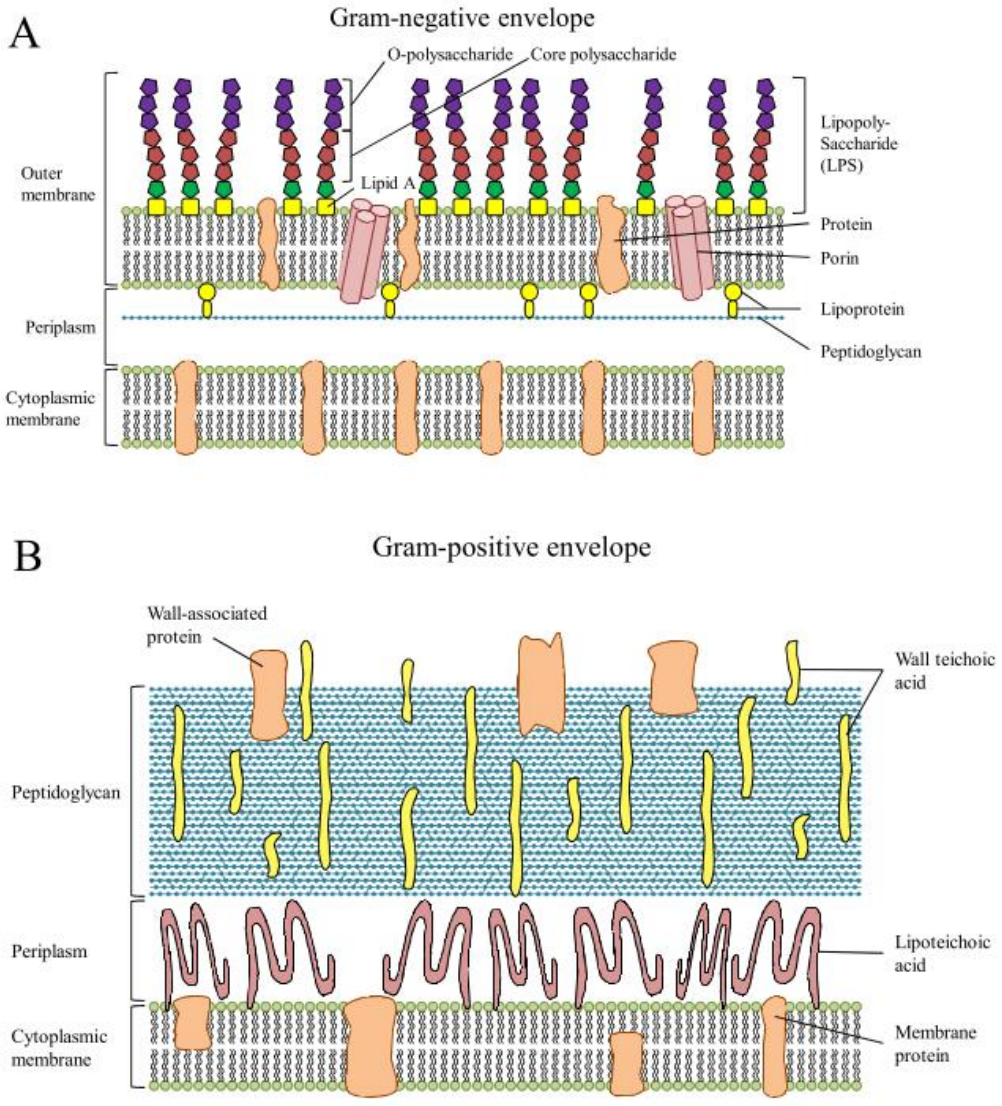

Figure 2.10- Schematics representing a cross-sectional view of the bacterial cell wall with A showing the Gram negative cell wall and B showing the Gram positive cell wall [(Wheeler, 2012)].

2.2.2.1- Gram negative

Gram negative bacteria (e.g. *Escherichia coli*) have an inner and an outer lipid membrane with a periplasmic region between them where a relatively thin (~6 nm in *E. coli* [(Vollmer and Seligman, 2010)]) peptidoglycan layer sits. The outer lipid membrane is full of lipopolysaccharides (LPS) and other proteins such as transport proteins which are responsible for the transport of nutrients and other molecules in and out of the cell. The inner membrane is a phospholipid bilayer which is full of a different set of proteins such as those responsible for energy production and lipid biosynthesis [(Hickman et al., 2017)]. The outer membrane is vital for the survival of Gram negative bacteria [(Silhavy et al., 2010)].

2.2.2.2- Gram positive

Gram positive bacteria (e.g. *S. aureus* and *B. subtilis*) have the same inner membrane set up as in Gram negative bacteria but do not have the outer membrane. On the outside of the cells is the relatively thick (15-30 nm [(Vollmer et al., 2008a)]) peptidoglycan cell wall to which some proteins are covalently bound as well as wall teichoic acids. There is a gap between the peptidoglycan cell wall and the inner membrane in *S. aureus* as seen by cryo EM data [(Matias and Beveridge, 2007)]. How this gap is maintained is currently unclear.

2.2.3- Wall teichoic acids

Wall teichoic acids are glycopolymers that are attached to the outside of the Gram positive cell wall. They are important for biofilm formation due to their charge aiding attachment to the surface and protecting the cells from antimicrobial agents [(Xia et al., 2010)] but are not vital for the *S. aureus* to live in laboratory conditions [(D'Elia et al., 2006)].

2.2.4- Peptidoglycan

Peptidoglycan (also known as murein) is made of glycan strands that are cross-linked by peptide bonds. There are two main glycan strands which are linked together, N-acetylglucosmaine (GlcNAc) and N-acetylmuramic acid (MurNAc), with the cross-linking being done by variations of amino acids, often including variations of Alanine and Glutamic acid as determined by high performance liquid chromatography (HPLC) [(Bottomley et al., 2014; Desmarais et al., 2013; Vollmer et al., 2008a)]. The specific peptidoglycan chemistry not only varies between bacterial species, as shown by Schleifer

and Kandler [(Schleifer and Kandler, 1972)], but can vary within a species depending on the conditions the bacteria are grown in [(Vollmer et al., 2008a)]. The average disaccharide chain length is also different between species with *Bacillus subtilis* having an average glycan length of 96 disaccharides while *Staphylococcus aureus* has an average of 6 to 10 disaccharides per chain. In both species there are much longer chains seen with 32.5% of chains having over 50 disaccharides in *S. aureus* and some *B. subtilis* chains being measured by AFM to be up to 5 μm in length [(Hayhurst et al., 2008; Vollmer and Seligman, 2010; Vollmer et al., 2004; Wheeler et al., 2015)].

Peptidoglycan synthesis has three main steps. Peptidoglycan precursor molecules are synthesised in the cytoplasm and then lipid linked to muropeptides, these are then flipped across the inner membrane by flippases before being polymerised into glycans and incorporating them into the cell wall by a process called transglycosolation. The crosslinking is performed by transpeptidases which form the peptide bonds between the glycan strands [(Lovering et al., 2012; Ruiz, 2015; Typas et al., 2011)].

Peptidoglycan hydrolases are enzymes that are responsible for hydrolysing bonds between peptidoglycan chains. There are specific hydrolases for each type of bond including glycosidases, amidases and peptidases. They can alter the surface of peptidoglycan layers causing the architecture of the peptidoglycan to change and can target specific regions on the cell to form pores for pili and flagella to form in [(Turner et al., 2014; Vollmer et al., 2008b)]. Yamada showed, with Electron Microscopy images of enzymes tagged with gold, that hydrolysing enzymes gather at the site of the next division septum of *S. aureus* [(Yamada et al., 1996)].

The machinery of bacterial cell division is conserved among many species of bacteria including FtsZ which forms a ring at the division site [(Wu and Errington, 2012)]. It is accompanied by other FtsZ interacting proteins, like FtsA, that help maintain the Z ring [(Bottomley et al., 2014; Loose and Mitchison, 2013)]. During peptidoglycan synthesis in *S. aureus* a set of proteins all localise at the site of division, the septum [(Pinho and Errington, 2005; Steele et al., 2011)]. The Z-ring appears to be continuous in *E. coli* but discontinuous in *B. subtilis* [(Buss et al., 2013; Holden et al., 2014)]. In Gram positive bacteria the FtsZ has been seen to form bead-like arrangements in *S. aureus* and *B. subtilis* [(Strauss et al., 2012)]. PBPs (Penicillin Binding Proteins) are responsible for incorporating the new peptidoglycan into the cell wall through transglycosylation and transpeptidation [(Mohammadi et al., 2011; Sauvage et al., 2008)]. There are low and high

molecular weight PBPs [(Scheffers and Pinho, 2005)] but in *S. aureus* only PBP1 and PBP2 are essential [(Reed et al., 2015)]. They both localise to the septum [(Pereira et al., 2009)]. PBPs are important to study as the β-Lactam antibiotics (the antibiotic class of penicillin) bind to the PBPs, stopping the new peptidoglycan from being added to the cell wall which results in the cell wall failing in a subsequent division event. MRSA has an extra PBP (PBP2A/MecA) which has a lower affinity for the β-Lactam antibiotics than the other PBPs allowing it to continue peptidoglycan synthesis [(Zapun et al., 2008)]. The divisome is formed of all of the proteins that are involved in division and septal formation and include the PBPs the DivI proteins and EzrA among others. EzrA is essential in *S. aureus* as it is needed to depolymerise the cell division machinery from the previous division site in Gram positive bacteria [(Levin et al., 1999; Steele et al., 2011)].

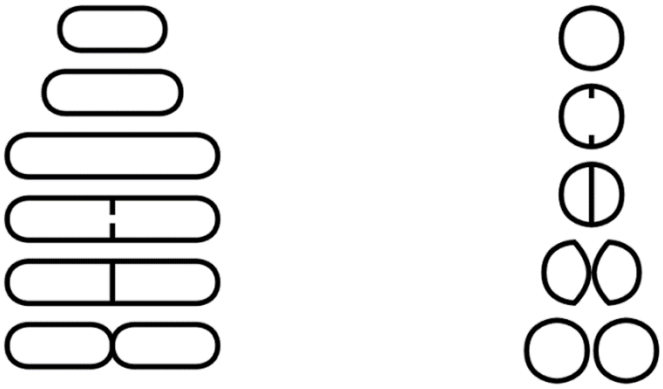

Figure 2.11- Diagram showing the division processes over time progressing from the top to the bottom of the image. On the left is *B. subtilis* and on the right is *S. aureus*. Reproduced from [(Turner et al., 2014)].

2.2.5- *Bacillus subtilis*

B. subtilis is an aerobic member of the Bacilli class and the Bacilli genus which all have the property of being able to form endospores in unfavourable conditions. These endospores can survive in varied extreme conditions and then can germinate and thrive once their environment changes [(Ben-Yehuda and Losick, 2002)]. *B. subtilis* is found naturally in soil in both spore and vegetative form. Due to the studies of the spore forming nature of *Bacillus subtilis* it has become commonly used as a model Gram positive bacterium in the same way that *E. coli* is used as a model Gram negative bacterium. This means that there is a wealth of knowledge and data on the structure and life processes of *B. subtilis* [(Alberts, 2002)].

B. subtilis begins its vegetative division process by elongating the length of the cell by adding new peptidoglycan material the whole way along the existing cell wall before forming a septum through the centre of the cell, half way along the long axis of the cell as can be seen in Figure 2.11. The septum closes and the cells on either side split apart leaving two daughter cells of equal size lying pole to pole. *B. subtilis* can form chains of cells lying end to end. Fluorescently tagged peptides have shown that *B. subtilis* adds new peptidoglycan in a helical pattern. In spore formation the division process involves an asymmetric septum forming towards one of the poles of the cell. The spore grows in the smaller region of the cell [(Ben-Yehuda and Losick, 2002)][(Tiyanont et al., 2006)].

2.2.6- *Staphylococcus aureus*

Staphylococcus aureus is a roughly spherical Gram positive species of bacteria from the Bacilli class and the Staphylococcus genus [(Alberts, 2002)]. It divides by a process of mitosis which is illustrated in Figure 2.11 with subsequent division events occurring in a plane that is orthogonal to the two previous events [(Turner et al., 2014)]. When a cell is ready to divide a septum made of peptidoglycan begins to grow from the cell wall towards the centre, some believe like the closing of a camera aperture [(Touhami et al., 2004)]. Fluorescent techniques such as STORM (Stochastic Optical Reconstruction Microscopy) or SIM (Structured Illumination Microscopy) have confirmed how the septum grows from the outside towards the centre of the cell [(Monteiro et al., 2015)]. Fluorescently labelled peptidoglycan precursors were added to cultures of growing cells at set time points of 5 minutes, 10 minutes and 15 minutes with each time point tagged with a different colour dye. The results showed slightly overlapping rings of different colours that marked septal peptidoglycan synthesis as well as showing evidence of off septal peptidoglycan synthesis in lower levels. These results are important as they prove the septal growth inwards and shows that there is peptidoglycan added in the rest of the cell in a similar fashion to *B. subtilis*, though at much lower rates of peptidoglycan addition than in the septum [(Lund, 2016)][(Pinho and Errington, 2005)].

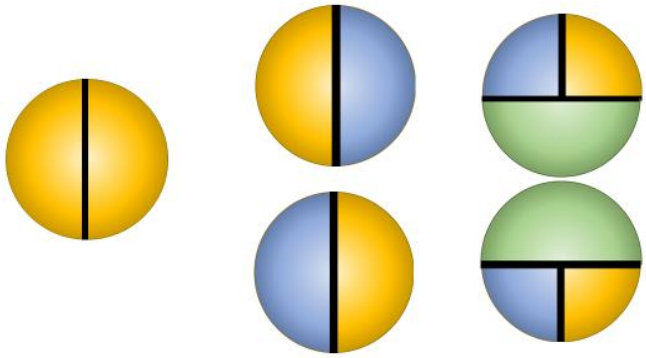

Figure 2.12- Representative cartoon of orthogonal division planes mechanism for dividing cells in *S. aureus.*

Two hemispherical daughter cells are formed once the septum has fully grown allowing a process of splitting to start where cell wall material that joins the two hemispheres is broken up, separating the two daughter cells [(Giesbrecht et al., 1998)]. Autolysins (Atls) are involved in the splitting and have been shown to localise in rings on the two daughter cells [(Yamada et al., 1996)]. Splitting and growth is theorised to be accomplished by a combination of mechanical stress and enzyme activity that weakens the cell wall with the splitting initially performed by hydrolases [(Giesbrecht et al., 1998)]. Fluorescence microscopy has been used to see a millisecond timescale re-organisation where the flat septal plate pops out to make a round but not fully inflated pair of daughter cells [(Zhou et al., 2015)]. The next division in *S. aureus* occurs in an orthogonal plane from the previous one. Approximately half of the cell is made of the old material and half by new material which forms the round cell by expansion of the septal plate (as seen in Figure 2.12). In the next division event the cells will divide in a plane that is orthogonal to the previous two planes of division forming a cell that has peptidoglycan from more than three generations of division events [(Turner et al., 2010a)]. The cells may not completely separate from each other but form "bunches of grapes" with other cells that can then grow to form colonies of cells [(Turner et al., 2010a, 2014)].

S. aureus is mostly non-pathogenic and some strains are commonly found in the noses and throats of humans [(Miller et al., 1991)]. There are strains that can cause infections in humans and animals like skin abscesses and bloodstream infections which can be fatal. Antibiotics, like those derived from penicillin, have long been used to treat these kinds of infections but growing numbers of *S. aureus* strains are mutating to become immune to the penicillin based β-lactam antibiotics [(Lim and Strynadka, 2002)].

Without the ability to effectively use antibiotics, routine surgeries and infections have become potentially fatal if a resistant strain is present and causes infection. MRSA (methicillin resistant *Staphylococcus aureus*) is a well-known "superbug" that can spread within a health care environment easily via the transiently colonised hands of hospital personnel. It is especially dangerous for the elderly or those with weakened immune systems. It is responsible for hundreds of deaths in the UK each year and more world-wide with numbers expected to increase due to the increasing numbers of resistant strains [(Lee et al., 2013; Office of National Statistics UK, 2013)].

2.2.7- *Escherichia coli (E. coli)*

E. coli is an anaerobic, rod shaped, Gram negative bacteria [(Alberts, 2002)]. It is used as a model organism for bacteria due the ease and low cost of growing it in laboratory conditions. It was one of the first organisms of any type to have its whole genome sequenced. It is found in the lower gut of animals and can be passed to new hosts through the spread of faecal matter. It can cause infections in humans that can be fatal [(Blattner et al., 1997)]. *E. coli* is widely used in biotechnology to produce proteins due to its fast growth rate, high yield and widely studied nature [(Huang et al., 2012)].

BtuB is an outer membrane protein of *E. coli*. It is responsible for the transport of vitamin B12 into the cell. Some nutrients that the cell need are too large to fit through porins or are in too low concentrations to spontaneously diffuse into the cell. The background about this protein and the mechanism that it uses to transport the large substrate into the cell is discussed in detail in Chapter 8.

2.2.8- Models for peptidoglycan structure

Peptidoglycan is present in nearly all bacterial cell walls and is fundamental for maintaining the shape of the cell, resisting the turgor pressure from within the cell and as an anchor point for proteins. Bacteria come in a range of different shapes and sizes with different cell wall thicknesses depending on whether it is a Gram positive or Gram negative bacteria.

Initial models of the how the peptidoglycan is arranged in the *E. coli* cell wall came from electron microscopy data that suggested a uniform monolayer of peptidoglycan where the glycans all run parallel to each other in the same plane and are linked together by T-shaped cross-link bonds [(Braun et al., 1973)]. Later *B. subtilis* was imaged using electron

microscopy, showing glycan orientation circumferentially around the cell [(Verwer and Nanninga, 1976)]. This became the standard model of the peptidoglycan arrangement in the bacterial cell wall [(Turner et al., 2014)].

NMR experiments on synthetic peptidoglycan fragments led to a scaffold model for the peptidoglycan structure in *S. aureus* [(Turner et al., 2014)]. The scaffold model involves glycans that are oriented perpendicular to the plane of the plasma membrane with peptide bonds in a zig zag conformation that join the glycans [(Dmitriev et al., 2003)].

AFM and TEM have been used to understand structures of bacterial cell walls. Cells can be broken open and purified into peptidoglycan sacculi that retain the structural architecture that was present in the cells or whole cells can be imaged under physiological conditions. The resolution of the data taken on these samples has allowed a greater understanding of the peptidoglycan structure and the differences between different bacteria.

2.2.9- Peptidoglycan in *S. aureus*

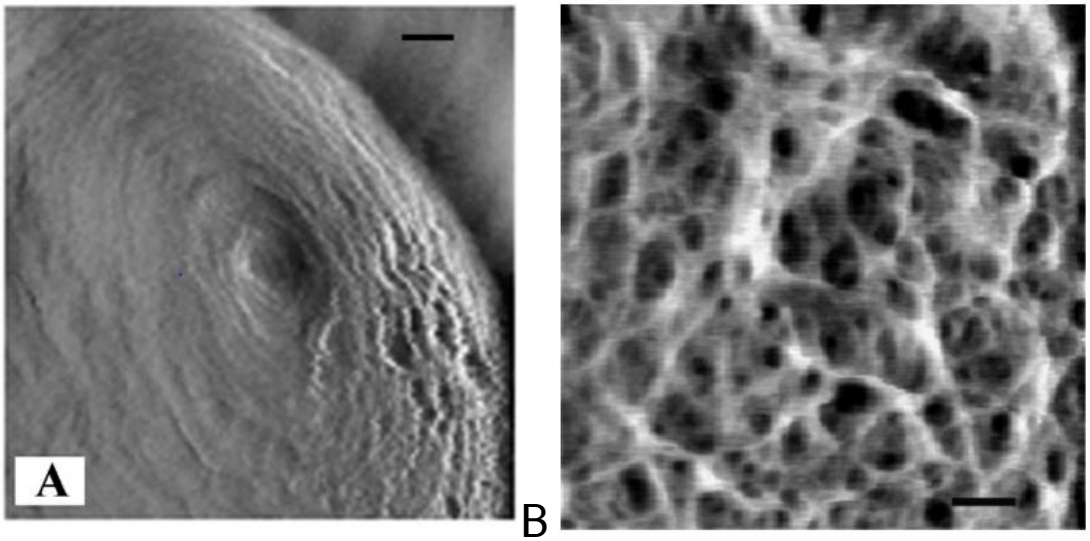

Figure 2.13- AFM images of whole *S. aureus* cells trapped in polycarbonate filter pores. (A) shows an AFM deflection image of a cell with concentric rings with a scale bar = 50 nm. (B) shows a topography image of an older cell wall with a scale bar = 50 nm. [(Touhami et al., 2004)]

Electron microscopy of freeze-fractured *S. aureus* cells was the first evidence of both the ringed structure and the "rough, irregular" structure on the surface of the cell. It was suggested that the concentric rings are the newly generated cell wall [(Amako et al.,

1982)]. This was the first suggestion of heterogeneity in the peptidoglycan structure on the same bacteria. The same structures were first seen when imaging whole cells with AFM by Touhami in 2004 as in Figure 2.13(A). Their paper showed that whole *S. aureus* cells could be trapped in filter pores and then imaged in growth media [(Touhami et al., 2004)]. The images show a ringed structure that revolved around a central depression that was measured to be 30 nm deep. They also measured the rings to have common spacings of 13 or 25 nm. Finally, they saw evidence of a mesh like structure (Figure 2.13(B)) with holes for the mature architecture of the cell with fibres as small as 8 - 14 nm in diameter resolved. They concluded that the scaffold model was the most likely model for the strand orientation with glycan strands lying perpendicular to the inner membrane.

Imaging of pure peptidoglycan in the form of sacculi was able to confirm that the rings that are seen are indeed formed of peptidoglycan without the teichoic acids or other proteins. The mature architecture was seen as a knobbled or rough structure. There was also the ability to look at peptidoglycan structures from inside the cell including the pie crust which is a thick band of material that forms during the division process as the septum is grown. There was evidence of multiple intersecting pie crusts which the cell could use as a marker for the orientation of the next division plane [(Turner et al., 2010a)][(Kent, 2013)].

The transition between the ringed structure and the mature structure has not been imaged using any technique.

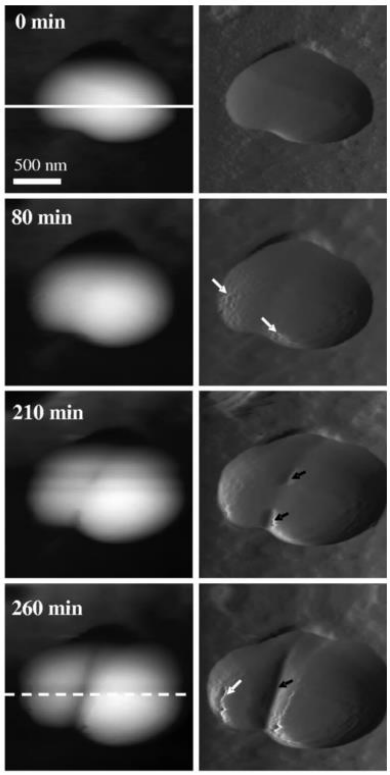

Figure 2.14- A series of height (left) and deflection (right) AFM images recorded of an *S. aureus* cell imaged in PBS with 16 µg/ml lysostaphin added at 0 minutes. The white and black arrows show splitting of the septum [(Francius et al., 2008)].

Previously published data by Francius studied the effect of the enzyme lysostaphin on the *S. aureus* cell wall with liquid AFM. The cells showed signs of nanoscale perforations in the cell wall over 260 minutes of imaging as shown in Figure 2.14 [(Francius et al., 2008)].

2.2.10- Peptidoglycan in *B. subtilis*

Work performed with fluorescent imaging techniques including using fluorescent antibiotics showed that peptidoglycan is added in a helical pattern in *B. subtilis* along the whole length of the cell as opposed to the majority of peptidoglycan addition happening in the septal plate in *S. aureus* [(Daniel and Errington, 2003; Tiyanont et al., 2006)]. An AFM study of *B. subtilis* sacculi showed evidence of thick bands of peptidoglycan that run circumferentially on the inside of the cell wall, which were likened to cables of peptidoglycan that had a measured width of 53 ± 12 nm. Glycan strands of up to 5 µm in length were measured which exceeds the length of the *B. subtilis* cell so a coiled coil model was proposed that then forms bands. At the septum of the bacteria a thick ring of peptidoglycan was seen. The structure on the outside of the cell was not as distinct

which was suggested could be due to partial hydrolysis of the band structure on the outside of the cell [(Hayhurst et al., 2008)]. Other techniques have not seen any evidence of the band structure and suggest a model similar to Gram negative peptidoglycan that has glycan strands that run circumferentially around the cell [(Beeby et al., 2013; Turner et al., 2014)].

2.2.11- Model of peptidoglycan in *S. aureus* and *B. subtilis*

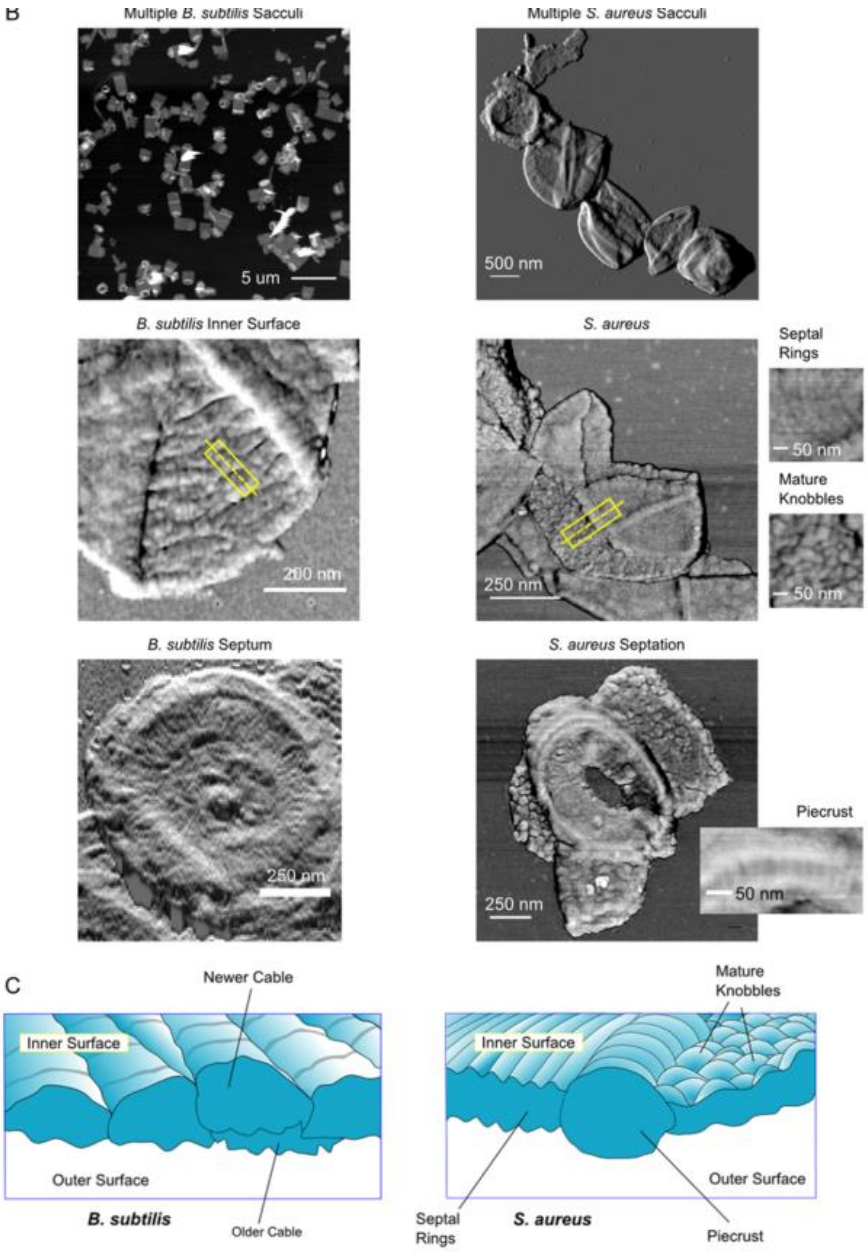

Figure 2.15- Top- AFM gallery of bacterial sacculi images showing key architectural features for *B. subtilis* (left, [(Hayhurst et al., 2008)]) and *S. aureus* (right, [(Turner et al.,

2010a)]). Bottom- interpretive diagrams of the peptidoglycan architecture based on the regions marked by the yellow box in the AFM images [(Turner et al., 2014)].

From all of the previous data Turner produced a set of cartoons to represent the cell wall structure for each bacterial species as seen in Figure 2.15. It shows the *B. subtilis* cell structure as the cabled structure that was seen by Hayhurst with a degraded or hydrolysed structure on the outside of the cell [(Hayhurst et al., 2008)]. The representative structures for *S. aureus* include the ringed structure that had been seen in many studies [(Amako et al., 1982; Bailey et al., 2014; Touhami et al., 2004; Turner et al., 2009, 2010a)], the pie crust structure that was seen in the sacculi work and a "knobbled" structure that is similar to that seen in the sacculi work [(Turner et al., 2010a)].

2.2.12- NMR peptidoglycan structure

Nuclear Magnetic Resonance (NMR) is a physical phenomenon involving the alignment of nuclei that have non-zero spin with a strong external magnetic field. The effect can often be enhanced by using proton rich atoms such as ^{13}C and ^{15}N [(Marion, 2013)]. Solid state NMR has been used to study the peptidoglycan architecture of Gram-positive bacteria including *S. aureus* and *B. subtilis*. Purified peptidoglycan fragments are used for the measurements. In *S. aureus* a helical 4-fold axial symmetry was measured with a period of 40 Å and a parallel stem architecture. In this parallel system a distance from glycan to glycan in *S. aureus* was measured to be 23 Å [(Kim et al., 2015; Sharif et al., 2009a, 2009b)]

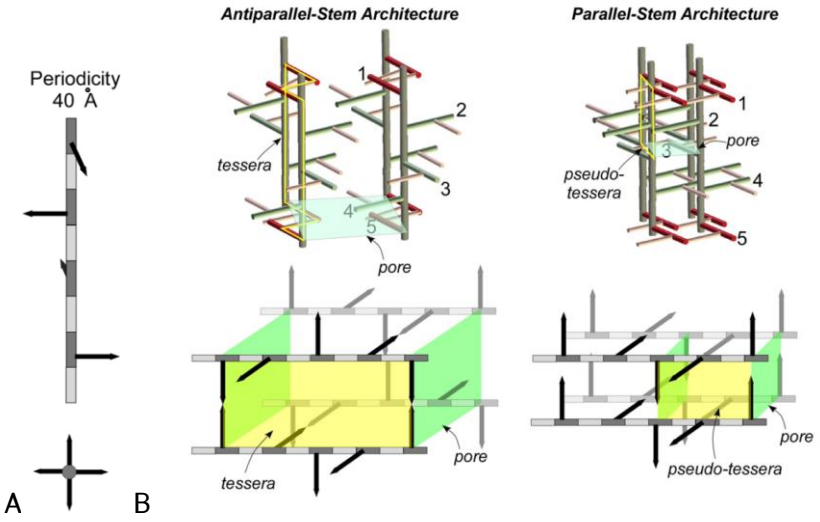

Figure 2.16.- (A) is a representative schematic of a 4 fold axial symmetry helical glycan backbone conformation with a periodicity of 40 Å [(Kim et al., 2015)]. (B) is a schematic

diagram of peptidoglycan architecture in antiparallel and parallel organisations with a hypothetical PG cell-unit structure below showing pores in green and tesserae in yellow [(Kim et al., 2015)].

The NMR data can also determine a crosslinking percentage based on the parallel or anti-parallel architecture. In the parallel system (*S. aureus*) the peptides can theoretically form 100% of the available bonds in the peptidoglycan while in the anti-parallel architecture (*B. subtilis*) a maximum of 50% of the bonds can be formed [(Kim et al., 2015)]. Crosslinking percentages have been measured for two strains of *S. aureus* giving values of 66% and 75% crosslinking [(Kim et al., 2002)][(Sharif et al., 2009a, 2009b)] and some Fem mutants had 70% and 50% [(Sharif et al., 2013)]. The Fem mutants have modified chemistry in their bridges.

2.2.13- Antibiotics

Antibiotics play a crucial role in the treatment and prevention of bacterial diseases and infections in modern day medicine. There is evidence of multiple ancient cultures using antibiotics at different times [(Aminov, 2010)] but the modern pioneer of antibiotics was famously Alexander Fleming in the late 1920s when he wrote about his discovery of penicillin which had been filtered from a mould fungus. He noticed that some bacterial plates that he had left to the side and monitored over time had been infected by a mould culture and that staphylococcus colonies around the mould had turned transparent because they had lysed [(Fleming, 1929)]. Antibiotic compounds are naturally produced by some organisms as a way of outcompeting bacteria for natural resources which is how the fungus had made the bacterial cells lyse [(Sengupta et al., 2013)]. A clinical version of penicillin was developed by Fleming and also by a team of chemists in Oxford. By the 1940s it was being prescribed to treat serious infections and was especially important in saving the lives of soldiers in World War II [(Aminov, 2010; Ventola, 2015)]. A wave of new antibiotics were discovered in the next three decades but the rate of discovery tailed off after the 1970s with the last novel antibiotic class to be used clinically being discovered in 1984 [(Silver, 2011)].

The timeline of discovery of new antibiotic resistant strains has closely followed the discovery of new antibiotics. In the 1950s the first evidence of penicillin resistant bacteria was seen and the first evidence of MRSA was seen in the 1960s. As novel antibiotics were being discovered around this time this resistance was combatable but since the rate of antibiotic discovery has slowed, resistance is a growing international issue. Vancomycin

was discovered in the 1970s and was used for treating the virulent strain MRSA, being labelled as the "last resort" antibiotic which would be effective against any resistant strain, however, in the 1980s cases of vancomycin resistance were reported [(Ventola, 2015)]. Antimicrobial Resistance (AMR) continues to be a growing problem globally with some reports estimating up to 10 million deaths per year from AMR related causes by 2050 [(de Kraker et al., 2016)].

Cell wall synthesis is an important process as a target for antibiotics with the PBPs being the target for β-lactam antibiotics like penicillin which stop new peptidoglycan from being added to the cell wall [(Coyette and Van Der Ende, 2008)]. Peptidoglycan is widely studied candidate for antibiotics as it does not have an equivalent in prokaryotic cells. Some other targets for antibiotics are essential proteins and DNA or RNA [(Andreu et al., 2010; Kohanski et al., 2010; Vollmer, 2006)]. There are also different antibiotics that are targeted only for Gram-positive or only for Gram-negative species of bacteria [(Lewis, 2013)].

2.14- Trapping bacteria for imaging.

Bacteria have evolved methods of propulsion and mechanisms for anchoring themselves to surfaces including with pili and with extracellular substances like mucus [(Bullitt and Makowski, 1998; Harshey, 2003; Le et al., 2013)]. There are large industries that are centred on avoiding the adsorption of bacteria with research into surfaces that try to stop them from sticking to surfaces [(Al Aani et al., 2017; Alves and Olívia Pereira, 2014; Appendini and Hotchkiss, 2002; Page et al., 2009; Whitehead et al., 2006)].

Despite the mechanisms for adsorption, during the AFM imaging of live bacteria in aqueous environments cells must be immobilised so that they can be effectively imaged. Cells can be easily imaged in air on a variety of substrates like silicon or mica but these are not suitable for imaging in liquid because the cells are able to be displaced from the substrate as the tip images. There are five main methods of cell immobilisation: mechanical trapping, adsorption to the surface of polymers, covalent binding, attachment via polyphenol proteins and lectins and immunospecific adsorption [(Kuyukina et al., 2013)].

Mechanical trapping involves physically confining the cells using a patterned substrate or a filter [(Kasas and Ikai, 1995; Turner et al., 2010a)]. The cells are trapped in spaces that are small enough that they cannot be easily knocked out of the holes while being big

enough that they do not physically constrain the cells and affect their properties. If the cells are trapped in holes that are too small it can disrupt the cell division and growth processes leading to deformations of the cell [(Kuyukina et al., 2013)][(Velegol et al., 2003)].

To fabricate the trapping substrate UV photolithography is used. The chosen pattern depends on the shape of the bacteria being imaged e.g. *S. aureus* uses ~1.25 μm diameter circular holes [(Kailas et al., 2009)]. For the filter pore method, the cells are passed through a membrane filter (can be polycarbonate tracked etched (PCTE) filters) with appropriately sized pores. The etched gratings hold an advantage over other trapping techniques because the tip does not have to image over the whole height of the cell; just the top surface of the cell is imaged so the risk of the tip being damaged is reduced. Other advantages of the substrates are that, once they have been made, they are durable and easy to clean so can be used repeatedly and they can be made to trap cells of varying shapes unlike the filter which can only trap spherical bacteria. The filter is an effective way of trapping cells that does not affect the chemical properties of the cell but the cells can be damaged in the trapping process or if a vacuum action is used to suck the cells into the pores [(Kuyukina et al., 2013)].

One type of grating that has been used to trap bacteria is a "bed of nails" silicon substrate which has tall spikes that stop the cells from being knocked away during imaging. This substrate comes with the problem that only force maps can be taken of the samples because acoustic waves that are created in liquid tapping mode dislodge the cells [(Bailey, 2014)].

The material used for fabricating the immobilisation grids has been experimented with. Polydimethylsiloxane (PDMS) is a silicon based polymer that is the common material for making microfluidic devices. Its physical properties can be tuned to suit the sample by varying the amount of crosslinking in the mixture. A higher concentration of the curing agent results in a more crosslinked and, therefore, a stiffer polymer. PDMS can be patterned by casting it onto a mould which is often made using photolithography as above. Flow channels can be incorporated into the design of the microfluidic device [(Formosa et al., 2015; Friend and Yeo, 2010)]. Obviously changing the material of the immobilisation also changes the chemistry of the surface that the cells will interact with, but PDMS is silicon based and is commonly used in experiments with bacteria [(Long et al., 2013; Wang et al., 2010)]. PDMS is not as expensive or labour intensive to make as the whole photolithography process that is used to make the silicon substrates, however, the

PDMS requires a silicon master to be made that is then used to cast the PDMS on. By using the PDMS it can reduce the potential damage that can occur on the silicon master. Agarose has also been used as a material for microfluidic patterns [(Bisson-Filho et al., 2017; Grant et al., 2014)].

2.15- Chemical trapping methods for bacteria

Selecting a chemical surface that can form bonds with the surface of the cell to anchor it to the substrate is a widely used technique in biology. Chemicals including poly-L-lysine, APTES, gelatine and polystyrene have been used. [(Bailey, 2014; Doktycz et al., 2003; Lonergan et al., 2013; Louise Meyer et al., 2010)].

Glutaraldehyde can be used to immobilise the cells without fixing them to the surface. It forms links between NH_2 groups [(Louise Meyer et al., 2010; Velegol et al., 2003)]. It has been found that in AFM studies of different bacteria that adding glutaraldehyde to the cells increases the mean height of the cell in all three species tested by between 38.79% and 112.31%, showing that the chemical clearly makes a change to the cell [(Liu et al., 2012)].

One potential issue with the chemical adhesive techniques is that they could change the physical properties of the cells so that they behave differently from in their natural conditions and they have been reported to not work in some buffer conditions including high salt like liquid growth media [(Louise Meyer et al., 2010)].

There is the potential for combining mechanical trapping and chemical treatments to help trap more cells. An example of this has been applying a layer of polystyrene to the holes used to trap *S. aureus* which gives the cells a stronger bond to the substrate so the risk of them being knocked out of the holes is reduced [(Bailey, 2014)].

Cell-Tak is an adhesive surface coating that has been extracted from the species of mussel *Mytulys edulis*. These mussels secrete a substance that is full of polyphenolic proteins that allow them to attach to surfaces. A commercial version of the adherent has been produced by Corning [(Corning, 2014; Louise Meyer et al., 2010)].

2.16- AFM studies of bacteria

AFM is an important tool in the study of bacteria due to its versatility and the fact that it is not subject to the diffraction limit as it does not use lenses or beams of light to illuminate

the sample [(James et al., 2016)]. It has also been possible to combine it with other fluorescence techniques [(Micic et al., 2004)].

One of the major areas of study of bacteria with AFM is high speed imaging of membrane proteins which has been pioneered by the Ando group (Kanazawa University, Japan). Using a bespoke experimental set up the protein bacteriorhodopsin, taken from *Halobacterium salinarum*, has been imaged at speeds of 1 frame per second. The proteins show a trimeric organisation that will rotate when exposed to a 532 nm light source [(Ando et al., 2003; Shibata et al., 2010, 2011)]. The imaging of the bacteriorhodopsin have been able to observe the hexagonal lattice that the crystals form [(Butt et al., 1990)]. They have also been able to perform the high speed imaging technique on whole living bacteria, revealing the structure of *Magnetospirillum magneticum* by immobilising them on a poly-L-lysine surface and adding glutaraldehyde to the cells revealing a net like structure [(Yamashita et al., 2012)]. The *E. coli* membrane protein OmpF has also been studied by High Speed AFM (HS-AFM) to study the dynamics and the diffusion of the proteins as they sit in the reconstituted membrane with a similar scan rate of ~1 frame per second [(Casuso et al., 2012)]. Other *E. coli* membranes such as FhuA have been imaged with a more conventional AFM set up [(Thoma et al., 2012)]. Imaging of the *E. coli* membrane protein BtuB will be discussed in Chapter 8.

Some bacteria produce a crystalline outer layer that is made of proteins. This surface layer (S-layer) has been imaged on living bacteria in high resolution that show a highly ordered structure [(Dupres et al., 2009)]. Similar paracrystalline structures can be produced by bacteria in spore formation. Imaging of this exosporium protein array of *C. sporogenes* has shown a nap-like fringe on the surface of the exospore as well as beaded fibrils that are attached to the exospore [(Janganan et al., 2016)]. Work has also been performed to study the crystallised proteins from the photosynthetic bacteria *Rhodobacter sphaeroides* [(Adams and Hunter, 2012; Cartron et al., 2014)].

Study of the bacterial cell structure has been a wide area of study with particular focus on the structure of the peptidoglycan cell wall in both whole living cells and fragments of cells [(Touhami et al., 2004; Turner et al., 2014)]. The structure of living Gram positive *Lactococcus lactis* bacterial cells was imaged with AFM, revealing parallel bands of peptidoglycan that have a period of ~25 nm. The cells were also shown to be undergoing a division event [(Andre et al., 2010)]. Using HS-AFM, living bacterial cells were imaged and then the structure was compared to *M. magneticum. E. coli* and *R. sphaeroides* were

shown to have a network of holes on the surface that were less than 10 nm in diameter [(Oestreicher et al., 2015)]. High resolution imaging of *Bacillus atrophaeus* spores revealed information about the disintegration of the spore coating layer and showed evidence of a repeating structure on the surface of the cell with a ~8 nm periodicity. Imaging inside the spore revealed a mesh like structure on the surface of the vegetative cell [(Plomp et al., 2007)]. High resolution imaging of living *Streptomyces coelicolor* cells showed a fibrous layer on the surface of the cells [(Del Sol et al., 2007)].

AFM is not only an imaging tool. Many experimental set-ups allow for force measurements to be taken with the AFM that can be used to study the physical properties of samples or measure the strength of interactions within or between molecules.

Protein pulling experiments can be performed that measure the unbinding of the individual bonds within the proteins which can provide insight into how and why proteins fold into particular conformations or to determine mechanisms for force activated switches in proteins [(Farrance et al., 2013, 2015)]. Bacteriorhodopsin has also been used in a similar type of experiment to find the unfolding force for the protein. An area of purple membrane was imaged with AFM then force spectroscopy was performed on the region, measuring the unfolding of the individual proteins in Bacteriorhodpsin, before imaging the region again with a topographic scan to identify the exact protein that was unfolded in the spectroscopy [(Oesterhelt, 2000)]. This has also been performed on bacteria, measuring the affinity between the peptidoglycan and antibody probes that were coated on the tip [(Beaussart et al., 2014)]. Spectroscopy can also be performed with whole cells as the probes by attaching them to polymer or glass colloids at the end of a cantilever and measuring their affinity to functionalised surfaces [(Beaussart et al., 2013; Kang and Elimelech, 2009)].

Using a similar concept of chemically modified tips, it is possible to make affinity maps of a sample surface. Vancomycin coated tips were used to take force maps of an *L. lactis* cell using force volume mode. Vancomycin has high affinity for a specific bond within the peptidoglycan (D-Ala-D-Ala) so binds to these points on a cell. Force curves taken at these binding points were used to calculate the adhesion force as well as map the location of the target chemical bonds [(Gilbert et al., 2007)].

Force volume mode can be used to measure how the physical properties of a sample change over an area of the sample. It has been used to study bacteria including *S. aureus* and *E. coli* among others [(Bailey et al., 2014; Kasas et al., 2013; Longo et al., 2012)].

Chapter 3- Materials and methods

This chapter will outline and explain the various methods that were used and developed throughout the project. The types of methods will be in three main classes: microbiology methods, sample preparation methods and AFM imaging methods. The methods used relating to the analysis of data are included with the relevant data in the results chapters.

3.1- Microbiology methods

3.1.1- Preparation of bacterial media, agar and buffers

For media preparation, Brain and Heart Infusion (BHI) (Fluka/ Oxoid), Tryptone Soy Broth (TSB) (Oxoid) or Nutrient Broth (NB) (Oxoid) powder were added to the desired volume of deionised water in the concentration instructed on the packet by the manufacturer. To make Lysogeny Broth (LB) media the components, in concentrations 10 g/l Tryptone, 5 g/l yeast extract and 5 g/l NaCl, were added to water. To make agar plates from the media either 1 % (w/v) bacterial agar was added to the media or a pre-mixed formula of media agar can be used according to the instructions on the packet. Magnetic stirrers were used to fully dissolve all powders in the water before autoclaving the media or agar at 121 °C for 20 minutes.

To make the agar plates for the growth of the bacteria the agar was melted it in the microwave for between 10 – 120 seconds until completely molten. The agar must be at 50 °C to stay molten so a water bath was used to maintain this temperature. A laminar flow hood ensures a clean flow of air that stops contamination so the plates were always poured under the hood. If antibiotics were used in the agar plate like Erythromycin or Kanamycin they were added into the molten agar at this point. All of the antibiotics were made using deionised water then filtered using a 0.22 µm filter and stored at -20 °C. The antibiotics in the bacterial plates were only added once the agar had cooled to below 50 °C and their purpose was to ensure that only the chosen mutant strain survived when the plates were grown. Approximately 25 ml of molten agar was poured into a 10 cm diameter petri dish and then left to set for over 20 minutes. Once set, the agar plates were stored at 4 °C.

PBS was made by fully dissolving pre made PBS tablets into deionised water then this was autoclaved for 20 minutes at 121 °C.

Imaging buffers were made at a range of salt concentrations of KCl and Tris and in some experiments with $MgCl_2$ added. Most commonly an imaging buffer of 300 mM KCl, 10 mM Tris at a pH of 7.8 was used. The desired mass of each salt was weighed out using a fine balance then added to MilliQ water and mixed until fully dissolved. The pH was then adjusted to the desired value, (most commonly pH 7.8) using a calibrated pH meter, by the addition of concentrated HCl or NaOH solutions. MilliQ water was added to reach the required final volume.

3.1.2- Bacterial plate preparation and bacterial culture growth

Bacterial cells from frozen lab stocks were streaked on agar plates and grown for 16 hours at 37 °C. When not in use, the bacterial plates were stored in the 4 °C room, upside down to avoid condensation from flooding the cells. Single bacterial colonies were picked from these plates and placed in separate 10 ml of fresh growth media in a Falcon tube with the lids screwed on loosely. These tubes were placed in a shaker, oscillating at 250 rpm, at 37 °C for 16 hours. An optical density (600 nm) reading was taken of this overnight suspension and then a volume of cells that resulted in a resuspended optical density of 0.05 was added to 10 ml of fresh growth media. The cells were span at 250 rpm at 37 °C until they had reached the desired optical density (either exponential phase or stationary phase depending on the experiment), then the cells were spun in 1 ml Eppendorf tubes at 14680 rpm for 90 seconds, the supernatant was discarded and the cells were resuspended in 1 ml of buffer or media (depending on the experiment) and spun again at the same speed and for the same duration. The cells were spun 3 times in buffer or media.

3.1.3- Checking cells under the optical microscope

To view the cells, a small volume of culture was imaged using an optical microscope. To prepare this sample 5-10 µl of cell culture was pipetted onto a glass slide. A thin glass coverslip was fixed into place above the sample with clear nail varnish. A droplet of immersion oil was placed on top of the cover slip and then the lens was brought down into focus on the sample.

3.2- Sample preparation methods

3.2.1- Clean room photolithography

Several times during the fabrication process there was a 3 stage wash where the silicon was successively submerged for 30 seconds in N-Butyl-acetate, acetone and isopropanol, always in this order. To start the fabrication process, a fresh silicon wafer was examined for residues using an optical microscope. If residues were found a 3 stage wash was repeated until the silicon wafer was completely clean.

There is an option for a layer of oxide to be deposited onto the surface of the silicon using the PECVD (Plasma Enhanced Chemical Vapour Deposition). The program called Oxide1 was used to deposit a layer of silicon oxide on the silicon. The PECVD was run empty prior to adding the sample to prepare the atmosphere in the chamber. The deposition program duration for depends on the thickness of the oxide layer required.

The UV exposure procedure was performed in the section of the cleanroom that has UV filtered lights to avoid unnecessary exposure of photoresist to UV. The silicon was placed on the 100 °C hotplate for 30 seconds. A plastic film was pressed onto the matte side of the hot silicon, improving the vacuum seal when the silicon was next placed on the spin coater polished side up. The vacuum pump was turned on and a test spin of the silicon was performed at 4,000 rpm. Hexamethyldisilazane (HDMS), which helps the photoresist adhere to silicon, was added to the sample. A 30 second spin was performed with the HDMS before adding a droplet of photoresist that covered the entire surface of the silicon with no air bubbles. The SPR350 photoresist was spun for 30 seconds.

The raised photoresist around the edge of the silicon surface was exposed using a straight-edged piece of silicon and the mask aligner to remove the accumulated photoresist that could prevent the mask from being flat against the silicon. The 4 edges were developed in the appropriate developer (MF26A) for 1 minute.

The chosen patterned mask was placed in the mask aligner (Suss MJB), aligned using the built-in optical microscope then held in place using the vacuum seal. The appropriate exposure time depends on the photoresist used and the width of features required. 15 seconds was approximately enough to expose the photoresist with the pattern for SPR350,

MF26A was the developer used for the photoresist SPR350, the exposed silicon was submerged in this developer for 1 minute and then dried using the air gun. The pattern can be checked at this point using the optical microscope and if the process did not have the desired pattern on the silicon a 3 stage wash can be performed to remove the photoresist and the whole process can be performed again.

Etching of the pattern into the silicon was performed using the ICP (Inductively Coupled Plasma) (OPT 100). The Oxide 1 (SF_6, O_2, Ar) program was used for these etched silicon patterns and was run prior to adding the silicon wafer to prepare the atmosphere. The amount of time that the program should be run for depends on the photoresist, the material and the desired depth of the pattern. For etched silicon of a depth of approximately 750 nm the program was run for around 30 minutes.

After the etching stage a final 3 stage wash was performed to clean the photoresist off the sample surface.

3.2.2- Preparation of PDMS and agarose

PDMS (Polydimethylsiloxane) (Sylgard) has an elastomer component that is mixed with a curing agent at the desired ratio, 10:1 for a standard stiffness and 13:1 for a more elastic rubber. Both components were weighed out using a balance then thoroughly mixed together. The silicon wafer was immersed in a solution of acetone and Brij52 (10 % w/v) for 10 minutes then dried before adding the PDMS. Brij52 prevents the PDMS from sticking to the silicon permanently. The patterned silicon wafer was placed polished side up in the bottom of flat bottomed glass dish that had a thin coating of lubricating oil applied to the bottom, then the PDMS mixture was poured on top, ensuring an even coverage across the base of the glass dish. The whole dish was placed in a vacuum chamber to allow the air bubbles in the PDMS to escape the gel (~5 minutes) then the dish was placed in an ~60 °C oven and left until the PDMS had set (3 hours). Once set, the PDMS was removed from the dish and the silicon was peeled away from the PDMS leaving a region of patterned PDMS.

To make agarose (Sigma) 10 ml of deionised water was added to a 50 ml falcon tube then agarose was added with the mass needed depending on the desired concentration. The concentration of agarose used widely in microbiology is 2% but a range of concentrations were tested in this project with the aim of matching the stiffness of the PDMS (2% to 14% were tried with 8% roughly matching the PDMS stiffness). Once the agar was dissolved in

the water it was melted in a microwave using 10 second bursts while aiming to avoid air bubbles. The molten agar was placed in a water bath at 55 °C to ensure the gel had a homogeneous temperature. The silicon wafer was placed at the bottom of a 10 cm petri dish then the agarose was poured on top in an even layer and left to set at room temperature, possibly in a laminar flow hood, for a 2-3 hours. When the gel had set it was peeled off the silicon leaving the patterned agarose. Agarose was prepared on the day of the experiment.

3.2.3- Trapping *B. subtilis* vertically in agarose

To perform an experiment to investigate the architecture of the poles of *B. subtilis* a mechanism for trapping the cells vertically in columns was required. Using a silicon master that was developed by Seamus Holden's group in Newcastle, holes that are approximately 4 µm deep and 1-2 µm in diameter (there are different diameter sections of the silicon master) can be formed in agarose which the Holden group have used successfully to trap the *B. subtilis* cells for fluorescence microscopy [(Bisson-Filho et al., 2017)].

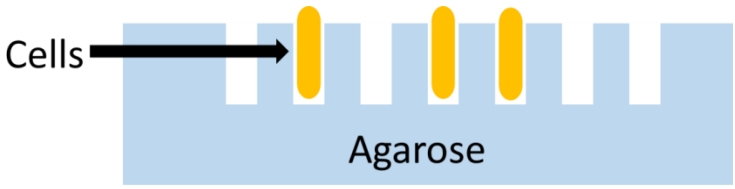

Figure 3.1- Cartoon showing the Holden method of vertically trapping *B. subtilis* bacteria.

Initially a gene frame was stuck to a glass slide then a 6% agarose solution was made in the same way as described in section 3.2.2. 350 ml of the molten agarose was pipetted into the gene frame on the glass slide using a 1 ml pipette that has the end cut off to allow the viscous liquid to be drawn up easier. A gene frame holds a volume of ~65 µl so some overflows. Immediately after the silicon master was pressed into the molten agarose, with pressure applied evenly to ensure there is no air trapped between the silicon and the agarose, this was then left to set for 5 to 10 minutes. Once set, the silicon master was peeled away, revealing the patterned agarose. The silicon master was cleaned immediately by gently rinsing with water, not scrubbing, to remove any residual agarose.

For imaging *B. subtilis* in this agarose system an overnight culture of cells was grown in growth media or in Time Lapse Media (TLM) then resuspended in growth media or Chemically Defined Media (CDM) then grown to an O.D. of 0.2- 0.4. 1 ml of the cells was

then spun in an Eppendorf using a desktop centrifuge, the liquid was discarded, then the pellet was resuspended in 10 µl of media or PBS. 2-4 µl of the cell suspension was added to the region of agarose holes on top of which a cover glass was placed to force the cells into the holes.

3.2.4- Cell-Tak *B. subtilis* trapping method

For the preparation of the Cell-Tak glass slides, 285 ml of $NaHCO_3$ was added to a clean glass slide then 10 µl of Cell-Tak and 5 µl of NaOH were added to the droplet. The slide was covered and left for the reaction to undergo for at least 30 minutes. Using MilliQ water the surface of the glass slide was rinsed 5 times with 0.5 ml of liquid before adding 100 µl of the cell sample which was left for approximately 30 minutes. The area of the glass slide with the cells was rinsed 5 times using 150 µl of fresh imaging buffer before a final 150 µl of buffer was added for imaging the sample under the AFM.

3.2.5- Preparing samples for imaging

The method of preparing the sample for imaging depended on the imaging mode that was used but the general steps were the same.

A layer of polystyrene can be applied to surface of the silicon to form a thin hydrophobic layer. A polystyrene bead (Sigma) was dissolved in toluene to form a concentration of 1 mg/ml then ~1-2 µl of this was added to a square piece of silicon with sides of length ~0.5 cm. The liquid was left to completely evaporate for over 20 minutes, leaving a thin coating of the polystyrene.

To add the cells to the silicon sample surface, approximately 20 µl of cell suspension was deposited onto a ~0.5 cm square size piece of silicon. A nitrogen gun was used to evaporate most of the liquid from the silicon, without completely drying out the cells. This process could be repeated once or twice more depending on the concentration of cells if required, however, the majority of the experiments involved a single droplet being added to the silicon.

Fresh liquid media or imaging buffer was added to the sample (normally 100-200 µl for imaging with the Bruker FastScan) so that there was enough liquid for the AFM liquid holder and sample surface to form a column of liquid with the cantilever fully submerged. Different AFMs required different amounts of liquid to form the column of liquid between the tip and the sample and it also depended on what type of experiment was

going to be performed. Using a sample that was at the bottom of a flooded petri dish required more imaging liquid.

In experiments where the sample was heated the heating stage was attached and turned on prior to adding the sample. The heated stage was often used with a petri dish that was flooded with media because of the increased rate of evaporation.

3.2.6- Cleaning the silicon substrate

After imaging whole cells using the etched silicon wafers they must be cleaned ready for the next experiment. A multiple stage cleaning process was performed to remove any residual bacteria or salts from the media. The first step in cleaning the silicon was sonication in a detergent. Washing up detergent or a detergent like 10 % SDS was used for this step which killed anything living on the surface such as bacteria. The silicon was immersed in the detergent mixed with deionised water for at least 10 minutes and was sometimes sonicated too. Sometimes the detergent step was performed overnight.

If polystyrene had been used as part of the trapping experiment this was dissolved off the silicon with an additional step of sonication in acetone for 5 minutes.

To remove any salts and detergent a wash step of Isopropan-2-ol was performed for at least 10 minutes and was also sometimes done in the sonicator before a final wash step in deionised water or MilliQ water was performed which was to remove any remnants that may be left behind. This water step was done for at least 10 minutes and was also sometimes done in the sonicator. Finally, the wafer was completely dried with a Nitrogen gas line leaving the wafer ready for the addition of cells.

3.3- Bacterial strains

Staphylococcus aureus

The most commonly used strain of *S. aureus* throughout the experiments was the lab strain SH1000. This was treated as the control bacteria when comparing the effects of genetic mutations in mutant bacteria.

SH1000: SagB is a mutant version of the wildtype that has had a gene removed that forms one of the proteins that produces an enzyme involved in cell wall hydrolysis, meaning the peptidoglycan has a higher crosslink density and has longer glycan chains due to the reduced level of hydrolysis [(Wheeler et al., 2015)].

SH1000:TagO is a wildtype mutant that has had the gene that produces wall teichoic acids removed so the peptidoglycan has a low teichoic acid density on the cell surface [(D'Elia et al., 2006)].

SH1000: SrtA is a mutant strain that does not have the covalently bound cell wall proteins [(Frankel et al., 2005)].

Bacillus subtilis

The *Bacillus subtilis* strain used was BS168, HR trpC2 which is the standard wild-type lab strain.

3.4- AFM methods

The AFM was set up before each experiment but the process varied depending on the model of the AFM and the sample that was being imaged. When imaging in liquid on a Veeco Dimension 3100 a special liquid tip holder was used which ensured no liquid could evaporate into the electronics in the AFM head. A rubber skirt was placed around the liquid holder to avoid any liquid splashing onto the AFM head. There is a similar liquid tip holder for the Bruker ICON head that has the same purpose. The JPK Nanowizard 3 Bio and the Bruker FastScan use the same tip holder when imaging in air and in liquid though care was taken in the presence of liquid to avoid it getting in the electronics.

To clean the liquid tip holder of the Veeco Dimension 3100 it was first sonicated for 5 minutes in detergent like hand soap or washing up liquid then it was rinsed off with deionised water before sonicating again for 5 minutes in isopropanol, before a final sonication in deionised water for 5 minutes. The holder was completely dried with nitrogen then put back for storage. The cleaning process was performed after every imaging session in liquid to ensure there was no residual salt or dirt that could contaminate the next experiment.

A similar cleaning process was performed on the glass tip holder for the JPK Nanowizard 3 while the Bruker FastScan has a specially designed liquid holder cleaner that houses the tip holder so that the high voltage socket is sealed from exposure to liquid. The same 3 steps were used with detergent, isopropanol and deionised water used to clean the holder. The FastScan holder was not submerged or sonicated to clean it but rather a soft tooth brush was used to remove any residues during the detergent cleaning step before the rinsing in isopropanol and water.

The models of cantilevers used throughout the project were all made by Bruker. Tapping mode in air was performed with TESPAv2 cantilevers. MLCT cantilevers were used for multiple imaging modes on different the Dimension 3100 and the JPK Nanowizard 3 including for QI mode in liquid and contact mode in air and liquid. FastScan-D tips were used on the Bruker FastScan AFM for tapping mode in liquid.

	Cantilever Model (all made by Bruker)							
		MLCT						FastScan -D
AFM Probe Property	TESPA v2	A	B	C	D	E	F	
Resonant Frequency (nom.) (kHz)	320	22	15	7	15	38	125	110 (liquid)
Spring Constant (nom.) (N/m)	37	0.07	0.02	0.01	0.03	0.1	0.6	0.25
Cantilever Length (nom.)(µm)	123	175	210	310	225	140	85	16
Cantilever Width (nom.) (µm)	40	22	20	20	20	18	18	4
Tip Height (µm)	10-15	2.5-8						1.5-4.5
Tip Radius (µm)	7	20						5

Figure 3.2- Table of AFM probe properties of all of the cantilevers used in experiments. Information from manufacturer website [(Bruker, 2017a, 2017b, 2017c)].

Chapter 4: Developing high resolution imaging of *Staphylococcus aureus*

Imaging whole living bacterial cells with AFM requires an experimental set up that can keep the cells from moving during imaging without constraining them to the point that their natural behaviour is affected. Using an immobilisation method, like the one developed to trap the spherical *S. aureus* cells in silicon holes, shows that an individual cell can be imaged with the AFM over repeated images without damaging the cell or moving it with the tip. Once the cells can be reliably trapped, the goal can switch to trying to achieve the highest possible resolution AFM images of bacterial cells to further understand how the molecules in the peptidoglycan are organised and how this organisation changes over time.

In this chapter the development of immobilisation methods for *S. aureus* will be outlined then the different imaging techniques that were used with the aim of obtaining the highest resolution images possible will be discussed. The structures that were seen will be discussed as well as the experiments that were designed to confirm that they are primarily made of peptidoglycan.

4.1- Established contact mode imaging technique for *S. aureus* cells with Veeco Dimension 3100 AFM

The initial experimental method of imaging the cells was taken from previous work done in the group with the Kailas method [(Kailas et al., 2009)] being the basis of the work along with the work of another recent group member, Richard Bailey [(Bailey et al., 2014)]. The silicon holes that were used were made by the photolithographic process outlined in Chapter 3. Tapping mode is often used when imaging soft samples because it is less damaging to the surface than contact mode which has higher lateral forces. When using tapping mode in liquid on a Veeco Dimension 3100 AFM, oscillation of the cantilever is performed by the Z piezo being moved up and down at close to the cantilever's resonant frequency in liquid or a frequency that produces a large amplitude response. The cantilevers used for imaging in liquid on the Dimension were the Bruker MLCTs which have a range of spring constants between 0.01 for the softest cantilever to 0.6 for the stiffest one (Figure 3.2).

Each of the triangular shaped cantilevers were tested using tapping mode in liquid on the *S. aureus* sample but it was not possible to image the cells because they were being removed from the holes. It is thought that acoustic waves caused by the oscillation of the cantilever in liquid tapping mode on this AFM were removing cells from the holes. Despite higher lateral forces, contact mode on this AFM had shown that it was capable of imaging the cells over multiple images using the same MLCT cantilevers. Using imaging settings of a low deflection set-point (low force), a slow scan speed and high feedback gains gave the best results of imaging the cells without removing them from holes. Figure 4.1(A) shows three cells within the silicon holes with two of them being knocked out of the holes as the AFM tip scans down the image. This shows that while liquid contact mode on the Dimension 3100 is more suited to this sample than liquid tapping mode, it still removes cells from the grid regularly so the imaging parameters must be constantly optimised to try to prevent cell removal. Figure 4.1(B) shows a cell that was imaged fully in 10 consecutive scans using contact mode without being removed from the hole.

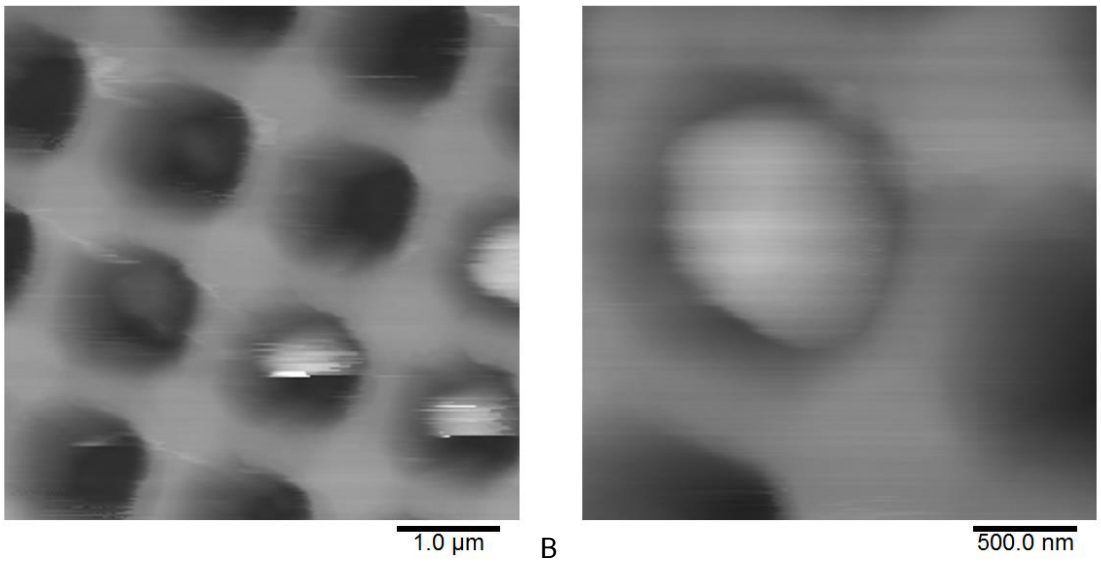

Figure 4.1(A) – Contact mode topographic image showing the silicon immobilisation grid with three *S. aureus* cells, two of which were removed during the scanning. Z scale (black to white) = 1.364 µm. 4.1(B) Contact mode topographic image showing an *S. aureus* cell being imaged in liquid contact mode without being removed by the tip. Z scale (black to white) = 1.18 µm

The technique for using the Dimension 3100 to image the cells allows for individual cells to be imaged over consecutive images but does not obtain high enough resolution images of features within the cell wall surface like those that have been seen using AFM of dried

sacculi [(Turner et al., 2010a)]. The lack of division events seen when using this technique is also a reason to try alternative imaging techniques and equipment as one of the goals of the work is to see how the cell wall changes over the course of the cell division cycle.

4.2- Experimenting with new AFMs and different modes

A variety of different AFM modes on different AFM equipment were used to test their suitability for imaging the live bacteria at high resolution without the tip removing them from the holes. Initially on the Veeco Dimension 3100, contact mode had been used with relative success but this method does not achieve the structural resolution on the bacteria that is required to answer questions about how the peptidoglycan is remodelled.

QI mode has been developed by JPK and can be used on their Nanowizard3 Bio AFM. This new mode works like a faster version of force volume, allowing for high pixel density scans while maintaining useable force curves that can be used to calculate physical properties of a sample and is explained fully in Chapter 2.

Experiments were performed to find a set of QI imaging parameters that would allow the cells to be imaged at a resolution that was improved over the established contact mode method while also reducing the chance of cells being removed from the immobilisation grid as QI mode applies smaller lateral forces to the sample than contact mode. It was found that with the right QI imaging parameters, which did not focus on the force data that was being measured, the normal imaging of bacterial samples in QI mode for a scan of 256 x 256 pixels was faster than taking a contact mode image of the same pixel density as the scan rate using contact mode needed to be <0.5 Hz to avoid dragging the cells out of the holes. QI mode is not designed to take high resolution images of samples but to allow for more detailed and faster force mapping capabilities so it was not suitable for obtaining images that show structural features on the bacterial cell surface.

Another mode called PeakForce Tapping, developed by Bruker and available for the Bruker FastScan AFM was tested on the bacterial samples. It has been adapted from tapping mode AFM but comes with the addition of the ability to make mechanical measurements while imaging at higher speeds than force volume mode and also allows for force control. The mode is explained in Chapter 2. The technique was briefly tested on the bacterial samples but it was found that there was no improvement over the QI

mode data in terms of imaging or contact mode, possibly because of the tall features of the immobilisation grid which caused interference in the data that was taken.

The Bruker Fast Scan has the option for using a smaller laser spot for the cantilever deflection measurements which can be with the FastScan-D probe without any laser overspill. The FastScan-D is designed for high speed and high resolution tapping mode imaging in liquid, taking advantage of the higher bandwidth Z-piezo which allows the feedback loop to respond faster to changes in the surface, reducing the error in the measurements. The FastScan AFM also has a smaller laser size that can be used with the FastScan-D probes which are physically smaller than a typical cantilever like a Bruker TESPA v2 or any of the cantilevers on the Bruker MLCT chip.

Initial experiments using the FastScan AFM with the FastScan-D probe driven at an amplitude of 1-2 nm in tapping mode showed that cells could be imaged over consecutive images without them being displaced from the silicon holes.

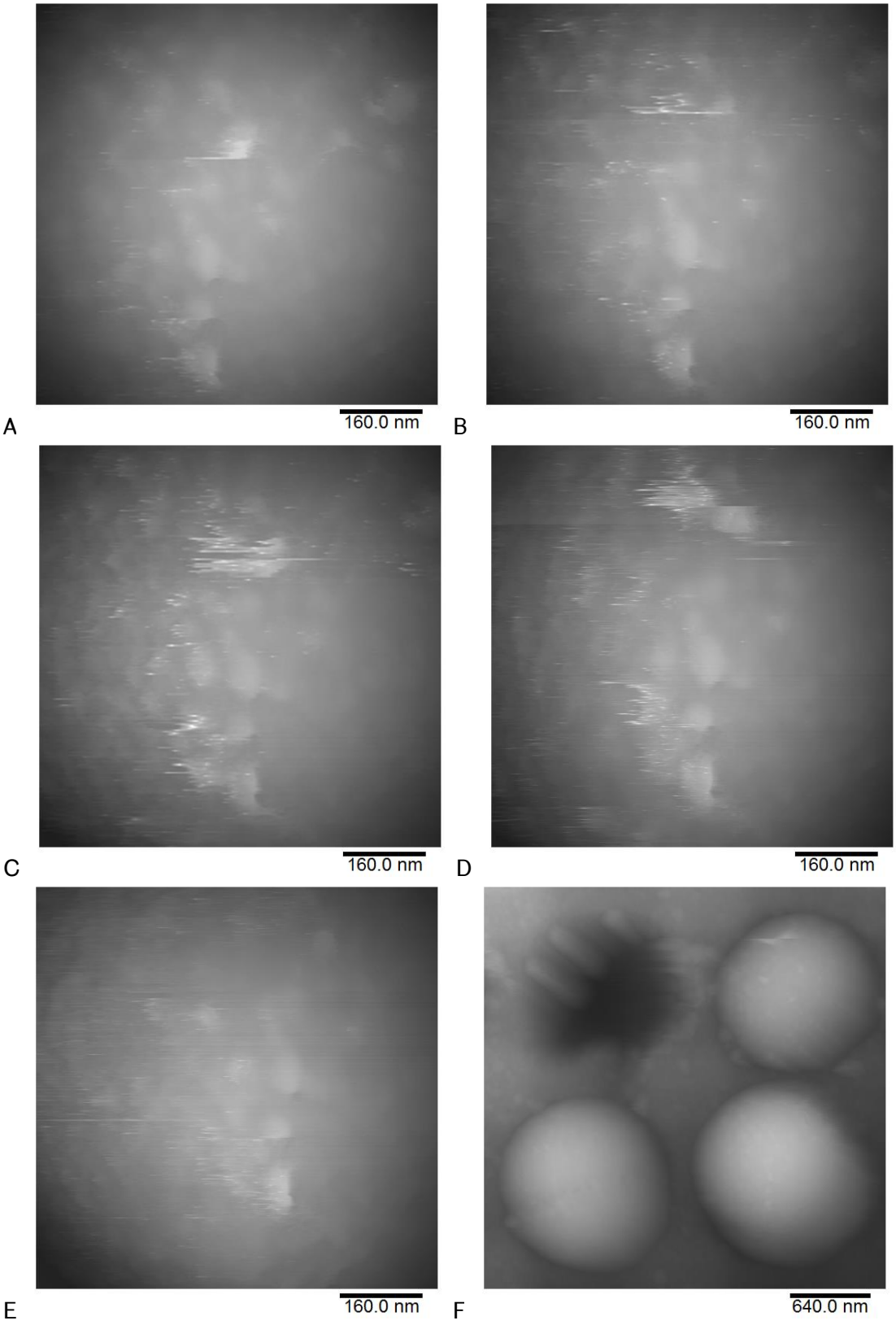

Figure 4.2(A)-(E) shows consecutive topographic images of *S. aureus* cells taken in tapping mode using the FastScan-D probe on the Bruker FastScan AFM over the course of 1 hour. (F) is a topographic image of three *S. aureus* cells in the silicon holes. Z scales (black to white) (nm) (A) = 430, (B) = 382, (C) = 415, (D) = 374, (E) = 434, (F) = 1336.

The ability to use tapping mode for imaging the cells is desired over using contact mode or one of the fast force spectroscopy modes because tapping mode can take images at higher pixel densities or higher scan rates for the same time per image allowing for either better spatial resolution when imaging or better temporal resolution when imaging dynamic processes and overall reduces the effect of thermal drift over time. Image 4.2(F) shows three cells in four holes that have not been removed by using the lower amplitude of oscillation.

The aim of the imaging is to take consecutive scans of the dynamic events of peptidoglycan maturation or of the cell division process at a resolution that these structures can be seen. To give the best chance of this occurring the cells were imaged in their growth media.

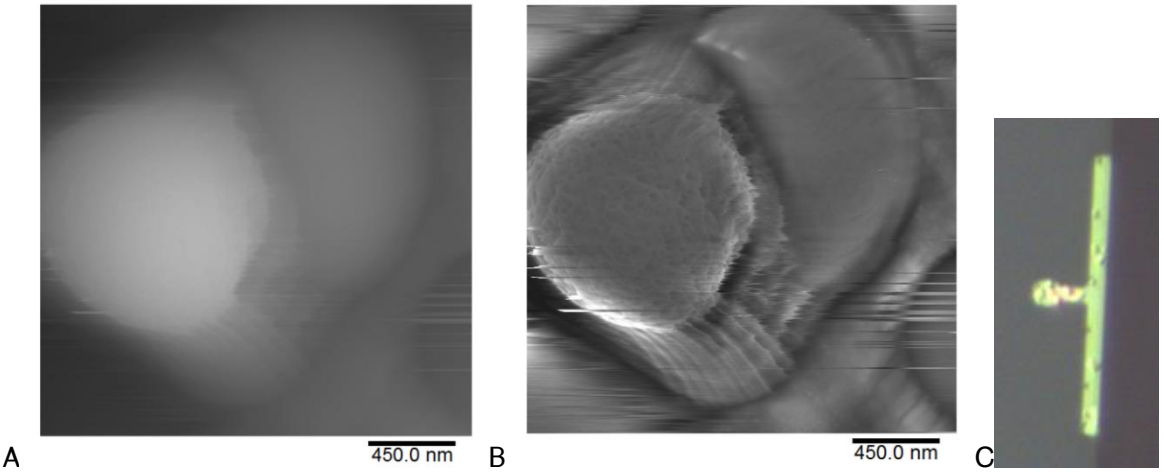

Figures 4.3(A) and (B) - *S. aureus* cells imaged with FastScan-D probe in tapping mode in TSB growth media. (A) is the topographic image with Z scale (black to white) = 3.1 µm while 4.3(B) is the high pass filtered topographic version of 4.3(A) with a filter size = 1.1 µm. 4.3(C) is an optical image of the FastScan-D tip during imaging with *S. aureus* cells attached.

There is the first evidence of some fine structure of peptidoglycan on the surface of the cell in Figure 4.3(A) and (B) using tapping mode which was not possible in the other modes tested so it was chosen to be performed on the samples and further optimised to achieve the best results. The small FastScan-D tips that are used can get contaminated with multiple *S. aureus* cells that are floating in the imaging liquid (as can be seen in Figure 4.3(C)) which can cause increased noise in the data so the concentration of bacterial cells must be tuned to have a high yield of cells to image while reducing the chance of them attaching to the back of the tip.

4.3- Imaging *S. aureus* with small amplitude tapping mode

Experiments were performed using small amplitude tapping mode on the Bruker FastScan AFM with Bruker FastScan-D cantilevers while imaging in TSB growth media which is the same growth media as the cells are grown in during their overnight culturing.

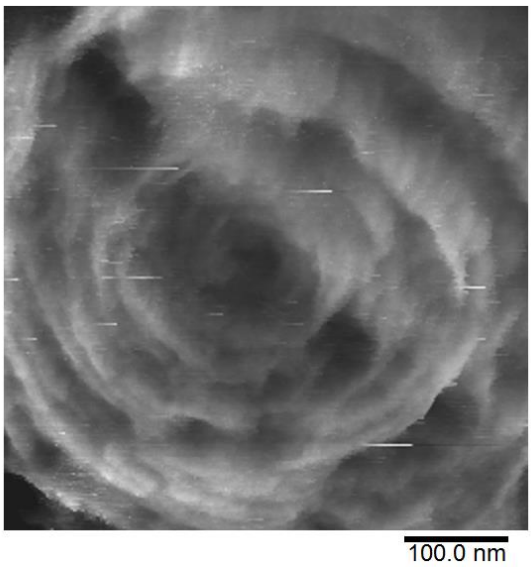

Figure 4.4- A topographic image of an *S. aureus* cell imaged in TSB growth media with a ringed structure. A 3rd order plane fit has been applied to the image. The Z scale (black to white) = 39 nm.

It was possible to resolve the ringed structure that was seen in previous AFM studies of *S. aureus* [(Bailey et al., 2014; Touhami et al., 2004; Turner et al., 2010a, 2014)] but at a higher resolution as can be seen in Figure 4.4. The cell was imaged over 10 consecutive scans but there was no restructuring of the peptidoglycan.

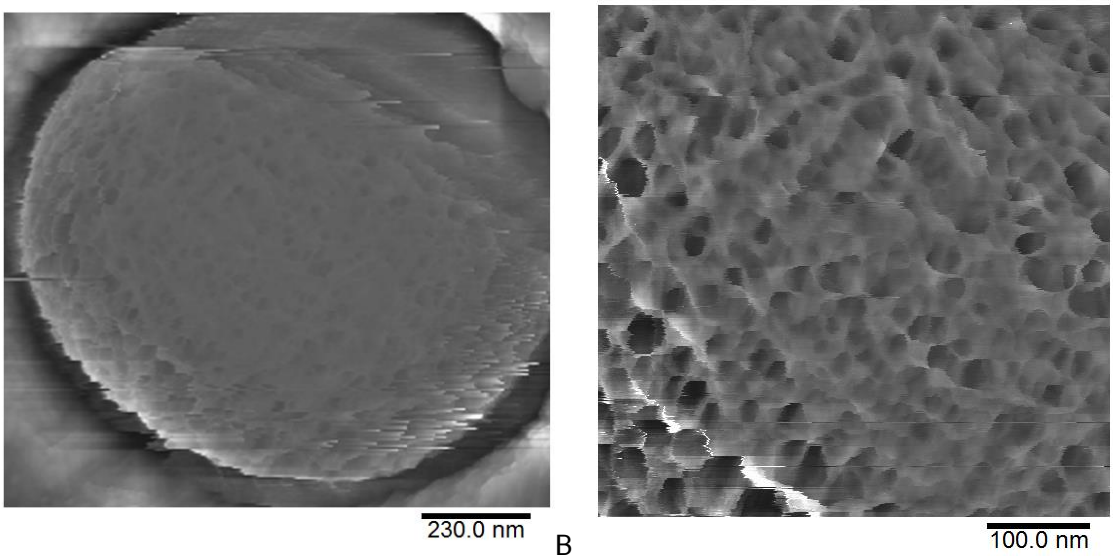

A B

Figure 4.5- An *S. aureus* cell showing mature architecture- (A) is a high pass filtered topography image with a filter size = 572 nm and (B) is a high pass filtered topography image with a filter size = 249 nm.

There was a different structure seen that did not show evidence of the rings but did not appear the same as the previously suggested knobbled architecture. The structure has a porous appearance with many holes as can be seen in Figure 4.5 This structure is closer to that seen by Touhami [(Touhami et al., 2004)].

To encourage cell growth and division or peptidoglycan maturation different imaging conditions were tested including heating the growth media of the cells as they were being imaged to 37 °C which is their optimal growth temperature.

To confirm that the architectures that are seen in the images are made of peptidoglycan, a series of experiments were performed to systematically rule out the other possibilities for what could show these structures.

4.4- Imaging TagO mutant *S. aureus*

Wall Teichoic Acids (WTAs) are glycopolymers that sit on the outside of many Gram-positive bacteria. They are covalently bound to the peptidoglycan and their function can range from helping to maintain the shape of rod shaped bacteria to being involved in resistance to antibiotics [(Brown et al., 2013)]. The teichoic acids form a negatively charged wall around the cell [(Swoboda et al., 2010)].

A strain of *S. aureus* has been created without the TagO gene which is the gene responsible for the first step in the synthesis of WTAs [(Holland et al., 2011)][(Vergara-Irigaray et al., 2008)]. AFM experiments were performed using the same method as the experiments on the SH1000 wild type strain. An imaging buffer of 300 mM KCl, 10 mM Tris at pH 7.8 was used, the same as frequently used for the wild type imaging, as this buffer had yielded the highest resolution images.

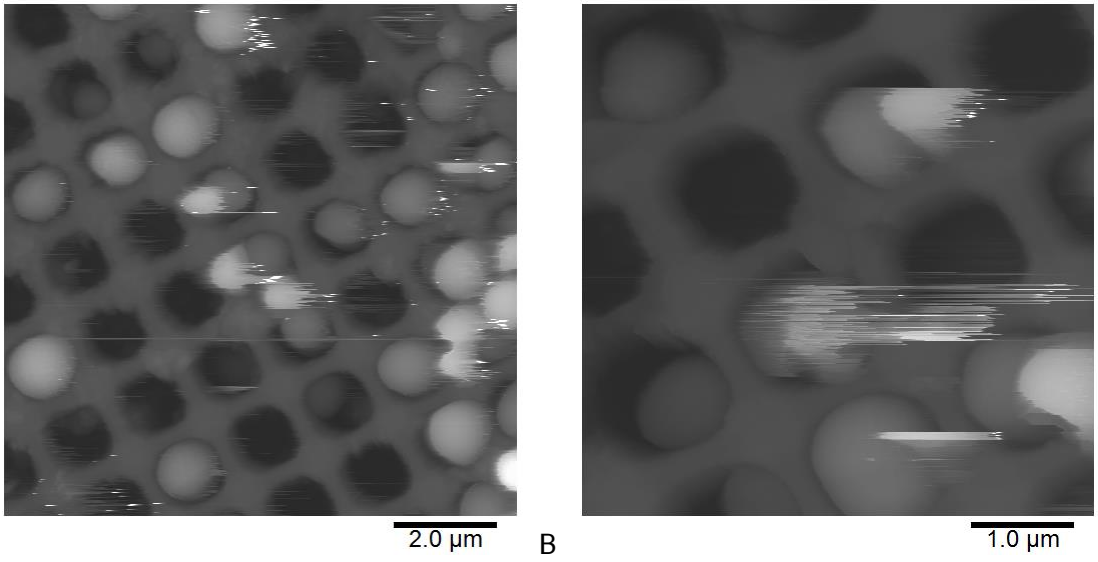

A B

Figure 4.6- Large area topographic scans showing multiple TagO *S. aureus* cells in holes. Z scales (black to white): (A) = 2.30 µm, (B) = 2.27 µm.

Large area scans of the TagO cells were taken to compare their sizes and shapes with the wild type cells as the teichoic acids play a role in the division cycle so cells that lack them could have some irregular division or structural characteristics. Figure 4.6 shows the cells trapped in the silicon holes in the same way that the wildtype strain is. The cells appear to be of a similar size to SH1000 cells.

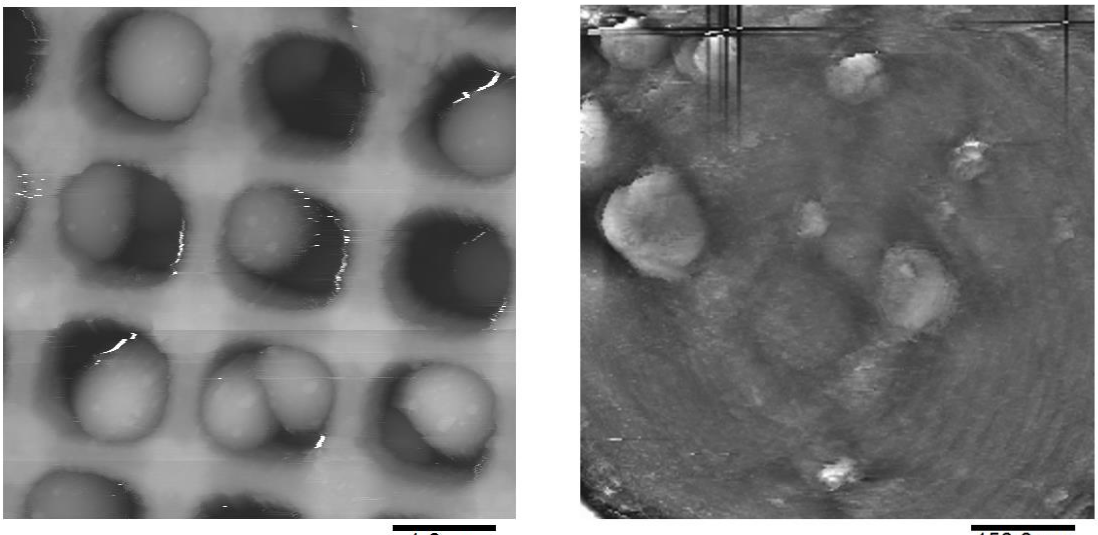

Figure 4.7- Topographic images of mutant TagO cells that had been grown to stationary phase – (A) is a field of cells with Z scale (black to white) = 1.18 µm. (B) is a high pass filtered topographic image with a filter size of 368 nm that shows lumps on the surface of the cell. The black crosses at the top of Figure 4.7(B) are an artefact of the high pass filtering process. They appear when a tall spike is high pass filtered.

On a separate imaging session of TagO bacteria that had been grown to stationary phase instead of exponential phase, the cells appear to be smaller in the holes and lumps appeared on the cells as seen in Figure 4.7. The lumps were only seen in a single imaging session of the TagO strain while no similar features were seen during imaging of wildtype bacteria. Investigating the lumps at a higher resolution gave no further insight into what they were as shown in Figure 4.7(B). In an experiment using growth media to image the cells at exponential phase there were no lumps present on the cells and the cells were of a normal size (similar to wild type).

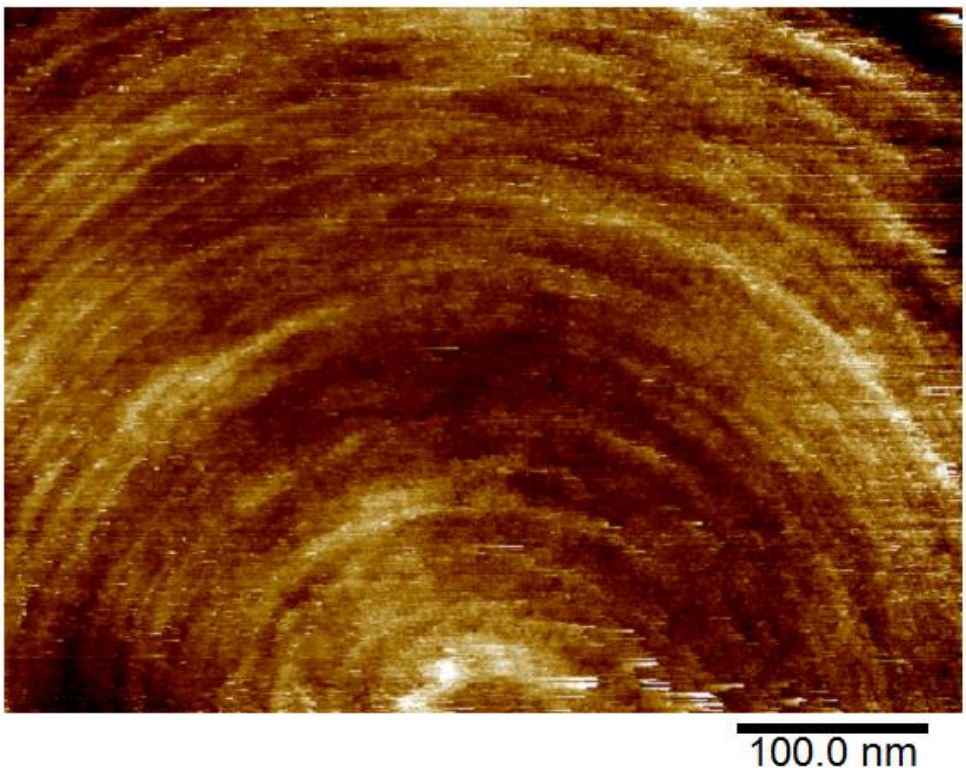

Figure 4.8- Topographic image of a TagO cell showing ringed architecture. The topographic image has had a 3rd order plane fit and a 0th order flattening performed on it. Z scale (black to white) = 20 nm.

Rings can be seen in Figure 4.8 which is significant in confirming that the rings are not a structure of the covalently bound polymers. The mature architecture of the TagO strain was also imaged to confirm that the structures seen are not an artefact of the presence of wall teichoic acids.

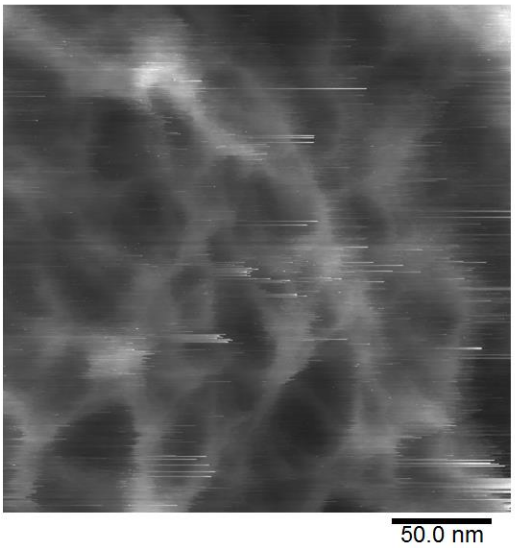

Figure 4.9- Topographic image of a TagO cell showing mature architecture. The image has had a 3rd order plane fitting performed on it. Z scale (black to white) = 52 nm.

A scan of an area of mature peptidoglycan was taken that shows an overall mesh like structure as seen in Figure 4.5. The scan is of a lower resolution which could have been due to movement of the sample, fluctuation of the salt conditions during imaging or possibly a changing of the shape of the tip due to something attaching to the end of the tip.

4.5- Imaging mutant SrtA *S. aureus*

Sortase (SrtA) is an enzyme that is involved in attaching proteins to the surface of Gram-positive bacteria [(Mazmanian, 1999; Mazmanian et al., 2000, 2002)]. It catalyses the binding of proteins to the outside of the cell wall, proteins that play an important role in the virulence of *S. aureus*. A mutant strain of *S. aureus* has been created that has the SrtA gene removed. When tested in a mouse model the strain needed a lethal dose concentration that was 100 times higher than the wild type cells [(Cossart and Jonquières, 2000)]. Removing covalently bound proteins from the outside of the cell wall can help confirm the structure of the peptidoglycan.

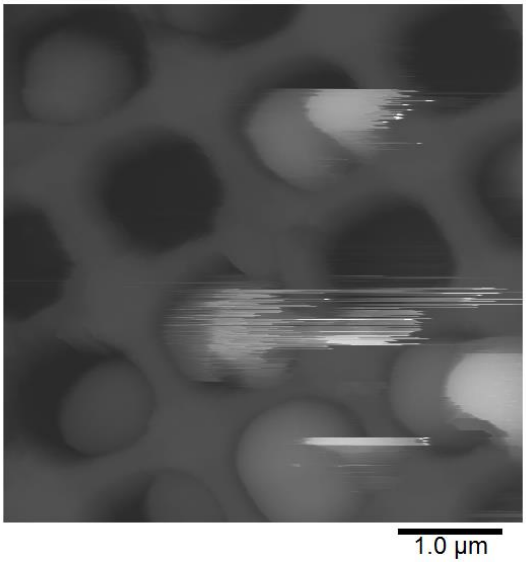

Figure 4.10- Topographic image of a multiple immobilised SrtA mutant *S. aureus* cells. Z scale (black to white) = 2.64 µm.

A small field of cells is shown in Figure 4.10 that has a number of cells with some larger cells and some smaller cells. The larger cells look to be typically healthy *S. aureus* cells while the smaller cells are likely to be less healthy. It is not uncommon to see some smaller cells in a field of view.

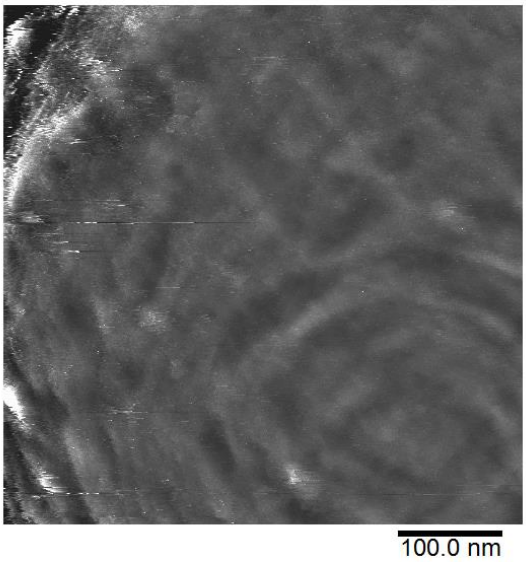

Figure 4.11- Topographic image of ringed architecture on SrtA mutant cells. The image has been high pass filtered with a filter size (black to white) = 248 nm.

Imaging rings in the SrtA would rule out that the young architecture is due to proteins on the cell surface, further validating the theory that the structures are made of

peptidoglycan. Figure 4.11 has some rings in a low resolution scan but they are clear enough to be used in support of the argument that rings are present in the SrtA mutant.

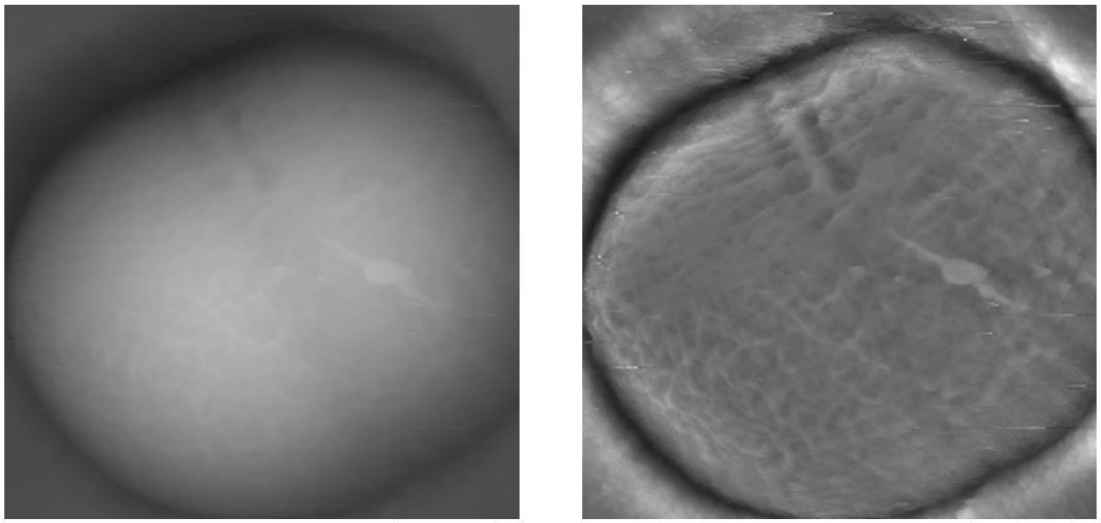

A B

Figure 4.12- Images of an SrtA mutant cell that shows the ringed and mature architecture. (A) is a topographic image with Z scale (black to white) = 925 nm. (B) is a high pass filtered topographic image with a filter size = 620 nm.

A cell with halves showing two different stages of the peptidoglycan maturation process is presented in Figure 4.12. In the half at the top of the images there are some rings that have a crack forming with a raised band emerging, while the bottom half of the images show the disordered mesh architecture. There is a clear boundary between the two structures and the fact that this emerging band is clearly seen among the rings but is not visible among the mesh may provide insight into the activity of cleaving enzymes that may localise on the ringed sections first during a division event, or it may be a consequence of a difference in the ease of the band to emerge, as in the rings may be structured in some way to part easily while the mesh has more homogeneous mechanical properties. These raised bands of material will be discussed further in Chapter 6. In the mesh region there is a thick feature on top of the surface that could be a remnant of a previous ring or something that is not originally of the cell.

The cell displays the mesh structure which builds onto the evidence that the structures that are seen in the AFM imaging of the cells are made of peptidoglycan.

4.6- Imaging *S. aureus* in the presence of the enzyme trypsin

Trypsin is an enzyme that hydrolyses proteins and is used in microbiology to "shave" the proteins off of the outside of cells [(Ythier et al., 2012)]. Trypsin can be added to a culture of cells to remove the cell wall proteins from the surface, leaving a cell with the peptidoglycan cell wall exposed.

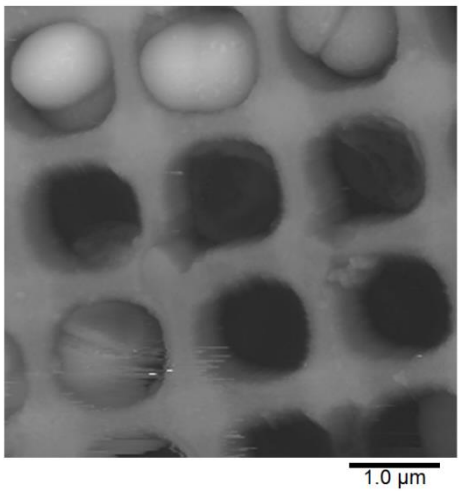

Figure 4.13- Topographic image of a field of trapped trypsin treated cells. Z scale (black to white) = 1.4 µm.

A larger image of multiple cells was taken and the cells appeared to look similar to wildtype cells and that the treatment did not affect their shape shown in Figure 4.13.

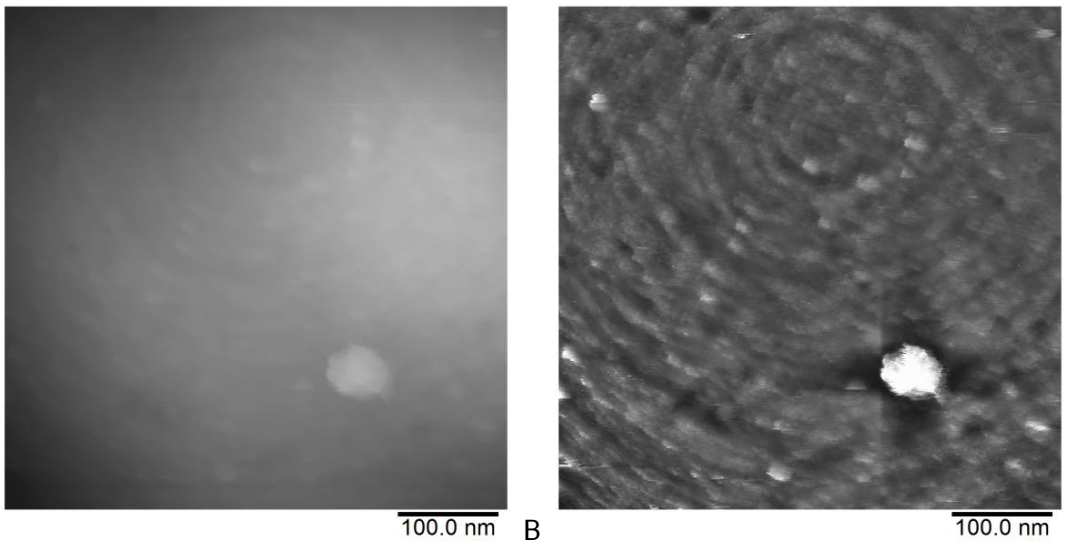

A B

Figure 4.14- Trypsin treated *S. aureus* cells that show a ringed architecture. (A) is a topographic image with a Z scale (black to white) = 258 nm. (B) is a high pass filtered topographic image with a filter size = 253 nm.

To confirm the existence of rings the cell in Figure 4.14 was imaged, showing a set of dense rings. In this experiment the cells were imaged in a standard PBS solution as a test of the protocol of adding trypsin to the cells. PBS has a lower salt concentration than the imaging buffer that has been used most frequently in the AFM experiments in the project.

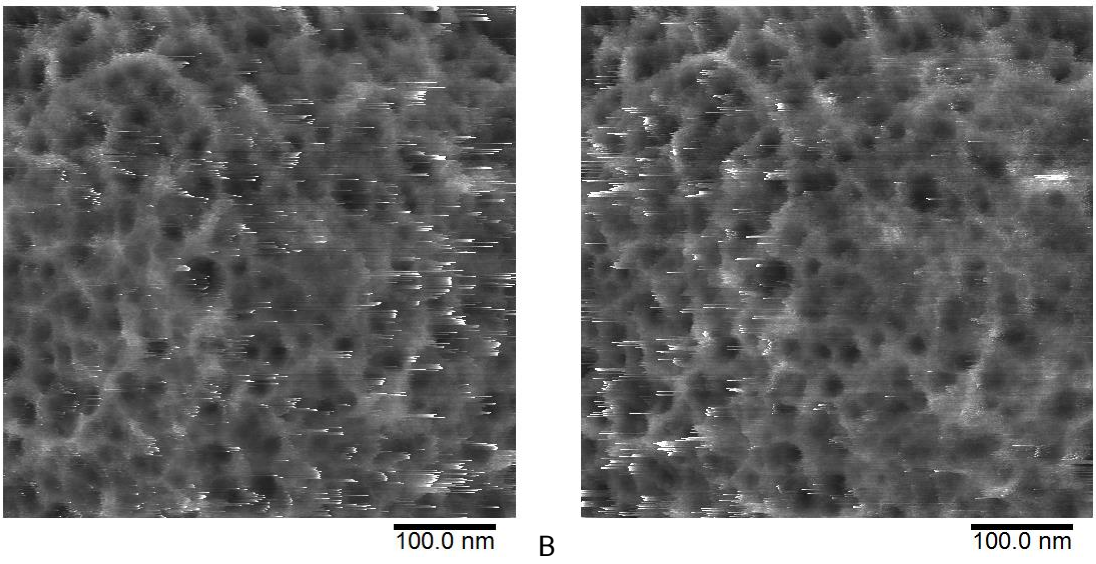

Figure 4.15- Topographic images of mature architecture of the trypsin treated *S. aureus* cells. (A) is the trace image (tip scans from left to right). The image has had a 3rd order plane fit applied and a Z scale (black to white) = 42 nm. (B) is the retrace image (tip scans from right to left). A 3rd order plane fit has been applied and the Z scale (black to white) = 39 nm.

Mesh images were also taken during the same PBS experiment, shown in Figure 4.15 which means the mesh architecture cannot be attributed to the proteins on the outside of the cell. Figure 4.15 shows the trace and retrace images of the same scan and features streaks that appear in opposite directions on the images. When imaging the mesh in the wild type cells streaks are sometimes seen that can be caused by the tip not tracking the surface accurately. If the mesh is loose and can be moved by the tip as it scans from side to side then these streaks will appear. Overall the two images show that the mesh structure can be loose and moved about by an external force which is not the case for the rings.

4.7- Imaging the SagB mutant of *S. aureus*

Hydrolases are responsible for breaking down the ringed structure of peptidoglycan. The glucosaminidase SagB is one of these hydrolases. It has previously been studied before by

force spectroscopy AFM, showing that of four hydrolases tested (Atl, SagA, SagB and ScaH), removing the SagB gene has the greatest effect on the stiffness of the cell wall of *S. aureus* causing an increased stiffness to the cell wall, close to the stiffness measured for young peptidoglycan [(Bailey, 2014; Wheeler et al., 2015)]. This lack of hydrolysis also results in longer peptidoglycan strands and some cell morphological defects. [(Chan et al., 2016)]. The aim of these imaging sessions was to study the overall shapes of the cells to see structures on these misshaped cells and to obtain high resolution images of the SagB mutant cells with enough resolution that the increased chain lengths could be seen.

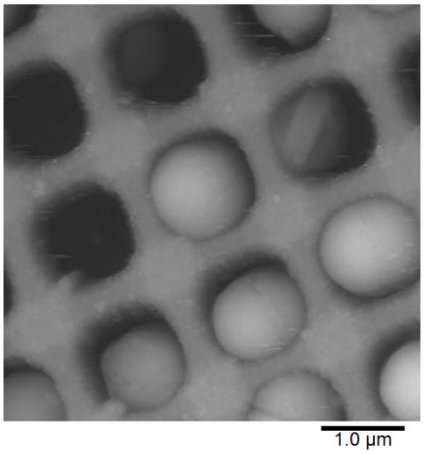

Figure 4.16- Topographic scan of SagB mutant cells. Z scale (black to white) = 1.475 µm.

The cells were imaged in the same 300 mM KCl, 10 mM Tris, pH 7.8 buffer that the other strains had been imaged in. In Figure 4.16 there is a larger area scan showing multiple cells that seem to be of the right size and are generally healthy apart from one cell that is in the top right hand corner. There were not the misshapen cells that might have been expected if the cell wall is not broken down and hydrolysed by the SagB. It was expected that there could be cells that showed a hemispherical shape or have a ringed half that did not complete the growth into a sphere because the rings would not have been broken down as much or as quickly resulting in the ringed structure being more common and to have a longer lifetime.

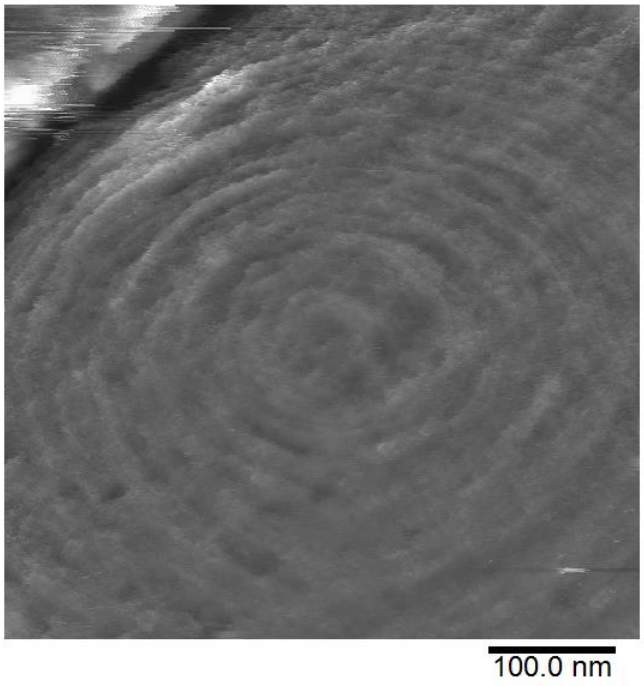

Figure 4.17- High pass filtered topographic image of the ringed architecture of a SagB cell. The filter size = 250 nm.

The rings shown in Figure 4.17 are similar to those of the wildtype at a resolution that is not able to distinguish individual glycan chains.

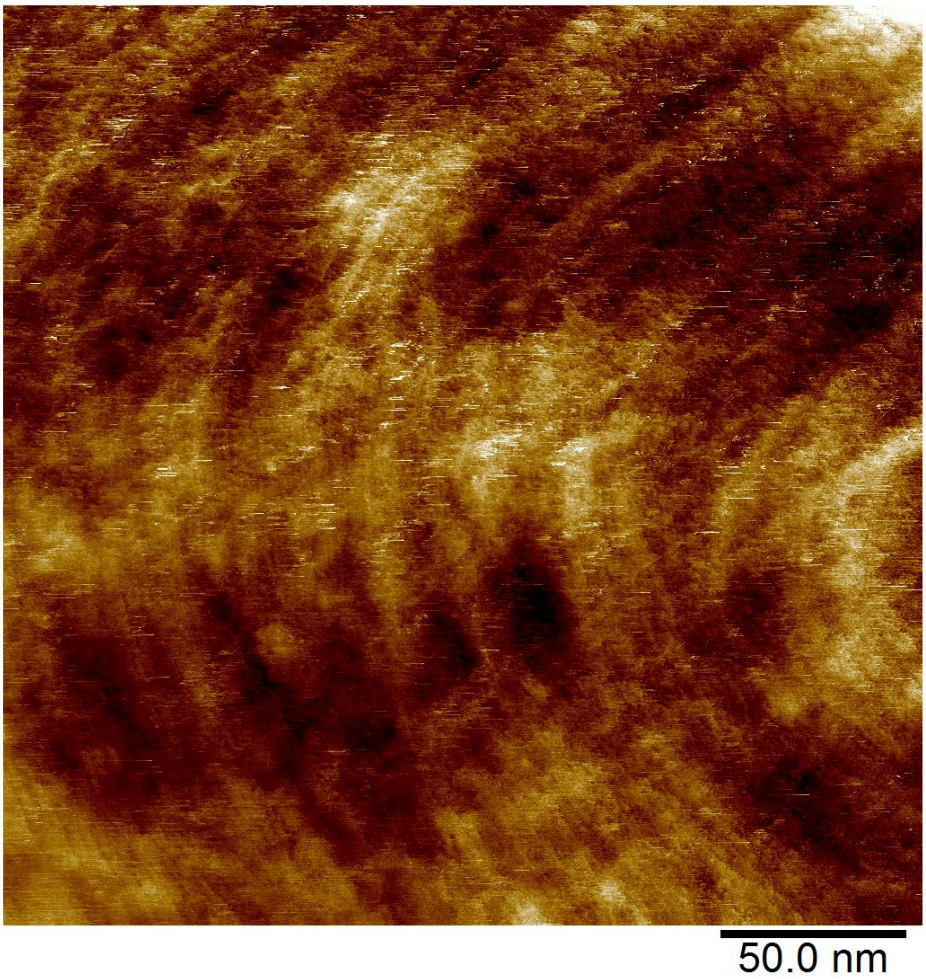

Figure 4.18- Topographic image of zoomed region of ringed architecture of a SagB cell. The image has been 3rd order plane fitted and has a Z scale (dark brown to white) = 11.5 nm.

While trying to obtain higher resolution images of SagB rings Figure 4.18 has evidence of dense rings in the bottom left corner of the image but not at the single strand resolution that would be needed to make the strand length comparison.

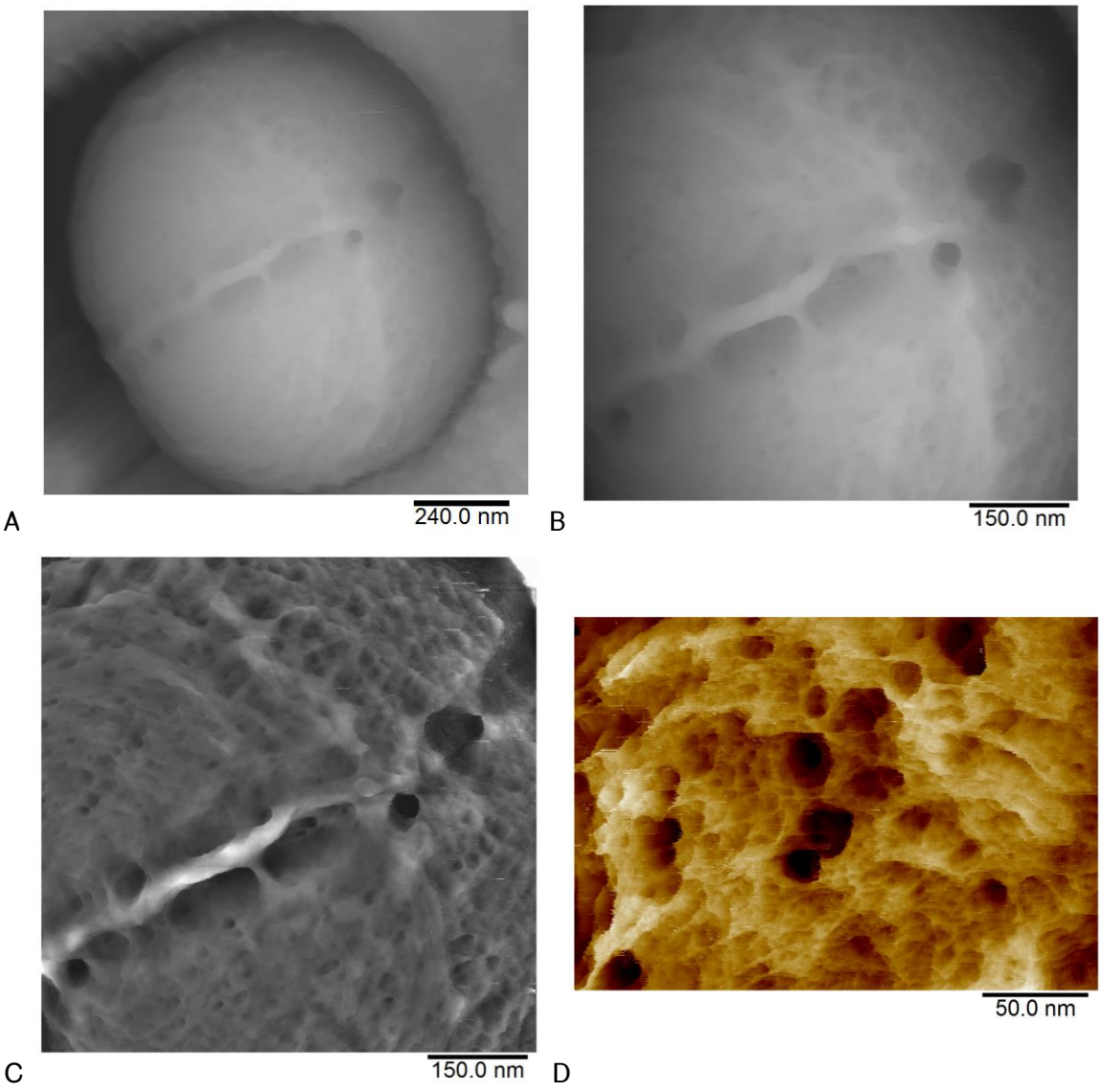

Figure 4.19- Topographic images of a SagB cell showing ringed structure and a raised band. (A) has a Z range (black to white) = 907 nm. (B) has a Z range (black to white) = 470 nm. (C) is a high pass filtered topography version of image B and has a filter size= 608 nm. (D) is a zoomed in image on the top left hand corner of image (C) and has been 3rd order plane fitted with a Z range (dark brown to white) = 27 nm.

A cell with more developed rings was found and imaged, producing cleaner images than were possible on the dense rings as shown in Figure 4.19. The cell shows evidence of the two different architectures with the ringed architecture on the left hand side of the cell and the mature architecture on the right hand side of the cell. The presence of the mature structure which looks similar to the mesh that has been seen in Figure 4.5 confirms that the peptidoglycan is eventually degraded into the final mature structure in the SagB mutant.

Focussing on one of the ringed regions that has some holes shows some possible single strands but the start and ends of the chains are not resolvable to be able to measure chain length to be able to compare it to the wild type. This cell had a crack through the rings, signalling a division event. Between the two halves of the dividing cell was a raised band of material which is similar to that seen in the wildtype cells in Chapter 6 which also have strands that bridge across the raised band.

4.8- Imaging *S. aureus* without performing a drying step during cell preparation

One step in the sample preparation involves the drying of the cells into the silicon holes using nitrogen flow as detailed in Chapter 3. An experiment was performed without the drying step to ensure that the architectures seen are not drying artefacts.

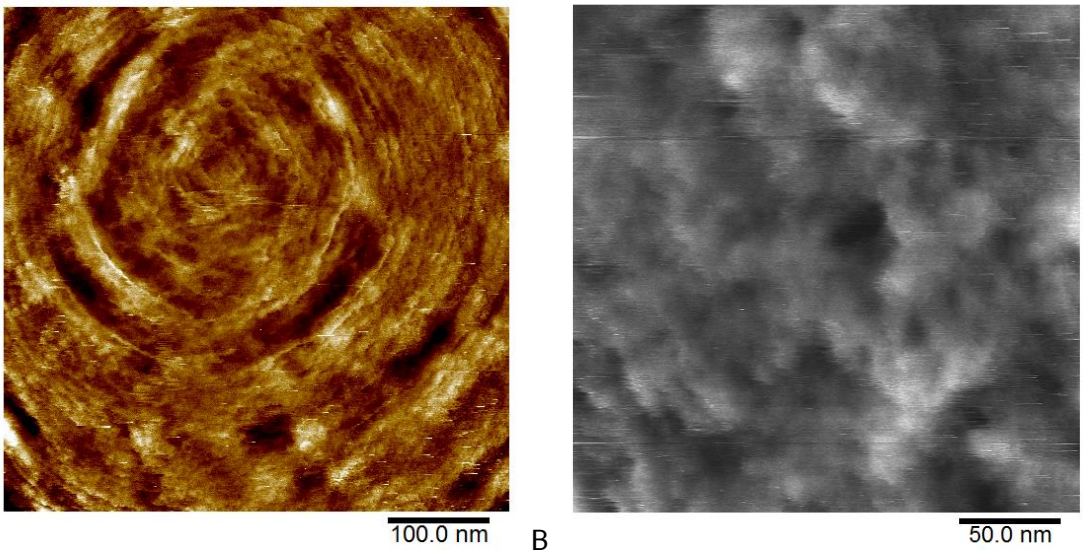

A B

Figure 4.20- Images of *S. aureus* cells taken without the nitrogen drying step in the cell preparation. (A) is a topographic image of a cell with ringed structure and has been 3rd order plane fitted and flattened. Z scale (dark brown to white) = 15 nm. (B) is a topographic image of a cell with mature structure and has been 3rd order plane fit then 0th order flattened. Z scale (black to white) = 25 nm.

Figure 4.20(A) shows a cell imaged during this experiment with a set of rings that matches the ringed architecture observed in Figure 4.4. The cell has few overlapping fibres but does have some holes within the rings and a concentric trough that looks like it follows where rings used to be. This trough is interesting in analysing a pattern of how the rings are broken down into the disordered structure. In Figure 4.20(B) there is

evidence of the mesh like mature architecture which is comparable to the structure seen in Figure 4.5 or Figure 4.9 as there are similar holes within the cell wall.

Using the nitrogen line to evaporate liquid off the cells that are pipetted onto the silicon surface improves the yield of cells in the holes which helps preserve the tip, as on average it will take fewer large area scans to find a cell for imaging. If the drying step is not performed, often it can take more scans of the highly topographic silicon which can cause damage, leading to a reduced resolution. The structures seen in the cells that did not have any drying performed on them are comparable to those from cells that were exposed to the nitrogen line so it is believed that the drying process does not have a large impact on the peptidoglycan structure. *S. aureus* cells typically live in the nose where they have to be able to survive varying environments including dessication and high salt, so it is unlikely that gentle drying will impact heavily.

4.9- Discussion and conclusions

This chapter presents the evolution of the method of AFM imaging techniques of *S. aureus* starting with the established method contact mode. Contact mode was successful in allowing for the cells to be imaged over repeated scans and was used to capture a dynamic process of cell division [(Kailas et al., 2009)]. To further understand the cell wall structure higher resolution imaging was sought so different AFM imaging modes were trialled to test their suitability in imaging the samples and the resolution that was obtainable using these methods.

Tapping mode imaging of the cells in liquid had previously had a low rate of immobilising the cells over multiple scans, possibly due to the acoustic waves that are created with the Veeco Dimension 3100 method of tapping in liquid where the whole Z piezo is oscillated. QI mode and PeakForce tapping mode both work as fast force mapping techniques where the tip is cycled on a full force curve at each pixel, indenting into the sample at a user defined force. They both exert lower lateral forces on the sample than contact mode and do not oscillate the tip at close to its resonant frequency like in tapping mode so they do not produce higher frequency acoustic waves in the imaging liquid.

QI mode was tested more extensively than PeakForce tapping mode on *S. aureus* samples and *B. subtilis* cells by myself and Richard Bailey (group member) and then latterly David Owen (group member). The other group members focussed on the ability to use QI mode for mechanical measurements at higher pixel densities than force

mapping mode and between the group members a technique was developed successfully for this purpose. For imaging at higher resolution, QI mode could not provide a resolution that improved on the previously used contact mode, although there was a decrease in the rate of cells being dragged out of the immobilisation grids compared to contact mode. When optimising for imaging the force data that was recorded in QI mode was not necessarily reliable as ringing was induced in some force curves. The other group members continued using QI mode successfully while optimising parameters to give them accurate force curves. QI mode allowed them to take higher pixel density force profiles of *S. aureus* surfaces in shorter time frames than standard force mapping mode.

PeakForce mode was tested briefly using the same cantilevers as had been used for contact mode and QI mode (MLCT E and F). The imaging sessions for PeakForce mode did not provide any images of *S. aureus* cells in the holes but imaging of the grid showed difficulty in the tip climbing over the features without interference patterns on the high gradient features which caused the automatically controlled parameters to reduce the imaging speeds to less than 0.5 Hz. The automatically controlled parameters like the scan speed, setpoint and gains were switched to manual control but this did not stop the interference patterns in the images.

There are specially designed cantilevers for PeakForce modes that were not tested which could result in better quality imaging. With the emergence of small amplitude tapping mode as an effective technique for imaging the cells in liquid PeakForce was not pursued further. For QI mode there is also the potential to test different cantilevers that could result in higher resolution images. Sharper or stiffer tips like the BioLever mini which are smaller and have a higher spring constant than the MLCT-E and F could give better control over the force applied to the surface.

Small amplitude tapping mode was the first and most repeatable technique for obtaining structural resolution images in liquid. The use of the Bruker FastScan-D cantilevers which had been specially designed for use with the Bruker FastScan in liquid tapping mode with the small laser spot size was one of the main factors in the ability to image structures on the surface of the cells. One of the main factors in subsequently improving the resolution of the images of the *S. aureus* cells was the optimisation of the imaging buffer by testing different salt concentrations.

The structures that were imaged on the wildtype cells correspond to those that have been published previously with the young architecture showing a ringed structure and

the mature architecture showing a lack of rings [(Touhami et al., 2004; Turner et al., 2014)]. To confirm that the structures that are seen are indeed the peptidoglycan cell wall, experiments were performed to try to systematically rule out the other candidates that could form the structures.

From the AFM images in Figures 4.8 and 4.9 there is clear evidence of architecture similar to that seen in the wildtype SH1000 strain with both rings and the mature architecture seen. The SrtA mutant showed evidence of the rings and the mature architecture as seen in the wild type cells. The SagB mutant did not produce misshapen cells to the extent that had been predicted by previous studies [(Wheeler et al., 2015)]. The ringed structure was seen to look similar to the wildtype ringed structure with evidence of dense rings and some that had been degraded. One cell that was imaged presented both the ringed and mature structure on the two halves of the same cell indicating that in SagB the rings are still degraded over time to eventually form the mature structure.

The wild type cells that were treated with trypsin would also have the outer wall proteins that were covalently attached removed as their bonds are hydrolysed by the trypsin. These cells were imaged and again showed no evidence of a different architecture of the cell wall.

These mutant and protein removal experiments tested the candidates that could be the cause of a structure on the outside of the bacterial cell wall. They all gave similar results in that they showed structured rings and then areas of mature less ordered or mesh like structure which is the same as had been seen in the wild type imaging. There was no evidence of misshapen or modified cell appearance when a field of multiple cells were imaged. The structures being the same as the wildtype SH1000 strain, leads to the belief that the structures that are seen are formed from peptidoglycan as originally theorised. It was not possible to resolve a big difference between the wild type cells and those that had had proteins removed from their surface which suggests that the imaging is not at high enough resolution or is too damaging to the proteins to be able to image them on the cell surface. By ruling out these other candidates the structures can be discussed as peptidoglycan structures that are remodelled over the course of the cell cycle.

Part of the experimental method of imaging the cells involves a partial drying step which increases the yield of the cells trapped in the silicon holes. This step is not vital to trapping cells but allows for a cell to be found more quickly after the start of imaging, reducing the likelihood of tip damage by repeated scanning of the highly topographic

silicon grid. Young ringed architecture and the mature disordered porous architecture were seen which is similar to the structures seen in the cells that have undergone the partial drying step. The drying step was performed in most experiments due to the improved yield of cells and the seeming lack of effect it had on the structure of the cells.

Overall, small amplitude tapping mode using the Bruker FastScan and Bruker FastScan-D cantilevers in liquid has been developed to allow for the imaging of *S. aureus* cell wall architecture at high resolution. The imaging of different mutants allowed for a probe into the features seen in the architecture of the *S. aureus* cell wall. Imaging a whole range of mutants would allow for further probing into the cell wall features and how certain genes change the division or maturation process. The SagB mutant that was imaged lacks one of the hydrolases involved in the remodelling of the peptidoglycan. It is one of many hydrolases including SagA, ScaH and AtlA which could all be imaged in future work to see if they have a different peptidoglycan organisation. It would also be interesting to characterise more extreme mutants that have growth defects to see how the growth defects affect their shape and structure at a whole cell shape and fine structure length scale.

Future work could also focus on the imaging of biofilms with AFM as this is the environment that bacteria often live in. This work would be challenging due to the size of the biofilms which make AFM imaging difficult but it would be interesting to see whether the cells have different features or structures when in large biofilms compared to when they are single cells.

Chapter 5- High resolution AFM of the young *S. aureus* rings peptidoglycan architecture.

During the division cycle of an *S. aureus* cell new peptidoglycan is predominantly added to the cell during the formation of the septum that will eventually create two approximately hemispherical cells. These two daughter cells will then split apart, exposing the septal plate that is made of the freshly inserted peptidoglycan. The flat septal plate deforms out to give the cell an almost spherical shape and then the cell grows slowly into the fully spherical shape [(Zhou et al., 2015)]. The young architecture has previously been seen to have a faint ringed structure which this chapter will investigate further. Understanding how the peptidoglycan is inserted into the cell wall is important as many antibiotics in the penicillin class work by targeting the cell wall synthesis process. Penicillin binding proteins (PBPs) are important in the insertion of glycans to the cell wall and for the formation of crosslinking peptides which does not happen properly in the presence of these antibiotics because PBP active sites are occupied by the antibiotic compound. The peptidoglycan insertion proteins have been seen to localise to the septum but the mechanism and pattern of the peptidoglycan insertion into the cell wall is not well understood. By imaging the ringed architecture with AFM at high resolution new information about how the molecules are ordered as they are added to the septum may be obtained, as this is where the majority of the peptidoglycan is added to the cell wall. This chapter will detail the findings of the imaging of the fresh architecture of the wild type cells and some of the mutants, which were also described in Chapter 4, with the differences outlined. The analyses performed on the images will also be described and discussed.

5.1- High resolution imaging of *S. aureus* rings

For the high resolution images the cells were most often imaged in the high salt buffer (300 mM KCl, 10 mM Tris, pH 7.8) as has been outlined in Chapter 3. Some of the images were taken in growth media or a slightly modified high salt buffer. Unless otherwise stated it should be assumed that the high salt buffer was used. Small amplitude tapping mode with the Bruker FastScan AFM and Bruker FastScan-D probes was used for all of the imaging.

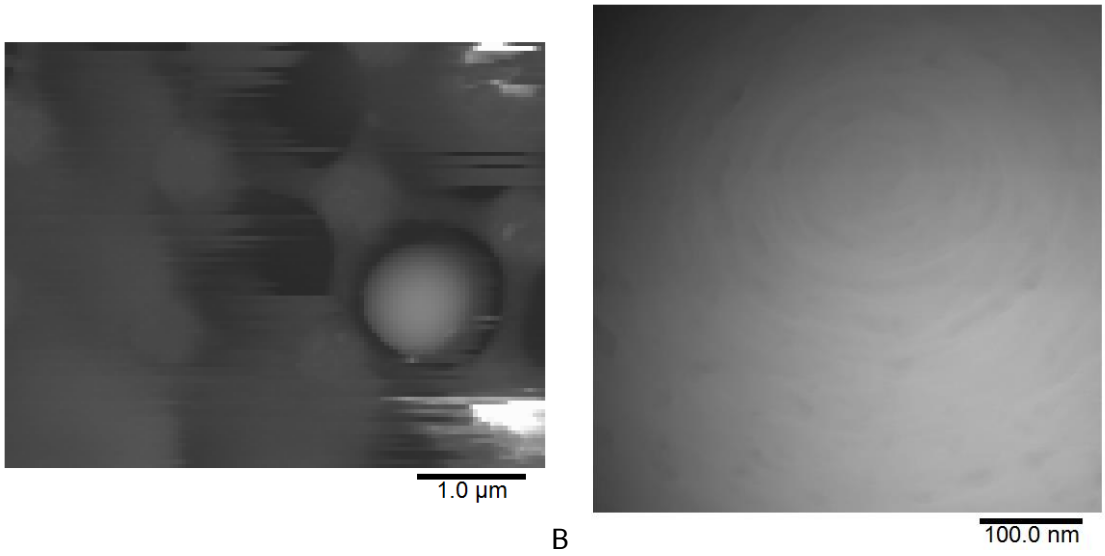

A B

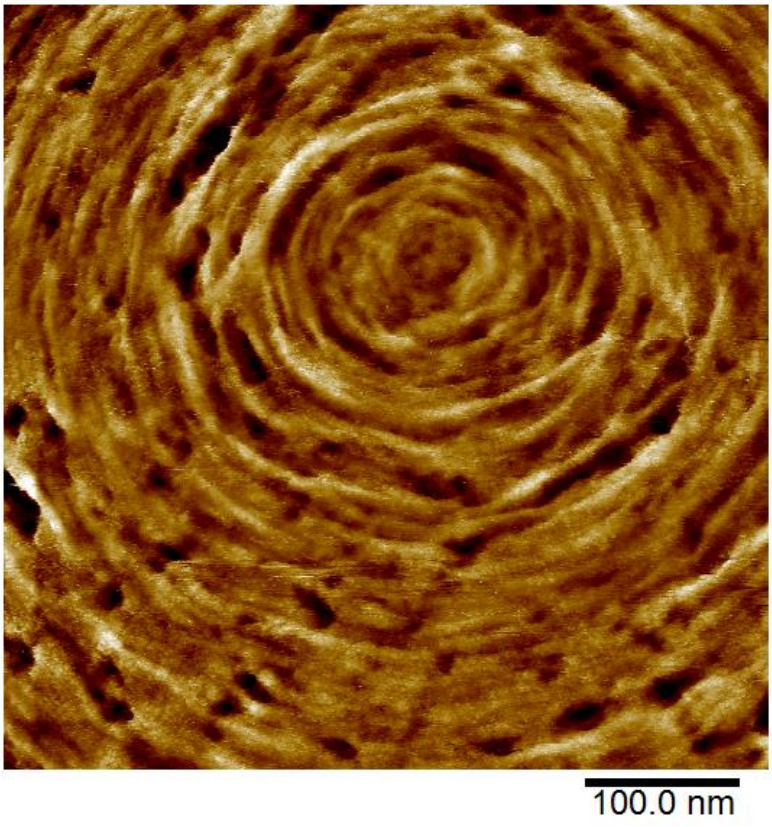

C

Figure 5.1- Topographic images of *S. aureus* cells showing ringed architecture immobilised in a silicon grid, imaged in small amplitude tapping mode. (A) is a large area topographic scan showing a single cell Z scale (from black to white) = 823 nm . (B) is a topographic image of the ringed structure on the surface of the cell in (A) with a Z scale (black to white) = 249 nm. (C) is a high pass filtered topography version of (B) with a filter size = 249 nm.

In Figure 5.1(A) there is single cell in the field of view at a resolution similar to that achievable using other imaging techniques like contact mode or QI mode. The resolution achievable with small amplitude tapping mode means that zooming in on top of this cell reveals a set of rings (as seen in Figure 5.1(C)) on the top of the cell in a detail that has been unobtainable using other imaging modes. It is possible to see individual rings and points where the rings overlap. There are regions where the rings are more ordered and some where there are holes in the structure of rings. To understand the nature of the ringed structure of peptidoglycan, *S. aureus* rings were imaged on multiple days using different conditions to ensure their structure was consistent.

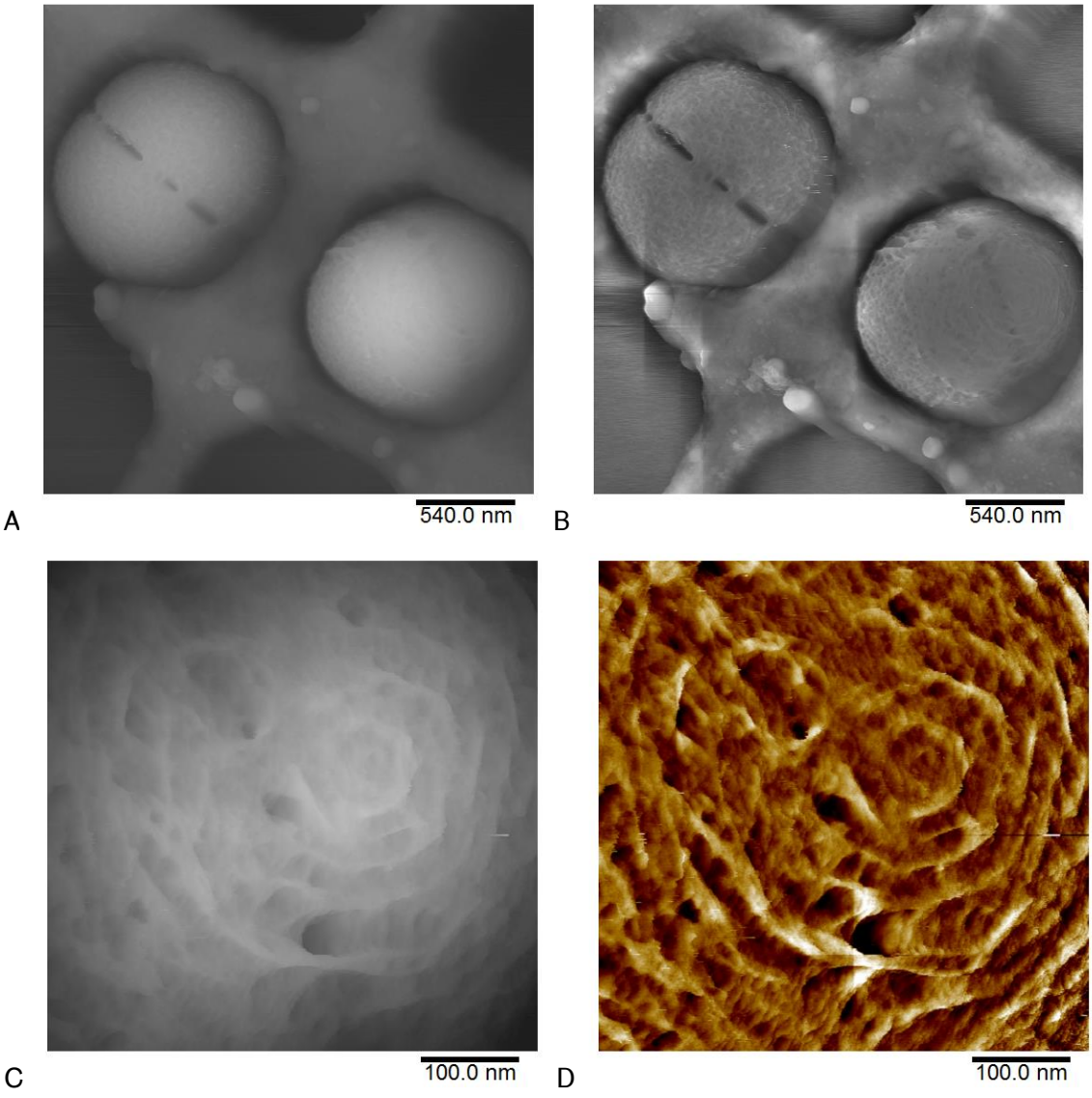

Figure 5.2- Topographic images of a *S. aureus* cells immobilised in a silicon grid. (A) shows a large area topographic scan of the two cells with a Z scale (black to white) = 1.1 µm. (B) shows the high pass filtered topographic image of the cells with a filter size of

1.34 µm. (C) is a topographic image of the top of the right hand cell from 5.2(A) & (B) with a Z scale (black to white) = 171 nm. (D) is the high pass filtered topography of the zoomed in region with a filter size = 249 nm.

The restructuring of the rings over the course of cell division cycle is not fully understood on a molecular scale. In Figure 5.2(A) and (B) there are two cells seen in the silicon holes with different peptidoglycan architecture. The cell on the right shows evidence of rings, though rings that are not as densely packed as seen in Figure 5.1, and an area of a seemingly disordered structure within the same cell. The disordered structure is also seen on the cell on the left hand side. Zooming in on the less dense rings of the right hand cell as seen in Figure 5.2 (C) and (D), it can be seen that there are gaps between the rings and that there are also fewer instances of the rings intersecting than in Figure 5.1.

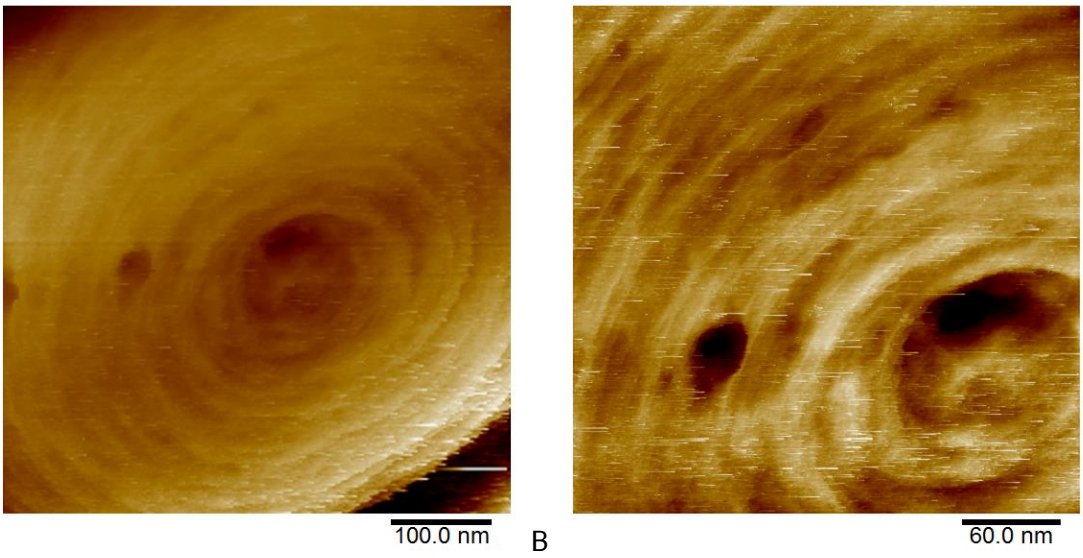

A B

Figure 5.3 - Topographic images of stationary phase *S. aureus* cells that show evidence of dense rings. Both images have been 3rd order plane fitted. (A) has a Z scale (dark brown to white) = 118 nm, (B) as a Z scale (dark brown to white) = 26 nm.

The images in the Figures 5.1 & 5.2 were taken on cells that were grown to exponential growth phase meaning the cells in the sample would be actively growing and dividing at their fastest rate. In Figure 5.3 the cells were grown to stationary phase which is the point that the growth media becomes saturated with cells and can no longer support the number of cells present. This experiment was performed to establish whether there is a difference in architecture seen in the two growth stages. Figure 5.3 shows the same dense rings seen in the Figure 5.1 with fibres packed close together. There are some holes within the rings but not to the same extent as in Figure 5.2. The rings are not seen

at the very centre of the septal plate which is the same as can be seen in the loose and dense rings. There is not a noticeable difference between the rings seen in the two growth stages.

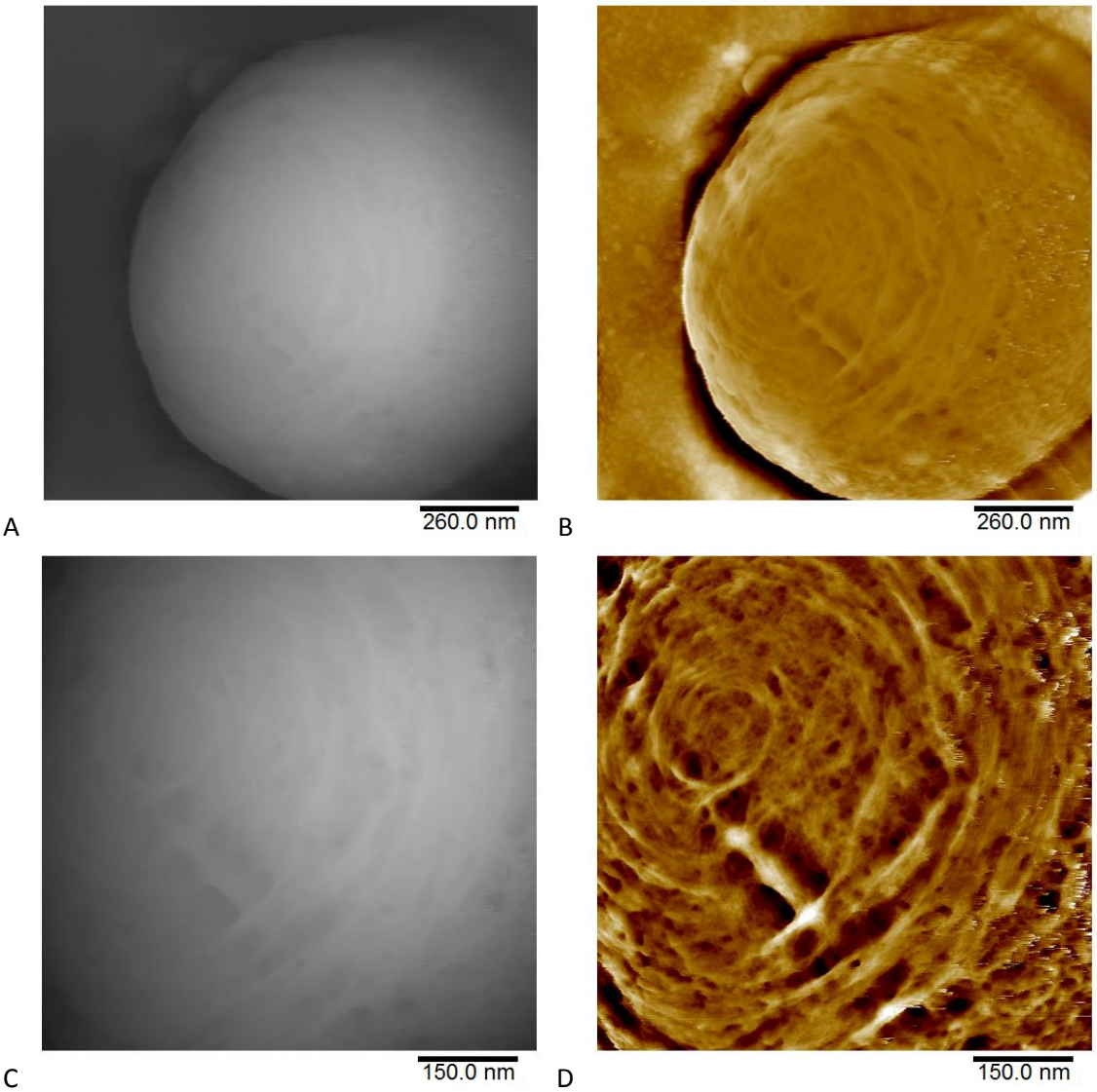

Figure 5.4- Topographic images of *S. aureus* cells imaged in TSB growth media that show evidence of degradation of the ringed structure. (A) has a Z scale (black to white) = 946 nm, (B) a high pass filtered version of image a with a filter size = 651 nm. (C) is a zoomed version of image a. It has a Z scale (black to white) = 508nm. (D) is a high pass filtered version of image c with a filter size = 373 nm.

A set of images of rings that were taken using TSB growth media as the imaging liquid are shown in Figure 5.4. The rings in the images are less dense than those seen in either Figure 5.1 or 5.2. Towards the top of the zoomed in Figure 5.4(D) there is a region where there are no longer any rings present due to the peptidoglycan ageing process. This

region is seemingly unstructured as strands of peptidoglycan are in a greater range of orientations when compared to the highly ordered, conserved orientations of the strands within the ringed region to the right of the images. Towards the bottom of the cell a crack can be seen going across part of the rings, though unlike in Figure 5.2(A) and (B) there is a raised band of material that seems to appear from under the rings in regions where there are no bridging ring fibres. This set of images shows an intermediate stage between the dense ringed structure and the mature structure which gives indications as to how the structure of the peptidoglycan is remodelled.

Based on these three sets of images of the cells a composite timeline of the peptidoglycan rings can be put together as they begin to be broken down by enzyme activity. The dense rings in Figure 5.1 show tight packing between the rings with no gaps between the fibres that make up the rings and no regions of disorder or holes among the rings. The rings seen in Figure 5.2 show a larger spacing between the rings though still show some long strands which could indicate that there is not a uniform or random localisation of the enzymes as long strands would be less likely to survive if this was the case. This timeline is referred to in Chapter 6 in Figure 6.29.

The rings of peptidoglycan that form during the growth of the septal plate are degraded over time due to enzyme activity and stress from the expansion of the cell. The bio-machinery that forms the septum starts at the outside of the cell, laying down peptidoglycan strands, moving towards the centre of the cell like the closing of a camera shutter [(Turner et al., 2010a)]. Studying the alignment and concentricity of the bundles of glycan chains that form the rings can provide information on how the glycans are added to the rings as the septum is formed.

5.2- Individual glycan chain imaging in the ringed architecture

Using a higher salt concentration or adding a divalent salt like $MgCl_2$ can increase the resolution of the images as explained in Chapter 2. In Figure 5.5 a buffer of 200 mM KCl with 10 mM $MgCl_2$ and 10 mM Tris at a pH of 7.8 was used to to image a set of rings with the aim of achieving molecular resolution in the peptidoglycan.

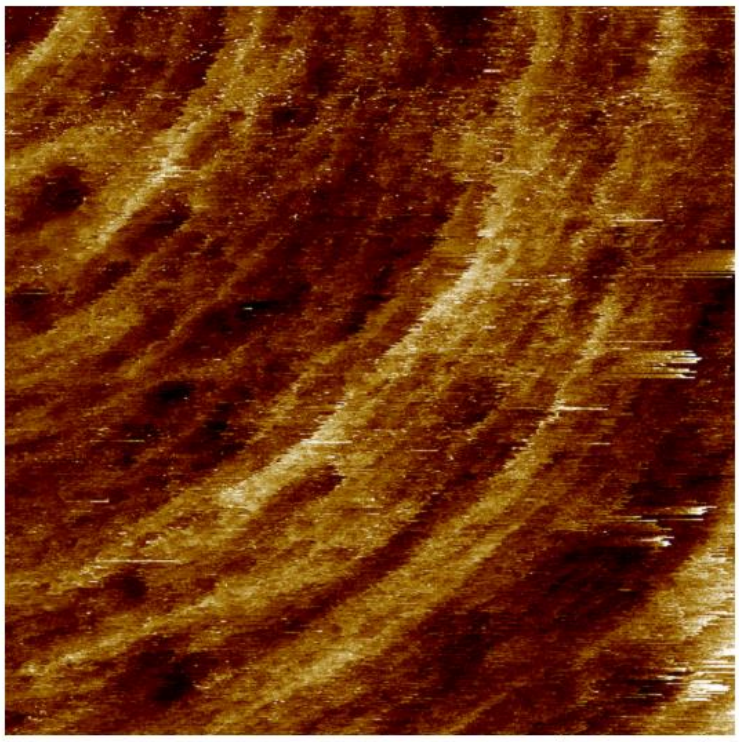

A

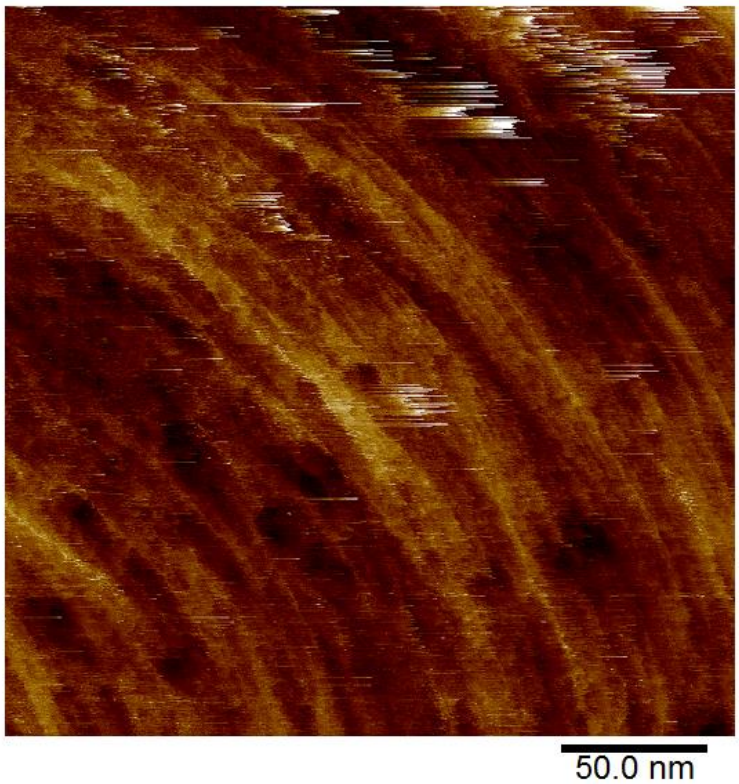

B

Figure 5.5- Topographic images of dense *S. aureus* rings that have been imaged in a buffer of 200 mM KCl, 10 mM Tris, 10 mM $MgCl_2$ at a pH of 7.8. The images have both been 3rd order plane fitted. (A) has a Z scale (dark brown to white) = 17 nm. (B) has a Z scale (dark brown to white) = 22 nm.

Figure 5.6 shows a zoomed in region of the ringed architecture in Figure 5.5 that shows very densely packed rings with few holes or disruptions to the rings. There is some overlapping and intersection of the rings but overall there is high order which suggests these rings are early in the maturation process.

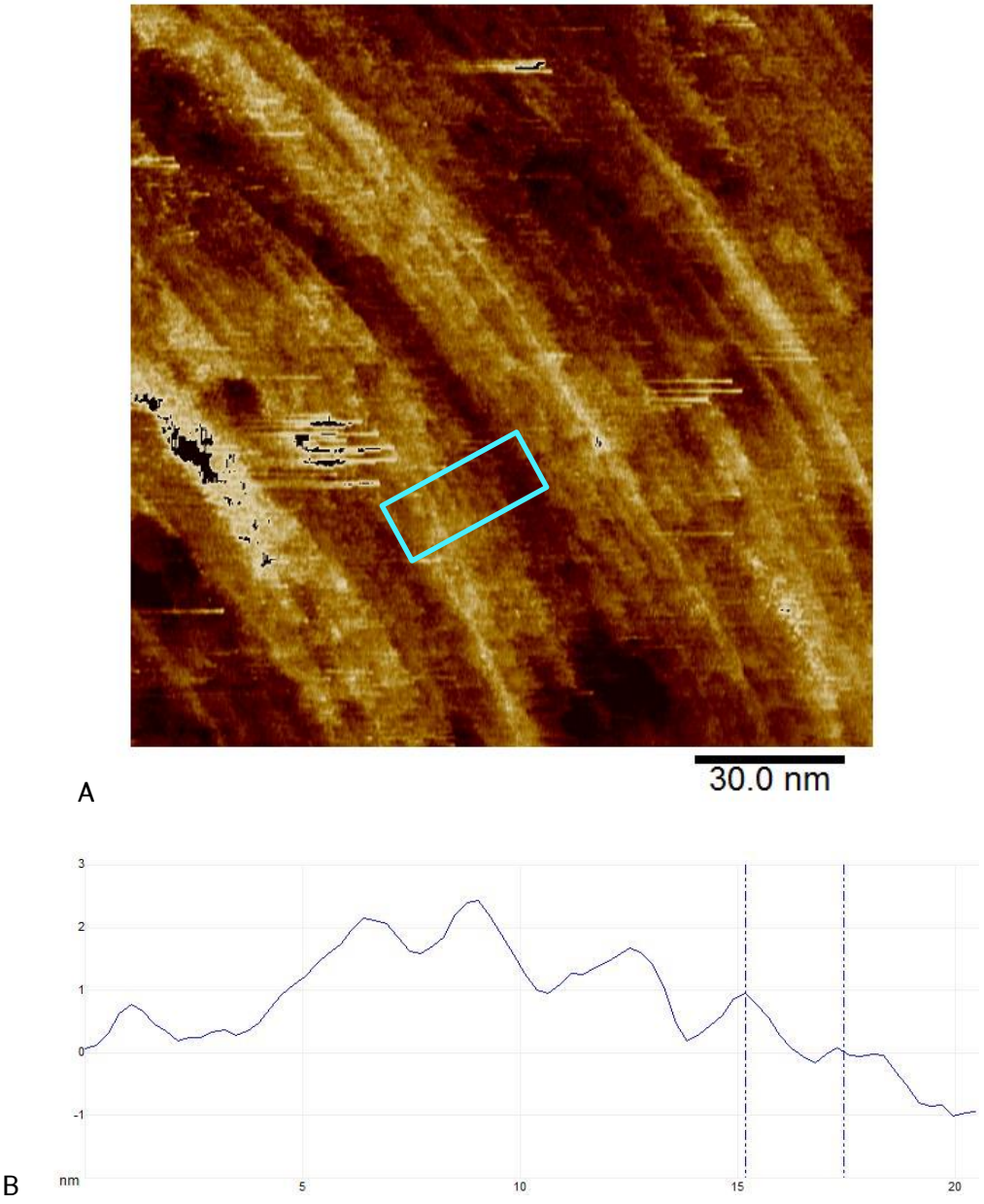

Figure 5.6- (A) is a topographic image of a zoomed in region of Figure 5.5(B) that has had a 3rd order plane fit applied and some thresholding to remove scanning artefacts. The Z scale (dark brown to white) = 14 nm. (B) is an averaged cross-section line profile of the topography of the glycan strands that are in the light blue box in image (A). The spacing between the two marked lines in the cross-section is ~ 2.7 nm.

The cross-sections of individual glycan strands seen in Figure 5.6 were measured with an average peak to peak distance of approximately 2.7 ± 0.5 nm based on 16 cross-section measurements, a value that corresponds to the NMR data that measures the glycan to glycan separation as 2.3 nm [(Kim et al., 2015)]. Individual strand resolution gives the ability to see how the molecules in the cell wall are ordered relative to each other.

5.3- Imaging repeating features along glycan strands in the ringed architecture

Imaging areas of rings over large scales shows the overall structure of the cell wall but to see how the individual glycan chains are ordered with respect to other chains, smaller, high resolution scans are needed.

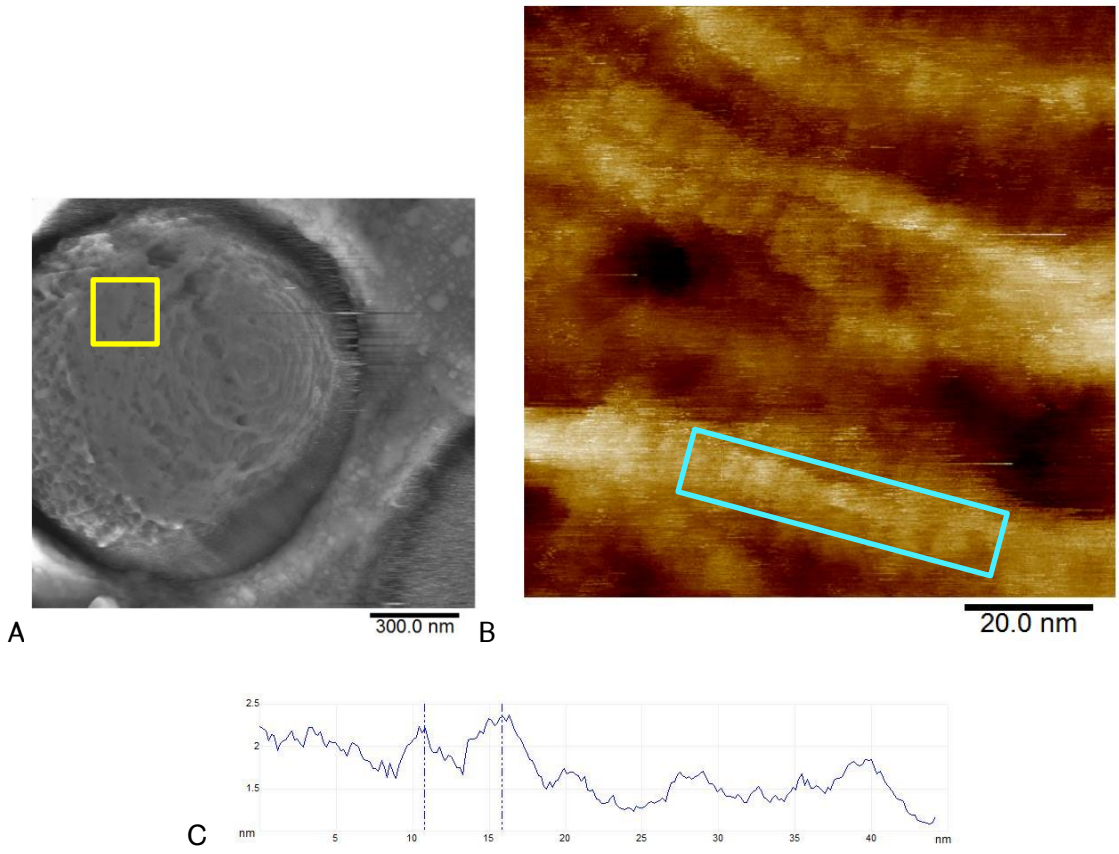

Figure 5.7- (A) is a high pass filtered topographic image of a cell showing ringed architecture with a filter size = 747 nm. (B) is region of the cell in (A) indicated by the yellow square that with ringed architecture. The image has had a 3rd order plane fit applied. The Z scale (dark brown to white) = 11 nm. (C) is an averaged cross-section line profile of the topography of the glycan strands that are in the light blue box in (B). The spacing between the marked lines is ~ 4.9 nm.

Scanning along the ringed architecture shows a repeating pattern along the rings that run horizontally on the image. This is the first evidence that there is some structure that is resolvable by AFM along the glycan chains, though the composition is not known due to the lack of chemical specificity of the imaging. The repeat of the pattern is approximately 5.1 ± 0.8 nm based on measuring the peak to peak distances of 14 repeating features with with the cross-section tool in the Bruker Nanoscope software.

Imaging the TagO mutant strain that does not have the teichoic acids on the outside of the cell was performed to determine whether the features seen along the glycan strands are these teichoic acid proteins. The imaging also produced images that showed evidence of a repeating pattern that was seen to run radially along the rings.

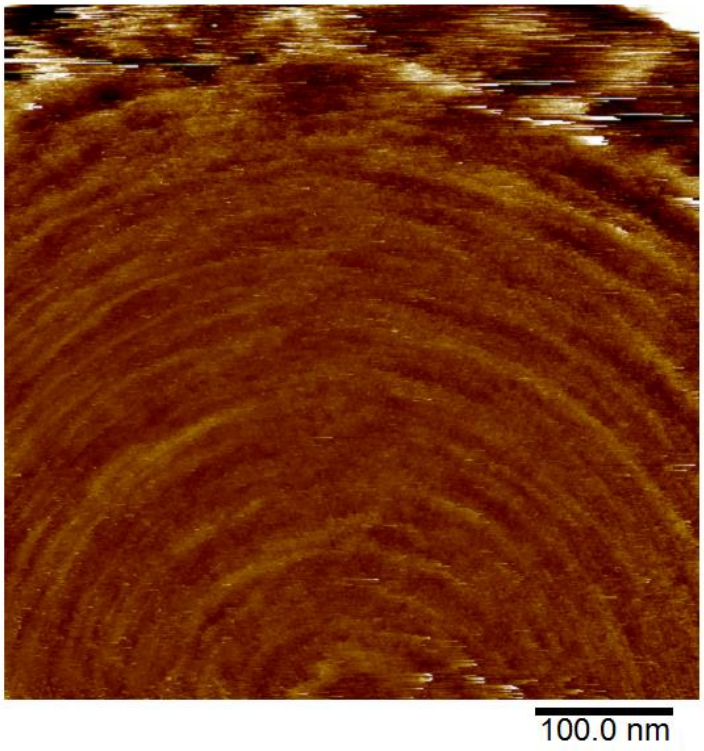

A

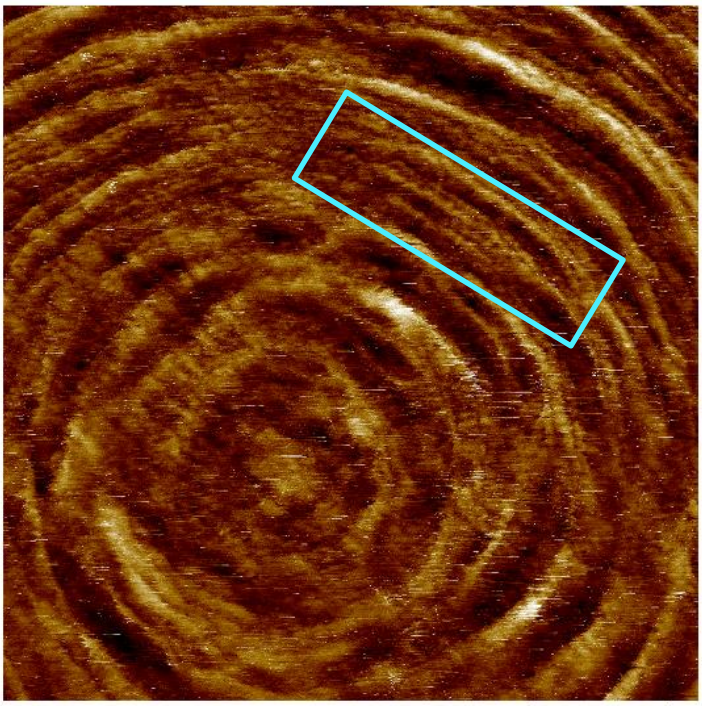

B

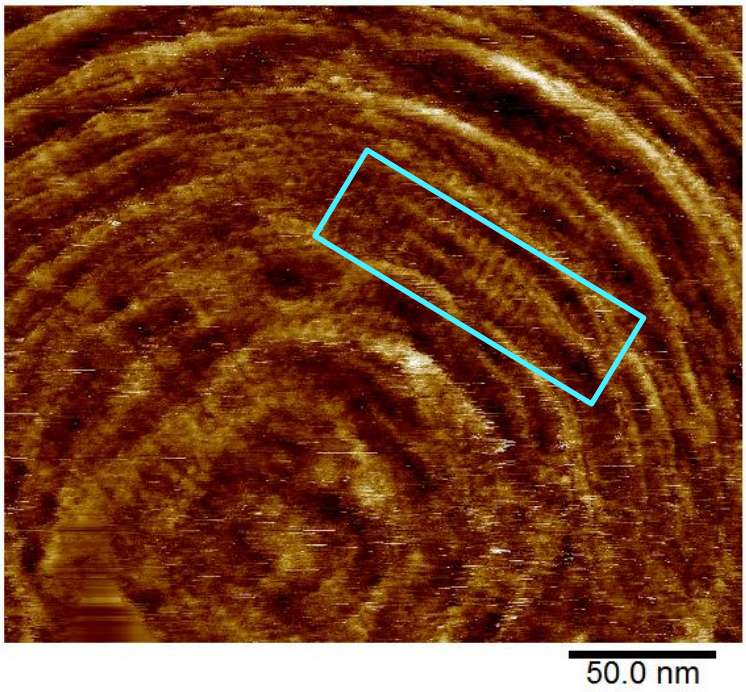

C

Figure 5.8- Topographic images of dense TagO mutant *S. aureus* rings. The images have all been high pass filtered. (A) has a filter size = 253 nm, (B) has a filter size = 125 nm and (C) has a filter size = 125 nm.

Rings can be seen in Figure 5.8 which is significant in confirming that the rings are not a structure of the covalently bound polymer as explained in Chapter 4.

Zooming in to the centre of the cell in Figure 5.8(A) shows a set of dense rings in Figure 5.8 (B) & (C). Some individual fibres are resolved in the top right hand corner of the Figure 5.8(B). In the top half of the (B) there is the evidence of the radial repeating pattern along the rings (marked with the blue rectangle) which, using the Bruker Nanoscope Analysis cross-section tool, was measured to have a period of approximately 5.1 ± 0.8 nm based on 7 measurements.

Figure 5.8(C) has an area of a clear repeating structure that runs along the rings marked by the blue rectangle. The period of this repeating pattern was also measured using the cross-section viewer and had a period of approximately 5.4 ± 0.9 nm in this region based on 9 measurements.

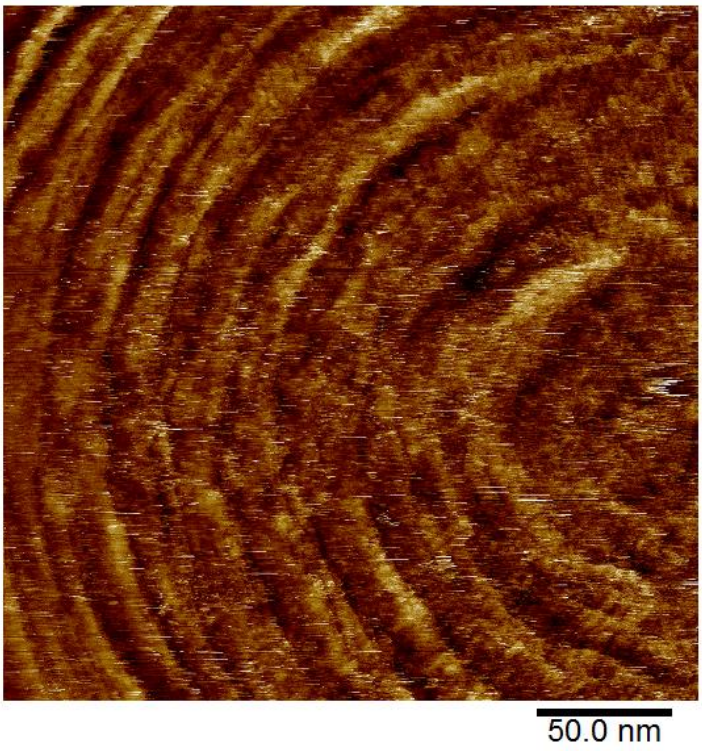

Figure 5.9- High pass filtered topographic image of radial feature on the ringed architecture with a filter size = 129 nm.

Another TagO mutant *S. aureus* cell was imaged that showed high resolution rings including radial features which supports evidence that there are features that can be seen on the glycans that run radially around the rings (Figure 5.9). It is possible that the features are easier to resolve on the TagO cells due to the absence of the teichoic acids.

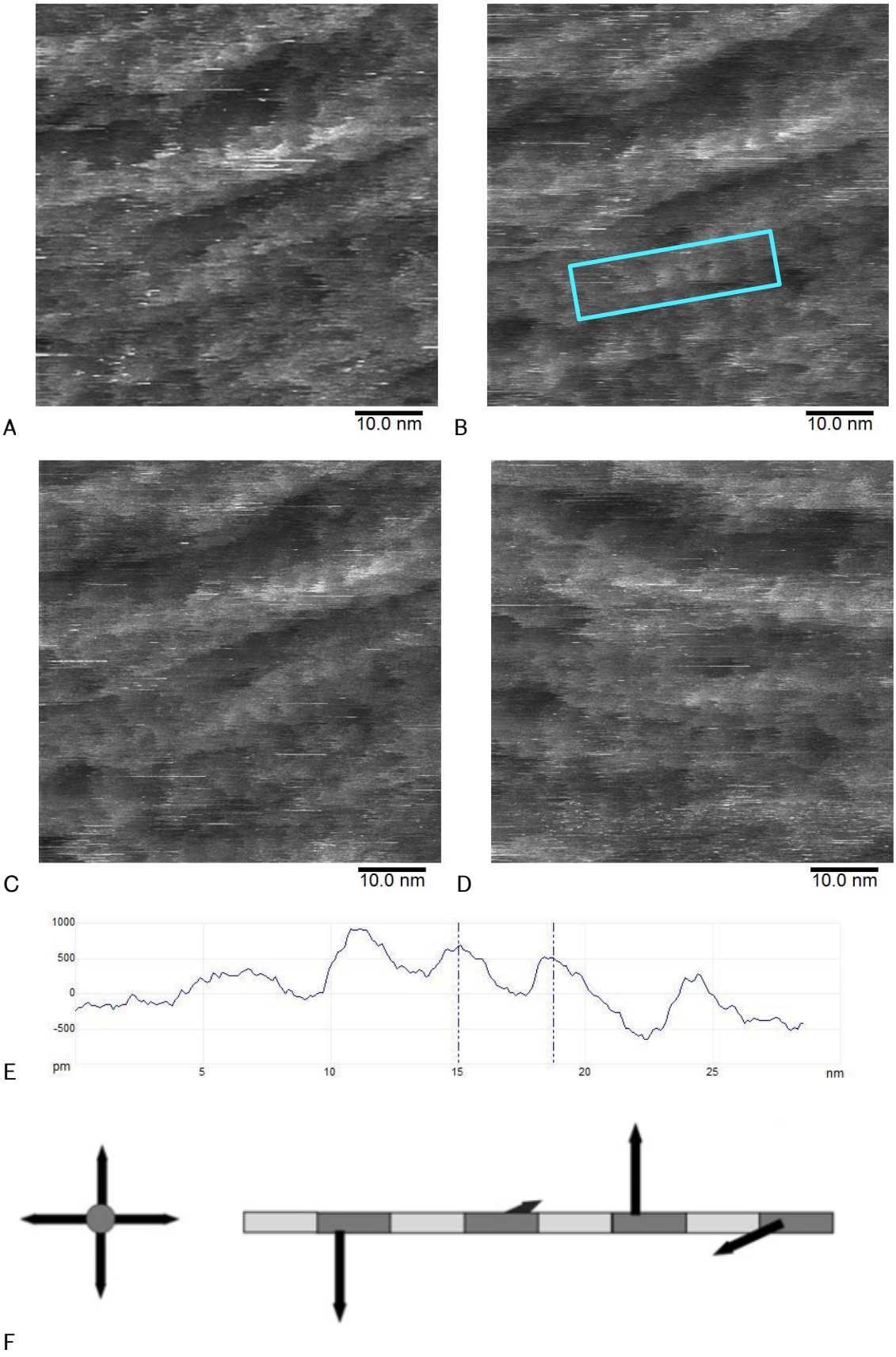

Figure 5.10- (A) – (D) are topographic images of peptidoglycan in the ringed structure. They have all had a 3rd order plane fit applied to the images with Z scales (black to white):

(A) = 10 nm, (B) = 11 nm, (C)= 11 nm and (D)= 10 nm. Figure 5.10 (E) shows the average cross-section topography within the area marked by the blue square on Figure 5.10 (B). The spacing marked is approximately 3.7 nm Figure 5.10 (F) is a diagram based on the NMR data that shows peptide side branches formed with a helical 4 fold axial symmetry with a period of 40 Å [(Kim et al., 2015)].

A different set of images were taken of a cell scanning along the glycan strands. When the scan direction is aligned with the orientation of the rings, the tip scans along the glycan strands in the rings. As the tip scans it does not change in height as much during the scanning of a line which can result in resolving features that are not seen when scanning across the strands like those seen in Figure 5.10. The four images in Figure 5.10(A)-(D) are consecutive scans of the same area and each shows the same features along the glycan strands. An example of a cross-section of some of the features is shown in Figure 5.10(E) which is the average cross-section of the area of Figure 5.10(B) that is marked by the blue rectangle. By measuring the peak to peak distance of all of the raised features, using the Bruker Nanoscope Analysis software's cross-section tool, in Figures (A)-(D) an average period of approximately 3.7 ± 0.8 nm based on 24 total measurements. This average peak to peak distance correlates well with the features being peptide side branches sticking out of the surface of the glycans every 4^{th} peptide branch which has been predicted, from NMR data [(Kim et al., 2015)], to have a period of 40Å as shown in Figure 5.10(F).

A repeating pattern was imaged on three different sets of images with two of the cells being the wild type strain SH1000 and the other being the TagO mutant strain. The periods of the raised features seen along the strands was measured to be approximately the same with averages of 5.1, 5.1 and 5.4 nm in Figures 5.7 and 5.8 (B) & (C) . The average of the repeating measurement taken of the images in Figure 5.10 has a lower average value of 3.7 nm. This differences could be due to resolution of the imaging with the images in Figure 5.10 being at a higher resolution. The larger scan sizes of these Figures 5.7 and 5.8 could contribute to the larger value for the period of the features seen in the TagO cell as the resolution of the images was not as good as they have larger pixel size so the pixels correspond to a larger area on the sample surface. The repeating structure in Figure 5.10 was measured over multiple images to give an average period for the raised features so this should be more representative of the true structure.

5.4- Analysis of central disordered region measurements

The central disordered region of the young rings is formed during the construction of the septal plate. There is biological machinery that builds the rings moving from the outside of the cell inwards, some believe like the closing of a camera shutter. At the centre of the rings there is the approximately circular region which does not have the same ringed structure as the rest of the septal plate as seen on cells like in Figures 5.1, 5.2, 5.3, and 5.4. Taking measurements of the central disordered region gave an average diameter of 60 ± 15 nm based on the measurements from 12 different cells with central disordered regions. There is also a drop in height of the cell of the plug region that has been measured to be on average 6 nm, measured using the cross-section tool. The value of the diameter could give an indication of the minimum radius that the ring forming machinery can work at, below which a different mechanism may be needed to complete the formation of the septal plate. Some modelling work has been performed that estimates that the force that FtsZ filaments can exert inwards on the underlying membrane decreases as the diameter of the curved surface decreases for a range of different diameters down to 74 nm [(González de Prado Salas et al., 2014)]. It is possible that the minimum curvature could be linked to the smallest radius that the can be made with the FtsZ filaments that still exerts a force. There is currently no agreed theory on how the peptidoglycan in the central disordered region is inserted into the middle of the rings. It has not been possible to obtain high enough resolution on the central disordered region to determine the molecular organisation of the peptidoglycan there.

5.5- Analysis of chain organisation in ringed regions

A series of approaches were devised for analysing the ringed structure that was imaged at high resolution with the aim of being able to quantify some of the features and organisation that was seen within the ordered peptidoglycan architecture.

5.5.1- Automated line recognition program using MATLAB

A code was written by Dr Robert Turner (Foster Lab, Krebs Institute, MBB, University of Sheffield) with the aim of being able to automatically trace the glycans in an AFM image, which would then allow the lines to be analysed to calculate properties of the glycans in the image such as an overall orientation or a strand length. The program was written in MATLAB and was initially created to trace glycan strands from AFM images of sacculi of *E.*

coli. The image of dense rings from Figure 5.1(B) was chosen to test how well the program could work on the mapping of rings.

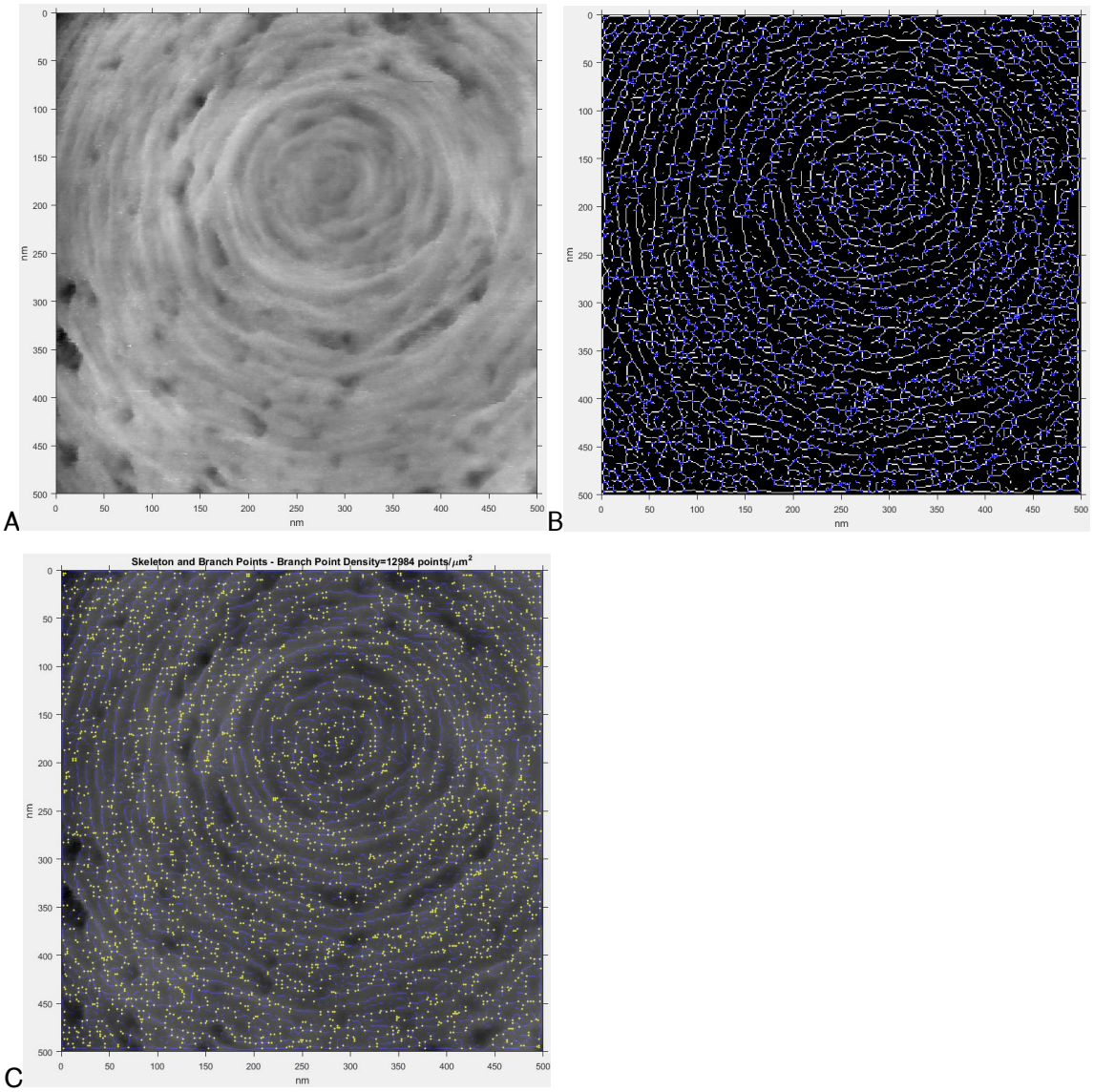

Figure 5.11- Results from analysis software that was run on the raw image from Figure 5.1. (A) shows the raw data after some flattening procedures. (B) shows the traces that the MATLAB program creates from the image with white lines correpsonding to the traces and blue dots corresponding to branching points where two traces meet. (C) is the traces overlaid on the raw data as a comparison with blue traces and yellow dots showing branching points.

The program runs a series of flattening procedures that aim to remove the curvature of the cells from the image as best as possible then thresholds are performed to try to differentiate between a glycan strand and background. The results show that the program over draws the rings with every white line in Figure 5.11 (B) representing a ring

according to the program. The points that two or more strands meet are indicated by the blue dots which are also over represented due to the extra rings that are mapped. The program also draws branching chains off the main rings that are not seen in the original image which adds to the number of lines drawn. From the image it does show that there is an overall circular pattern to the images that tracks the rings. The program finally overlays the traced lines back onto the AFM image showing where the script has overlaid too many lines on the rings. The branch point density is a value that is automatically calculated and would be a useful parameter to obtain from the images as it would indicate how regularly the glycan chains merge into each other, potentially giving information about the protein machinery that travels around septal plate as this ringed structure is initially formed. The program was designed to be used on *E. coli* sacculi which are extracted peptidoglycan that has been laid flat on a mica surface. The majority of *E. coli* peptidoglycan is only one layer thick so the overall height profile and curvature of the images that the program was designed for is vastly different from the images of whole *S. aureus* cells.

5.5.2- Analysis using NeuronJ tracing software

The idea of mapping the rings to be able to calculate strand lengths, orientation and branching points was developed into an analysis technique that would not overestimate the number of strands in the images. The rings were traced using a program that allows the user to manually select points on an image while tracing with the software snapping the traces to the rings in the image. To perform the analysis on the rings NeuronJ, which is a plugin for the software ImageJ, was used. NeuronJ was designed to be used to trace elongated structures in images and uses an algorithm to fit a trace to highly contrasting lines in images. Often the structures that are mapped using NeuronJ can be thresholded which makes the tracing process work more effectively, however using a threshold on these AFM images was not appropriate as it discards the range of Z values that are important in these AFM images. Instead the images had their curvature removed using a 4^{th} order plane fit and then NeuronJ was used to map the rings with traces by hand with the fitting software of NeuronJ assisting. The fitting software computes the optimal path along the strand by snapping to lighter pixels within a chosen snapping region as the traces are drawn with the mouse. The rings were generally simple to trace.

The traces were extracted and the x and y values were copied into MATLAB. A code, which was developed alongside Sandip Kumar (Hobbs Lab, Physics, University of

Sheffield), that fit a circle to the traces was run which produced a result of the co-ordinates of the centre of the fitted circle and the circle radii. The traces and circles could all be plotted and overlaid on the original image.

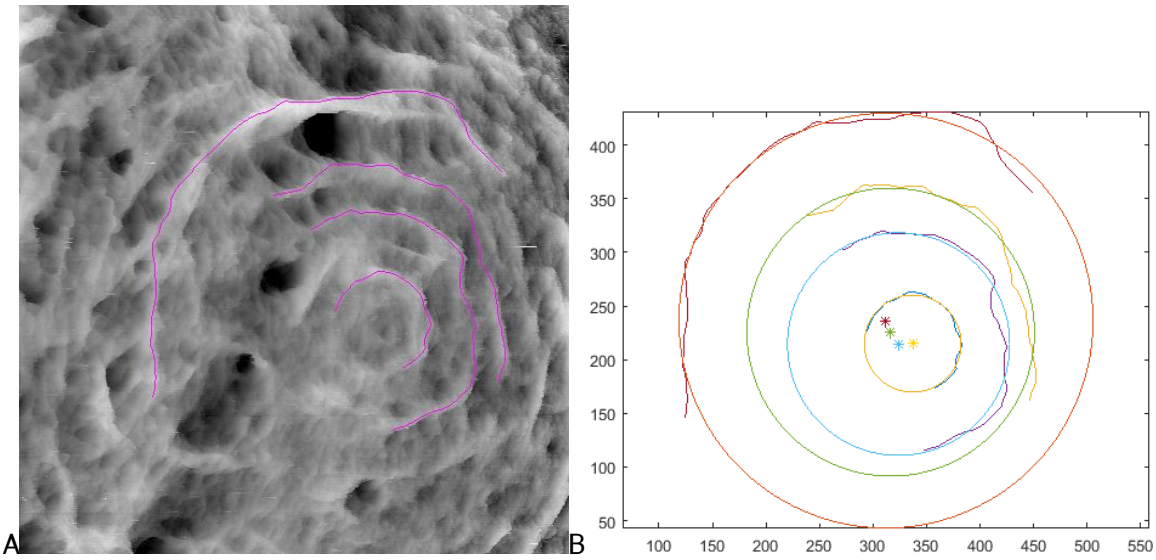

Figure 5.12- Image showing the NeuronJ tracing method results for the image in Figure 5.2. (A) is the raw AFM topography image with the tracings that were mapped using NeuronJ overlaid in pink. (B) is an image of the tracings that have been extracted and the MATLAB code has been used to fit circles and centre points to the traces.

The tracings are shown on the original AFM image in Figure 5.12 with the extracted traces and corresponding fitted circle to the right for comparison. The circle that is plotted works well for the length of traces that are shown in this image. It also shows that the fitting places the centres of the arcs approximately where they appear in the AFM image.

It was hoped that mapping the rings would enable individual glycan strands to be identified, allowing their minimum length to be estimated and to measure their density. Using NeuronJ, in images where the resolution is good enough to be able to resolve single glycans, the single glycans can be traced. However, often the start and end point of a glycan cannot be determined so the chain length analysis is not possible. It is easier to see where glycan fibres (bundles of multiple glycans) start and end so these can be traced, however, the length of these fibres does not necessarily provide useful parameters for a model as the fibres can merge together to form any length.

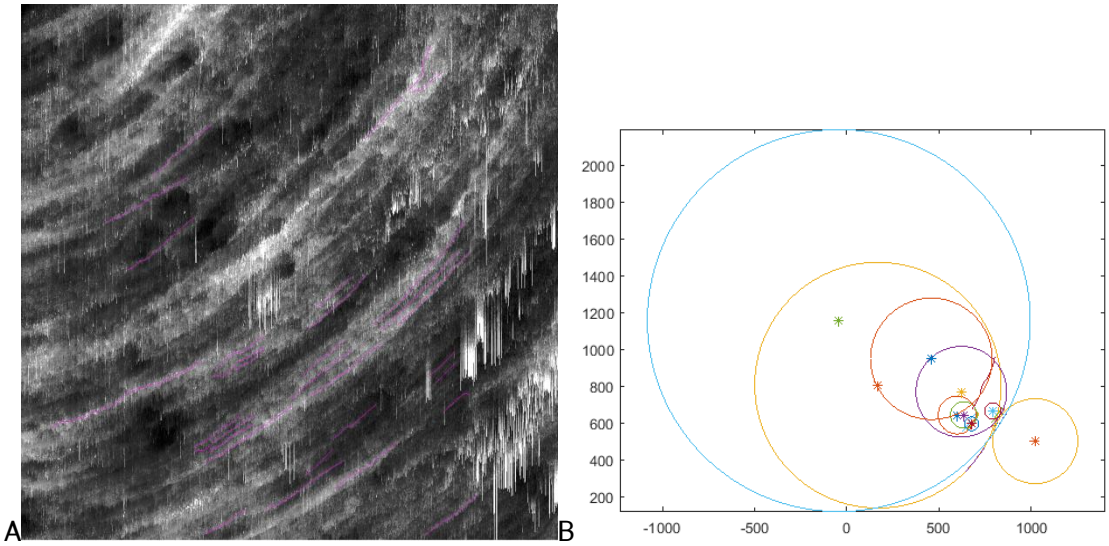

Figure 5.13- (A) The tracings that have been drawn on individual glycan strands on the image from Figure 5.5(B). (B) is the fitted and extracted tracings from some of the tracings from 5.13(A). The MATLAB code has been used to fit circles and centre points to the traces.

The short traces that were mapped in Figure 5.13 were of what appeared to be individual glycans that were of shorter lengths that the traces in Figure 5.12 as the individual strands are generally not resolvable over their whole length. When put through the fitting program, the short traces produce circles with a large range of radii and centre points. If the tracing is short the fitting program does not have as many points along the trace to calculate the equation for the circle as with a longer tracing. With a shorter trace there is also a problem that if there is less curvature to the line, the small curvature that is present is seen by the fitting program as a deviation from a straighter line leading to a circle equation with a large radius and a larger residual. In general the fitting program produces more accurate fits when the tracing subtends a larger angle around the centre of the ring as can be seen in Figure 5.12 when only the longest traces were drawn.

One comparison that can be made using the ring tracing method is between the densely packed rings and the slightly more mature rings that are less dense. Two images that are typical of the two ring densities were chosen and the tracing process was performed.

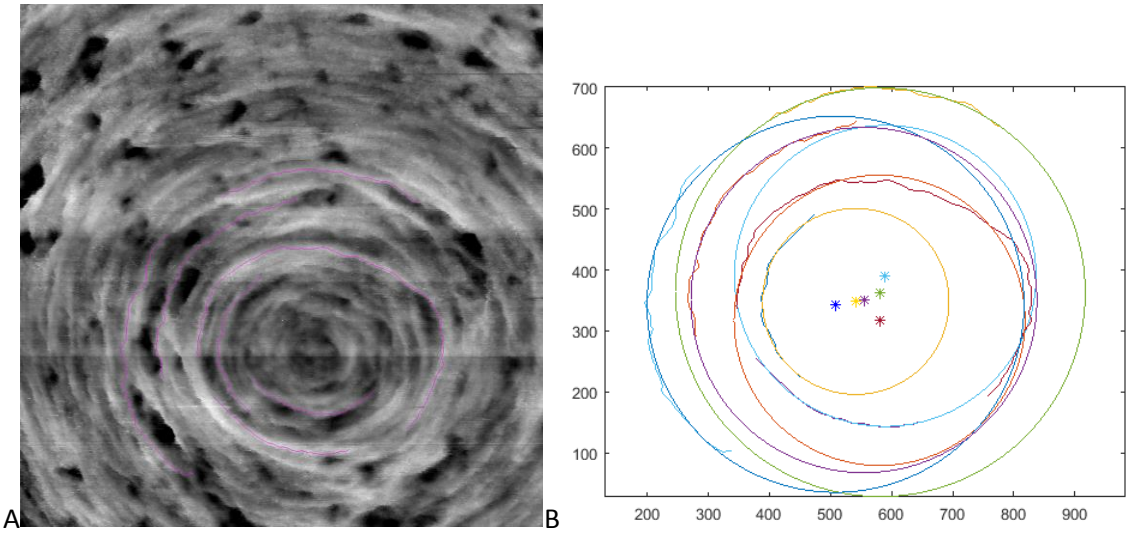

Figure 5.14- Images showing the NeuronJ tracing method results for dense rings (Figure 5.1) and less dense rings (Figure 5.2). (A) is the raw AFM topography images with the tracing that were mapped using NeuronJ overlaid in pink. (B) is the tracings that have been extracted and the MATLAB code has been used to fit circles and centre points to the traces.

Comparing Figure 5.12 and Figure 5.14 shows how the analysis works well in mapping the longer strands and fits circles to the arcs without any unrealistic diameter circles. The denser rings of Figure 5.14 are shown to overlap more than the looser rings of Figure 5.12 in the tracings but the centre points are located within the central disordered region of the septal plate which was discussed in Section 5.4. The higher density of rings means that there is more opportunity for overlapping of fibres as the rings are formed.

5.6- Discussion and conclusions

AFM images of the young peptidoglycan architecture have been taken to develop the understanding of the organisation of the peptidoglycan molecules as they are first inserted into the cell wall. Small amplitude tapping mode using an optimised high salt buffer has allowed for AFM images of the ringed architecture to be taken that have achieved molecular scale resolution on multiple occasions.

When the two halves of the dividing cell split apart, two approximately hemispherical daughter cells are formed with the flat sections of the hemispheres being the freshly laid down septal plate. At this point the peptidoglycan is at its earliest structural time point and soon after this the septal plate pops out in the time frame of milliseconds into an almost spherical shape. This popping out from turgor pressure inside the cell forces the

two daughter cells apart [(Zhou et al., 2015)]. It is likely that there is some change in the structure of the rings at this popping stage due to the sudden and dramatic change in volume of the cell however it has not been possible to see a cell that is hemispherical with a septal plate facing up towards the AFM probe in any of the imaging sessions, possibly due to how short lived this stage in the cell cycle is.

Cells have been routinely found that show dense rings (e.g. Figures 5.1, 5.3, 5.5, 5.6, 5.8) which is the earliest time point of the cell wall peptidoglycan structure that has been possible to image by AFM. The dense rings show ordered fibres (bundles of single strands) of peptidoglycan that have been laid down in arcs around an approximate common central point of the cell. The fibres appear to overlap or merge with other strands that are at slightly different angles, as the orientation of the fibres does not appear perfectly concentric. The fibres do not seem to spiral in towards the centre of the ringed structure, but rather are laid down in a circular fashion. Within the rings are some small and relatively shallow holes that presumably form due to the degradation process and could be due to the strain that was put on the cell during the millisecond timescale expansion event.

As the rings are degraded by the activity of enzymes like hydrolases and the action of turgor pressure applies a force outward on the cell wall, the rings are shown to become less dense and more holes begin to form within the structure as can be seen in Figures 5.2 and 5.4. The fibres are not packed as close together allowing the tip to resolve individual rings more easily. The spaces between the rings does not show structure on Figure 5.2, however, Figure 5.4 shows evidence that where the rings have been broken down there is the mature mesh architecture instead (which will be discussed further in Chapter 6). The rings that remain are still made of relatively long fibres which is interesting as this could suggest that these are selectively left untouched by enzymes or are broken by enzymes more slowly, possibly due to their structural importance. If the enzyme activity was uniform then the likelihood of long fibres being left at seemingly uniform spacing as well as their length would be lower.

The high resolution imaging that was possible on the rings allowed for individual molecule scale measurements to be taken of the rings with the distances between the rings and the period of the repeating structure along the rings being measured from the images.

Imaging along the strands showed raised features with a period of approximately 4 nm based on averaging 24 peak to peak measurements within the images in Figure 5.10 and

corresponds well with the measurements taken in Figure 5.7 and 5.8. NMR results suggest that along the glycan backbone there is a peptide chain every 1 nm sticking out of the glycan chains in a 4 fold helical pattern resulting in peptide chains pointing in the same direction every 4 nm [(Kim et al., 2015)]. The peptides have a height of ~1 nm based on the NMR data which correlates with the results of the AFM measurements in Figure 5.10, however, these AFM height measurements have a larger uncertainty on them than the peak to peak distances due to the difficulty in removing curvature from the images. The ~4 nm period of bumps that was measured in my data agrees with the structure predicted from the NMR data. The ability to directly measure these distances is important in understanding the structure of the peptidoglycan as well as being able to predict the level of crosslinking within the peptidoglycan.

Imaging at a molecular scale between two strands allows for direct measurements to be taken of the glycan to glycan separation which can be seen in Figure 5.5 to be approximately 2.7 ± 0.5 nm which is again in good agreement with the value measured using NMR of 2.3 nm [(Kim et al., 2015)]. Individual glycans have been resolved for the first time in a living system with the ability to see how the polymers chains that make up the peptidoglycan are organised within the larger peptidoglycan cell wall to provide a specific function for the cell. The AFM measurement is a direct measurement on an entire cell in physiological conditions so the sample has undergone the least amount of processing possible and the technique causes very little damage to the sample. With AFM there can be broadening of features that are being imaged when the tip is not sharp enough to track in between sharp gaps which could have an effect of increasing the diameter of the feature that is measured. This tip convolution happens when the sides of the tip feel the interaction force and change the amplitude of oscillation before the very end of the tip does. This issue can be improved upon by using sharper tips but then these tend to be more fragile with damage to the tip causing the tip to become blunt again, creating the same problem. By understanding the positions of the strands an updated model of the peptidoglycan cell wall architecture can be created. The small amplitude tapping technique has achieved a resolution that is far beyond what has been possible with the other imaging techniques that were tested.

At the centre of the septal plate there are not continually smaller rings but rather a central disordered region. The diameter of this region has been measured for all of the cells that were imaged that showed the architecutural feature (N=12) and an average value of approximately 60 ± 15 nm was measured and an average change in height of

approximately 6 nm. The existence of the this central dip has been reported before by Touhami [(Touhami et al., 2004)] who saw a hole at the centre of the rings that was 30 nm deep and approximately 70 nm in diameter. The existence of this feature indicated that there is another mechanism for the insertion of peptidoglycan at the end of the septal formation, perhaps due to the insertion machinery not operating at smaller radii. It was not possible to achieve high resolution on the central region but there was no evidence of rings or mesh structure there. Presumably the plug structure is eventually remodelled into the mesh structure as no evidence for previous plugs or even a dip in the cell wall are seen in the images of the mature structure.

The automated analysis program was tested but was found to draw too many fibres with some branching off the actual fibres which resulted in too many branching points. The analysis led to the idea of tracing the rings and calculating parameters like the strand length and comparing how concentric the rings are.

To try to design a parameter that could be used to analyse the concentricity of the rings the NeuronJ tracing plugin for ImageJ was used then these arcs were plotted to calculate the best fitted circle to these arcs. Initially the idea was to measure the length of individual glycan strands within the rings, however, it was difficult to accurately trace the whole length of an individual strand as they tend to bundle into fibres or the resolution of the imaging at such a high resolution was not maintained over the course of a whole scan. Traces were made of some of the individual glycan strands within the rings and run through the analysis process with some individual chains measured to be over 60 nm in length which is much longer than the average that has been measured by HPLC of 6 disaccharide units (1 disaccharide~ 1 nm [(Vollmer et al., 2004)) with glycan strands over 26 units measured 10-15% of the time [(Boneca et al., 2000)]. Longer glycan strands would not fit into the scaffold model of glycan orientation which theorises the glycans are oriented perpendicular to the cell membrane. It is difficult to resolve some long strands over their whole length but there is the potential that they could be some over 100 nm long within the rings of Figure 5.5(B). Glycan length has previously been measured with HPLC for different strains of *S. aureus.* The SagB mutant strain, which lacks one of the key hydrolases involved in the remodelling and degradation of the peptidoglycan, showed evidence of some substantially longer glycan chains than in the wild type SH1000 strain using the HPLC technique. This could mean that some of the chains that are inserted into the cell wall are longer and are then remodelled. The rings are made of the most recently

inserted peptidoglycan which could explain the presence of some of the longer chains in the ringed architecture [(Wheeler et al., 2015)].

The results (Figure 5.13) showed that the short strands were not fitted well by the circle fitting program as without a great amount of curvature or a small angle subtended around the centre of the circles, the program fitted the arcs as straighter lines leading to fitted circles with much larger radii than the radius of the whole cell that was being imaged. The analysis could not be used for the shorter individual strands or for measuring strand length.

Instead the analysis was performed on some of the longer fibres of glycans that subtended a larger angle and had clearer start and end points. This means that there would have been a selection bias as some of the shorter strands were not mapped due to the error that the analysis process produces for them. These analyses cannot be treated as a conclusive look at how every glycan within the dense cell is oriented and how it was laid down, but it can be used to give an idea of the difference between the dense rings and the less dense rings as can be seen in Figure 5.14. Fewer rings were mapped on the looser rings than on the higher density rings so the sample size of mapped rings is smaller on the loose rings, however, it was easier to trace these rings due to the reduced density so their traces should be more accurate. Figure 5.14 shows that the fitting worked well for these rings and did not fit any circles that had obviously erroneous radii.

The dense rings in Figure 5.14 show that there are overlapping ring fibres which suggests that there is not a completely circular nature to the machinery that inserts the rings. It could be that multiple versions of the machinery are travelling around and creating the rings and that some rings are created at different angles. The centres of the calculated circles for the dense rings are all located within the radius of the central disordered region of the rings so they have a common centre which suggests that the machinery that makes them is revolving around a central region rather than forming lines at random orientations. The slight variation in the circle centres could account for this overlapping of strands.

The small amplitude tapping mode has been extremely effective at imaging the whole *S. aureus* cells allowing for molecular resolution images to be taken of the ringed architecture. In future work imaging the ringed architecture, a push could be made for higher resolution with the aim of being able to trace along the entire length of a single glycan strand which would allow for a direct meaurement of the glycan strand length.

Higher resolution may be achievable with the use of sharper tipped cantilevers which have a reduced radius of curvature leading to a smaller area that is interacting with the sample surface. There is also scope for further optimisation of buffer conditions and the use of smaller cantilevers that can be utilised stably at both smaller amplitudes and faster imaging speeds.

Another question that remains from this work is whether the radial features that were seen are the peptide side chains sticking out of the glycan strands. To determine this, isolated peptidoglycan could be imaged to look for the same features in pure peptidoglycan.

In terms of analysis of the ringed structure, improving the automated tracing software from Section 5.5 so that it can accurately trace the rings and map the branching points would be an improvement on the manual tracing method as it would ensure consistency in the traces drawn. This could then be used in a concentricity analysis, with the fitting of the circles to the traces and then in a fibre length and branching point density calculation.

Chapter 6- Imaging the mature cell wall and cell division.

Over the course of the cell cycle, the peptidoglycan ageing process causes the ringed structure, discussed previously in Chapter 5, to be remodelled into a mature architecture that has glycans at seemingly random orientations. To investigate the structure of the mature material it was imaged using small amplitude tapping mode in the same type of buffer conditions as the young architecture was imaged in with the aim of further understanding the organisation that the molecules in the cell wall finish in. This chapter will present the findings from imaging this mature architecture then go on to present the analysis techniques that were designed to probe how the mature architecture is different from the rings. Parameters were measured like the size of the holes that are seen within the mesh architecture and the depth that these holes go down into the mesh. Finally the entire peptidoglycan degradation timeline will be discussed going from the dense rings to the final structure, the mesh.

The previous model of the mature cell wall described the architecture of the peptidoglycan as knobbled [(Turner et al., 2010a)] but there had also been some evidence of a porous structure from some AFM images obtained in liquid [(Touhami et al., 2004)] so the goal was to determine the true architecture of the mature cell wall using these high resolution AFM techniques on living cells. The data used to build the model of the structure of the mature cell wall was taken by cryo EM and AFM of flattened sacculi which are both techniques where the cells have to be altered before the data can be taken. Using liquid AFM on whole live cells allows for conditions that are closer to the natural conditions of the bacteria.

The division process in *S. aureus* begins with a large septum being grown, in a plane orthogonal to the previous division plane, inside the cell with peptidoglycan added until the cell is completely bisected. From the outside of the cell the first evidence of the division event happening is the formation of a crack between these two new hemispherical daughter cells. The crack should always form through the centre of a set of rings due to the orthogonal division planes. Based on evidence from AFM imaging of sacculi the mechanism for the cell knowing which plane to divide in next is due to a remnant “pie crust” inside the cell [(Turner et al., 2010a)]. This “pie crust” is formed at the very beginning of the septal formation. The pie crusts from previous division events are still present in the images of sacculi, where they can be seen to cross in T junctions showing that the previous division events had been in orthogonal planes.

6.1- Imaging mature peptidoglycan

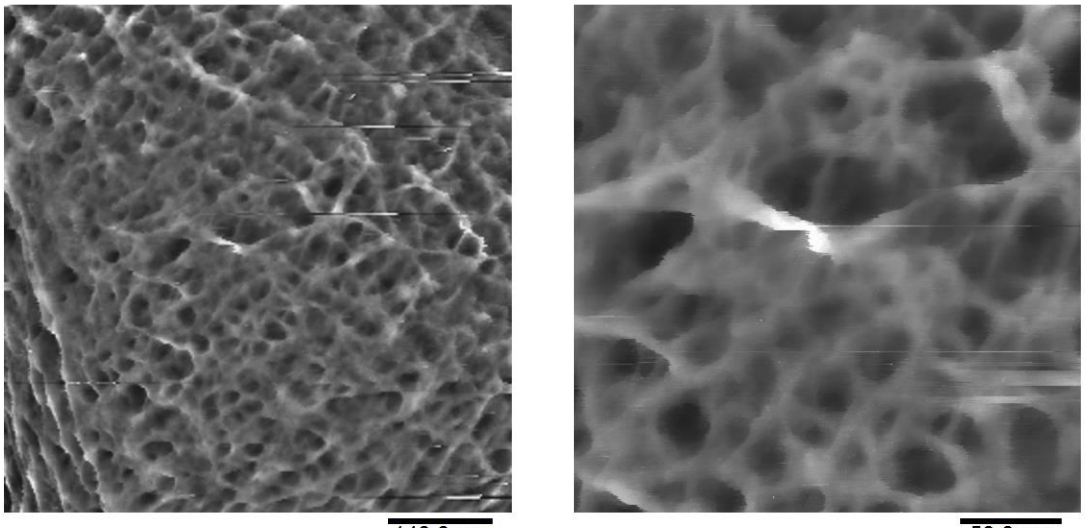

Figure 6.1- Topographic images of *S. aureus* cell showing mature mesh like architecture- (A) high pass filtered topography image with a filter size = 339 nm. (B) is a topographic image with a 3rd order plane fit applied. It has a Z scale (black to white) = 30 nm.

Investigation into the mature region shows evidence of a fibrous architecture as opposed to the knobbled or bumps structure as seen in previously published work [(Touhami et al., 2004; Turner et al., 2014)]. The images show longer strands than the knobbled architecture might predict and also holes within the structure that were also not predicted from the previous data. The process of sample preparation in the previous data could be the reason for the lack of holes as flattening and drying the sacculi onto a surface could cause the fibres made of glycans to be squashed together, filling in the gaps that would be there on a whole cell or there could be residual water that is not evaporated as it is trapped in the holes in the mesh, resulting in images showing a knobbled structure.

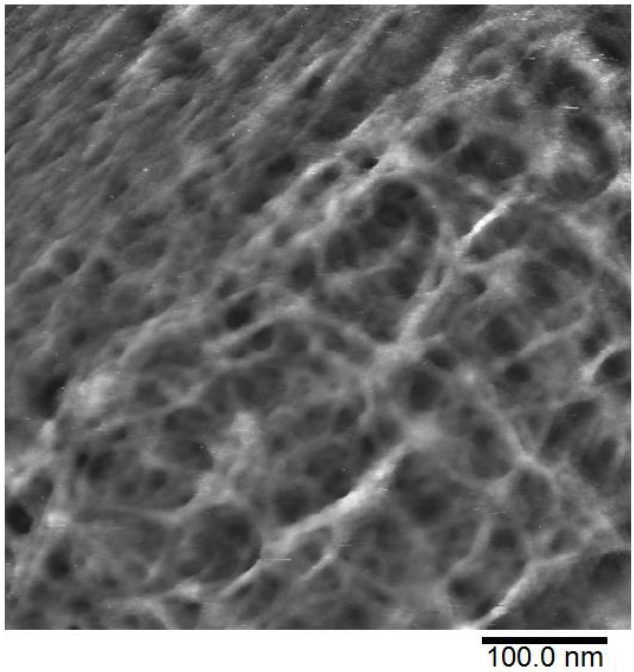

Figure 6.2- High pass filtered topographic image of an *S. aureus* cell showing ringed architecture (top left half) and mature mesh like architecture (bottom right half). The image has a filter size = 250 nm.

The mesh state is thought to be the final structural organisation of the peptidoglycan in the cell wall and is formed by remodelling the dense rings. In Chapter 5 there is evidence of the beginning of the breakdown of the rings into the mature state for instance in Figure 5.2 and Figure 5.4. Figure 6.2 shows a region of the cell that is on the boundary of the mesh and ringed architectures. Comparing the orientation of the strands suggests that the rings are highly oriented while the mesh like structure shows strands with seemingly no orientation. It has been reported that the cell division process occurs in an orthogonal plane to the previous division plane so the strands in the mesh structure would have been oriented from top left to bottom right, however, there is not a strong orientation in this direction.

In Figure 6.3(A) and (B), in the top right hand corner of the cell, there is a section of dense rings that seem to be from a different (likely more recent) division event than the rest of the image. In Figure 6.3(B), (C) and (D) the remnants appear to run at various orientations compared to the previous rings.

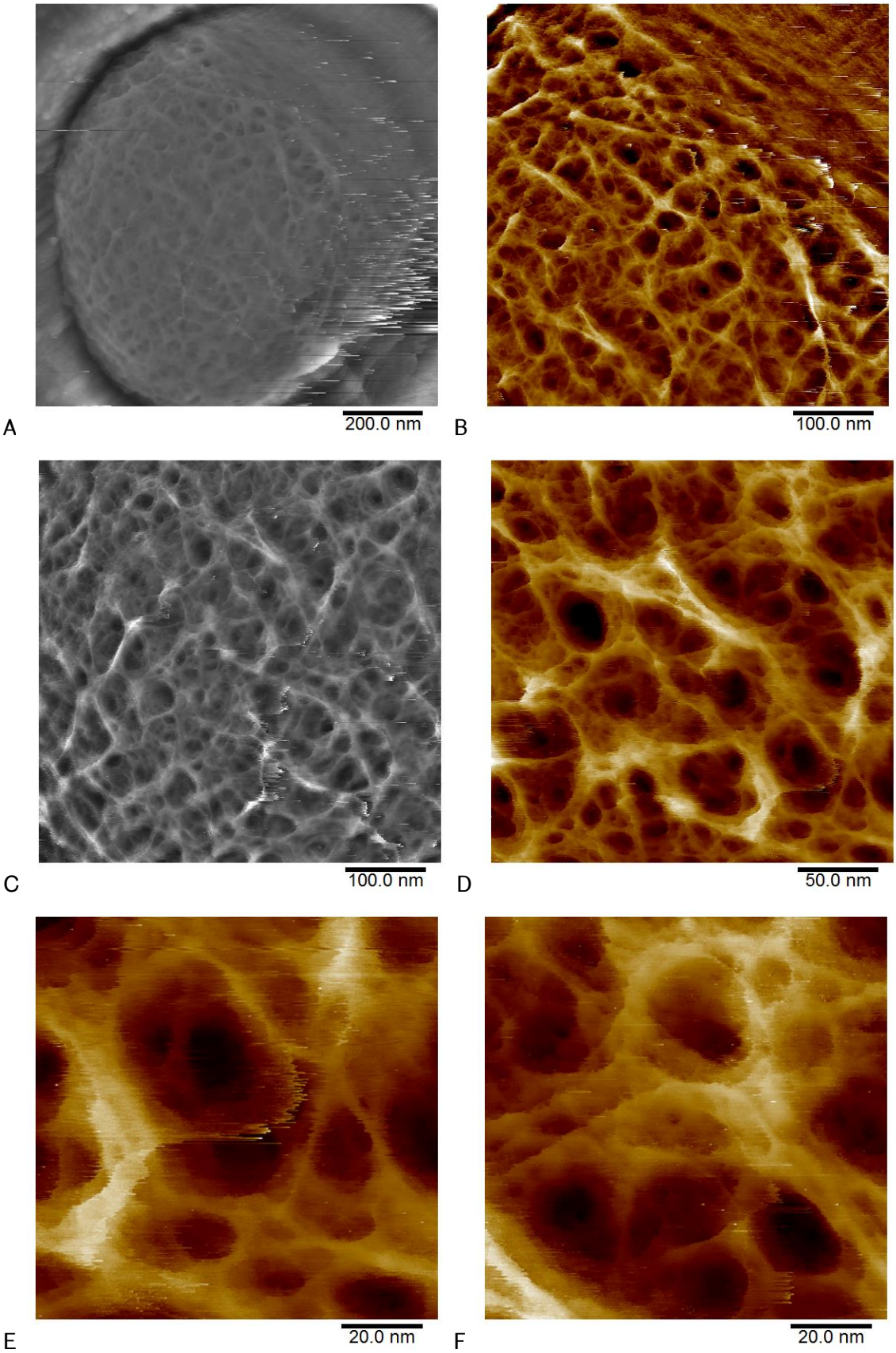

Figure 6.3- Topographic images of *S. aureus* cell showing mature mesh like architecture- (A) is a high pass filtered topography image with a filter size = 506 nm. (B) is a high pass

filtered topography image with a filter size = 250 nm. (C) is a high pass filtered topography image with a filter size = 250 nm. (D) is a 3rd order plane fitted topography image with a Z scale (dark brown to white) = 29 nm. (E) is a post imaging zoom on the bottom right corner of the image in Figure 6.3(D). It is a 3rd order plane fitted topography image with a Z scale (dark brown to white) = 29 nm. (F) is a post imaging zoom on the top middle area of the image in Figure 6.3(D). It is a 3rd order plane fitted topography image with a Z scale (dark brown to white) = 27 nm.

To investigate this mesh like structure there needed to be some higher resolution data taken. Figure 6.3(A) is a mesh made up of some longer fibres with seemingly randomly orientated shorter fibres and many holes. Zooming in on different regions of the mesh (Figure 6.3 (B), (C) and (D)) reveals thinner strands that were not resolved in the larger scans and smaller holes within holes that were also not resolved in the larger scans. In Figures 6.3(D), (E) and (F) the density of fibres can be seen down to single glycan scale in some places. There are examples of two fibres meeting at a branching point and cases of small holes being seen within larger holes.

The potential depth of some of the holes within the mesh can be seen with the largest hole on the left of the centre of the Figure 6.3(D) reaching down below 20 nm deep from the top of the image scale bar. Holes as deep as 20 nm have not been seen or predicted in previous studies of the mature peptidoglycan architecture, so their presence opens up questions about their function [(Turner et al., 2014)]. In Gram negative bacteria there are channels through the outer membrane called porins that are involved in transporting larger molecules across the membrane. *S. aureus* does not have an outer membrane but perhaps the holes are necessary for the transport of large molecules through the thick peptidoglycan layer.

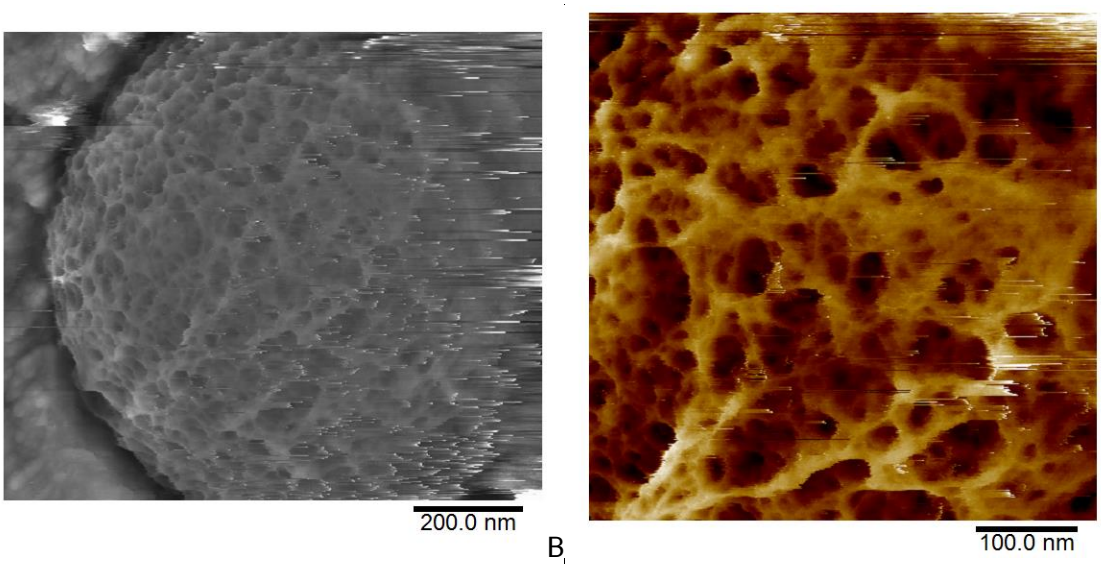

Figure 6.4- Topographic images of *S. aureus* cell showing mature mesh like architecture with areas of denser mature architecture- (A) is a high pass filtered topography image with a filter size = 494 nm. (B) is 3rd order plane fitted with a Z scale (dark brown to white) = 59 nm.

Figure 6.4(A) shows a cell with a mostly mature architecture, however, there is a band of slightly denser mesh material that runs diagonally from the top right hand side of the cell to the bottom left. This region is zoomed in on in Figure 6.4(B) which shows that this denser region to the right of the image still contains smaller holes but the large holes have not formed fully. This could give an idea about how the larger holes are formed with many small holes in the denser material forming and overtime joining together to create the larger, deeper holes.

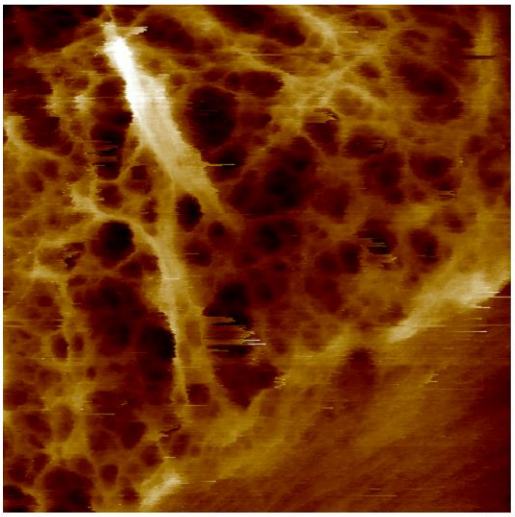

A

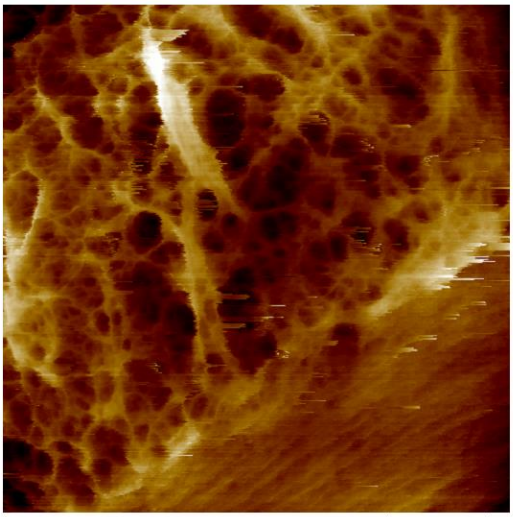

B

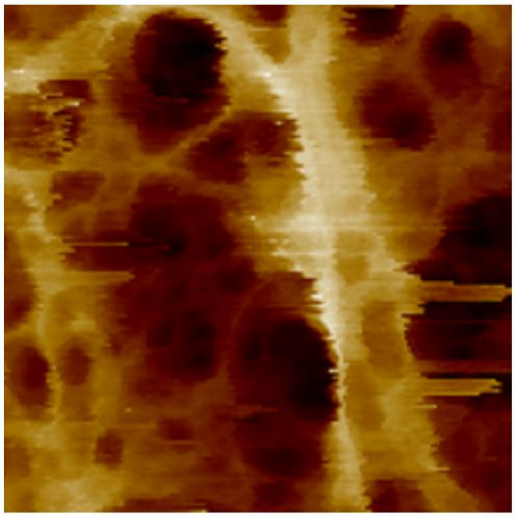

C

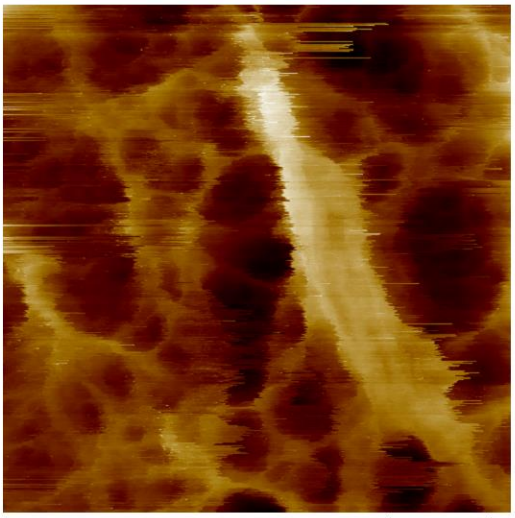

D

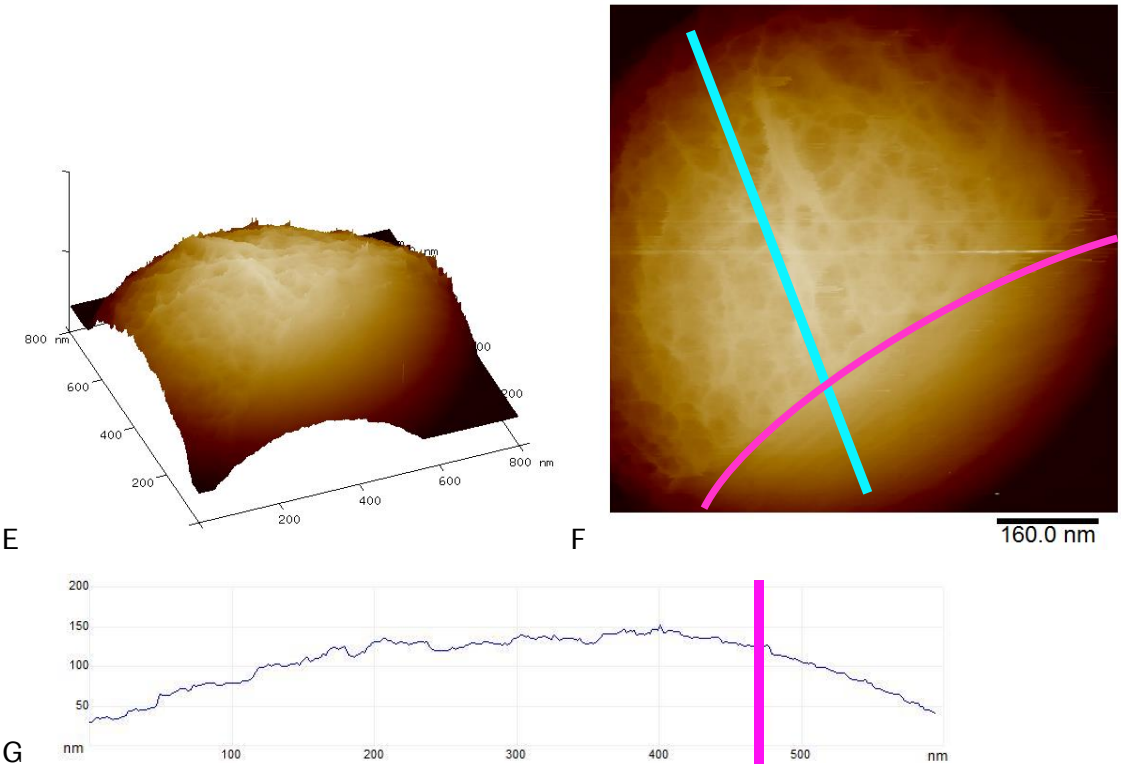

Figure 6.5- Topographic images of TagO *S. aureus* cell showing both ringed architecture (top) and mesh architecture (bottom) with features of dense material within the mesh- (A) is a 3rd order plane fit topography image with a Z scale (dark brown to white) = 65 nm. (B) is 3rd order plane fitted topography with a Z scale (dark brown to white) = 58 nm. (C) is 3rd order plane fitted with a Z scale (dark brown to white) = 58 nm. (D) is 3rd order plane fitted with a Z scale (dark brown to white) = 58 nm. (E) is a 3D topography image of the cell with a Z scale (dark brown to white) = 468 nm. (F) topography image of the cell showing the ringed and mesh architectures (boundary marked with a pink line) with a Z scale (brown to white) = 398 nm. (G) is a cross-section measured from the image in Figure 6.5(F) from top left to the bottom right of the image (blue line) showing the difference in topography profile between the mesh and the rings (pink line marks the boundary between them.

The cell in Figure 6.5 shows a dense mesh work with seemingly disordered fibres of peptidoglycan covering most of the cell. In the centre of the mesh there is a thick band of material that sticks up above the mesh background which may be the remnant of previously ringed architecture. The peptidoglycan maturation process has been seen to occur gradually as there is evidence of different densities of rings and some regions of disorder amongst areas of ordered rings. In the bottom right hand corner of the cell in Figure 6.5 there is a set of dense rings with a sharp boundary between the two structures

(as marked by the pink line in Figure 6.5(F)). Due to the two structures being imaged on the same cell it is possible to directly compare their features by the use of an average cross-section that can be seen in Figure 6.5(G). The ringed region is smooth compared to the mesh region and shows no holes within the structure. The mesh region looks to protrude above the height of the rings which could be due to the way that glycan fibres and strands are broken up, leaving loose ends that stick up as is illustrated in the 3D image in Figure 6.5(E). These fibres that protrude above the height of the rings could be the same ones that were remodelled in the formation of the holes as a change in fibre density is not observed and does not correlate with stiffness measurements that showed the young architecture is stiffer than the mature architecture [(Bailey et al., 2014)].

Within the mesh, especially to the left hand side of the image there is evidence of some features that are of the order of the diameter of single glycan strands. A zoom on this region is shown in Figure 6.5(C), achieving the resolution of thin fibres where it can clearly be seen that the fibres are merging together. There is also potentially evidence of features that have diameter approximately similar to that of a single glycan strand. It is not known whether the degradation process ends with an architecture made completely of single stranded mesh, but from the images taken no region has been seen that is made entirely of single strands so it seems as though a network of fibres is the final structure.

The thick band that may be remnants of the previous ringed structure appears at a 90° angle to the new set of rings which is consistent with the fact that *S. aureus* division events occur on orthogonal planes to previous division events. Figure 6.5(D) is an image that is focussed on this thick raised band with the aim of being able to determine whether there was evidence of rings in the band or not, however, the resolution of the imaging had begun to decline once again so it is not possible to determine.

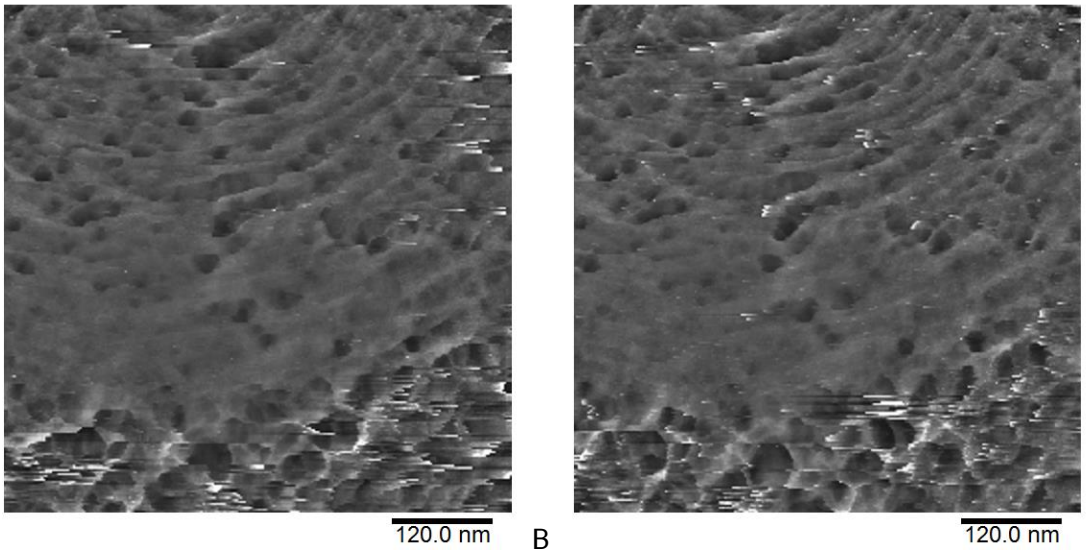

Figure 6.6- Topographic images of *S. aureus* cell showing both ring and mesh architecture with the mesh architecture forming streaks as the tip scans the sample- (A) is the trace (scanning from left to right) high pass filtered topography image with a filter size = 360 nm. (B) is the retrace (scanning from right to left) high pass filtered topography image with a filter size = 360 nm. Note the streaks are in opposite directions in the two images due to the change in the scan direction.

Images taken of the boundary between the mesh and the ringed structures on a cell show the trace and retrace images of the same scan and features streaks that appear in opposite directions on the cell on the mesh towards the bottom of the images. When imaging the mesh streaks are sometimes seen that can be caused by the tip not tracking the surface accurately. If the mesh is loose and can be moved by the tip as it scans from side to side then these streaks can appear. On the same image, so in the exact same conditions, the ringed structure (top of the image) does not show the same streaks. Overall the two images suggest that the mesh structure can be loose and moved about by an external force which is not the case for the rings. This phenomenon was also seen in the Trypsin treated cells in Figure 4.15.

6.2- Analysis of the mature peptidoglycan architecture

The previous model for the structure of the mature peptidoglycan architecture was called “knobbles” and was thought to consist of small bumps. The rings would be broken apart by the growth of the cell and the activity of peptidoglycan hydrolases, forming the smaller lumps that had no overall strand orientation. Based on the data collected from cryo EM and AFM of broken up sacculi the surface was predicted to be rough but

undulating instead of the structure that has been seen in this chapter where the surface is porous and comprised of longer individual strands and fibres of peptidoglycan [(Matias and Beveridge, 2007; Touhami et al., 2004; Turner et al., 2014)]. To be able to build a new model of the mature architecture some information needs to be extracted from the AFM images that can form a basis for a model, with measuring distances and thicknesses being a good starting point. The AFM images that were selected for the analysis of porosity were chosen based on their resolution. Only the highest resolution images that had areas of mesh that showed close to single glycan resolution were used for the bearing analysis technique as this showed that the tip was imaging the surface well for these images so the measurements were more likely to be accurate.

6.2.1- Bearing analysis

Bearing analysis is a tool in the Bruker Nanoscope analysis software that can be used to determine the regions of the image of a surface that exist below a chosen height on the sample surface. It can also be used to calculate the total percentage of the area imaged that is below this height and then can be further manipulated to calculate the average hole size at a particular depth into the sample. Using the bearing analysis feature, an inverted version of each image was processed at a range of threshold depths from the deepest point in the holes up to the cell surface. The bearing analysis function in the Bruker Nanoscope Analysis software selects data above a chosen threshold height so to calculate the area below the threshold height the image must first be inverted. These bearing images were then processed in ImageJ where a threshold was applied to leave only the areas that the bearing analysis had calculated were below the threshold depth. The idea with the images was to make a contour map with the different layers of the bearing analysis laid on top of each other to show the depth profile of the mesh images. This contour map was made by taking the thresholded images and overlaying them using Inkscape. To calculate the average hole area and the hole density the ImageJ particle analysis function was used. The deepest layer of the bearing analysis was processed first and the number of holes and average hole area were calculated, then before the values for the layer above were calculated, any holes that had appeared in the previous layer were removed to ensure that the average hole size and hole numbers were not counting the same hole multiple times. This means that the hole density is the density of newly appearing holes at that depth and the hole area is the area of the new holes. A bearing depth analysis was also performed at the height that corresponds to the midpoint on the Z axis between 1% and 99% of the total area under the histogram, this is done to remove

the effect of the tails on the histogram that extend for several nanometres but account for less than 1% of the total image area. A final bearing analysis was performed at the height corresponding to 50% on the histogram area, i.e. the depth where half of the material is above the threshold and half is below. Any holes that went off the side of the images were not included in the calculations to ensure that every hole in the statistics was a complete one.

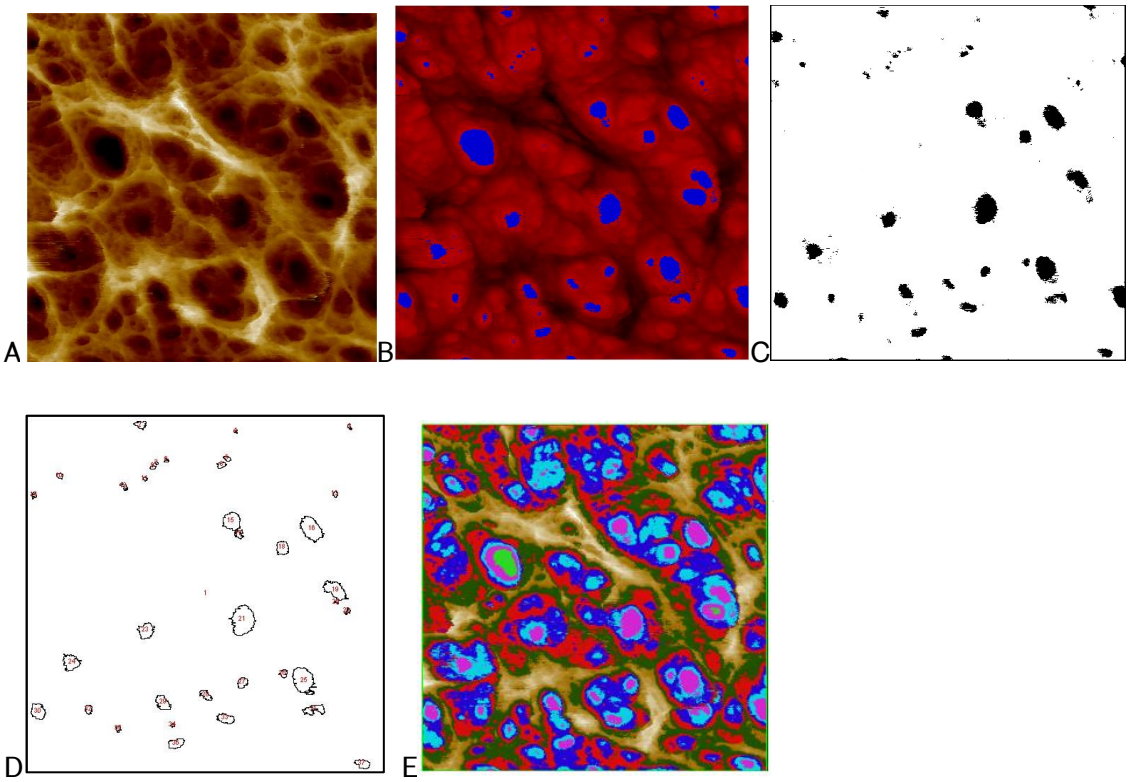

Figure 6.7- Images showing the process of performing the bearing analysis. (A) is the original image, (B) is the inverted image with the bearing analysis taken at a chosen depth, (C) is the thresholded image with the holes that appeared at a deeper depth removed and (D) is the holes that have been put through the ImageJ particle analysis software which also produces a table of the information on each hole that it measures which can then be processed in Microsoft Excel. (E) is the final composite bearing image with all of the bearing heights laid over each other.

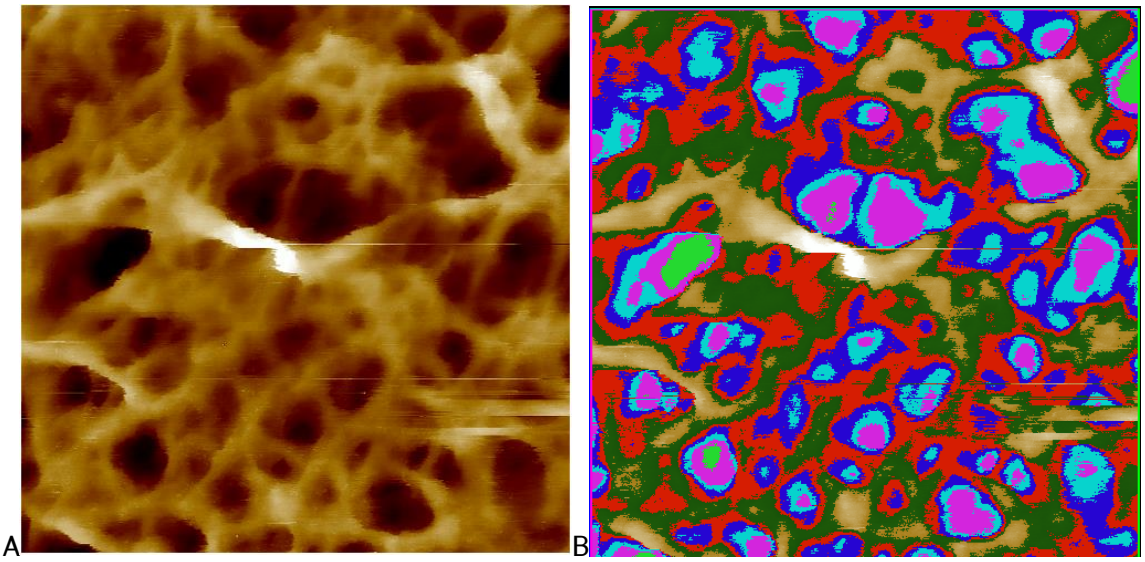

A B

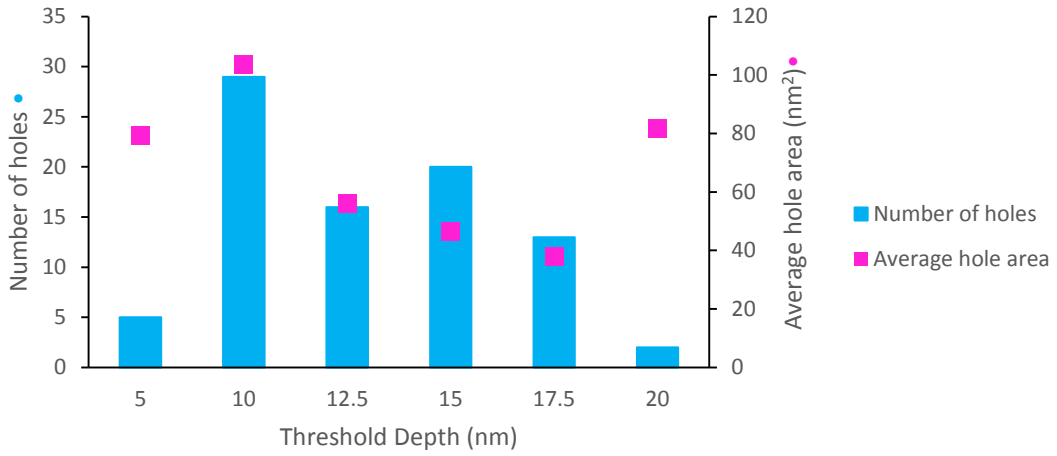

C

D

Threshold Depth (nm)	Number of holes	Average hole area (nm^2)	Total area (nm^2)	% hole coverage
5	5	79.35	396.75	0.64%
10	29	103.45	3000	4.82%
12.5	16	56.09	897.5	1.44%
15	20	46.30	926	1.49%
17.5	13	37.87	492.25	0.79%
20	2	81.50	163	0.26%

Figure 6.8- Bearing Picture 1 (Figure 6.1(B)) - (A) is the original topography 250 nm image of an *S. aureus* cell, (B) is the final composite bearing image with all of the bearing heights laid over each other. Scales for (B) from the bottom up. First 5 nm = Light Green, 5-10 nm = Pink, 10-12.5 nm = Light Blue, 12.5-15 nm = Dark Blue, 15-17.5 nm = Red, 17.5-20 nm = Dark Green, Above 20 nm= Gradient from Brown to White (low to high). (C) is a graph showing

the number of holes and the average hole size at each bearing depth. (D) is a summary table of the number of holes, average hole area, total area at the bearing depth and the percentage of hole coverage with new holes that have appeared in that depth range.

The light green regions on the overlaid image are the deepest holes which corresponds to over 15 nm into the cell wall which is over half of the thickness of the cell wall based on the current understanding of the cell wall [(Vollmer et al., 2008a)]. Some of the deepest holes in this image extend over 25 nm deep. The data shows that there are few shallow holes (~5 nm from the cell surface) that appear that are not a part of some larger deep network of holes. The average hole size is different at each depth and appears to show no trend.

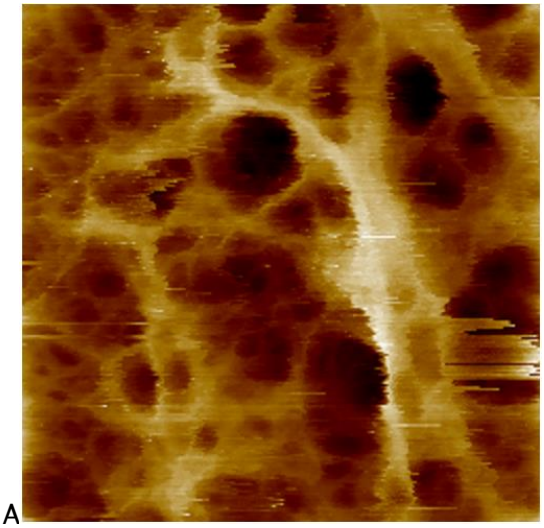

A

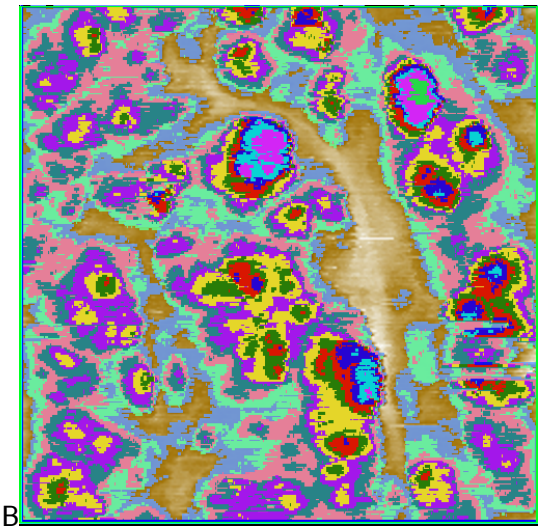

B

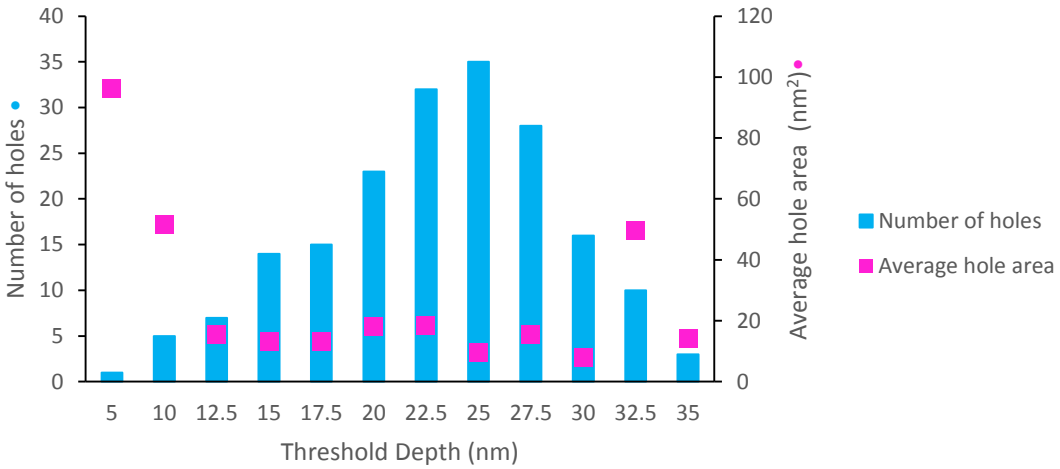

C

D

Threshold Depth (nm)	Number of holes	Average hole area (nm^2)	Total area (nm^2)	% hole coverage
5	1	96.25	96.25	0.15%
10	5	51.55	257.75	0.41%
12.5	7	15.32	107.25	0.17%
15	14	12.98	181.75	0.29%
17.5	15	13.27	199	0.32%
20	23	17.98	413.5	0.66%
22.5	32	18.34	586.75	0.94%
25	35	9.44	330.25	0.53%
27.5	28	15.54	435.25	0.70%
30	16	7.98	127.75	0.20%
32.5	10	49.48	494.75	0.79%
35	3	14.08	42.25	0.07%

Figure 6.9- Bearing Picture 2 (250 nm area zoom on Figure 6.5(A))- (A) is the original topography 250 nm image of an *S. aureus* cell, (B) is the final composite bearing image with all of the bearing heights laid over each other. Scales for (B) from the bottom up. First 5 nm = Light Green, 5-10 nm = Pink , 10-12.5 nm = Light Blue, 12.5-15 nm = Dark Blue, 15-17.5 nm = Red, 17.5-20 nm = Dark Green, 20-22.5 nm = Yellow, 22.5-25 nm = Purple, 25-27.5 nm = Turquoise, 27.5-30 = Pale Pink, 30-32.5 nm = Pale Green, 32.5-35 nm = Pale Blue, Above 35 nm= Gradient from Brown to White (low to high). (C) is a graph showing the number of holes and the average hole size at each bearing depth. (D) is a summary table of the number of holes, average hole area, total area at the bearing depth and the percentage of hole coverage.

The images in Figures 6.9 and 6.10 were both taken on the same TagO mutant cell and were chosen partially because of the high resolution obtained on the images but also to see whether two regions on the same cell would give similar results from their analysis. Using two images from the same cell allowed the analysis technique to be tested to then see how easily these parameters can be compared between images of different cells.

A 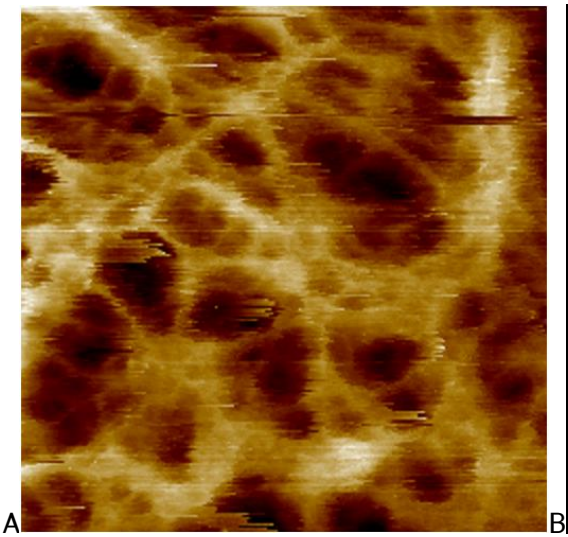 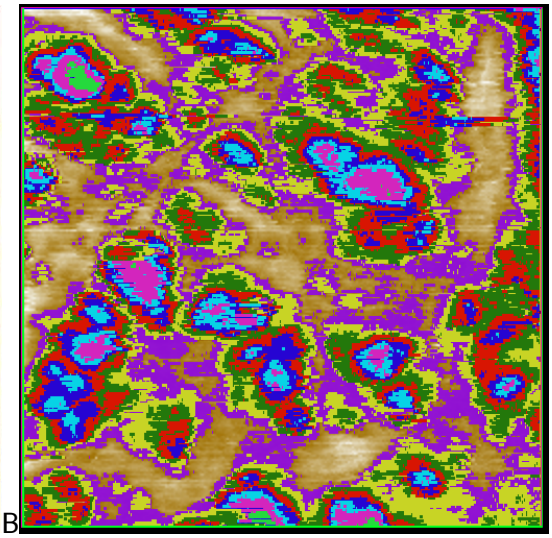 B

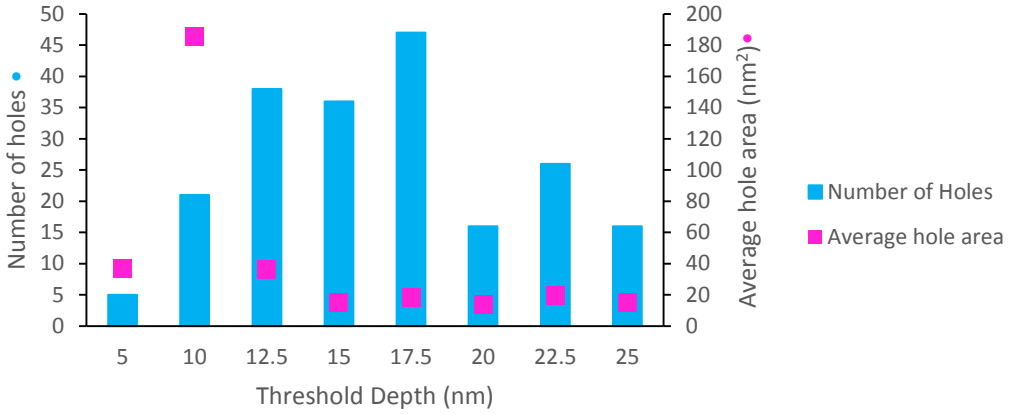

C

D

Threshold Depth (nm)	Number of holes	Average hole area (nm^2)	Total area (nm^2)	% hole coverage
5	5	37.05	185.25	0.30%
10	21	185.25	789.5	1.27%
12.5	38	35.91	1364.5	2.19%
15	36	14.98	539.25	0.87%
17.5	47	18.38	863.75	1.39%
20	16	13.39	214.25	0.34%
22.5	26	19.22	499.75	0.80%
25	16	15.27	244.25	0.39%

Figure 6.10- Bearing Picture 3 (250 nm zoom on Figure 6.5(A))- (A) is the original topography 250 nm image of an *S. aureus* cell, (B) is the final composite bearing image with all of the bearing heights laid over each other. Scales for (B) from the bottom up. First 5 nm = Light Green, 5-10 nm = Pink , 10-12.5 nm = Light Blue, 12.5-15 nm = Dark Blue, 15-17.5 nm = Red, 17.5-20 nm = Dark Green, 20-22.5 nm = Yellow, 22.5-25 nm = Purple,

Above 25 nm= Gradient from Brown to White (low to high). (C) is a graph showing the number of holes and the average hole size at each bearing depth. (D) is a summary table of the number of holes, average hole area, total area at the bearing depth and the percentage of hole coverage.

The image in Figure 6.9 has an overall larger height range than the image in Figure 6.10, possibly due to a larger bit of peptidoglycan that has not been fully broken down. In both images there is evidence for a small number of larger holes at the deepest parts of the image (deeper than 10 nm), but then in both images, above the deepest 10 nm the average hole size is more consistent with average hole areas between 10 and 20 nm^2 for the majority of the chosen depths. This 10-20 nm^2 area does not compare closely with the average hole size in Figure 6.8 which has larger hole areas at all of the threshold depths. This could be due to how the different depths were chosen for the bearing analysis or it could be due to some kind of resolution difference where Figures 6.9 and 6.10 were taken at higher resolution so small fibres that bridge across some holes could be resolved which would have made the average hole sizes smaller. Alternatively this could be a real hole size difference between two different cells as the cell was a TagO mutant.

A 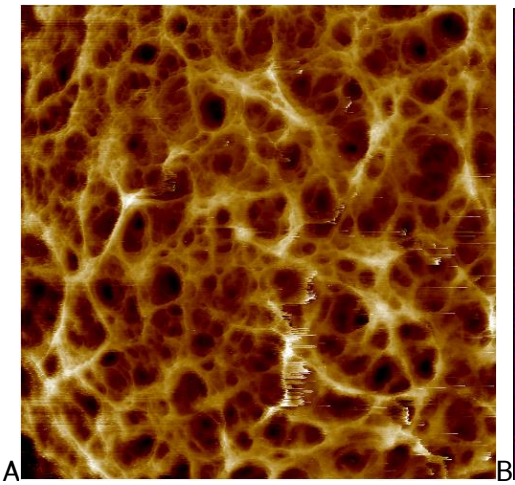 B 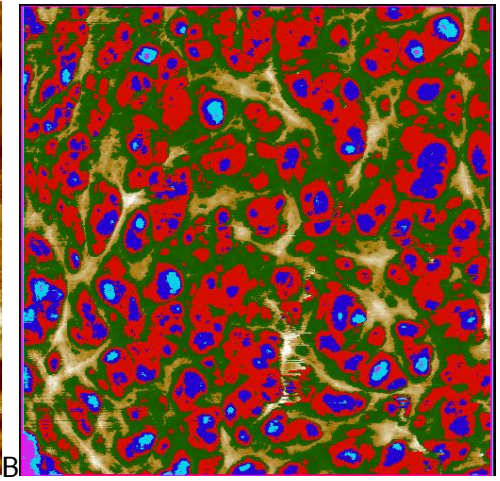

C

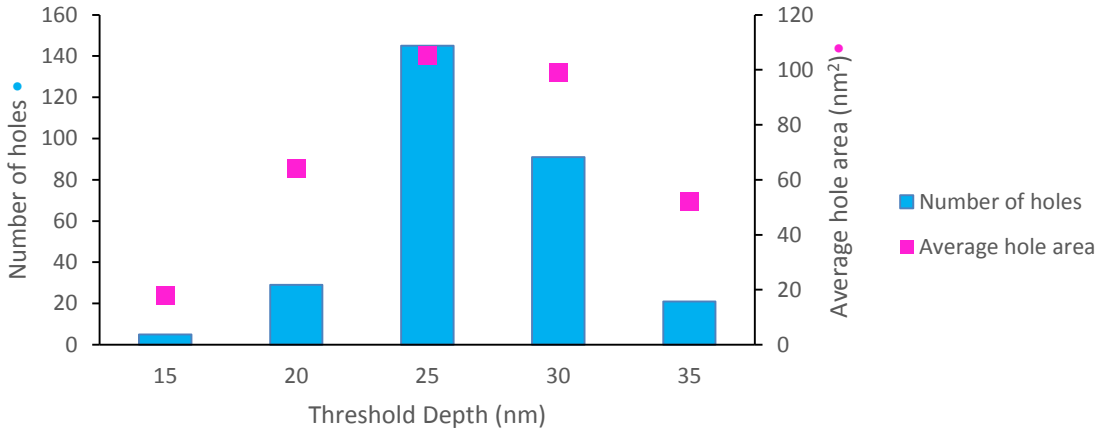

D

Threshold Depth (nm)	No of holes	Average hole area (nm^2)	Total area (nm^2)	% hole coverage
15	5	18.00	90	0.04%
20	29	64.17	1861	0.75%
25	145	105.11	15241	6.11%
30	91	98.91	9001	3.61%
35	21	51.90	1090	0.44%

Figure 6.11- Bearing Picture 4 (Figure 6.3(C)) - (A) is the original topography 500 nm image of an *S. aureus* cell, (B) is the final composite bearing image with all of the bearing heights laid over each other. Scales for (B) from the bottom up. First 15 nm = Pink, 15-20 nm = Light Blue, 20-25 nm = Dark Blue, 25-30 nm = Red, 30-35 nm = Dark Green, Above 35 nm= Gradient from Brown to White (low to high). (C) is a graph showing the number of

holes and the average hole size at each bearing depth. (D) is a summary table of the number of holes, average hole area, total area at the bearing depth and the percentage of hole coverage.

The images in Figure 6.11 and 6.12 were taken of the same area but with two different scan sizes. The idea of comparing the two images was to see how the depth and hole sizes of a larger area compare with the smaller scan area and whether they are consistent.

A 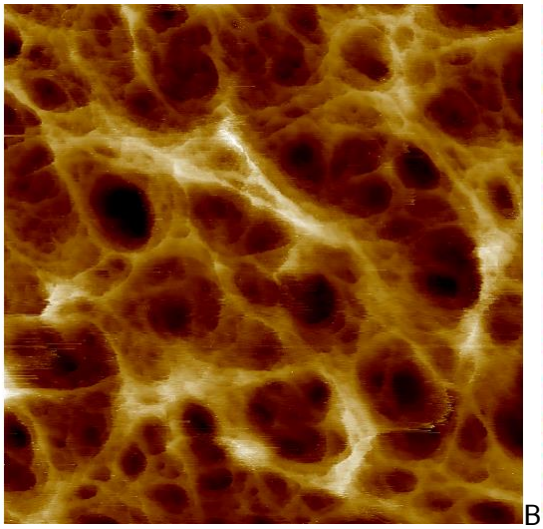 B 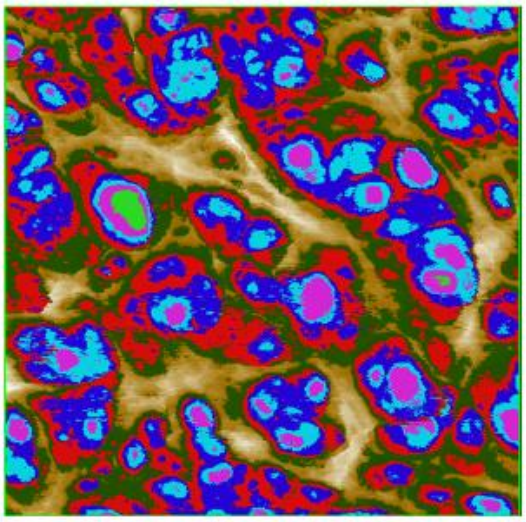

C

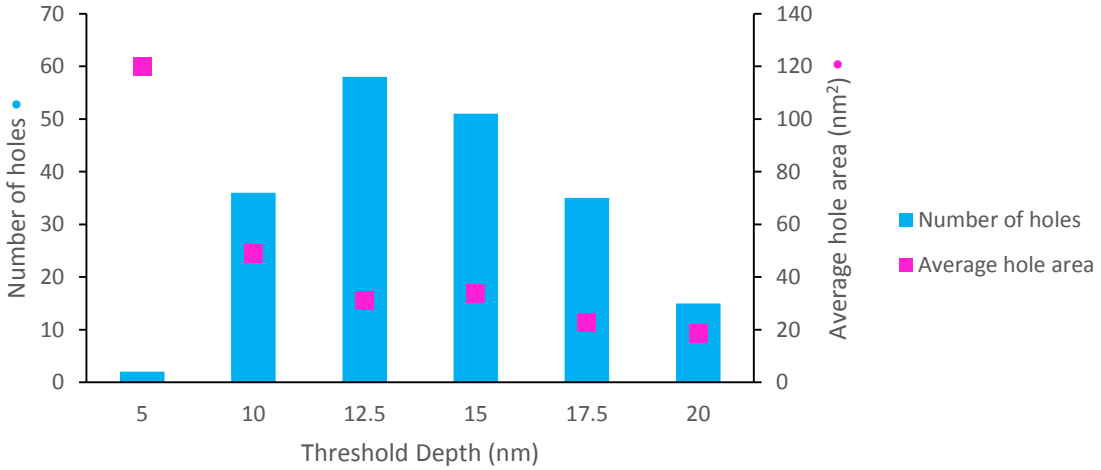

D

Threshold Depth (nm)	Number of holes	Average hole area (nm^2)	Total area (nm^2)	% hole coverage
5	2	120.13	240.25	0.39%
10	36	49.15	1769.25	2.84%
12.5	58	31.11	1804.25	2.90%
15	51	33.93	1730.25	2.78%
17.5	35	22.56	789.75	1.27%
20	15	18.75	281.25	0.45%

Figure 6.12- Bearing Picture 5 (Figure 6.3(D)) - (A) is the original topography 250 nm image of an *S. aureus* cell, (B) is the final composite bearing image with all of the bearing heights laid over each other. Scales for (B) from the bottom up. First 5 nm = Light Green, 5-10 nm = Pink, 10-12.5 nm = Light Blue, 12.5-15 nm = Dark Blue, 15-17.5 nm = Red, 17.5-20

nm = Dark Green, Above 20 nm= Gradient from Brown to White (low to high). (C) is a graph showing the number of holes and the average hole size at each bearing depth. (D) is a summary table of the number of holes, average hole area, total area at the bearing depth and the percentage of hole coverage.

The larger scan area shows a greater range in the height which could be due to deeper holes that are occurring in the cell wall but could also be due to a better removal of the background curvature of the cell for the smaller scan size. The bottom left of Figure 6.11 looks to fall away and would not have been as easy to plane fit accurately when the curvature was removed.

Figure 6.12 is the highest resolution image of the mesh that has been taken and analysed using the bearing analysis technique.

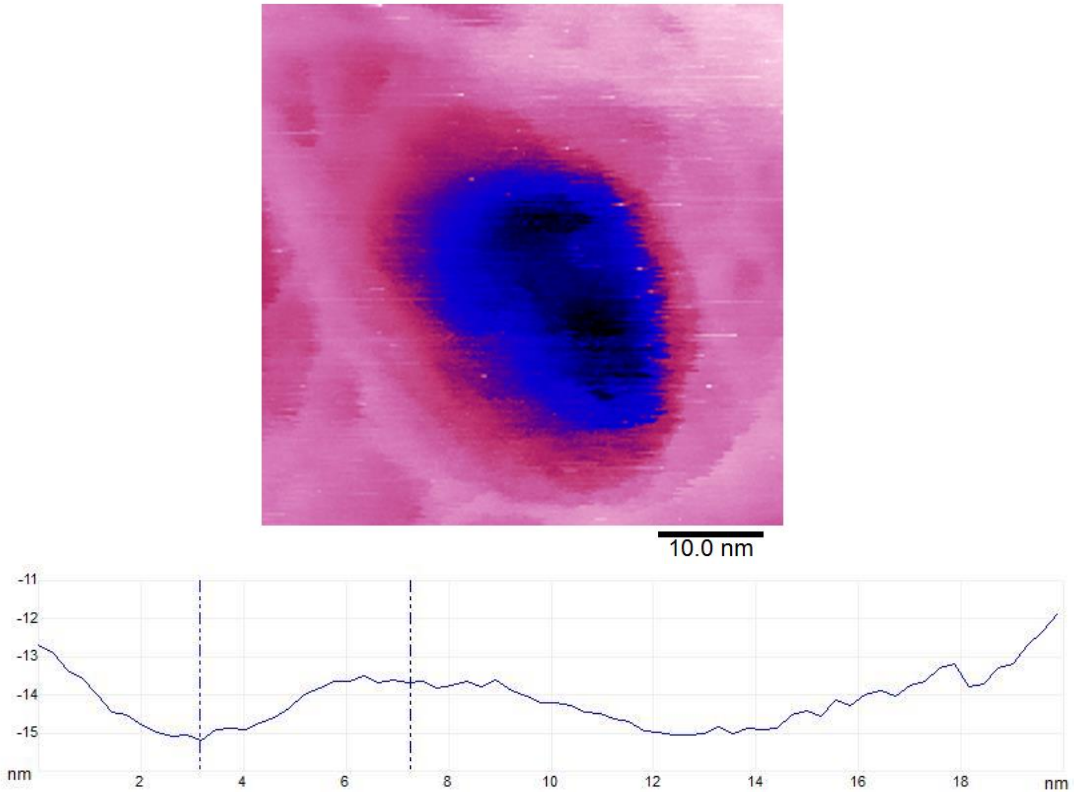

Figure 6.13- Zoom of the deepest hole in Figure 6.12(B) (light green in the Figure). (A) is the topography of the hole with the Z scale (black to blue to pink to white) = 35 nm. (B) is the averaged cross-section profile of the blue area diagonally from top left of the blue area to the bottom right.

Figure 6.12 shows a larger hole that reaches at least 25 nm deep compared to the outermost layer of the wall based on cross-sections taken across the entire image. This

hole posed questions about the largest hole diameter that could exist in the cell wall without the cell bursting due to turgor pressure as one of the roles of the cell wall is to maintain the cells shape while the cell is exerting a high force outwards. Taking a cross-section of just the deep hole (Figure 6.13) showed that the hole tapers down as it goes deeper into the cell wall layer. At the bottom of the hole there appears to be two smaller holes separated by approximately 5 nm with an approximately 1 nm tall raised feature between them as seen from the cross-sectional profile. It appears that the hole traverses the full thickness of the cell wall and that it is spanned by a thin layer of peptidoglycan at the bottom breaking the hole in two.

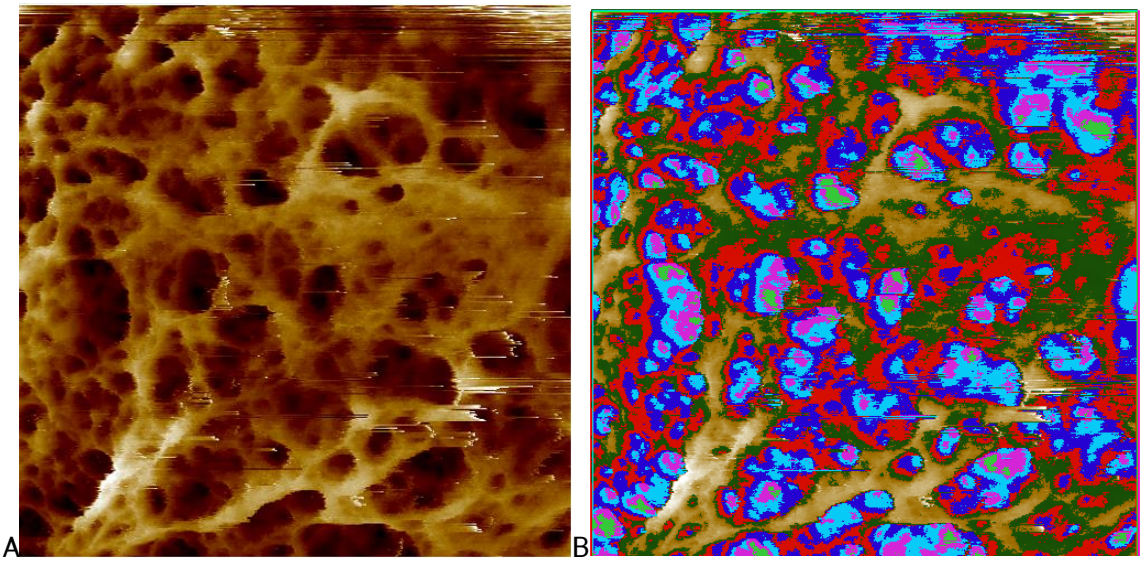

A B

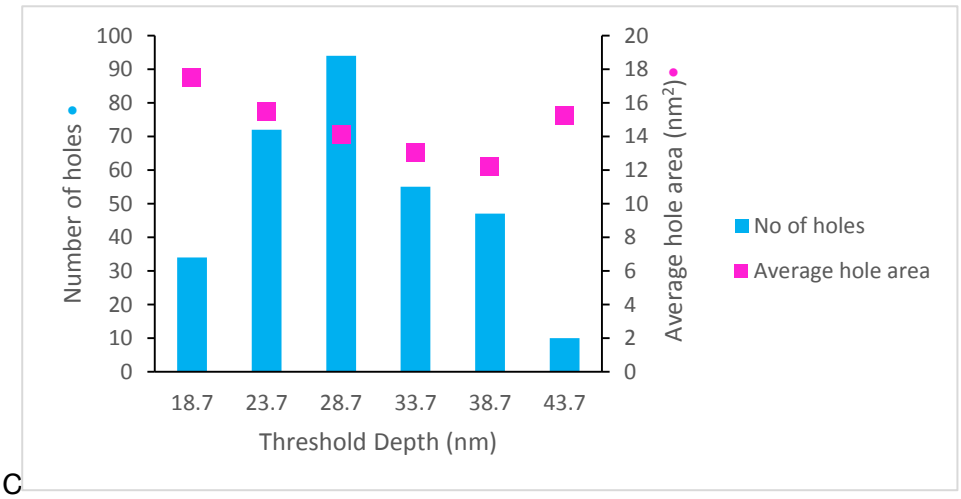

C

D

Threshold Depth (nm)	Number of holes	Average hole area (nm^2)	Total area (nm^2)	% hole coverage
18.7	34	17.48	594.25	0.96
23.7	72	15.49	1115.25	1.80
28.7	94	14.13	1328.00	2.14
33.7	55	13.04	717.00	1.15
38.7	47	12.20	573.25	0.92
43.7	10	15.25	152.50	0.25

Figure 6.14- Bearing Picture 6 (Figure 6.4(B)) - (A) is the original topography 250 nm image of an *S. aureus* cell, (B) is the final composite bearing image with all of the bearing heights laid over each other. Scales for (B) from the bottom up. First 18.7 nm (1% of the total area) = Light Green, 18.7- 23.7 nm = Pink, 23.7 –28.7 nm = Light Blue, 28.7 – 33.7 nm = Dark Blue, 33.7-38.7 nm = Red, 38.7-43.7 nm = Dark Green, Above 43.7 nm= Gradient from Brown to White (low to high). (C) is a graph showing the number of holes and the average hole size at each bearing depth. (D) is a summary table of the number of holes, average hole area, total area at the bearing depth and the percentage of hole coverage.

Figure 6.14 is a 500 nm scan of a mesh area that shows some individual strands. It is different from some of the other mesh images as it has a patch of denser material on the right hand side of the image that has relatively few holes. This region could be a patch of peptidoglycan that has yet to be broken up or some other material such as surface proteins or extracellular polymeric substances (EPS) that is filling in the holes. In the bearing analysis layer picture this area can be seen as the predominantly dark green and red area to the right hand side of the image. This image was processed in a slightly different way from all of the previous bearing analysis data as the effective bottom of the image was taken to be the histogram height that corresponded to 1% of the total area of the image. Taking the bearing slices at 5 nm intervals up from this height (18.7 nm) resulted in a contour image that did not have too many slices that were close together while still having enough slices to differentiate the holes that went deep into the cell wall thickness from the shallower holes. The graph of the average new hole size shows that the deepest holes are on average the largest with the hole area decreasing at shallower depths until the shallowest depth (43.7 nm up from 1%) which could be due to the low number of new holes at this depth which could mean one hole with a larger area skews the average hole area higher.

Bearing Picture	Height difference between 1% and 99% on histogram (nm)	Depth above which 50% of material exists (difference in height 99% to 50% area coverage) (nm)	% of image in deepest 10 nm	Average new hole radius (nm)
1	19.35	11.32	36	4.57
2	33.76	18.27	11	2.62
3	24.37	14.44	23	3.23
4	22.65	11.73	36	4.47
5	19.06	9.69	53	3.62
6	39.03	19.31	18	4.31

Figure 6.15- Summary table comparing parameters calculated from each of six bearing analysis images.

It is difficult to draw conclusions about the density of holes and size of holes at different depths between images as the cells and conditions were not the same for the images. Using the values in Figure 6.15, comparing Bearing Picture 2 vs 3 there is a large difference between the total heights of the images due to some unbroken peptidoglycan which made the total Z scale on the images very different, even on the same cell. If the bearing depths were chosen from the bottom of the Z scale going up then there is a problem if there is one much deeper hole like in Bearing Picture 5 that skews the rest of the data, making it hard to make comparisons. It is important for the images to have their curvature removed effectively otherwise there is the situation like in Bearing Picture 4 where the bottom left corner skews the Z scale.

The histogram height difference between 1-99 % is a simpler and perhaps more useful parameter to calculate for the images as it gives an effective total depth of the holes that is measured in the images while ignoring the tails of the histogram. Over the 6 images this parameter shows that all of the cells have holes that reach at least 19 nm deep. Comparing this thickness measurement to the thickness theorised in the knobbled model of the cell wall structure and the cell wall thickness of 15-30 nm as measured by electron microscopy, this is unexpected as the holes are reaching down most of, if not all of the way through the cell wall thickness [(Turner et al., 2014; Vollmer et al., 2008a)]. There is no model for the function of the holes and what potential role they play for the cell but it could be theorised that the holes that reach so deep into the cell wall could be involved in the transport of substances or chemicals through the cell wall. The cell wall actively remodels over the cell life cycle so there must be some benefit for the cell to

change from the rings into the mesh structure, perhaps the potential nutrient channel function of the holes is part of this reason.

The height difference between 50% of the bearing area and 99% of the bearing area gives an idea of how deep down from the surface the majority of the cell wall material lies from the surface. This value can be used as an indicator of how most of the cell wall material changes in height. The values for the parameter show that the cell wall is more topographic than previously expected [(Turner et al., 2014)]. When compared to the height difference between 1% and 99% (the effective total height of the topography measured) it shows that 50% of the area of the image lies between 50-60% in the shallower half of the cell wall and 40-50% in the deeper half of the cell wall. This is interesting as these percentages are similar. If the value for the percentage area in the top half was low it would indicate that more material sits close to the surface with small number of deep holes, conversely, if the value for the percentage in the top half was high it would indicate a structure with material generally deep into the holes with some sharper raised features that extend up to the cell wall surface. The roughly even split of area between the shallow and deep half of the depth show that the distribution of material is approximately the same between deep holes and shallow holes.

The percentage of the area of each image that is in the deepest 10 nm of the height as measured up from 1% on the histogram shows a range of different values on a cell by cell basis or even within a single cell. Bearing Pictures 2 and 3 have lower values for this parameter; however, they are still different from each other which shows that different areas on the same cell will not necessarily look the same. Bearing Pictures 1 and 5 show that there is a difference in the number of deeper holes in the mesh that are seen even when the thickness of the cell wall (1 to 99% height) that is imaged is similar.

In every image that the analysis was performed on, over 10% of the area in the image extends more than 10 nm deep down from the top surface of the cell wall which is not predicted in the knobbled model of the mature architecture. A value of 2-4 nm for an average radius of new holes, assuming circular holes, gives a parameter that can be used to build a mathematical model for the cell wall architecture.

6.2.2- Fibre width analysis

NMR techniques have been used to calculate a glycan-glycan separation and to measure the crosslink density of isolated cell walls. One of the advantages of AFM is that it is

capable of imaging samples in their natural conditions so a similar calculation can be made by direct measurement. Assuming that there is a 4 fold axial helical symmetry to the peptides in *S. aureus* peptidoglycan, which has been stated in [(Kim et al., 2015)] and evidence has been seen with the AFM images in Chapter 5, the average fibre diameter can be used to estimate a maximum crosslinking percentage by calculating how many glycan strands make up a fibre if the glycan to glycan distance is 2.3 nm as measured using NMR [(Kim et al., 2015)].

Three of the highest resolution mesh images were used for diameter measurements which were taken using the Bruker Nanoscope cross-section function. On each image every fibre was measured across the centre of the fibre, perpendicular to the orientation of the fibre meaning the shortest possible distance across the fibre was measured. Some individual glycans that were not part of fibre bundles were also measured and counted in the statistics as this is one of the possible strand organisations is single glycans.

The three images chosen included two images of the wildtype strain (Figure 6.1(B) and 6.3(D)) and one of the TagO mutant (Figure 6.5(A)).

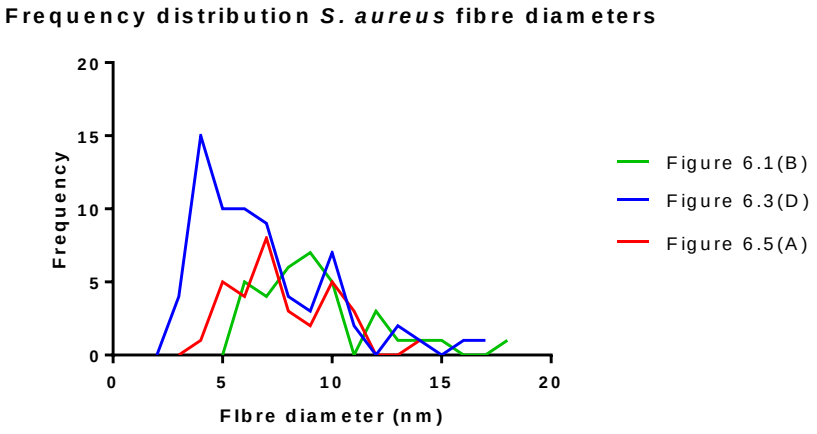

Figure 6.16- Histogram showing the frequency distribution of three topography images. Fibre diameters were measured using the cross-section tool on Bruker Nanoscope Analysis software.

The histogram of all of the measured diameters indicates that there was a similar distribution of diameters for the Figure 6.1(B) and Figure 6.5(A) while the peak of the distribution for Figure 6.3(D) is shifted towards narrower fibres which could be due to increased resolution seen in Figure 6.3(D) meaning there is an error associated with the measurements due to tip convolution artefacts that make the diameters wider than in

reality. It was not possible to account for the differences in the tip when calculating the diameters but it is something to consider when comparing between images. All three distributions have a longer tail towards the thicker diameter strands which could be some remnants left from the rings that are still in larger bundles of strands. The histogram in Figure 6.3(D) has thinner diameter fibres and some that have diameters that would potentially make them single fibres while the other two images do not, which perhaps gives a numerical indication that the resolution of Figure 6.3(D) was better than the other two images. This increased resolution could lead to a different measurement of the crosslinking but by using multiple images for the analysis the resolution difference will be averaged out.

A

Image	Number of fibres measured	Mean (nm)	Median (nm)	Mean Glycans/fibre	Median Glycans/ fibre
Figure 6.1(B)	34	9.2 ± 2.7	8.9	4	3.9
Figure 6.3(D)	69	6.8 ± 3.1	6.1	3	2.7
Figure 6.5(A)	32	7.7 ±2.3	7.1	3.3	3.1

B

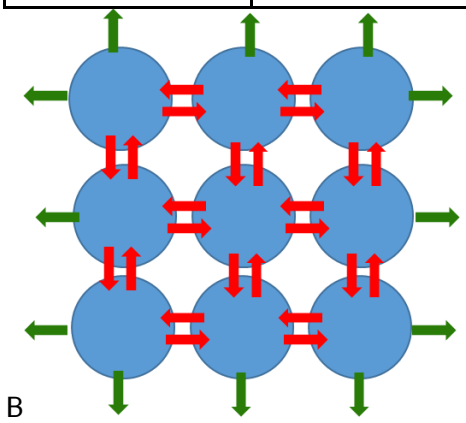

Figure 6.17- (A) is a summary table of the averages (mean and median) of the fibre diameters and the number of glycans per fibre for each average value. (B) is a diagram of how glycan chains could pack in a 3 x 3 wide fibre with red arrows representing made cross-links and green arrows representing sites available to make cross-links. For a 3 x 3 fibre there is a theoretical maximum cross-linking percentage of 66%.

The summary of results in Figure 6.17 shows a difference between the mean and median values of the fibre diameters that were measured. The fact that the median values are all lower than the mean values confirms the existence of a tail towards the thicker diameter

fibres. Figure 6.3(D) has a higher fibre count within the same image scan size which is possibly due to the higher resolution imaging that was possible on this cell.

To calculate the theoretical maximum crosslinking percentages based on the diameters measured in the three images the NMR value of 2.3 nm from glycan to glycan [(Kim et al., 2015)] was used. The mean and median values of the average fibre diameter was divided by 2.3 nm to give the mean and median glycans per fibre which came out to be between 3 and 4 for the mean glycans per fibre and between 2.7 and 3.9 glycans per fibre for the medians. Restating the assumption that the glycans make peptides with a 4-fold axial symmetry and that every possible peptide crosslink is formed, the maximum crosslinking percentage can be calculated. A 3 x 3 glycan fibre (such as the one in Figure 6.17(B)), which would correspond to the lowest value of the mean glycans/ fibre that was measured, gives a crosslinking percentage of 66%, while a 4 x 4 glycan fibre, corresponding to the highest mean, would give a value of 75% crosslinking. These crosslinking values of 66 and 75% agree well with the NMR measurements of crosslinking with average *S. aureus* crosslinking measured as 66% [(Kim et al., 2015)] and 75% [(Sharif et al., 2009a)]. This shows that the maximum crosslinking percentage from the direct measurement technique has good agreement with the previously published NMR data as all but one of the statistical averages for the glycans per fibre would correspond to a crosslinking percentage between the two measured values. This measurement shows that despite the loose mesh architecture with thin fibres rather than a dense walled structure, it is still possible to have a crosslinking density that is as high as that measured by NMR. There are some issues with the method for direct measurement of the crosslinking percentage as narrower fibres or fibres that are close together may be measured as one larger single fibre and also due to the limit of the resolution the tip may broaden the fibre diameters which would result in an overestimation of the crosslinking percentage.

6.3- Imaging division events in *S. aureus*

During the imaging of *S. aureus* some cells were captured that had been undergoing a division event.

6.3.1- Division events in wild type cells

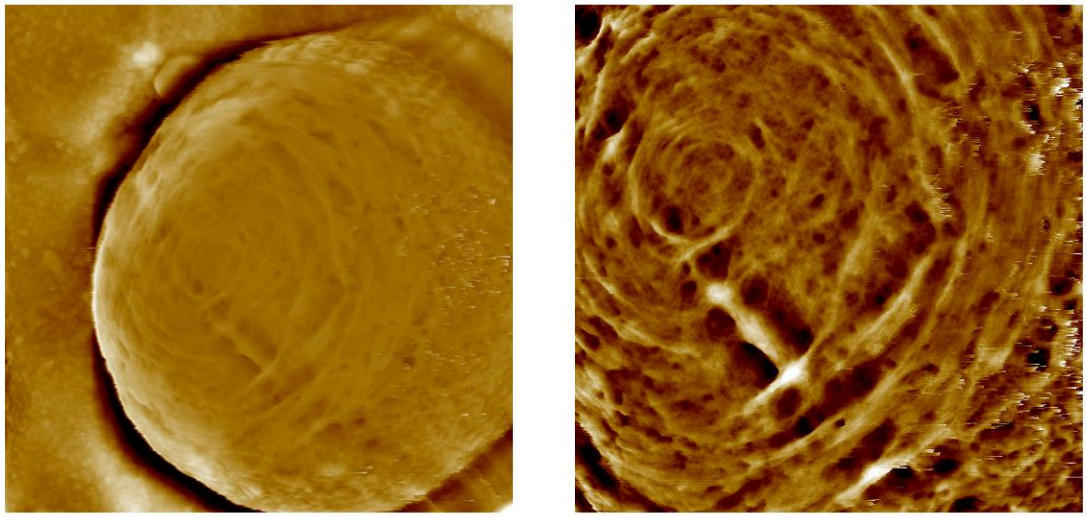

A B

Figure 6.18 – Topographic high pass filtered images of a cell undergoing a division event with a crack seen appearing through the centre of some ringed architecture. (A) has a filter size = 651 nm. (B) has a filter size = 373 nm.

In Figure 6.18 there is evidence of a division event occurring on the cell with a crack beginning to form across a set of rings that have been partially degraded. Where the crack is forming in Figure 6.18(B), there is a straight, raised band of peptidoglycan that is being bridged by some remaining ring fibres. This straight band of peptidoglycan could be the pie crust that is now external to the cell. This type of thick band feature was seen frequently on dividing cells which suggests that it is a part of the division process.

Another feature to notice from Figure 6.18 is that there is a definite boundary between the last two division planes. There is no transition in structure from rings to mesh but rather a definite line where the rings will have grown out from a septal plate. The boundary is the location of the crack from the previous division event.

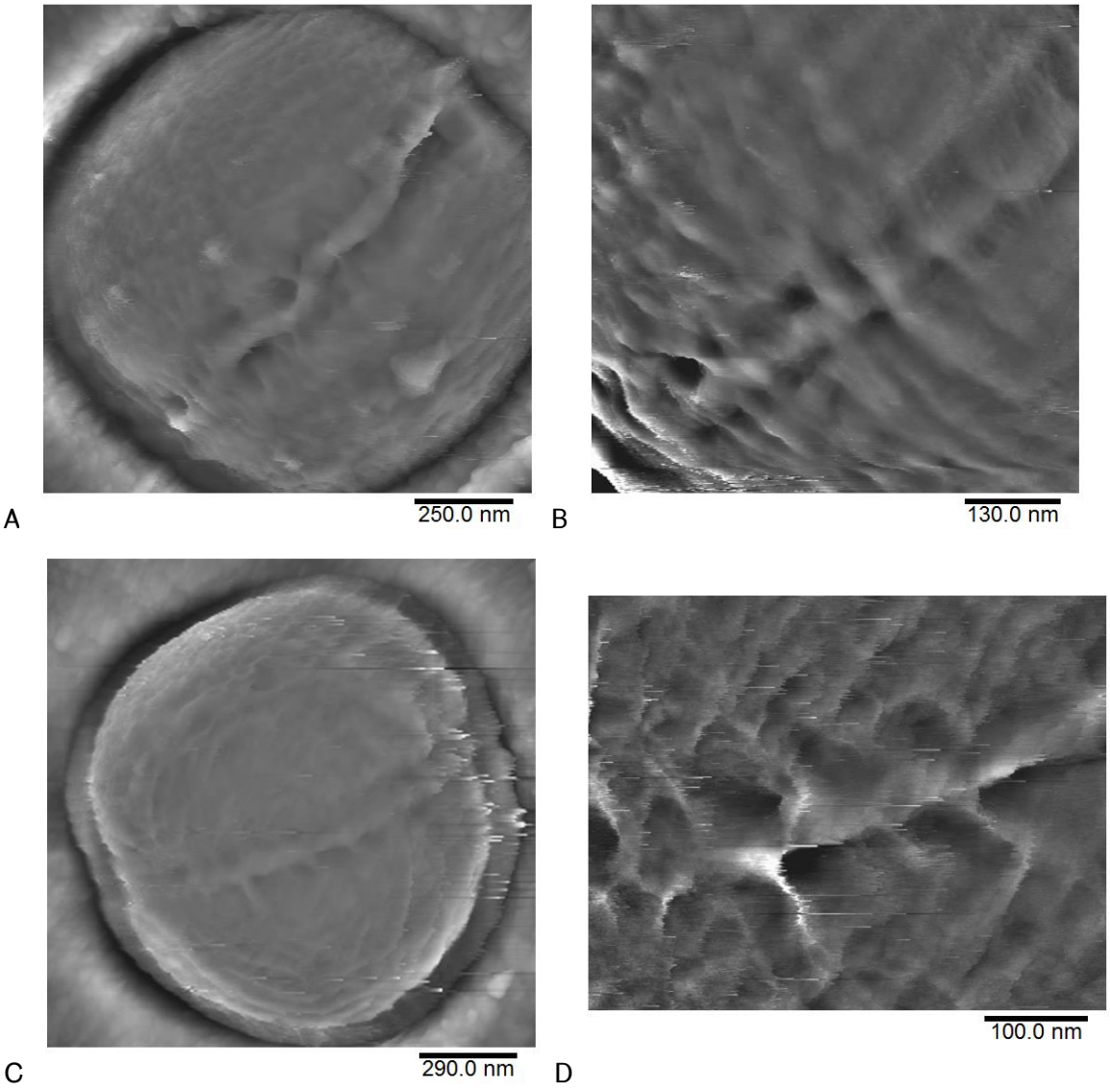

Figure 6.19- Topographic high pass filtered images of a two cells undergoing division events with cracks and a raised band appearing to emerge. (A) has a filter size = 618 nm. (B) has a filter size = 331 nm. (C) has a filter size = 722 nm. (D) has a filter size = 250 nm.

Figure (6.19(A) and (C)) are more examples of the raised band of material between the two halves of a dividing cell, with some strands that are bridging across the divide and over the raised band. On Figure (6.19(A)) there is a band present that is not straight and is protruding from between the two halves of the cell. Towards the bottom left of the cell there is evidence of some strands that are bridging the two halves of the dividing cell that could be keeping the raised band contained and straight as seen in Figure 6.19(B). Figures 6.19(C) and (D) show another external band of material that is raised between the two halves of the dividing cell. It also shows evidence of some strands that are bridging across the raised band along the whole length of the raised band, keeping the raised band

straight. The bridging strands look like they are part of a set of rings, however, the resolution on these images makes this unclear.

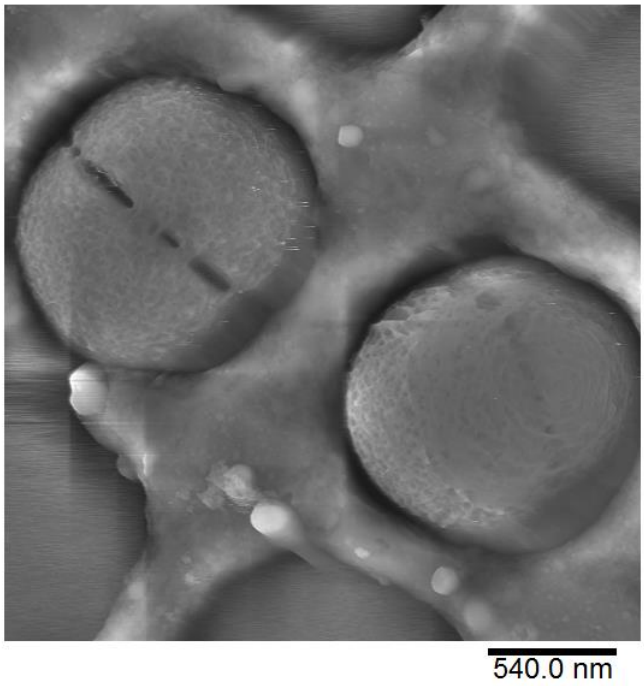

Figure 6.20- High pass filtered topography images of two cells undergoing division events with a filter size = 1.34 µm.

The raised band is not a universal feature of dividing cells. In Figure 6.20 there are two dividing cells seen without the raised band. The left hand cell is entirely made of the mesh structure and has an almost fully formed gap between the two hemispherical daughter cells while the cell on the right has just begun the dividing process, with a high number of bridging strands. It should also be noted that the right hand cell has a stark boundary between the two structures.

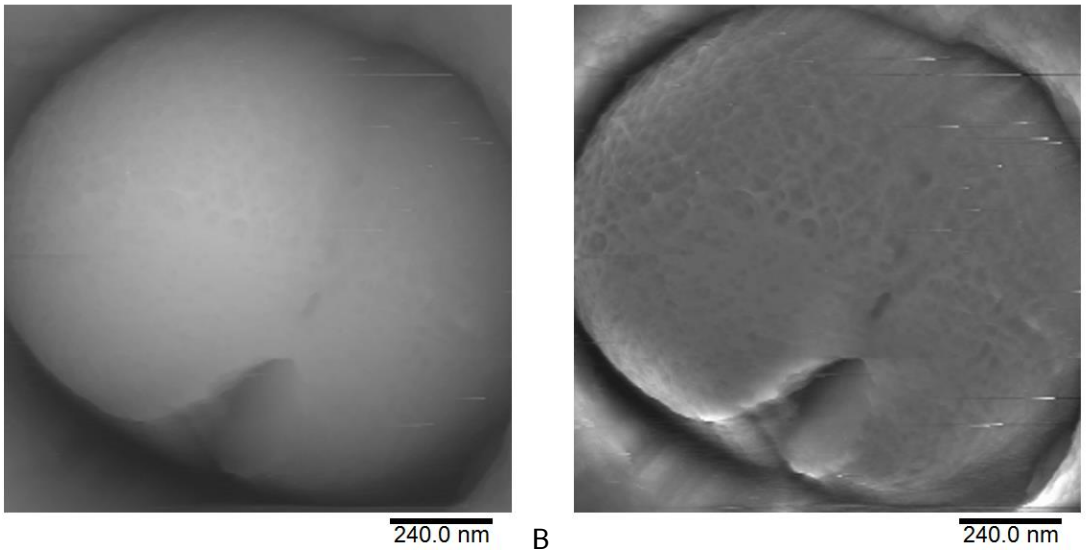

Figure 6.21- Topography and high pass filtered topography images of a cell undergoing a division event. The cell has begun splitting through the ringed architecture but has not split in the mesh region. (A) has a Z scale (black to white) = 691 nm. (B) has a filter size = 591 nm.

The cell in Figure 6.21 has begun to split and looks to have mostly split on the bottom half of the cell. The structure of the side towards the bottom of the image appears to be rings while the top of the cell is the mesh architecture where the cell has not split anywhere near as much. This could be evidence that the propagation of the division crack happens first to the ringed structure on the cell. This could then lead to a discussion of whether the mesh architecture holds the two halves of the cell together more and if this architecture is stronger, or perhaps the ringed architecture is the initial target of the enzymes that break down the peptidoglycan that the cell needs to cut for the two hemispherical cells to divide.

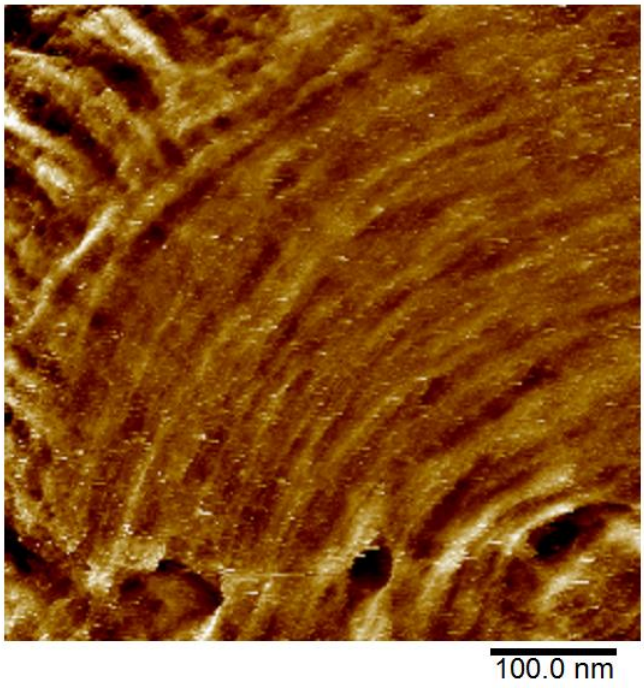

Figure 6.22- Topographic high pass filtered image of a cell showing evidence of orthogonal sets of rings. The filter size on the image = 252 nm.

Figure 6.22 has a cell with a set of dense rings with the start of a division event causing some holes to appear across the cell. There is no evidence of a raised band emerging underneath the holes. A notable feature of this cell is that in the top left hand corner there is a structure that appears to be a previous set of rings that is orthogonal to the set of fresh dense rings seen in the rest of the image. Based on the frequency of finding this combination of structures this configuration of architectures is assumed to be quite rare.

6.3.2- Division in TagO mutant cells

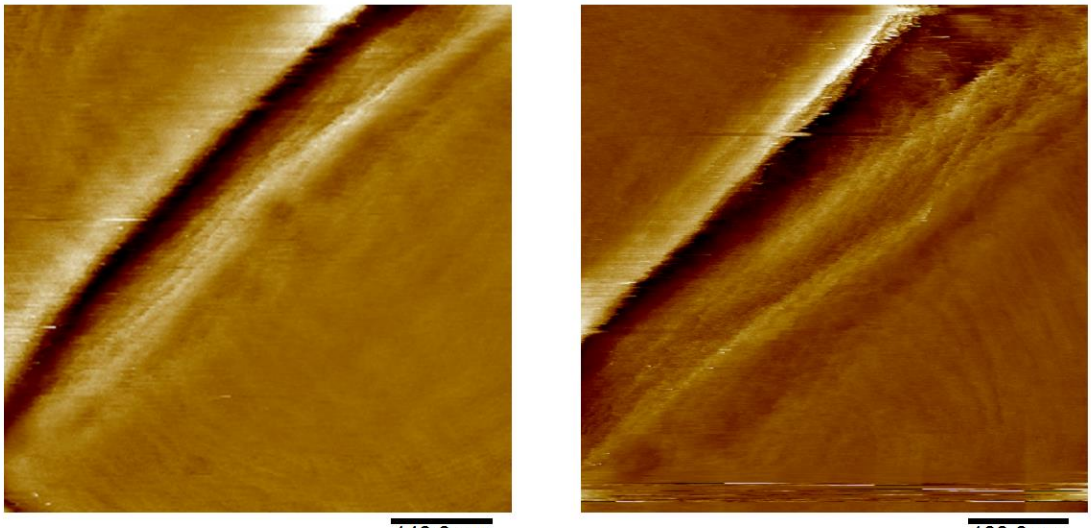

Figure 6.23- Topographic high pass filtered images of a TagO mutant strain cell that is undergoing a division event. The crack between the two halves of the splitting cell can be seen. (A) has a filter size = 347 nm. (B) has a filter size = 253 nm.

Figure 6.23 shows a TagO cell with rings that is undergoing a division event with a crack across the centre of a set of rings. TagO is the mutant bacterial strain that lacks the teichoic acids on the outside of the cell wall. Towards the top right of the crack the two halves of the cell appear to have come apart slightly, revealing the corner of the septal plate. Imaging this region of newly uncovered septal plate produces images that show signs of a ringed structure, however, due to the angle of the tip imaging this region, it is difficult to obtain high resolution structure from the area. There was no evidence of the raised band of material in this cell.

6.3.3- Division in SagB mutant cells

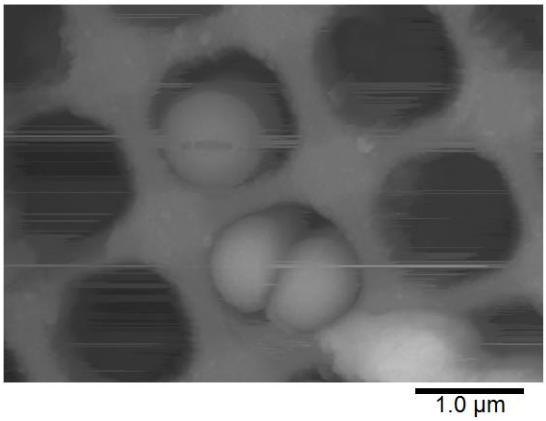

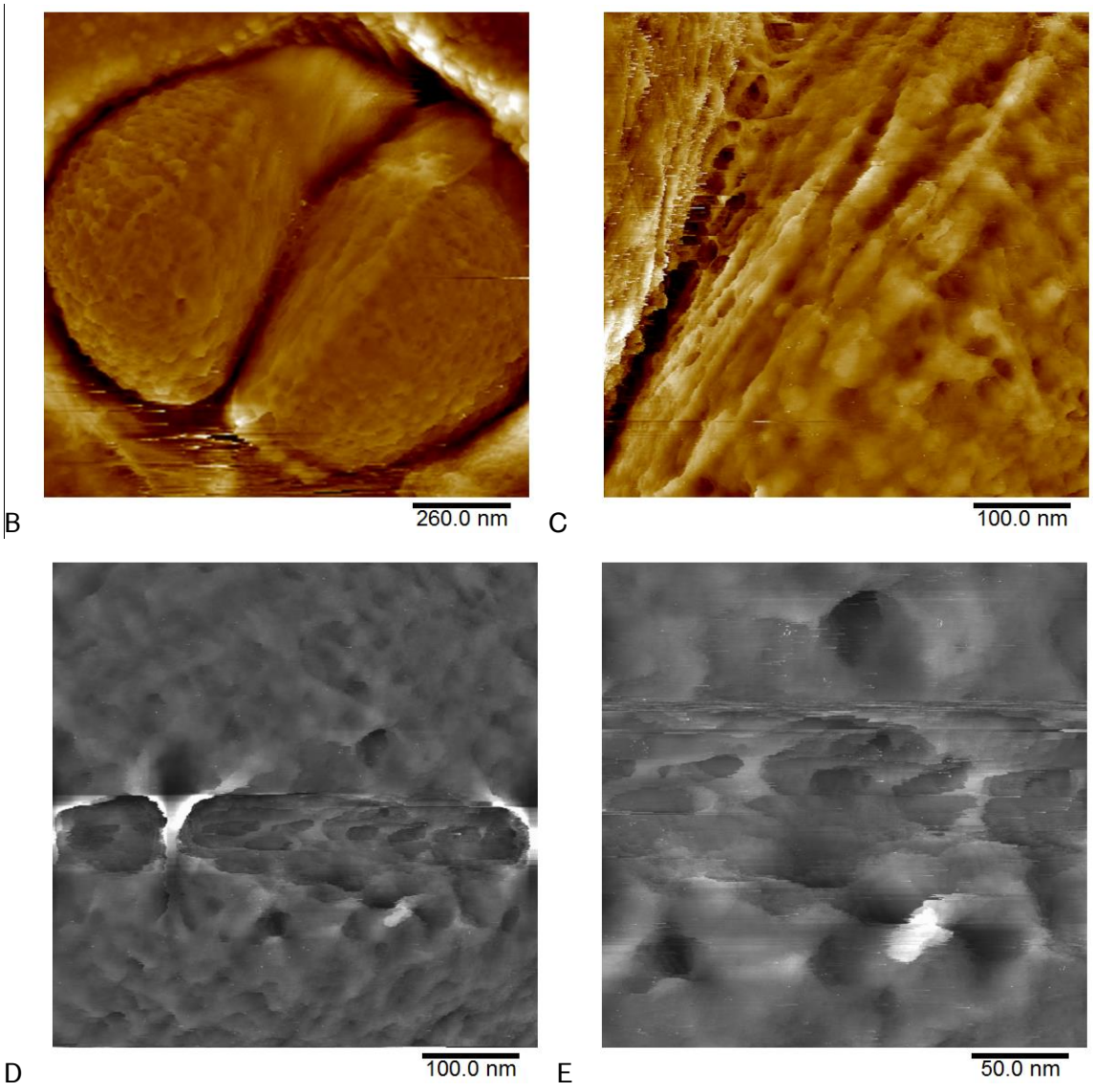

Figure 6.24- Images of a SagB mutant strain cells that are undergoing division events. (A) shows a topographic image of a field of cells with two undergoing a division event. (B) and (C) are high pass filtered topographic images showing the cell from Figure 6.24(A) with the two hemispherical daughter cells splitting apart. (D) and (E) show the cell at the top of Figure 6.24(A) showing a crack between the two halves of the splitting cell. (D) is a high pass filtered topography image and (E) is a topography image. (A) has a Z scale (black to white) = 1.72 µm. (B) has a filter size = 639 nm. (C) has a filter size = 249 nm. (D) has a filter size = 250 nm. (E) has a Z scale (black to white) = 47 nm.

The SagB mutant lacks one of the key hydrolase enzymes that is responsible for breaking down the peptidoglycan, allowing the cells with the SagB gene to grow correctly into spheres. The absence of the SagB enzyme causes longer glycan strands. Two SagB cells showed the bridging strands feature which was not seen in any other cells during the

entire project of imaging *S. aureus*. These strands may be present due to the lack of rapid rounding in the SagB cells which could be responsible for the breaking of the bridging strands in other strains of *S. aureus*. The cells in Figure 6.24(A) are undergoing division events with the two halves of the cell showing mesh architecture. Focussing in between the cells on the septal plate there are some strands that are still bridging the two septal plates. In other images of two halves of dividing cells it was not possible to image as far down into the space between the dividing cells to know whether this is typical or not. Other strains only showed bridging strands on the outer most surface of the cells, never down in the division crack between the two septal plates. The presence of extra bridging strands could also be due to the lack of the hydrolases as the bridging strands are not broken or are broken down at a slower rate than in the wild type.

6.4- Artificially disrupting the cell wall structure

6.4.1- Detergent

One of the benefits of using liquid AFM as a technique to image bacteria is the ability to track dynamic processes. Detergents are widely used as cleaning products that will kill bacteria that live on clothes, the skin and other household surfaces. The death of the bacteria happens because the detergent breaks up the cell membrane which is inside the cell wall, causing the insides of the cell to spill out of the cell [(Cunningham and Wickner, 1989)]. A commonly used detergent in microbiology is SDS (Sodium Dodecyl Sulphate) which is used in the protein analysis technique SDS-PAGE where it denatures proteins. The aim of this experiment is to take a series of AFM images of the death of a cell caused by the addition of SDS detergent to the imaging liquid and to record any changes in the structure of the cell wall. A cell was chosen to be the subject of the experiment (shown in Figure 6.25) then 10% SDS was added to the imaging liquid.

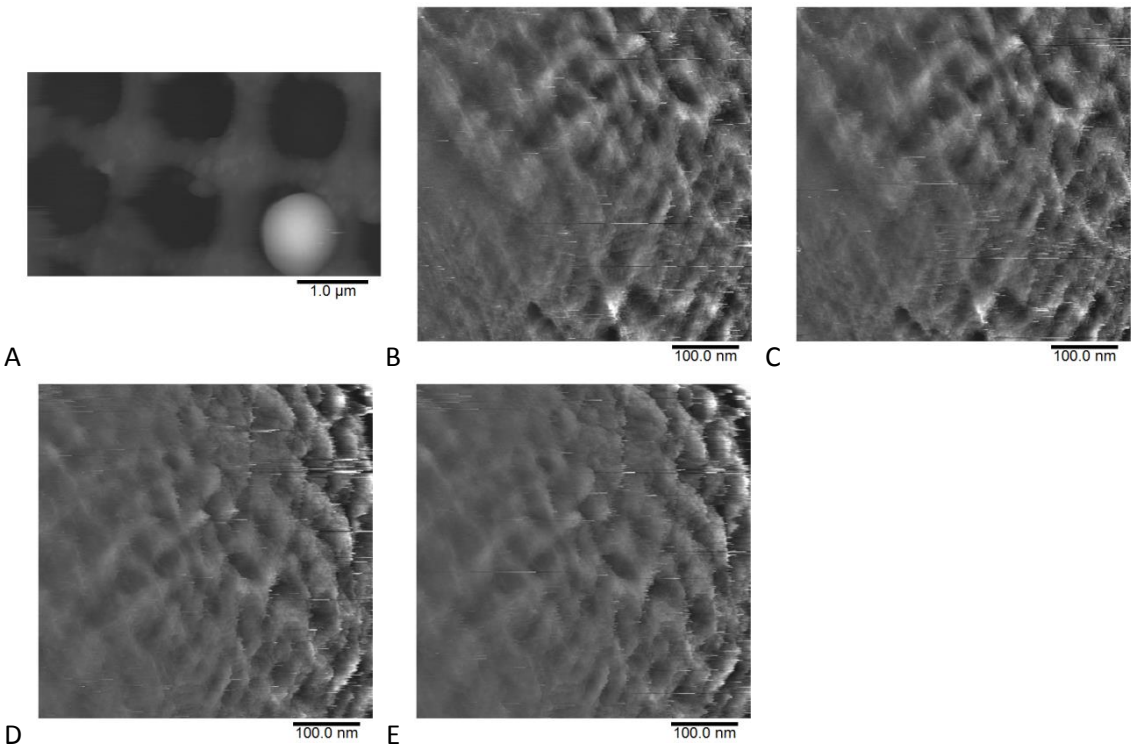

Figure 6.25- A series of topography images of cells that have been treated with SDS detergent. (A) is a topography image of a large area scan showing a single cell. (A) has a total Z scale (black to white) = 1.04 µm. (B)-(E) are topographic high pass filtered images of the cell from Figure 6.25 that are being imaged with the addition of SDS detergent The filter size on images (B)-(E) = 249 nm.

The cell was imaged over 1 hour with no changes seen as shown in Figure 6.25. One reason this may have been the case is that the detergent is active on the cell lipid membrane as opposed to the cell wall which is the part of the cell that is imaged with the AFM.

6.4.2- Lysostaphin treatment of cells

Another technique that can be employed to force the lysis of the cells is adding the enzyme lysostaphin to the imaging buffer. Lysostaphin breaks the pentaglycine bridges of the peptidoglycan which causes hydrolysis of the cell wall. The effect of lysostaphin on *S. aureus* cells has previously been studied [(Francius et al., 2008)] and was shown to cause some structural changes in the cell wall over time. The study used a concentration of 16 µg/ml lysostaphin in their high salt imaging buffer (10 mM PBS, 150 mM NaCl, pH 7.4) which caused some structural changes in the cell over 260 minutes of imaging the same cell as shown in Figure 2.14.

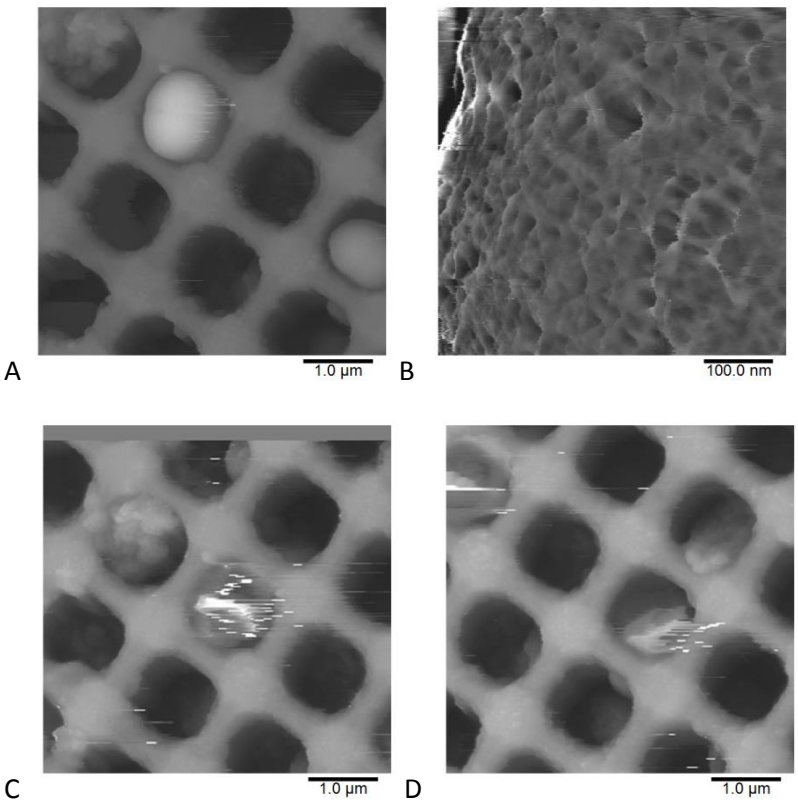

Figure 6.26- Images showing the effect of the enzyme lysostaphin which was added to the imaging buffer. (A) is a topographic image with a Z scale (black to white) = 1.41 µm. (B) is a high pass filtered topographic image with a filter size = 251 nm. (C) is a topographic image with a Z scale (black to white) = 1.2 µm. (D) is a topographic image with a Z scale (black to white) = 1.1 µm.

The same lysostaphin concentration of 16 µg/ml was used in the experiment with an imaging buffer of 300 mM KCl, 10 mM Tris, pH 7.8 also used. A cell was found that would be the subject of the experiment (Figure 6.26(A)) and the high resolution structure was imaged as being able to see cell wall changes on a molecular scale is the aim of the experiment. The AFM tip was withdrawn and the lysostaphin was added after the taking of Figure 6.26(B) then the AFM was re-engaged on the surface to begin imaging again. No cell was seen in the hole that the target cell had been less than 25 minutes post addition of lysostphin. In the hole there was a poorly resolved object which could not be imaged effectively due to the streaks formed on the image. The cell seen to the right of the target cell in Figure 6.26(A) was also imaged to see if it had lysed which, as can be seen in Figure 6.26(D), it had done.

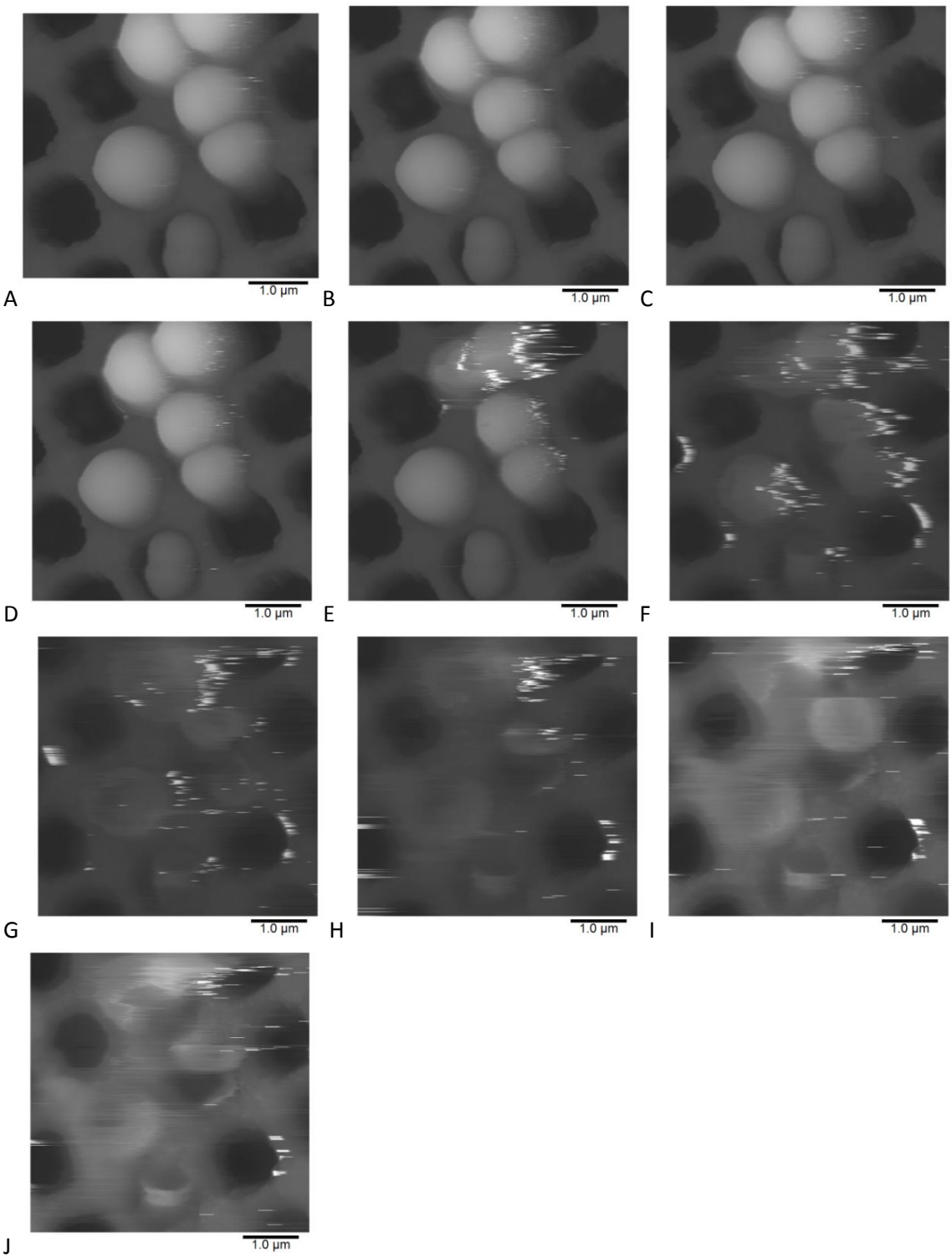

Figure 6.27 – A series of topography images showing the lysing of multiple *S. aureus* cells due to the addition of the enzyme lysostaphin to the imaging buffer. The lysostaphin is added immediately after image (A) had completed scanning. The Z scales (black to white) for the images are: (A) = 2.8 µm, (B) = 2.8 µm, (C) = 2.8 µm, (D) = 2.8 µm, (E) = 3.1 µm, (F) = 3.9 µm, (G) = 3.6 µm, (H) = 2.7 µm, (I) = 1.6 µm and (J) = 1.5 µm.

The experiment was repeated using a lower concentration of lysostaphin (2 µg/ml) and without withdrawing the tip from the surface to add in the lysostaphin.

A field of view with multiple healthy looking cells was found and imaged at the first time point in Figure 6.27(A). The lysostaphin was added to the imaging buffer and the field of cells was immediately imaged with the first image shown in Figure 6.27(B). At 11 minutes after the addition of the lysostaphin there is no sign of any changes to the overall shape of any of the 6 cells in the field of view but after a further 5.5 minutes there are the first signs of a change with the cells at the top of the image producing streaks when imaged. From the cells looking seemingly healthy in Figure 6.27(E), the cells all lyse by the time point in Figure 6.27(G) which is a time frame of between 10 and 16 minutes.

Based on the two lysostaphin experiments that were performed using the same method as Francius, the action of the lysostaphin is faster than recorded in that study [(Francius et al., 2008)]. The result is also more dramatic as instead of some structural changes seen, there is a complete lysing event that leaves little behind of the cell. There is a 15- 25 minute window after the addition of the enzyme where the cells seem as normal before they begin to burst within one frame (5.5 minutes) of them looking normal. After all of the cells have lysed there were some images with streaks taken which could be some of the burst cell wall, cell membrane or cell insides that were being dragged by the tip.

6.5- Timeline of the structure of peptidoglycan in *S. aureus*

From Chapter 5 and from this Chapter, a large set of images at different times in the peptidoglycan remodelling process have been presented. These images can now be arranged into an order that represents these different distinct stages.

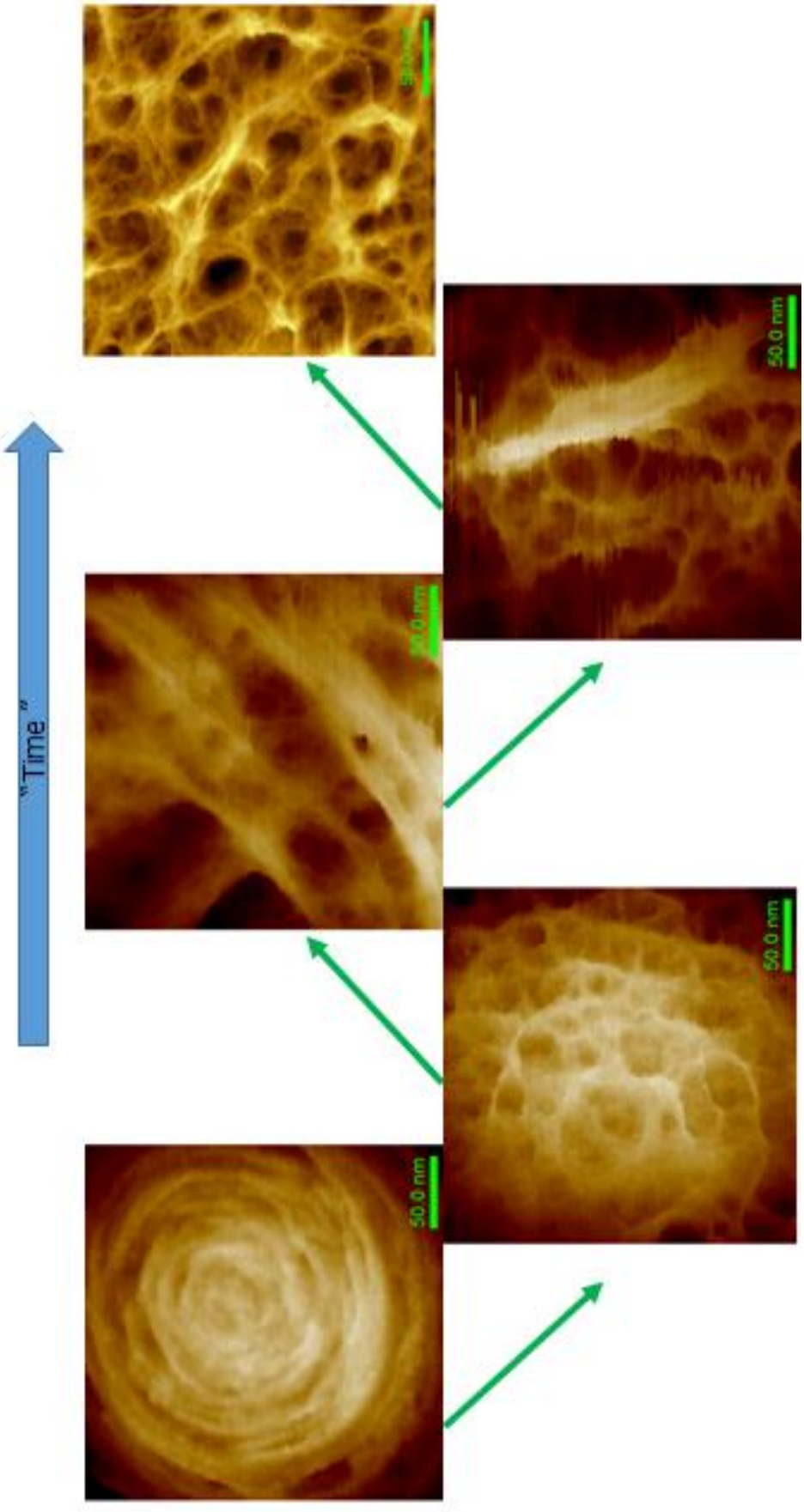

Figure 6.28 – Composite timeline of peptidoglycan aging process.

The images in Figure 6.29 show how the cell starts in the dense ringed structure which is formed during the growth of the septal plate in the cell division cycle. The peptidoglycan's structure is broken down, partly by the force of the turgor pressure of the cell which causes the slow expansion of the cell into a fully round cell and partly due to the activity of enzymes like the hydrolases which break the bonds in the peptidoglycan. The second time point shows some looser or less dense rings with large gaps between the rings. The third time point shows some rings that are even more broken down with some holes forming to the sides of the peptidoglycan fibres. In this image there is also evidence of the disordered structure so the cell is showing the first signs of the mature architecture. In the fourth time point the porous mesh structure dominates the cell with seemingly randomly oriented strands and only the thick remnant fibre of a ring which is now only a short length of a fibre. The final time point shows the mature mesh structure with deep holes, overlapping strands and seeming random orientation.

Of the large number of cells that have been imaged over the project it has been rare to see two sets of orthogonal rings on the same cell with it only occurring once, while it has been common to see rings and mesh on the same cell with the rings at various stages of degradation. Based on these observations it can be extracted that the time span of the degradation process is within the same time scale as the division process. If the cells were observed to have multiple sets of rings the time scale of the degradation process would be longer than the division cycle as there would be evidence of multiple division events on the outside of the cell. If the degradation process happened in a shorter time scale than the division process it would be less common to find cells that have rings with cracks through the centre which has been seen on many cells.

6.6- Discussion and conclusions

The mature architecture of peptidoglycan had previously been studied with AFM, either by imaging sacculi or by imaging whole cells at a resolution that struggled to resolve the structure of the peptidoglycan [(Touhami et al., 2004; Turner et al., 2009, 2014)]. The mature structure is important to understand as this is the final organisation of the peptidoglycan of the cell. By using small amplitude tapping mode, it was possible to image the mature architecture at a molecular scale with some individual glycans being resolved within the peptidoglycan network. The technique has allowed for a great improvement in the resolution that can be seen routinely on the cells. From the imaging of the mature structure the knobbled description that was derived from the dried out sacculi was not

seen while a structure closer to that seen by Touhami was seen [(Touhami et al., 2004)]. It could be the case that the knobbled features are an artefact of the sacculi preparation process which involves many steps including boiling the cells in detergent and potentially a treatment in hydrofluoric acid to get the cells to isolate the peptidoglycan before they are then dried down flat on a surface so the structures that are seen could be a drying artefact or due to water being trapped in holes during the evaporation of the water causing the knobbled artefact on the sacculi when imaged [(Turner et al., 2010a)].

The images of the mesh show an overall porous mesh of fibres of peptidoglycan with some long strands. There appears to be large, deep holes within the network and the strands seem to have no overall orientation including in the direction that the rings were in.

In some images, two distinct structures can be seen on the same cell. This gives the ability to directly compare the two structures as the exact conditions they were imaged in are the same. From these images it can be said that the rings are flatter than the mesh structure and have an overall smaller height profile to them, meaning they do not have holes that go deep into the cell wall structure. The mesh by comparison seems to be sticking up from where it would have been in a ring formation which could indicate how the rings are cut then bonds are formed creating a 3D structure rather than the almost 2D like rings. On all of the cells that show both rings and mesh there is a clear boundary between the two architectures which would be expected from the knowledge of how the division in *S. aureus* happens. During division the whole cell will tear apart into two daughter cells leaving hemispherical cells that have one flat septal plate side which has the dense ringed architecture and one curved side which is made of peptidoglycan which was added in previous division events. The reveal of the flat side and the splitting process is what causes such a stark difference and dividing line between the two halves of the cell. When imaging the two structures on the same cell it can sometimes be seen that the mesh is less rigid and moved more easily by the scanning of the tip than the rings as is evident by the streaks that appear in the same direction as the tip is scanning on the trace and retrace images.

The peptidoglycan cell wall is completely restructured from the rings to a mature mesh structure over the course of the cell division cycle. A different set of analysis methods are needed for the quantitative analysis of the mesh. To understand how the depth profile of regions of mesh that are seen, a bearing analysis technique was devised that gives values

of the average hole sizes within the mesh and builds a map of how the depth profile changes through the mesh.

Bearing analysis was used to create contour map like images of the mesh cells and then average hole size and hole density at various depths were calculated. One of the most important observations from this analysis was that the cell wall has holes that are over 20 nm deep into the cell wall which is possibly the entire thickness of the cell wall. These holes are not present in the ringed structure so are developed in the peptidoglycan maturation process. The validity of the method was tested by making maps of two areas on the same cell. The results showed that different areas on the same cell did not necessarily have the same values for the average new hole radius or the depth within the image. From the analysis the histogram height from 1% to 99% of the total area of the histogram was calculated for each image which showed that for each of the six images, the height changes were all greater than 19 nm which is almost if not all the way into the cell wall layer.

From the whole image analysis the percentage area that is below 10 nm deep into the cell wall can be calculated. The value of 10 nm is an arbitrary depth but illustrates that at least 10 and up to 50 percent of the surface topography can be deeper than 10 nm below the cell surface in a structure that was not previously thought to be highly porous. The existence of the holes raises questions as to their purpose for the cell. In a model without holes in the peptidoglycan there is not a conclusive mechanism for the transport of large molecules through the peptidoglycan. The purpose of the remodelling could be in part due to the need for the cell to be able to transport nutrients and proteins into and out of the cell. A study of *S. aureus* protein secretion saw that deletion of the SagB protein, responsible for the cutting of glycan strands in the young peptidoglycan, resulted in a reduction of the amount of secreted proteins compared to the wild type [(Chan et al., 2016)], which suggests that the cell needs to restructure the peptidoglycan for these proteins to be secreted. The remodelling could also be needed for the expansion of the cell as it grows to form a whole sphere.

Measuring the fibre diameters in the mesh using the Nanoscope Analysis software allowed for an estimate of the numbers of glycan strands that make up a fibre of glycans. The measurements are open to errors due to tip broadening which can widen the features that are imaged; due to this the results are best used as an estimate for the average number of glycans in the fibres. Using the mean and median number of glycans in the fibres the maximum total percentage of crosslinking was calculated, assuming a 4-

fold axial helical symmetry to the peptide side chains along a glycan and that every available crosslink is made. The results for crosslinking from the AFM measurements of 66-75% compares well to the values that have been reported from NMR data of 66% [(Kim et al., 2015; Sharif et al., 2009b)]. In other words, it is possible for 66-75% of the peptidoglycan peptide sidechains to be crosslinked even considering the highly fibrous nature of the mesh images.

All of the AFM data collected from imaging whole *S. aureus* cells can only provide information about the peptidoglycan remodelling that happens on the outside of the cell wall. It is interesting to think about how peptidoglycan is rearranged through the whole thickness of the cell wall. It has been shown that the peptidoglycan is initially inserted in the septal plate in the ringed structure which has been seen by AFM of whole cells, sacculi and EM data but it is not clear whether the rings only exist on the outer surface of the septal plate in something like a ringed cap. The fresh peptidoglycan could be inserted in rings the whole thickness of the cell wall, or after the surface rings are laid down, a less ordered structure could be inserted. The large difference in height of the surface that is seen in between the rings and the mesh means that, if the structure is entirely ringed, the peptidoglycan through the whole cell wall thickness must be broken down by hydrolases and remodelled. Alternatively the mesh structure including deep holes could exist already under the septal plate of rings which is degraded away revealing the already formed mesh. The rings could form on the leading edge of the septal formation and then the mesh structure is inserted behind the rings leaving only the thin layer of rings.

Division in *S. aureus* is the target process for many antibiotics including the β-Lactam class of antibiotics which disrupt the peptidoglycan synthesis step which is at its peak during the formation of the septum. The mechanism for how the cell dies due to the antibiotics is still unclear so it is important to study to develop understanding of how antibiotics work. To help this, imaging the cell wall structure as it is undergoing division events can provide new information into the division process, especially at the resolution that AFM can achieve.

It has been seen that the division crack that forms is positioned through the rings of the previous division event which corresponds with the expectation built from data taken on sacculi and agrees with the consecutive orthogonal plane division in *S. aureus*.

Between the division crack on some of the dividing cells there appears to be a raised band of material emerging between the two halves of the cell with glycan strands or

fibres (bundles of strands) that still bridge the crack, often still as part of the ring formation. The raised band of material could be part of the remnant pie crust architecture that has been seen in studies imaging the sacculi of *S. aureus*, especially the inner surface of the cells which shows evidence of more than one previous division event [(Turner et al., 2010a)]. The raised band being visible on the outer surface is interesting if it is indeed the pie crust as this could be a piece of the pie crust that detaches from the cell because there is no evidence of a thicker band on the outside of whole cells in other images. The raised band is mostly bridged by strands which could keep the raised band in place as seen in Figure 6.1 and 6.2(C) & (D) the raised band is relatively straight as they have the bridging strands the whole length that the raised band is exposed while in Figure 6.2 (A) & (B) the cell appears to be contained only in the bottom left hand part of the cell in the image and then in the rest of the cell, where there do not appear to be bridging strands, the raised band is not straight which could indicate that it is looser. The worse resolution on these images means that it not possible to conclusively say whether there are no bridging fibres across the non-straight part of raised band. The raised band may or may not be the pie crust and it is not clear what happens to it when the cell has completely split.

While imaging the mutants there were distinctly different features seen. The TagO mutant showed a cell that had a sharp division crack with the two hemispheres completely separated while the SagB mutant shows a cell that has bridging stands between the two halves of the cell but between the two septal plates as opposed to the outer wall. The clear gap seen in the TagO cell is not necessarily uncommon but the cell is the only one to show potential evidence of rings on the septal plate that is about to emerge from the division event. This fresh plane is difficult to image due to the orientation of the cantilever as it images the sample from above so these rings could be an artefact of the tip imaging the sharp gradient of the cell but this is the only direct evidence so far of the newly uncovered septal plate having the rings with AFM on a whole cell.

The SagB having bridging strands deeper between the two halves of the cells is the only substantial difference that was noticed between the SagB and the wild type strain and could be due to the lack of the hydrolase enzyme that breaks bonds in the peptidoglycan as part of the remodelling process.

The previous AFM experiment investigating the effect of lysostaphin on the cell showed small morphological changes to the cell with a small crack appearing. Replicating the

conditions of the experiment using the same concentration of lysostaphin (16 µg/ml) as the previous experiment the cells in the field of view lysed before images could be taken showing the process of death of the cell. Using a concentration of 2 µg/ml and by not withdrawing the tip a field of cells was imaged over 1 hour and showed that all of the cells had completely lysed within 25 minutes of the lysostaphin being added which would suggest that the effect of lysostaphin is greater than had previously been reported in AFM experiments [(Francius et al., 2008)], given the same total lysing effect was seen for multiple cells in a field and was seen on multiple experiments at different concentrations. This total lysis agrees with other literature on the effect of lysostaphin [(Schindler and Schuhardt, 1964; Wu et al., 2003)].

Small amplitude tapping mode has proven effective at being able to resolve fibre within the mesh structure in the mature peptidoglycan architecture in *S. aureus.* The resolution of the images has not yet been high enough to conclusively image a single glycan fibre within the mesh network so developing the imaging technique to this point is necessary. One of the major questions with the mesh like structure is what biological purposes it serves for the cell so experiments could be performed to test this. One such experiment could involve the addition of a phage to see if they use these holes in the cell wall to make their way through to the cell membrane.

One of the main aims of the project, which was not achieved, was to be able to image the maturation process of *S. aureus* via AFM at structural resolution in real time. The cells were imaged in their growth media at 37 °C on many occasions but no division or maturation was seen. Experiments including changing the immobilisation method and imaging conditions should be performed to try to see these dynamic processes happening as this would allow for a real time line of the maturation process at a structural and potentially molecular scale to be formed.

Chapter 7- High resolution imaging of *Bacillus subtilis*

A successful method for trapping spherical bacteria for AFM imaging has been developed with the use of silicon holes to trap *S. aureus* cells. There are a whole range of different shaped bacteria, from spheres to rods to spirals, all with different lengths and diameters. It is desirable to develop a method for the trapping of rod shaped bacteria to then be able to study their cell wall structure in the same way as has been possible with the spherical bacteria so a range of different methods of trapping them have been tested in this chapter. The silicon holes that are used for the imaging of *S. aureus* have been shown to be effective in keeping the cells immobilised over a succession of scans, and a similar degree of stability is required for rod shaped bacteria.

There are many potential immobilisation techniques that could be used for the trapping of rod shaped bacteria including physical trapping (like the holes and filter pores [(Kailas et al., 2009)][(Turner et al., 2010b)]), chemical fixing (like poly-L-lysine [(Kuyukina et al., 2013)]) or biological immobilisation (like Cell-Tak [(Louise Meyer et al., 2010)]). The rod shaped bacterium that was chosen as part of the development of the trapping technique was *Bacillus subtilis* which, like *Staphylococcus aureus*, is a widely studied Gram positive strain of bacteria. Previous AFM studies of *B. subtilis* have looked at small fragments of broken apart cells and showed evidence of long rope like peptidoglycan structure [(Hayhurst et al., 2008)].

Photolithography is a technique that is widely used in the manufacturing of semiconductor related devices. It allows for structures with features of down to the nanometre scale to be patterned onto a surface with high accuracy. The pattern can be etched into a silicon wafer to a desired depth leaving a robust, reusable patterned substrate. A previous member of the group had experimented with a range of different patterns for the trapping of various bacteria. Some of these patterns were tested with the *Bacillus subtilis* to assess whether they could be used for a different strain of bacteria.

The development of an immobilisation method capable of being used with AFM to image living *B. subtilis* cells will be outlined with resulting images of the cells presented. The images will be analysed using some of the techniques that were developed in Chapter 6 along with discussion about the features that are seen on the bacteria.

7.1- Development of custom surface patterns for immobilising *B. subtilis*

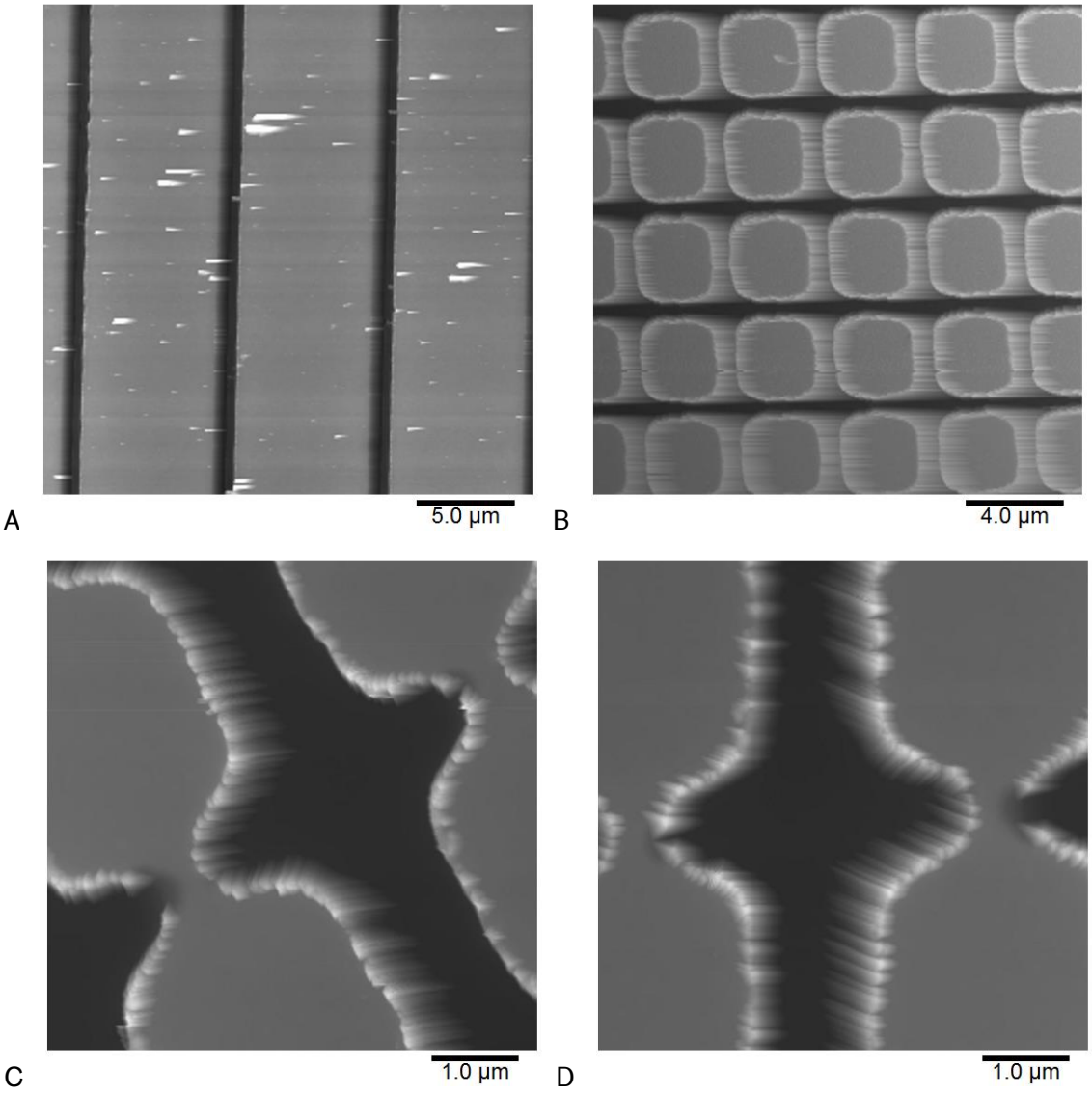

Figure 7.1- Topographic images of silicon etched with different patterns by a photolithographic process imaged in tapping mode in air. (A) is a 3rd order plane fitted topography image with a Z scale (black to white) = 78 nm. (B) is a topographic image with a Z scale (black to white) = 1.5 µm. (C) is a topography image with a Z scale (black to white) = 1.2 µm. (D) is a topography image with a Z scale (black to white) = 1.2 µm.

Initial *B. subtilis* experiments using the previously manufactured patterned silicon were performed in air in tapping mode to get an idea of how the cells interacted with the patterned surfaces and how they fit with the dimensions of the patterns. A survey of the different patterns made by a previous group member revealed some sets of grooves that were spaced far apart and then others that were closer and had grid like patterns.

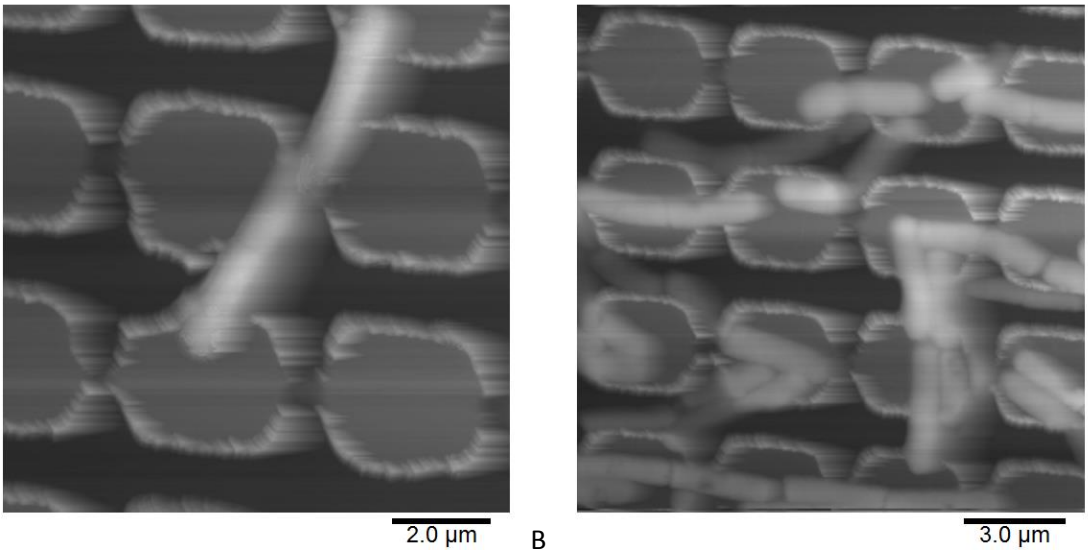

A B

Figure 7.2- Topographic images of *B. subtilis* fried on a silicon grid, imaged in tapping mode in air. (A) is a topography image with a Z scale (black to white) = 1.7 µm. (B) is a topography image with a Z scale (black to white) = 1.8 µm.

The cells in Figure 7.2 are seen to mostly sit above the patterned surface which could be because the cells need more space to be able to fall into the pattern. Unlike with the spherical cells, the rods need to be aligned in the same direction as the troughs otherwise they cannot fit into the shapes and will bridge across the channels. None of the previously made substrates worked well at trapping the cells so a new patterned substrate needed to be made.

While designing a pattern to trap the ~3 µm long, ~1 µm wide rod shaped *B. subtilis* cells, the first set up that was attempted was two sets of grooves that were oriented at 90 ° to each other, forming a grid system, similar to those seen in Figure 7.2 but with wider channels so cells can fall into the channels more easily. Using the photolithographic method that was outlined in Chapter 3 (Materials and Methods) a grid was created with the aim of trapping the rod shaped cells more effectively.

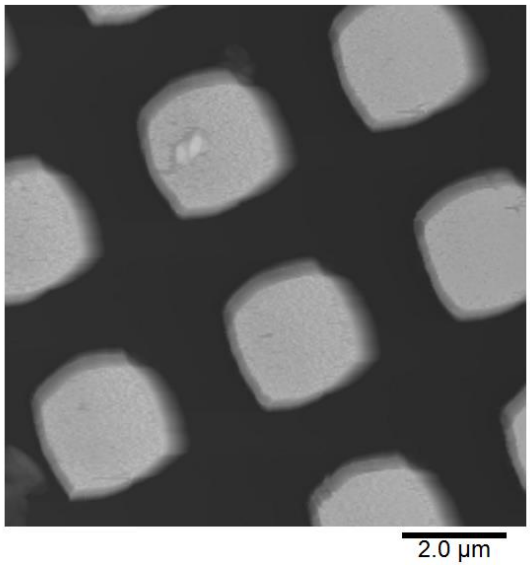

Figure 7.3- Topographic image of a silicon surface that has been etched to have channels in a grid pattern. The image has a Z scale (black to white) = 845 nm.

The new grid was measured to have peaks and troughs with a period of ~2.5 µm and a height of ~ 750 nm which gives a channel width of approximately ~1.25 µm. The raised areas are not as square as they should be based on the pattern on the UV mask which suggests that there was some spillage of UV around the edges of the mask.

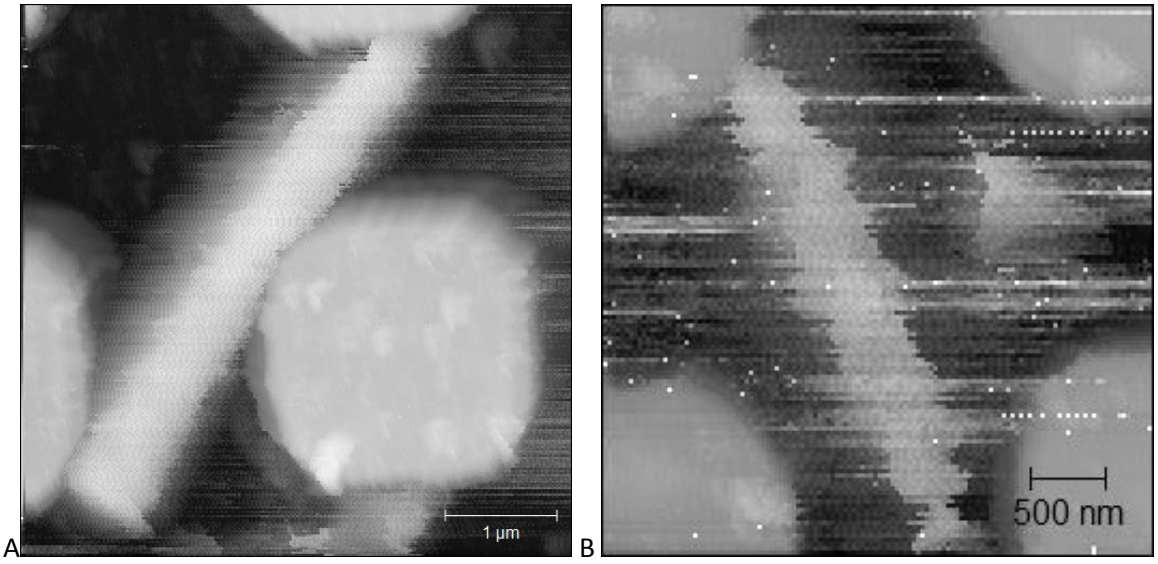

Figure 7.4- Topography images of *B. subtilis* cells taken using QI mode in liquid growth media. (A) is a topography image with a Z scale (black to white) = 919 nm. (B) is a topography image with a Z scale (black to white) = 1.1 µm.

The new grid design was tested with whole cells being imaged in liquid growth media. QI mode on the JPK Nanowizard 3 AFM was chosen for imaging as the lateral force could be

controlled more precisely than with contact mode on the Bruker Dimension 3100. The initial sample preparation protocol was the same as the one used for *S. aureus* so modifications were made such as increasing the concentration of cells after the final wash step to increase the numbers of bacteria that are put on the surface. In general the grids were seen to be mostly empty of cells and some imaging sessions would pass without a single cell being imaged. When a cell was found, the images were normally streaky as the cells are not tightly immobilised in the grid as can be seen in Figure 7.4. QI mode allowed for some cells to be imaged for multiple frames but would get moved or dragged away after more scans. QI mode involves taking force curves at a controlled trigger force so there should be smaller lateral forces than contact mode, however, based on the images in Figure 7.4 it appears that the tip is still able to move the cells from side to side.

The grid channels appear to be too wide for the cells with a width of approximately 1.5 µm due to the overexposure of the UV light. A new grid was fabricated to attempt to make channels that were narrower to give a width that is closer to the diameter of the cells. The same mask was used but the exposure time was reduced to avoid over exposure. It was also proposed that a wafer with some grooves that are closer together than those previously made (Figure 7.1) should be fabricated as it could potentially reduce the likelihood of cells being dragged away by the tip through one of the gaps in the grid. The other steps in the fabrication process are the same as the previous grid that was made.

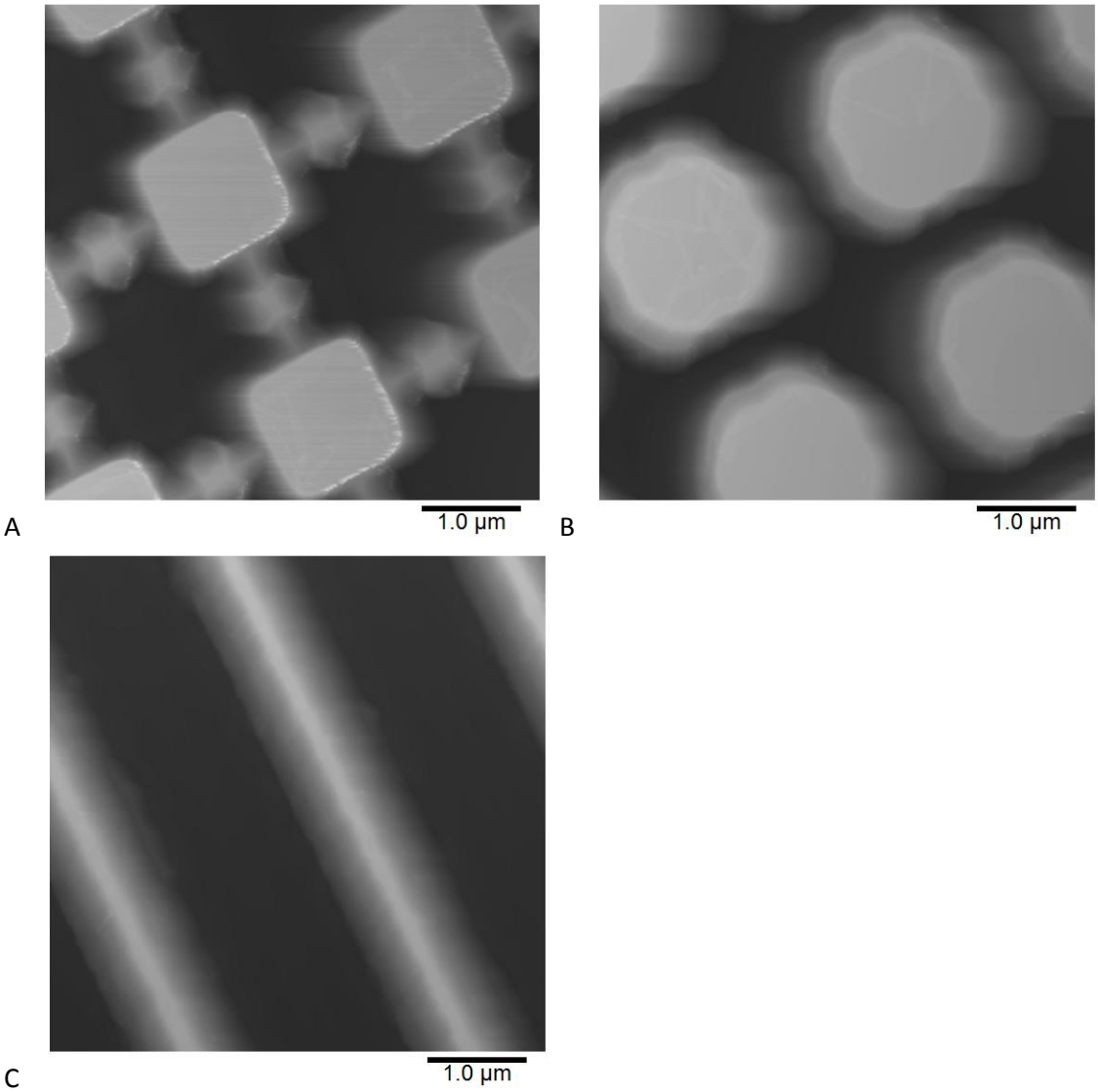

Figure 7.5- Topographic images of silicon that has been patterned by a process of photolithography. (A) is a topography image with a Z scale (black to white) = 1.2 µm. (B) is a topography image with a Z scale (black to white) = 1.4 µm. (C) is a topography image with a Z scale (black to white) = 1.2 µm.

Characterisation scans of the new grid showed some raised features in between some of the channels but other areas of grid that do not have the raised features. Figure 7.5(C) shows a set of channels that are approximately 2.5 µm wide which is the distance that corresponds to the period of the channels on the mask that was used. The method of fabricating the grids requires the photoresist to be exposed through the mask then the mask to be rotated 90° before a second exposure. The mask has a blank cross in the centre for alignment purposes which is the cause of these channels as the region was only exposed to the mask once due to the cross not lining up after it was rotated.

B. subtilis cells were added to the grid and imaged using the JPK Nanowizard3 Bio using QI mode MCLT-E in NB growth media with settings that allowed for higher pixel density images, sacrificing the validity of any force data that was being collected. The settings used were a large Z distance (600 nm) for the curves so that the tip was definitely lifting off the surface of the cells and so that the tip could travel the whole height of the grids which are approximately 800 nm deep. The speed of the imaging was adjusted to give a 256 x 256 image in about 10 minutes which caused the force curves in QI mode to sometimes include high levels of noise.

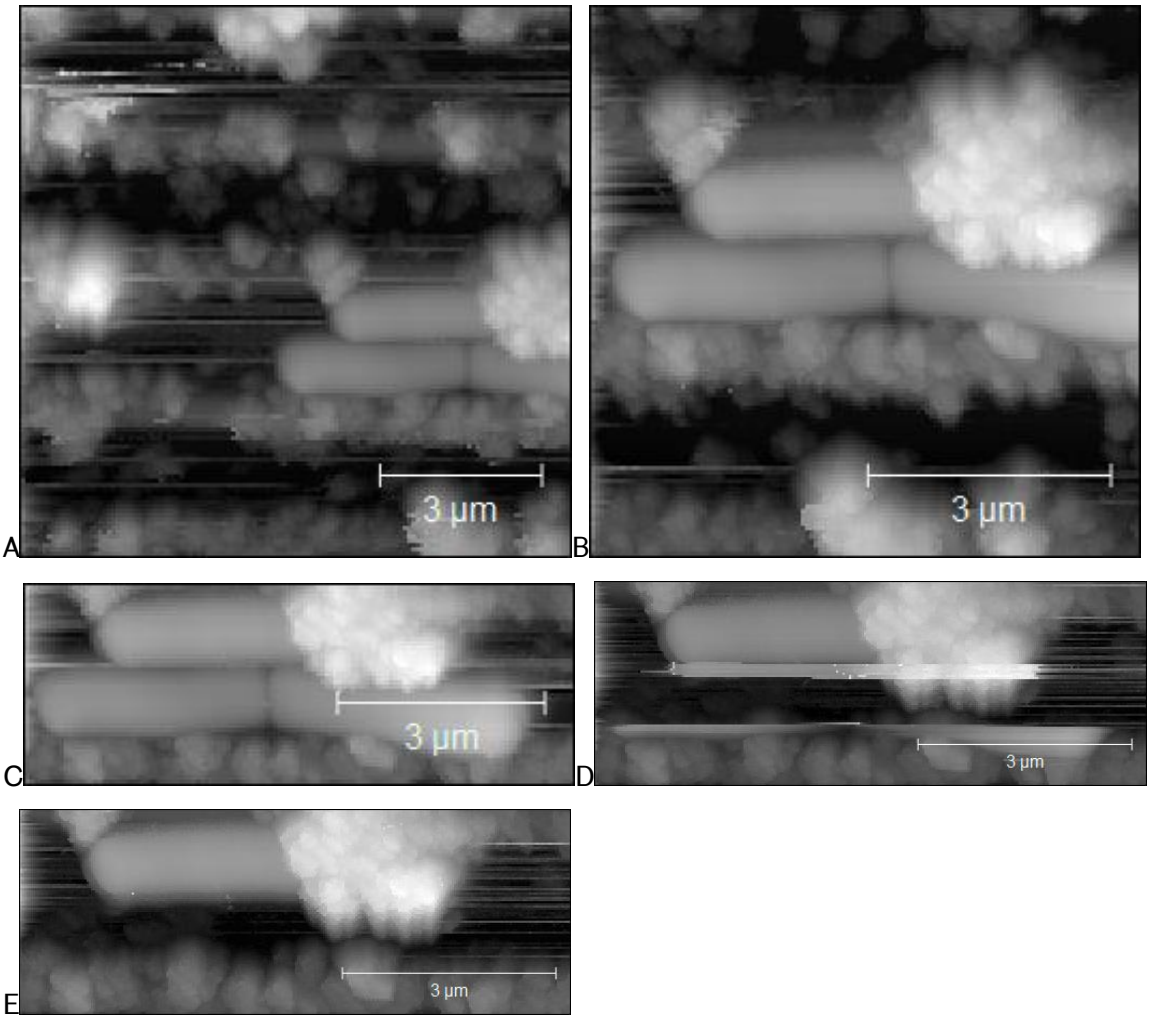

Figure 7.6- Topographic images of *B. subtilis* cells that are imaged in a silicon patterned trapping system in QI mode in growth media. (A) is a topography image with a Z scale (black to white) = 2.1 µm. (B) is a topography image with a Z scale (black to white) = 1.8 µm. (C) is a topography image with a Z scale (black to white) = 1.8 µm. (D) is a topography image with a Z scale (black to white) = 2.0 µm. (E) is a topography image with a Z scale (black to white) = 1.8 µm.

An area of the large grooves that were formed in small regions of the wafer, as described above, was imaged with some whole cells that had been trapped. In the Figure 7.6 there are three cells that look to be pinned down by some dirt that is present in the sample which allows the cells to be imaged without them moving too much. No architectural features are visible during this imaging session. Three complete scans of the cells were possible before the two bottom cells were dragged away by the tip, leaving the one cell that was more securely trapped by the dirt. The removal of the cells can be seen to occur in Figure 7.6(D). The images show that the grooves can be used to trap the cells but the trapping could actually be due to the dirt that seems to have pinned the cells in to the groove.

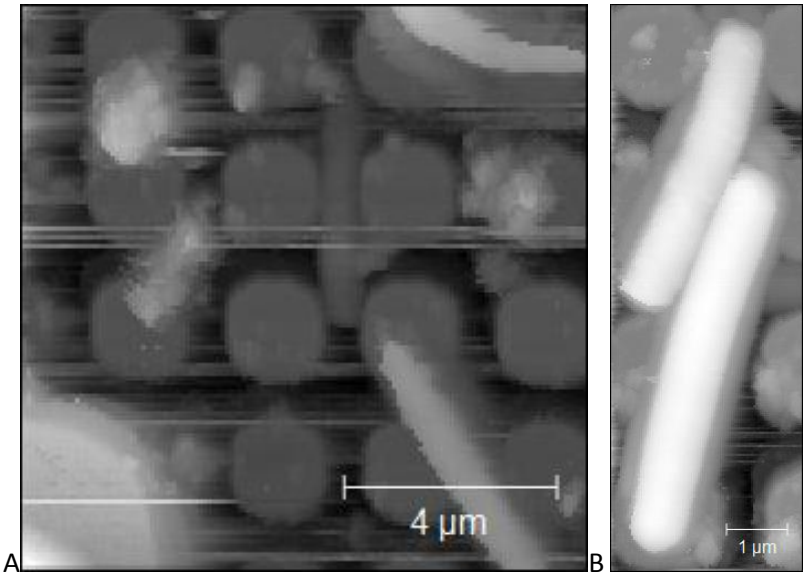

Figure 7.7- Topographic images of *B. subtilis* cells imaged with QI mode in liquid growth media. (A) is a topography image with a Z scale (black to white) = 2.8 µm. (B) is a topography image with a Z scale (black to white) = 1.6 µm.

Experiments using the silicon patterned with the grid were continued with some more whole cells being imaged. In Figure 7.7 multiple cells can be seen in Figure 7.7(B) including two cells that are sat on top of the grids as well as three that are in the channels. The cells that sat on the top of the grids were imaged over multiple frames, using similar settings in QI mode as Figure 7.6 with the aims of either seeing high resolution structural detail or seeing the cells in their division cycle. The fact that the cells were sat on top of the grid meant that they were not constrained which could have meant they were more likely to divide, however, after multiple frames there was no evidence of division events occurring in either cell. The cells were not dragged away during scanning even though they were sat on top of the grids which is unexpected when compared to the cells in

Figure 7.7 which we even pinned down by dirt and were dragged away. The reason for this apparent stability is unclear.

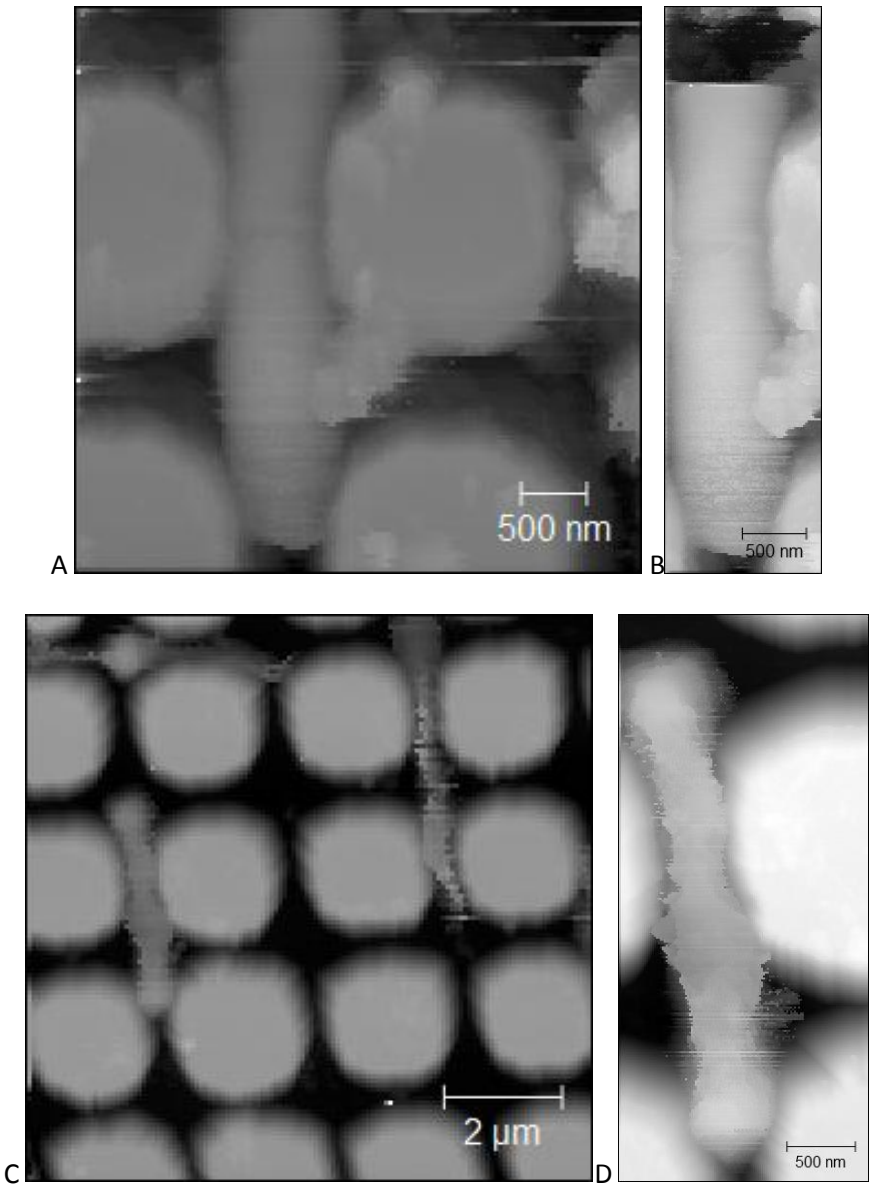

Figure 7.8- Topographic images of *B. subtilis* cells trapped in patterned silicon imaged with QI mode in liquid growth media. (A) is a topography image with a Z scale (black to white) = 1.9 µm. (B) is a topography image with a Z scale (black to white) = 1.2 µm. (C) is a topography image with a Z scale (black to white) = 1.7 µm. (D) is a topography image with a Z scale (black to white) = 1.1 µm.

Based on Figures 7.7 and 7.8 the refined grid pattern with narrower channels showed that it could be used to trap rod shaped cells in the right conditions, however, the set up was not consistently effective at trapping the cells tight enough or for long enough to stop them from being moved from side to side or from being dragged away by the tip.

Figure 7.8 shows a cell that is trapped and is being imaged in (A) then in (B) is dragged away by the tip even though only the end of the cell is not between the two raised pillars of the grid. This could also be due to the unsuitability of QI mode for imaging these samples at a resolution that can show structural features. If the cells are not unseated during imaging they are often being moved or there is a lot of noise in the imaging as seen in Figures 7.8 (C) and (D) which show cells that have streaks across the cell and shows a narrowing and widening artefact along the length of the cell as the tip has to climb the whole height of the cell when scanning along intersecting channels. Overall, the grid system combined with the use of QI mode on the JPK Nanwizard3 Bio did not allow for a trapping and imaging set up that could give structural resolution on the surface of the bacteria. QI mode outperformed contact mode, which was the imaging mode used for previous bacterial imaging on the Veeco Dimension 3100, when tested on the JPK Nanowizard 3 AFM. QI mode allowed for faster imaging and reduced lateral forces which actually allowed the *B. subtilis* cells to be imaged at a comparable resolution to the *S. aureus* images that had been taken previously in the group, however, the method did not give the architectural information that was desired.

Small amplitude tapping mode has been used successfully on the Bruker FastScan AFM using the FastScan-D probes and has allowed for high resolution images of the cell wall structure of *S. aureus* as can be seen in Chapters 4, 5 and 6. The aim of the *B. subtilis* work is to achieve a similar level of resolution to these images so a trapping method was required that could fully immobilise the rod shaped *Bacillus subtilis* cells.

Cell-Tak is a protein solution that has been used to functionalise surfaces to be able to immobilise bacteria previously [(Louise Meyer et al., 2010)]. It can be used to coat glass slide which the sample can then be added to, causing the whole cells to adsorb to the glass. This method has a disadvantage over a patterned silicon wafer because with the silicon the cells sit in a hole so the AFM cantilever does not have to travel the whole height of the cell for each scan, normally only a quarter of the height depending on the specifications of the patterned silicon.

A similar set up as the one used for the imaging of *S. aureus* was used initially to test how well the Cell-Tak worked on the rod shaped bacteria. A high salt buffer was used to resuspend the cells in as this was the buffer that was used to obtain the highest resolution *S. aureus* images. It was possible to see the *B. subtilis* cells on the surface of

the glass with the AFM optics, however, when scanned the cells were moved from side to side by the tip.

The high salt could be the cause of the lack of adsorption as the salt can reduce the strength of the charged surface by charge screening leading to the cells not being as attracted to the Cell-Tak coated surface. The lower attraction force could result in the cells being displaced more easily by the scanning of the tip. The experiment was repeated using deionised water as a buffer and with a similar concentration of cells added to the surface. There was a similar density of cells coating the surface as seen in the AFM optics but when scanned the cells did not move with the tip.

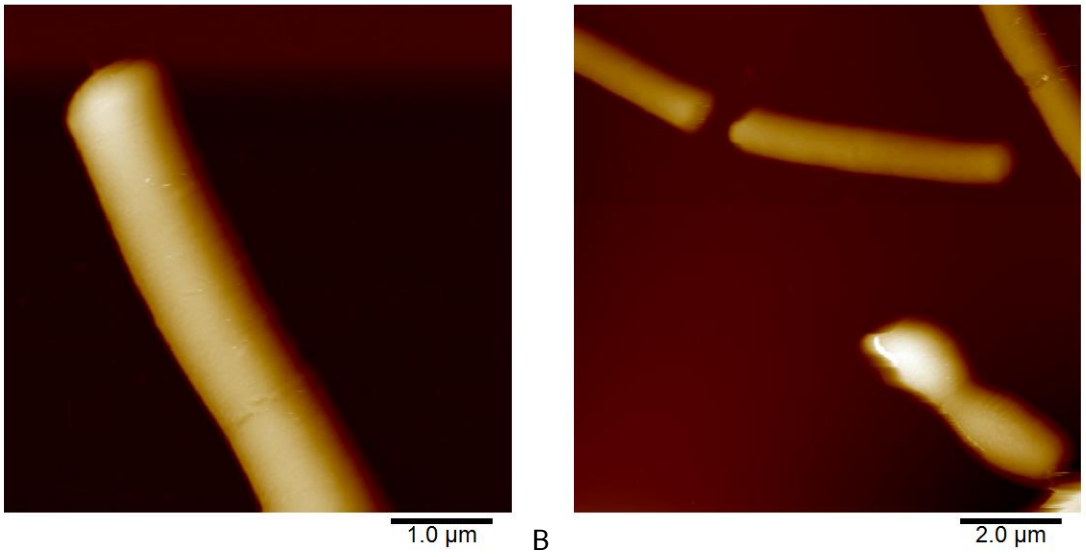

Figure 7.9- Topographic images of *B. subtilis* cells immobilised on a glass surface coated in in Cell-Tak while imaged using small amplitude tapping mode in deionised water. (A) is a 3rd order plane fitted topography image with a Z scale (dark brown to white) = 1.1 µm. (B) is a topography image with a Z scale (dark brown to white) = 1.7 µm.

Whole cells were imaged using small amplitude tapping mode without the same streaking that was seen in the QI mode imaging and the cells were not dragged away by the tip, even with repeated scanning as can be seen in multiple cases in Figure 7.9.

7.2- High resolution imaging of living *B. subtilis* cells using Cell-Tak.

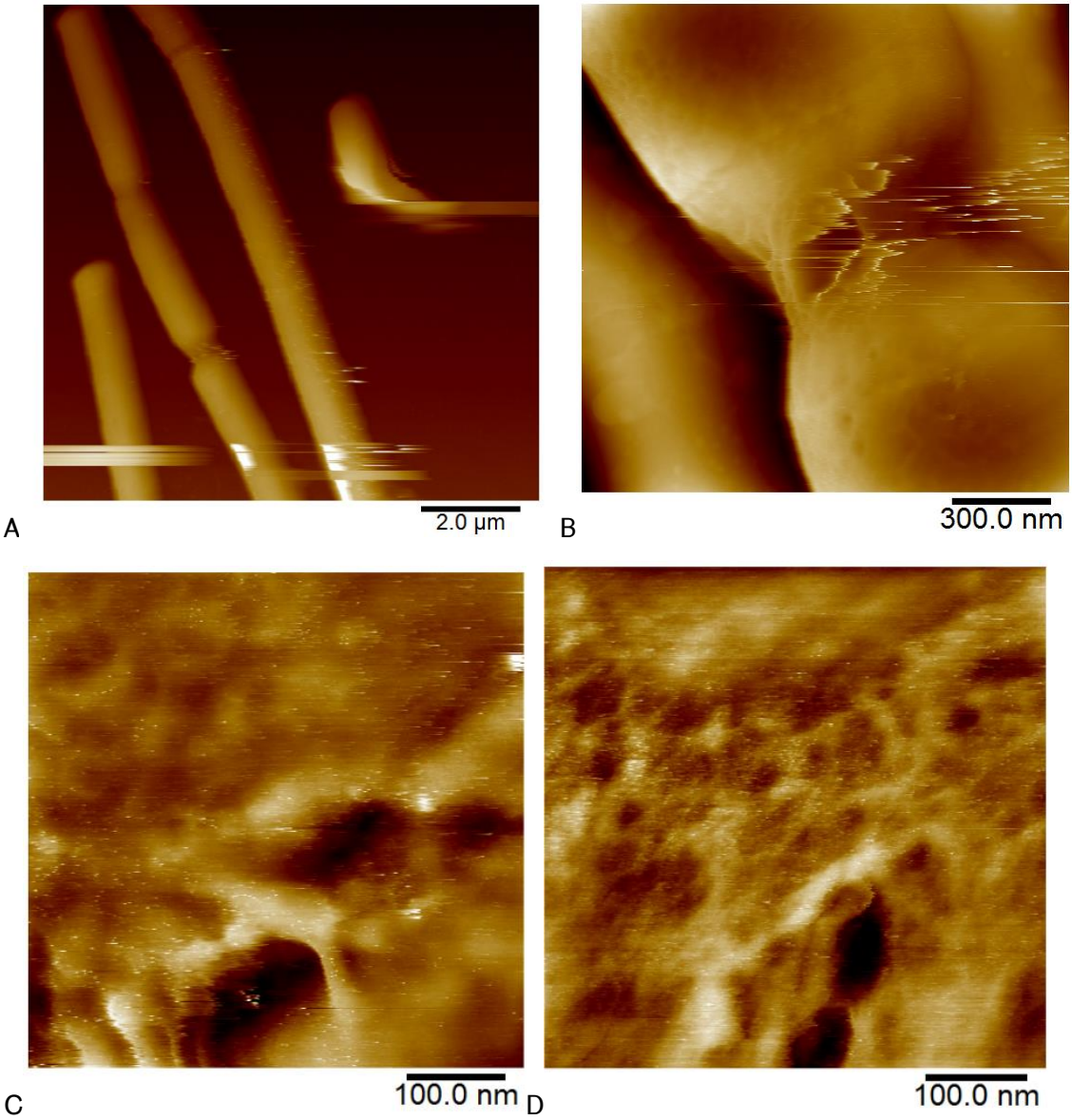

A B C D

Figure 7.10- Topographic images of *B. subtilis* cells immobilised on a glass surface coated in in Cell-Tak while imaged using small amplitude tapping mode in deionised water. (A) is a topography image with a Z scale (dark brown to white) = 2.2 µm. (B) is a 3rd order plane fitted topography image with a Z scale (dark brown to white) = 878 nm. (C) is a 3rd order plane fitted topography image with a Z scale (dark brown to white) = 87 nm. (D) is a 3rd order plane fitted topography image with a Z scale (dark brown to white) = 54 nm.

The ultimate aim of the imaging is to obtain the highest resolution images possible of the cells so high pixel density scans of features of interest like the septum were taken. There is evidence of some structure around the septa seen in the cell in Figure 7.10 (B) and the cell in Figure 7.10 (C) and (D) where some peptidoglycan architecture may be seen. In the

images there are fibres crossing the septum as the two cells have not fully separated. Figure 7.10(B) shows some clearer evidence of a structure, as some holes can be seen away from the poles of the cell. The structure does not appear to run circumferentially as had been theorised but looks closer to the structure seen in the high resolution images of *S. aureus* from Chapter 6. At the poles there appears to be a dividing line on both cells that could indicate a boundary of two distinct structures on the cell. It is not possible to resolve structure of the polar region partly because this is the area of the cell that has the highest slope, to image the pole the cells would need to be oriented so the cells are standing on end. Between the two cells there are some strands that are bridging between the two poles which are similar to the features seen in Figure 7.10 (C) and (D). The separation of the two cells will be complete when all of the bridging strands have been broken. In *S. aureus* there is a similar phenomenon of bridging strands across the two halves of the dividing cell that are broken apart in stages.

The Cell-Tak immobilisation seems to work better under low salt conditions while the high resolution imaging has had best results when in higher salt conditions. If the cells are in deionised water there is no control in the buffer for the pH which means there could be large changes over time in the imaging that could affect the cells. Using a low concentration of a Tris buffer means the pH can be controlled while keeping the salt levels low. A pH of 7.8 was chosen as it is the same as the pH that was used for the similar *S. aureus* experiments.

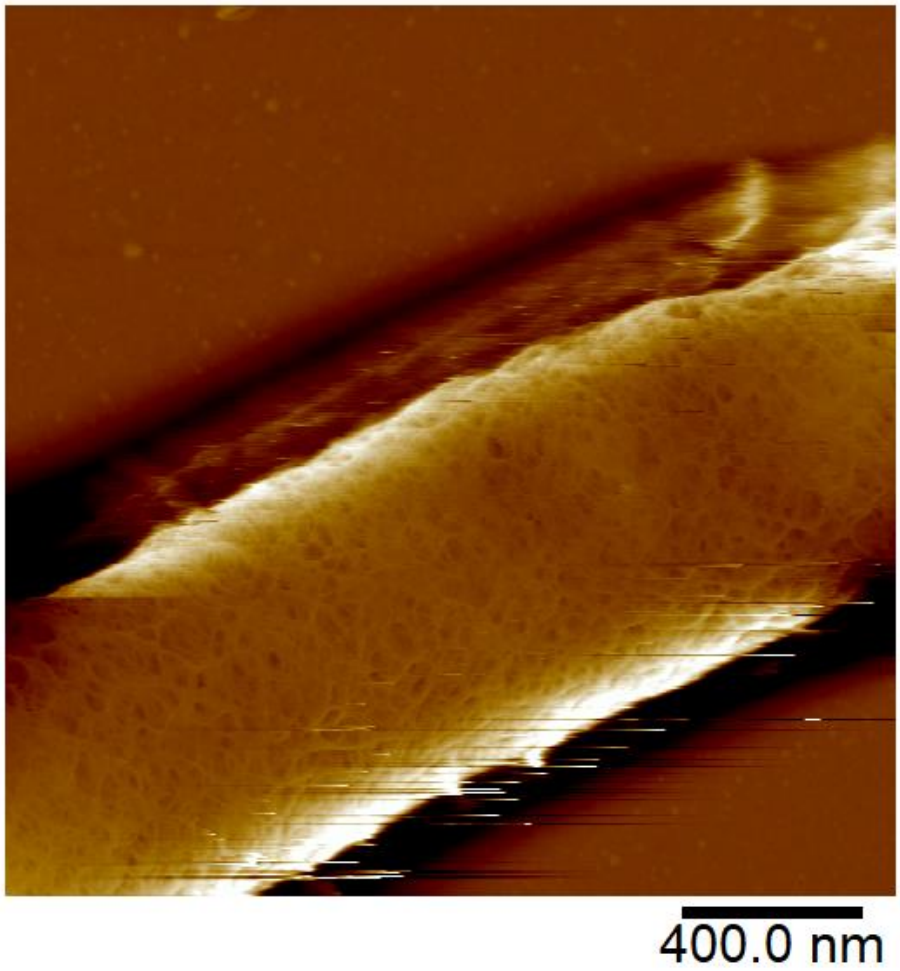

Figure 7.11- A *B. subtilis* cell adsorbed to a Cell-Tak covered glass surface, imaged with small amplitude tapping mode. The image is a high pass filtered topographic image with a filter size = 996 nm.

The experiment was set up in the exact same way as with the water experiment except a 5 mM Tris buffer at pH 7.8 was substituted in. It was possible to see a good sample surface coverage of the cells in the optics of the AFM. Whole cells were imaged without dragging away or shaking any of the cells. A large scale scan of a cell was taken that showed structural features that are similar to those seen in the mature architecture of the *S. aureus* peptidoglycan. The cell from Figure 7.11 was zoomed in on with images taken along the length of the cell.

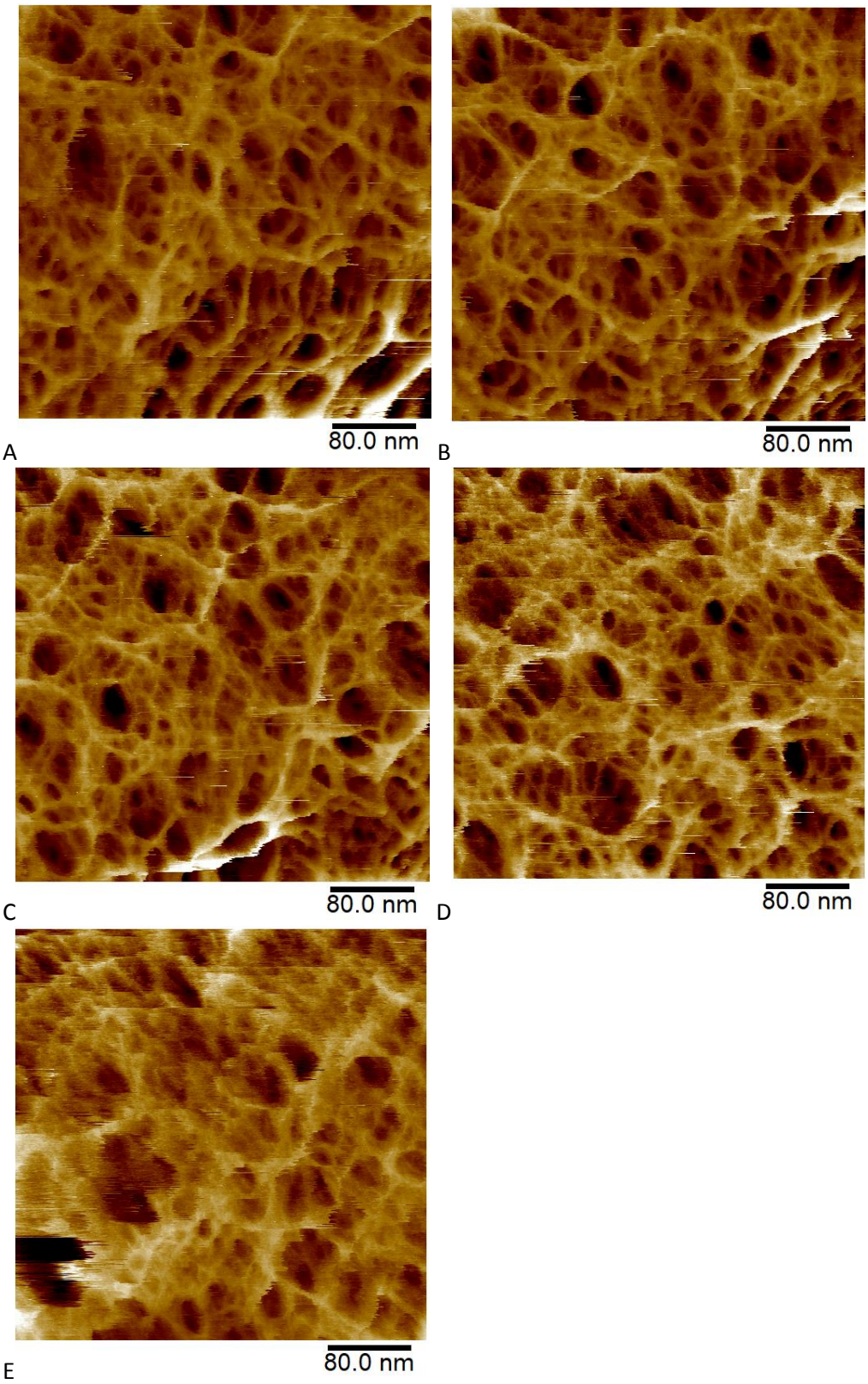

Figure 7.12- Zoomed images taken along the long axis of the cell in Figure 7.11. All are 3rd order plane fitted topographic images. (A) has a Z scale (dark brown to white) = 36 nm. (B) has a Z scale (dark brown to white) = 33 nm. (C) has a Z scale (dark brown to white) = 29 nm. (D) has a Z scale (dark brown to white) = 23 nm. (E) has a Z scale (dark brown to white) = 40 nm.

The smaller images give high resolution details of the surface and show that there appears to be similar structural features to the peptidoglycan as there were in the *S. aureus* images, including the same holes within the cell wall layer and an overall lack of circumferential orientation to the glycans.

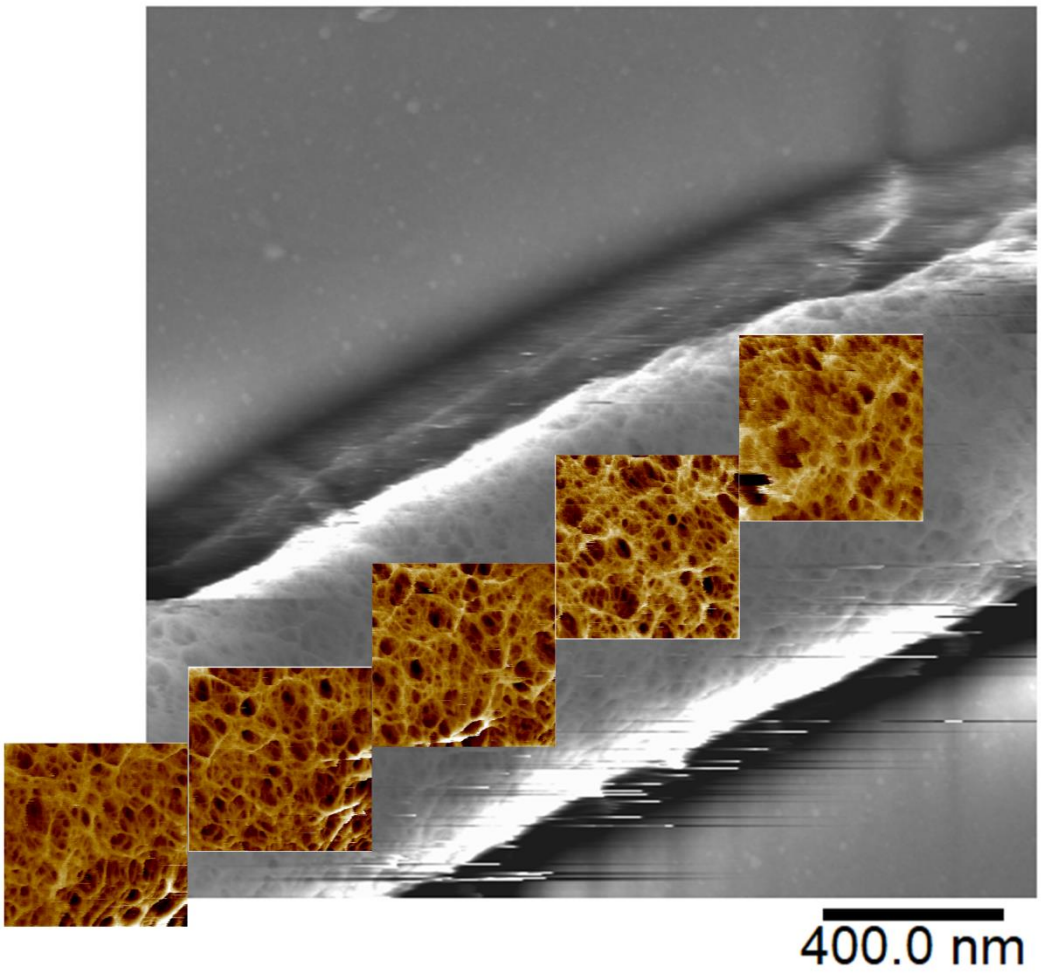

Figure 7.13- A composite image of Figure 7.11 with the individual images from Figure 7.12 overlaid on top in the correct locations.

The smaller images have been overlaid to show their position on the Figure 7.12 and indicate that there does not seem to be substantial heterogeneity to the structure along the length of the cell, except possibly at the poles which could not be probed with the cells in this orientation. There has previously been evidence from the inner cell wall of a thick banded structure that is formed circumferentially along the long axis of the cell [(Hayhurst et al., 2008)] with some glycan strands that are longer than the length of the whole cell. There were none of these extremely long glycan strands seen in these experiments but it is possible that some of the strands that make up the mesh structure could be this length and are running around the whole circumference of the cell or fold

back on themselves following a convoluted path. There appears to be more branching points and holes than the model of the inner cell wall structure suggests. The model for the outer surface of *B. subtilis* was not as well defined based on previous data [(Hayhurst et al., 2008)], however, it had not been thought to be similar to the mature structure of the outer wall of *S. aureus*.

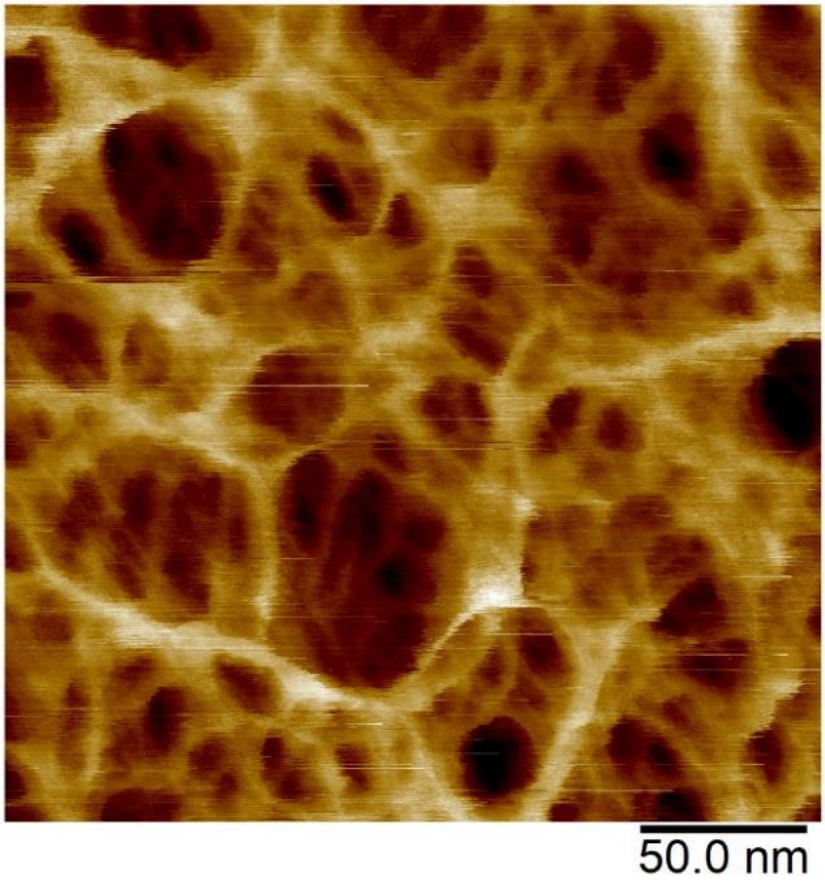

Figure 7.14- High resolution topographic image of a region on the cell from Figure 7.11. The 3rd order plane fitted image has a Z scale (dark brown to white) = 20 nm.

In Chapters 4, 5 and 6 there was a focus on achieving molecular resolution images of the cell wall surface which is also an aim with the *B. subtilis* cells. These images could then be used to compare analysis parameters calculated from both bacteria. 250 x 250 nm images were taken to match those that were analysed for *S. aureus* at the same pixel density of 1024 x 1024 px images. The area in Figure 7.15 seemingly shows no general orientation to the peptidoglycan and shows that there are some smaller deep holes within large holes.

7.3- Method for imaging the poles of the rod shaped *B. subtilis* cells.

In Figure 7.10(B) there appears to be a line close to the end of the cell that marks the pole of the cell. During imaging of the rod shaped cells it was not possible to resolve the structure of this region, possibly due to the gradient of the ends of the bacteria which is difficult to track with the AFM. Dr Seamus Holden (Centre for Bacterial Cell Biology, Newcastle University) studies the localisation of FtsZ in *B. subtilis* using TIRF microscopy [(Bisson-Filho et al., 2017)]. The group uses holes made of agarose to trap the *B. subtilis* cells with the poles facing up for the fluorescence microscopy. Using the same silicon master as the Holden group the pattern was cast into agarose to create the columns that the *B. subtilis* cells should sit in.

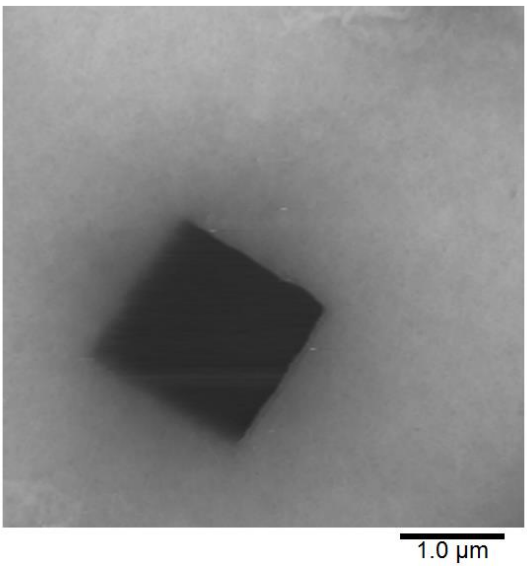

Figure 7.15- Small amplitude tapping mode scan of an agarose hole imaged in 5 mM Tris. The topographic image has a Z scale (black to white) = 977 nm.

The method of trapping the cells was attempted with the aim of imaging the poles of the *B. subtilis* cells. No cells were seen in the holes despite the cells being visible on the surface of the agarose in the AFM optics. The lack of success when trapping for AFM imaging could be due to the addition of a glass cover slip in fluorescence imaging which might stop the cells from escaping the *B. subtilis* holes. Or could be due to the media used as some successful experiments using this technique used a minimal media instead of the nutrient rich media used here. Minimal media discourages the formation of long chains of cells.

7.4- Analysis of *B. subtilis* peptidoglycan

Bearing analysis was used on the *S. aureus* images to obtain quantitative information about the depth and density of the holes seen within the mesh like structure. The peptidoglycan seen in the *B. subtilis* cells is comparable to the mesh structure so the same analysis technique was performed. Two images were chosen that had the same scan area, pixel density and were taken using the same imaging technique with the same experimental set up apart from the imaging buffer. The *S. aureus* image (Figure 6.12) was taken in a high salt buffer (300 mM KCl, 10 mM Tris, pH 7.8), while the *B. subtilis* image was taken in a low concentration of Tris (5mM Tris, pH 7.8).

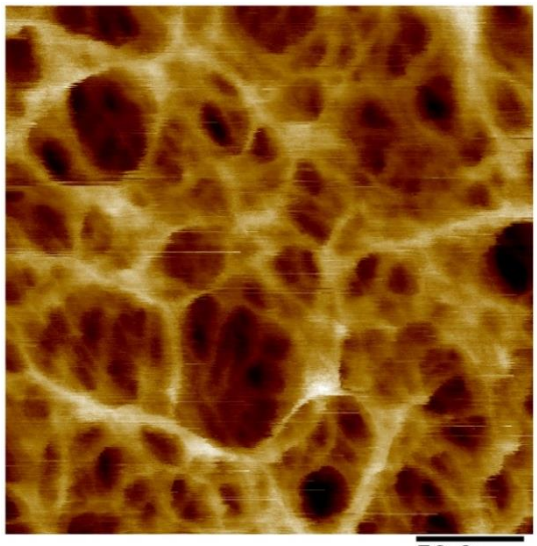

A

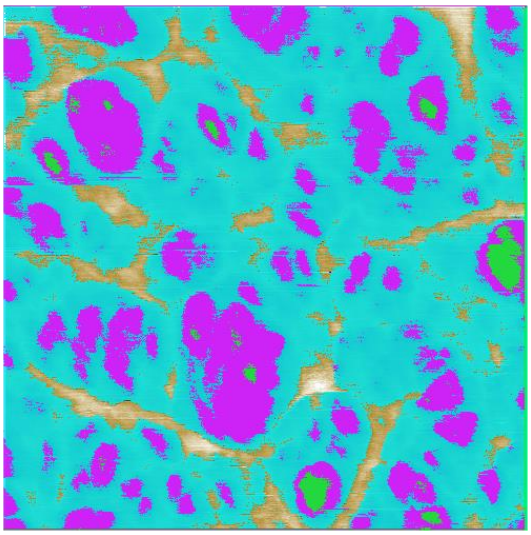

B

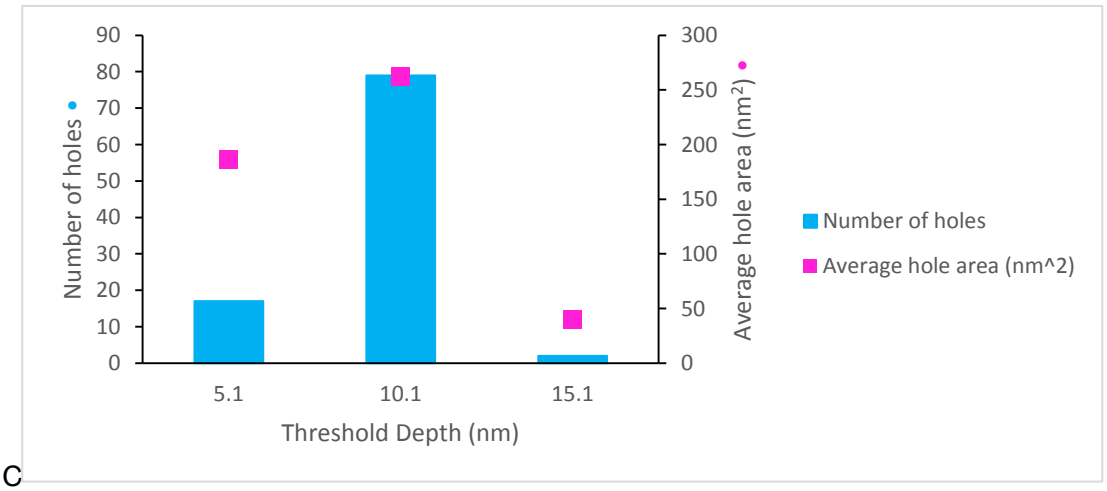

C

D

Threshold Depth (nm)	Number of holes	Average hole area (nm^2)	Total area (nm^2)	% hole coverage
5.1	17	46.60	792.25	1.28%
10.1	79	65.66	5186.75	8.35%
15.1	2	10	20	0.03%

Figure 7.16- Bearing analysis for *B. subtilis* of cell imaged in Figure 7.14. (A) is the original topography image, (B) is the final composite bearing image with all of the bearing heights laid over each other. Scales for (B) from the bottom up. First 5.1 nm (1% of the total area) = Light Green, 5.1-10.1 nm = Light Blue, 10.1-15.1 nm = Purple. Above 15.1 nm= Gradient from Brown to White (low to high). (C) is a graph showing the number of holes and the average hole size at each bearing depth. (D) is a summary table of the number of holes, average hole area, total area at the bearing depth and the percentage of hole coverage with new holes that have appeared in that depth range.

The first slice was taken at the histogram height corresponding to the depth at which only 1% of the area of the image was covered or in other words the deepest 1%. This decision was taken to try to exclude the long tail of the histogram in the analysis that gives a false impression of the thickness of the cell wall. Slices were taken every 5 nm up from this height. Figure 7.16 shows relatively few deep holes compared to the Figure 7.17. There were fewer holes across all heights in the image of *B. subtilis*, though this could be partly due to worse resolution in this image than in the image of *S. aureus* which could mean smaller holes may not be seen when imaged. The total height of the image or the thickness of the cell wall that was measured was thicker in *S. aureus* than in *B. subtilis* with a 1-99% histogram height difference of 13 nm for *B. subtilis* and 19 nm for *S. aureus*. Of the 6 *S. aureus* images (Figure 6.8-6.12 and 6.14) that were analysed using this technique, this image had the smallest value for the 1- 99 % height difference and on average *S. aureus* had a 26 nm height difference. This value is not actually the cell wall thickness; it is the depth in the topography of the cell that the AFM imaged. There is no way of knowing how deep into the total thickness of the cell wall the AFM is imaging as it only measures the topography on the top of the cell. The smaller "thickness" value for *B. subtilis* could be a real effect that the holes are not as deep as in *S. aureus* or it could be that the AFM imaging did not allow for the tip to image in some of the deeper holes.

To find an average of the "thickness" for *B. subtilis* the individual images that were taken in the overlay image in Figure 7.13 along the length of the rod shaped cell were analysed to calculate their 1-99% height difference.

Images from Figure 7.12	1- 99% height (nm)
A (far left on overlay in 7.13)	22.65
B	19.25
C	17.95
D	14.62
E (far right on overlay in 7.13)	24.46
Average (including Figure 7.16)	**18.82**

Figure 7.17- Summary table of 1-99% height differences for *B. subtilis* images

They were shown to all have greater 1-99% heights than Figure 7.16 but still had a smaller average height than the average value for *S. aureus*. The average heights for *S. aureus* and *B. subtilis* are not necessarily an accurate measure of the thickness of the cell wall due to the differences in image size and pixel density as well as surface curvature. For the five values in Figure 7.17, the image size and pixel density were all the same (400 nm, 512 px) but there is still a variation in the height measured. This could be partly due to individual features in the scan region for example in Figure 7.12(E) (far right) there is a large hole in the bottom left corner of the image. A large hole gives the tip a greater chance of imaging to the bottom of the hole as the feedback system does not need to alter the height as much and there is less chance of the sides of tip hitting a tall feature before the end of the tip hits the bottom of the hole. Another factor that could affect the height measurement is curvature of the cell and how well the curvature can be removed by plane fitting. The imaging was performed on a whole rod shaped cell which has different surface gradients in the different images so the plane fitting could be slightly different for the different cells. The five images that were taken along the cell were all on the same cell in the same conditions and produced slightly different values for the height difference so there can be variation along a cell let alone between different cells that were imaged on different days.

The thickness of the *B. subtilis* cell wall is reported to be 20-40 nm [(Ojkic et al., 2016)] thick so these measurements show that the tip is imaging anywhere from half to the whole depth of the cell wall thickness, as was seen in *S. aureus*. The structure of the cell wall of *B. subtilis* from the previous model was a partially digested architecture that had

lost the banded structure that is seen on the inside of the cell wall. The structures that are seen in these images have holes that were not predicted from previous data that could have some nutrient transport function. The existence of the banded structure on the inside of the cell wall as reported by [(Hayhurst et al., 2008)] has been questioned by [(Beeby et al., 2013)], however, if they do exist then there has to be some currently unexplained mechanism for the turnover and the degradation of the cell wall as it is remodelled from the banded structure into the mesh like structure that is seen in these images. There is a similarity between the mature structure of the *S. aureus* and the outer wall structure of *B. subtilis*. The outer wall structure is also the mature structure as the peptidoglycan is added on the inner side of the cell wall. There could be a link between the two mature structures that are seen in *B. subtilis* and *S. aureus* with the mesh like structure provides the cell with some benefit like improved transport of nutrients or it could be the most stable structure.

7.5- *B. subtilis* fibre width analysis

For *S. aureus*, fibre widths were measured from the mesh architecture to calculate an average glycan fibre width. Using the high resolution image of *B. subtilis* that was also used to perform the bearing analysis in Figure 7.16, the same calculation can be made. The mean and median fibre widths were calculated and used to give an estimate of the crosslinking using the value for the *S. aureus* glycan-glycan distance as measured by NMR of 2.3 nm [(Kim et al., 2015)].

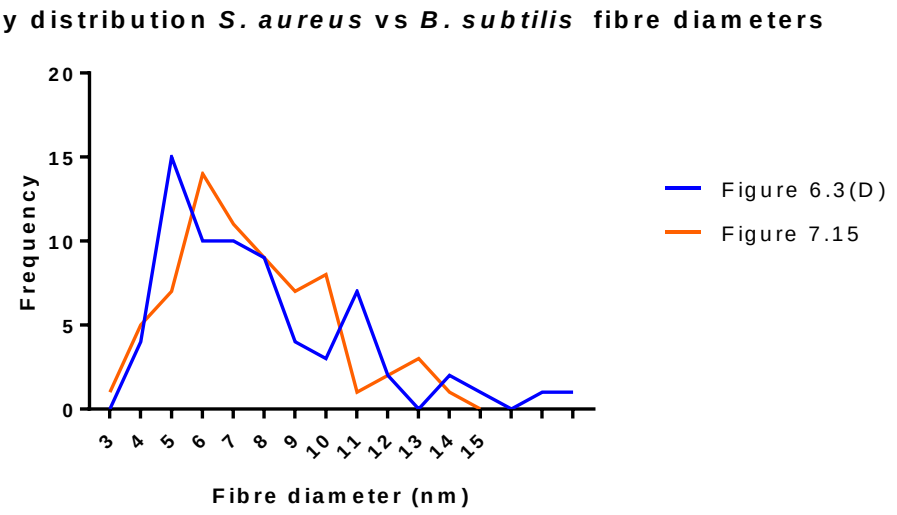

7.18- Histogram showing the frequency distribution of fibre diameters of *S. aureus* (Figure 6.3(D)) and *B. subtilis* (Figure 7.15).

The mean diameter of the *B. subtilis* fibres was measured to be 7.5 ± 2.4 nm with a median value of 7.2 nm compared to a mean value of 6.8 ± 3.1 nm and median of 6.1 nm for *S. aureus*. From the histogram it shows a broadly similar distribution to *S. aureus* with a peak at shorter fibre diameters and a longer tail towards thicker fibre widths. The thicker fibres could be caused by the inability to resolve some features with the tip, for example, two fibres close together could appear as a single thicker fibre.

Using the NMR value of 2.3 nm from glycan to glycan for *S. aureus* as an approximation for the glycan separation distance in *B. subtilis*, this gives a mean glycans per peptidoglycan fibre of 3.3 and a median value of 3.1. These are similar to those calculated for *S. aureus* of 3 and 2.7 for the mean and median respectively for the Figure 6.12 in the histogram and between 2.7 and 4 for the averages calculated for the three images that were analysed using this technique, as can be seen in Section 6.2.2.

The smallest fibre width measured in the *B. subtilis* image was 3.4 nm in diameter compared to 2.7 nm in the *S. aureus* image. These measurements, especially the small features like a single glycan strand, are subject to tip broadening where the tip shape causes the features to appear wider by some unknown amount due to the way it interacts with the small surface feature. It is believed that these narrowest fibres measured are single glycans in both *S. aureus* and *B. subtilis* and they are shown to have similar diameters.

To calculate a theoretical value for the maximum crosslinking percentage of the peptide bonds in the peptidoglycan based on the fibre widths that were measured in the high resolution images, a similar method can be used as in Chapter 6 for *S. aureus*. The glycan chains in *B. subtilis* are believed to be arranged in an anti-parallel manner rather than the parallel organisation seen in *S. aureus,* so the values are being reported as a hypothetical maximum crosslinking percentage. These averages for *B. subtilis* result in maximum crosslinking percentages of 69 and 68% for the mean and median values respectively. From the NMR data, *B subtilis* is reported to have a theoretical maximum cross-linking percentage of 50% due to its anti-parallel stem architecture [(Kim et al., 2015)].

7.6- Discussion and conclusions

Experiments were performed to try to emulate the success of the immobilisation method that has been developed for *S. aureus* but now for *B. subtilis*. The same physical trapping technique was developed with various iterations of silicon wafers with a grid system

designed to allow the rod shaped cells to lie in the holes for scanning by AFM. Firstly, using contact mode and then QI mode on the JPK Nanowizard 3 AFM, these grids showed some limited success at being able to trap the whole cells in the grid, however, the use of these imaging modes along with the etched silicon did not produce the AFM images that gave structural resolution of the peptidoglycan.

The use of small amplitude tapping mode on the Bruker FastScan AFM has produced structural resolution images of the peptidoglycan cell wall structure in *S. aureus* (Chapters 4,5 and 6) so this was combined with the use of Cell-Tak to trap the whole cells on a glass surface. It had previously not been thought that the AFM imaging would disrupt the cells on the surface without some physical constraint but work by Dr Sandip Kumar [(Kumar et al., 2017a)](Hobbs Lab, Physics, University of Sheffield) and work on imaging BtuB proteins that is discussed in Chapter 8 showed that the imaging technique allows for high resolution and low lateral force imaging on highly curved, soft samples.

Optimising the imaging buffer was a key step in the efficacy of the Cell-Tak being able to immobilise the cells on the glass. Initial experiments used the same high salt buffer that had proved successful in imaging the *S. aureus* cells, however, when tested on the Cell-Tak, the cells were easily moved by the tip. The best results came when using a 5 mM Tris buffer at pH 7.8. At high salt there is more charge screening that disrupts the attraction between the Cell-Tak and the cell wall.

Using the Cell-Tak it was possible to image whole *B. subtilis* cells without them being moved by the tip including taking some images at high resolution that showed a mesh like structure that resembled the mature structure that was seen for *S. aureus*. The previous model for the outer cell wall structure of *B. subtilis* was just of a partially hydrolysed structure [(Hayhurst et al., 2008; Turner et al., 2014)], possibly with the indication of the banded circumferential structure that has been imaged on the inner wall of the cell. There did not appear to be an overall orientation to the strands which might have been expected considering the peptidoglycan in *B. subtilis* is inserted in bands that run circumferentially [(Tiyanont et al., 2006)].

One cell was imaged with high resolution in a large area scan then smaller scans were taken along the cell length (Figure 7.13) to probe whether there is a difference in structure at any point along the length of the cell which there did not look to be. The only evidence of a different structure came when attempting to image the poles of a cell in Figure 7.10. A line around the pole shows a possible boundary between two architectures.

An experiment was performed using a trapping method that has been successfully used to trap *B. subtilis* cells for TIRF microscopy [(Bisson-Filho et al., 2017)] though it did not trap any cells in the sessions it was tested with AFM. One major reason for this is likely to be the fact that a cover slip is laid on top of the cells when they are put in the holes for TIRF imaging but this is not possible with AFM as the glass would block the access for the tip. It is important to understand the structure of the cells at the poles to be able to build a complete model of the peptidoglycan structure for the whole *B. subtilis* cell.

A set of analysis techniques were devised to extract physical properties and information from the high resolution *S. aureus* images. Since the structures in *B. subtilis* resembled the structures seen in *S. aureus*, the same analyses were used on the *B. subtilis* data. The bearing analysis was performed on Figure 7.15 as it had the best resolution of the images of *B. subtilis*. This was then compared to the bearing analysis data for *S. aureus* from Chapter 6. For this particular image (Figure 7.15) the *B. subtilis* had a smaller overall height or depth to the cell wall material of 13 nm compared with the lowest value measured in *S. aureus* bearing analysis of 19 nm.

Comparing the average 1-99% heights of all of the high resolution images of *S. aureus* and *B. subtilis* gave values of 26 nm and 19 nm respectively. The depth of the *S. aureus* cell wall could be greater due to the tip being unable to image as deep into the *B. subtilis* architecture or it could be that there is an architectural difference. If the *B. subtilis* peptidoglycan is inserted as a banded circumferential structure on the inner cell wall then the peptidoglycan at deeper depths may not be as porous as *S. aureus* all the way through the thickness of the cell wall, resulting in the reduced depth that is measured. Peptidoglycan in *B. subtilis* is also continuously added along the inner cell wall to enable elongation of the cell, whereas there is only a small amount of additional synthesis in *S. aureus* away from the growing septum meaning the peptidoglycan deep in the *B. subtilis* cell wall is continually replenished. The *B. subtilis* hole sizes were measured to be larger on average though this may be due to the lower resolution of the image resulting in some smaller holes within holes being missed.

Overall the porous mesh like structure was not predicted and the existence of these deep holes that can extend beyond 20 nm deep into the cell wall raise interesting questions as to the function of the holes and how this architecture is created. The banded structure that has been seen on the inside surface of the cell wall may be

degraded as the new peptidoglycan is inserted and the cell wall is cycled, forcing peptidoglycan to be pushed towards the outside of the cell.

A fibre width analysis was performed on Figure 7.15 and compared to the data collected from all of the *S. aureus* fibre width analysis. The results showed a similar distribution of fibre widths as measured for *S. aureus* including the presence of what could be single glycan chains. The theoretical maximum crosslinking percentage was calculated for *B. subtilis* and then compared to the same values that were calculated for *S. aureus*. This calculation showed a similar value of the maximum crosslinking percentage to *S. aureus* with the assumption that there is all of the available crosslinks are formed and that there is a glycan to glycan distance of 2.3 nm which is the value that has been measured for *S. aureus* [(Kim et al., 2015)]. This is clearly a false assumption but, given the similarity of the distribution of fibre widths, it can give and idea for the density of glycans in the fibres. The maximum crosslinking percentages were calculated to be 68 and 67% for the mean and median respectively. It has previously been reported that *B. subtilis* has an anti-parallel glycan orientation which is not the same glycan orientation as *S. aureus* and means there is a theoretical maximum crosslinking density of 50% for *B. subtilis*.

The silicon trapping system that has proven to be effective in *S. aureus* (Chapters 4, 5 and 6) were not as effectively developed for *B. subtilis* as a pattern was not found that could effectively trap the cells for stable, prolonged imaging by AFM. Developing a general physical immobilisation technique for rod shaped bacteria would allow for many more species of bacteria to be imaged. In future work an effective method of trapping the cells could involve using a different material for trapping like agarose. A physical immobilisation technique could also allow the cells to be imaged during a dynamic process like growth and division, allowing for the probing of how the organisation of the peptidoglycan changed during the division such as the elongation of the cell and then the formation of the septum.

The architecture along the main length of the cell has been seen in high resolution but the poles of the cells, which appear to have a different architecture (Figure 7.10(B)), have not been imaged at high resolution. Continuing to adapt the method of imaging the rod shaped cells standing vertically in holes for AFM would allow the poles of the cells to be imaged at a similar resolution to the rest of the cell, completing the model of the cell wall architecture of *B. subtilis*.

Different mutant strains of *B. subtilis* could be imaged (as was done for *S. aureus* in Chapter 4) to probe what different genes have an effect on the peptidoglycan organisation at a molecular scale.

Chapter 8- Imaging the *E. coli* protein BtuB in lipid membrane vesicles

Developing methods for AFM imaging of living bacterial cells that can still undergo biological processes will enable these dynamic systems to be studied at high spatial resolution and with high temporal resolution. Proteins are important for all types of living organisms as they perform a wide variety of functions. Bacteria have a vast set of proteins that are critical for their survival with some being common among many species and some that have evolved particularly for that species.

For bacteria to thrive they must receive a constant supply of nutrients. In Gram negative bacteria there is an outer membrane that these molecules and ions must pass through while in Gram positive bacteria there is no outer membrane. Small molecules at high concentration can diffuse through porin channels in the outer membrane but for larger molecules (>600 Da), that are present in low concentrations, specialised transport systems are needed [(Krewulak and Vogel, 2011)].

To begin to understand the processes that proteins can perform in living bacteria it is important to be able to image them and understand their structure which can be done in an *in vitro* set up before applying the same techniques to *in vivo* samples. By imaging proteins in lipid membranes and understanding how they interact with other proteins, as well as the best techniques to image them, a method for imaging the proteins in the living cells can be developed. This chapter will focus on imaging one of these transporter proteins, BtuB, which is involved in transporting vitamin B12 into *E. coli* cells. The X-ray structure of BtuB has been determined to a resolution of ~3 Å so the AFM experiments are not to find the structure of the protein but rather to see how the protein sits in a lipid membrane, conditions that are closer to its natural environment, and to try to resolve the different domains of the protein [(Chimento et al., 2003)].

8.1- BtuB- the vitamin B12 transport protein in *E. coli*

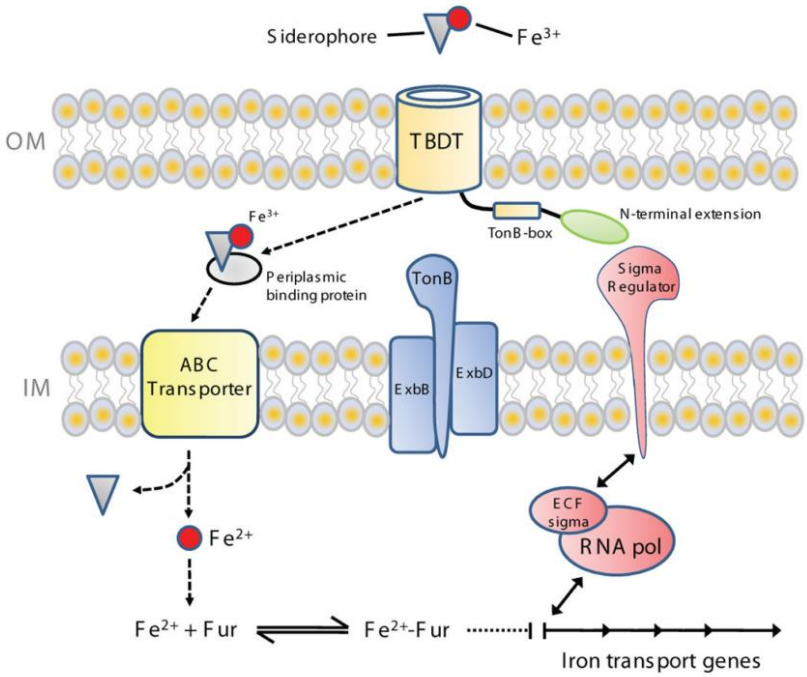

Figure 8.1- Schematic of how TBDTs sit in the membrane relative to the TonB complex. Reproduced from [(Noinaj et al., 2010)].

There is a group of nutrient transporting outer membrane proteins called TonB Dependent Transporters (TBDTs) that all require the presence of an inner membrane protein TonB, which is shown in the schematic in Figure 8.1 in complex with ExbB and ExbD proteins which act as a scaffold [(Jana et al., 2011)] for the TonB and allow it to use the proton motive force [(Fischer et al., 1989)]. The outer membrane has no way of powering the transport mechanisms without coupling to inner membrane proteins [(Hickman et al., 2017)]. TBDTs all have the conserved genetic sequence called a "TonBox" which is the part of the protein that interacts with the TonB during the active transport cycle. BtuB is a TBDT that is responsible for transporting vitamin B12 into the cell. It has two domains; a 22 stranded β barrel and a hatch or plug which is a globular domain. The outer diameter of the barrel is ~4 nm [(Chimento et al., 2005)] and acts as the pore through which the vitamin B12 can pass; the TonBox part of the protein is situated near the periplasmic opening of the barrel. When BtuB is not bound to a vitamin B12 substrate the hatch blocks the barrel so the nutrient channel is closed but when vitamin B12 is bound, the TonBox will change its relative position, allowing it to interact with TonB, causing a conformational change (seen in Figure 8.2) in the plug domain so the vitamin B12 can pass through the pore and through the outer membrane. [(Hickman et al., 2017),

(Gumbart et al., 2007), (Chimento et al., 2003, 2005), (Shultis et al., 2006), (Lathrop et al., 1995), (Noinaj et al., 2010), (Krewulak and Vogel, 2011)]

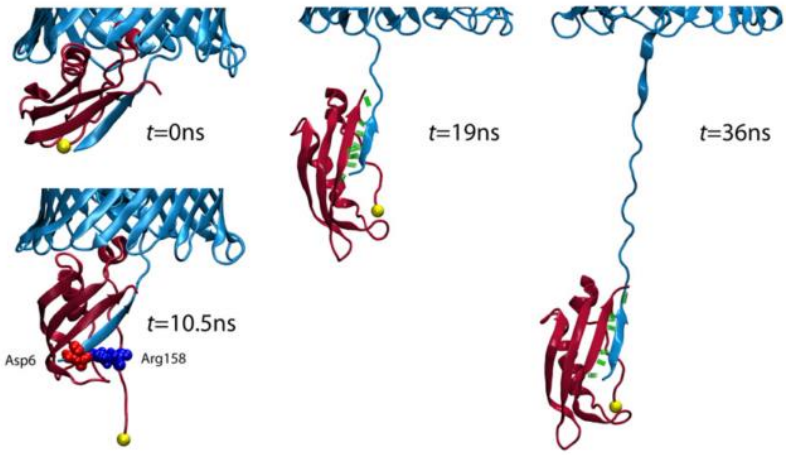

Figure 8.2- Steered Molecular Dynamics (SMD) Simulation showing the interaction between TonB and the TonBox of BtuB during its conformational change. BtuB is shown in light blue, TonB is shown in red and the yellow sphere marks the atom that is pulled in the simulation. Reproduced from [(Gumbart et al., 2007)].

Phospholipid vesicles have positively charged outer surfaces that are attracted to the negatively charged mica surface through electrostatic attraction. Once on the surface the vesicle will partially collapse while potentially fusing with other vesicles to form larger vesicles. The vesicle will then collapse or lyse to form a layer of lipid on the mica surface as seen in Figure 8.3 [(Kaufman and Freger, 2011)].

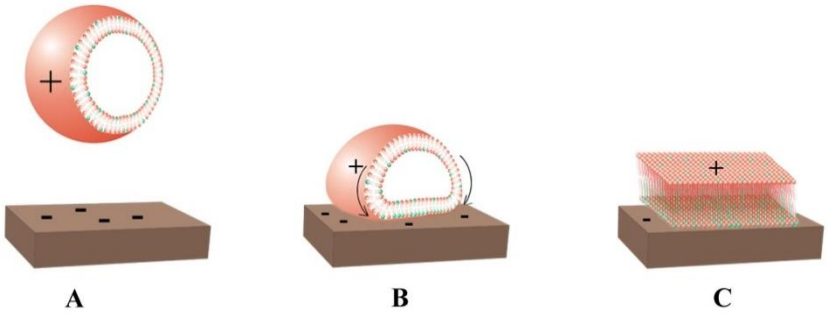

Figure 8.3- Cartoon of lipid vesicle adsorption to a mica surface. Reproduced from [(Kaufman and Freger, 2011)]

Work done by Dr David Brockwell's group (Astbury Centre, FBS, University of Leeds) including experiments performed by Samuel Hickman (FBS, University of Leeds) have aimed to test the strength of the protein- protein interactions between BtuB and the

TonBox using Force Spectroscopy AFM. By attaching a TonBox protein to an AFM tip and TonB to a silicon nitride surface they were able to measure the rupture force of the protein-protein interaction to be 113 ± 13 pN at 1 μm/s which is classed as mechanically strong [(Hoffmann et al., 2013)]. Due to the high mechanical strength of this interaction, a theory of force application from the TonB on the BtuB as the mechanism for unblocking the transport channel in BtuB could be tested. The BtuB protein was overexpressed and inserted into polar lipid vesicles which were then adsorbed onto mica, with the TonB attached to the AFM tip as in the previous experiment. The tip was brought close to the surface then retracted at a constant velocity of 1 μm/s with the deflection of the cantilever tracked. A third of experiments showed a single event in the force extension profile which was similar in force to the TonB-TonBox experiment (98 ± 8 pN) while the other two thirds of experiments showed two rupturing events with rupturing forces of 61 ± 4 and 91 ± 23 pN which indicates that the BtuB undergoes a partial unfolding event in the majority of cases before dissociation. It suggests that the intramolecular bonds in the plug domain are weaker than the intermolecular bonds between the TonB and TonBox. The 50 amino acids downstream from the TonBox were removed from the BtuB crystal structure and then molecular dynamics simulations were run that show the creation of a channel through the BtuB with dimensions of 30.2 Å diameter and 12.5 Å depth [(Hickman et al., 2017)].

To investigate how BtuB sits in the membrane and interacts with other proteins, BtuB was overexpressed, purified and then inserted into polar lipid vesicles in the same method as the BtuB-TonB experiments described above and then imaged with AFM.

8.2- Methodology

The BtuB experiments used a sample preparation method based on Thoma's work [(Thoma et al., 2012)] and then fully described by Hickman [(Hickman et al., 2017)] in collaboration with Samuel Hickman and David Brockwell (FBS, University of Leeds) who performed the protein force spectroscopy experiments on the same samples. The preparation of BtuB-lipid samples involves many steps and takes a few weeks from start to finish but once the batch of sample has been made it can be used for many months if it is divided into small volumes and frozen at -80 °C. To begin the sample preparation, the BtuB expressing strain of *E. coli* was made by transposing a plasmid into *E. coli* cells by adding the plasmid to the cell mixture then heat shocking the cells at 42 °C to swell the cells for 30 seconds, making them more permeable to the plasmid. The cells were then

iced to shrink them which locks the plasmid in. These cells were plated out onto antibiotic (100 µg/ml ampicillin) plates which ensures that only the cells with the plasmid can grow. Ampicillin resistance can be transferred into a target strain using a plasmid. Using an agar plate with additional ampicillin means only the resistant target strain of bacteria will grow while wild type or other mutants will be killed by the antibiotic [(Karami et al., 2007)].

A colony of the BtuB *E. coli* cells was taken from the agar plate and added to 150 ml of LB which was then grown overnight at 37 °C while shaking at 200 rpm. 12 x 1 l conical flasks of fresh Liquid Broth media (LB) with 100 µg/ml ampicillin were also warmed at 37 °C overnight. After 14 hours, 10 ml of the overnight culture was added to each 1 l conical and grown until the cells reached an OD ~ 0.7. Once the cells reached this concentration 0.15 % (w/v) L-(+) arabinose was added to each conical flask and incubated overnight at 20 °C.

In the morning the cells were centrifuged (9500g) for 15 minutes at 4 °C then the supernatant was discarded and the cells were resuspended in 50 ml per 10 g of buffer comprising of 10 mM Tris-HCl, pH 8.0, 0.25% (w/v) lithium diiodosalicyulic acid. The cells were then disrupted by blasts of sonication making sure not to leave the nozzle in the liquid for more than 5 seconds at a time due to the heat produced by the instrument. The mixture was then centrifuged and the insoluble material was discarded.

The liquid with the membranes was ultra-centrifuged (158,000g) to separate out the membrane fraction and then the membranes were resuspended in 50 ml of buffer containing 10 mM Tris-HCl pH 8.0, 0.25 % (w/v) lithium diiodosalicyclic acid with additional 2 % (v/v) Triton X-100 detergent. The liquid was mixed then ultracentrifuged for 1 hour (158,000g at 4 °C) before the supernatant was discarded and the step was repeated. The pellet was resuspended in 56 ml of BtuB purification buffer (10 mM Tris-HCl, pH 8.0) mixed together, then ultracentrifuged again for 1 hour at 4 °C leaving only a pellet after the supernatant was discarded. 56 ml of a buffer containing 10 mM Tris-HCl, pH 8.0, 1 % (w/v) n-octyl-β-D-glucopyranoside (β-OG) and 5 mM EDTA was used to homogenise the cells using a hand homogeniser, then they were ultracentrifuged (158,000g at 4 °C) for 1 hour.

The supernatant was put into a 5 ml DEAE-Sepharose column (GE Healthcare) pre-equilibrated in 90 % buffer A (containing 50 mM Tris-HCl, pH 7.5, 5 mM EDTA, 0.54 % (w/v) β-OG) and 10 % buffer B (which is Buffer A with additional 1 M LiCl) at room

temperature using a AKTA prime plus (GE Healthcare). The anion exchange column ran an automated program of wash steps with different combinations of buffers A and B before the BtuB precipitated from the column. An SDS-PAGE gel can then be run to confirm the identity of the BtuB.

The *E. coli* polar lipid was prepared for the dialysis process. The lipid was dissolved in chloroform at the concentration 10 mg/ml. The protein and lipid components were mixed in a protein: lipid ratio of 1:2 with respect to the mass of their dried powder. The chloroform was evaporated off the protein and then both the lipid and protein were separately dissolved in a buffer of 128 mM NaCl, 25 mM Tris at pH 8 with 1 % (w/v) β-OG detergent. The quantities used in these experiments were 0.3 mg of the BtuB protein dissolved in 100 µl of buffer mixed and 0.6 mg lipid in 100 µl buffer.

The 100 µl of each component were added to a 12-14 kDa dialysis bag using a needle and syringe. A buffer comprising of 10 mM Tris, pH 7.5, 300 mM KCl, 400 mM $CaCl_2$ and 0.01 % (v/v) NaN_3 was put in a beaker with a magnetic stirrer set to slowly stir (speed setting 3) the liquid. The dialysis bag was attached to a piece of foam and put to float on the surface of the buffer. The beaker was covered with foil to ensure the buffer did not get contaminated. The buffer was replaced every day for the 7 days the dialysis took place.

After the dialysis period the liquid inside the dialysis bag was drawn out with a needle and syringe and then diluted and divided into smaller vials and frozen at –80 °C.

For AFM imaging a concentration of 0.1-0.5 mg/ml was needed so the protein/ lipid vesicles were diluted using an adsorption buffer of 300 mM KCl, 10 mM Tris at pH 7.8 that had been filtered using a 0.22 µm filter. 200 µl of this mixture was pipetted onto freshly cleaved mica and then incubated at room temperature for 30 minutes. An imaging buffer of 150 mM KCl, 10 mM Tris at pH 7.8, that had been filtered using a 0.22 µm filter, was used to wash the mica with ~100 µl of buffer being added and removed from the sample 9 times with the final 100 µl being left on the sample on the final wash step.

The imaging buffers used in the experiments were also taken from Thoma's method [(Thoma et al., 2012)] with a 300 mM KCl, 10 mM Tris buffer used as the adsorption buffer and a 150 mM KCl, 10 mM Tris buffer used for the imaging buffer in initial experiments. Different concentrations of these buffers were experimented with during the imaging including just using the adsorption buffer concentrations for imaging which yielded the best results. The Bruker MLCT-E probe was used in the earlier experiments in liquid tapping mode while the sample concentration was tested. For higher resolution scans the

Bruker FastScan-D probes were used. All of the images presented here were taken using the FastScan-Ds. To obtain high resolution AFM images the Dimension FastScan AFM was used in liquid tapping mode.

8.3- Imaging flat membranes

The lipid vesicles should lyse and lay flat when they hit the surface of the mica due to electrostatic attraction between the sample and the surface. Flat sample surfaces are desirable for high resolution AFM because the Z range of the imaging system can be reduced allowing for more sensitive Z measurements and the feedback system does not have to be as active in making large changes in height as the sample is imaged.

Some areas of the lipid were seen to have largely empty flat regions with some bumps on them.

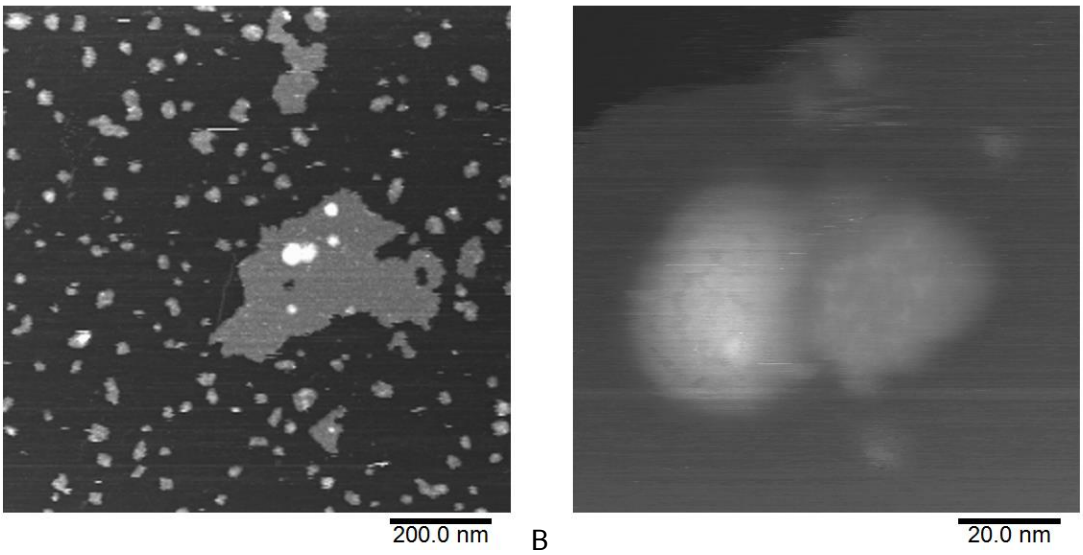

A B

Figure 8.4- AFM topography images of flat lipid and 9 nm high features seen within the lipid. (A) has a Z scale (black to white) = 19 nm. (B) has a Z scale (black to white) = 11 nm.

The lipid surface seen was often fragmented into small parts as in Figure 8.4 and was regularly measured to be ~4 nm in height above the mica surface which corresponds to the height of a single layer of lipid. There were some areas of intact lipid with the bumps that are larger than the expected size of single BtuB proteins. It has been theorised that the larger bumps could be bits of dirt trapped in the lipid or possibly aggregations of BtuB proteins that the AFM has been unable to resolve.

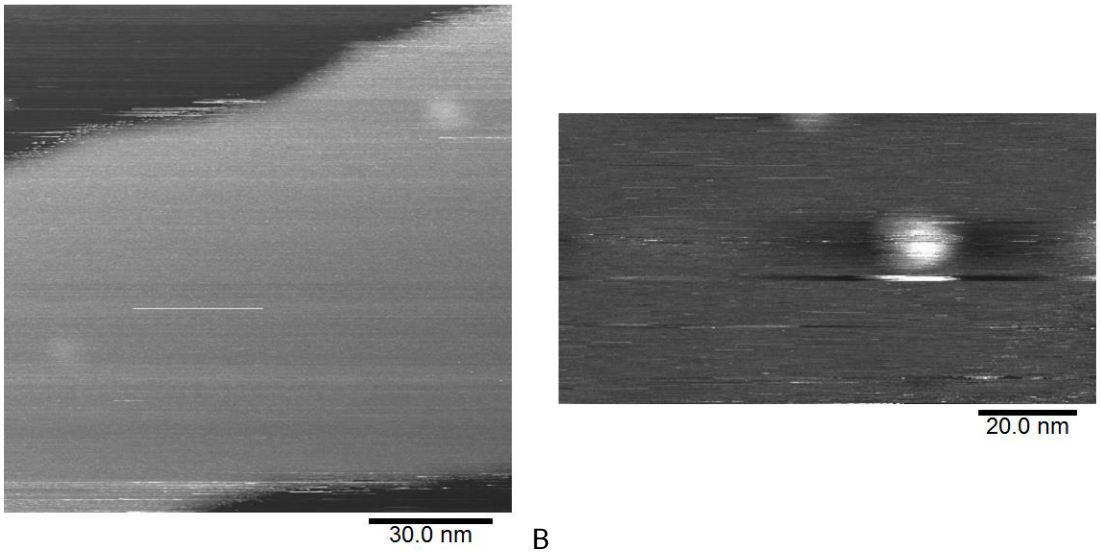

A B

Figure 8.5 - Topography images of a features seen within flat lipid membrane regions. (A) has a Z scale (black to white) = 11 nm. (B) has a Z scale (black to white) = 3 nm.

Patches of lipid that were two layers thick were not as common as the single layer thick lipids and even when the bilayers were found they were often found to be broken or fragmented into small pieces.

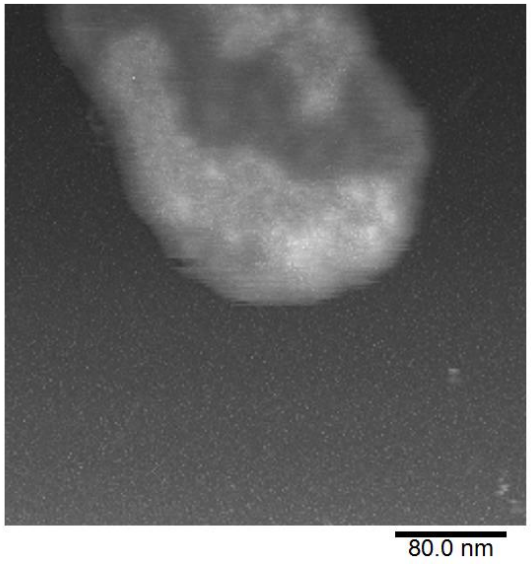

Figure 8.6- Topography image of a lipid bilayer with some raised features. The image has a Z scale (black to white) = 15 nm.

Fragments were imaged that showed patches of lipid with features but these features were not resolvable to determine what they were as in Figure 8.6.

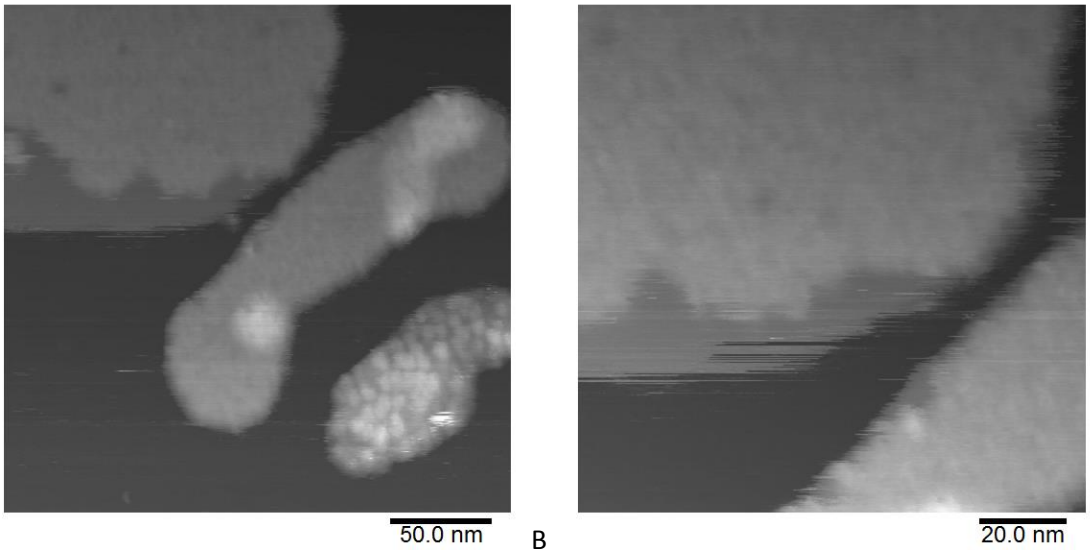

A B

Figure 8.7- Topography images of flat lipid double layer showing raised features. (A) has a Z scale (black to white) = 21 nm. (B) has a Z scale (black to white) = 17 nm.

The region of bilayer in Figure 8.7 shows lipid that has features that could be protein. The imaging settings were modified to try to get the best possible images of the region but it was not possible to resolve individual units within the lipid to ascertain whether the features are protein.

8.4- Imaging deflated vesicles

It was not possible to see individual protein units when imaging flat lipid membrane so imaging on top of vesicles was tested, a technique that has been used to successfully image light harvesting proteins with AFM at the resolution that would be able to resolve the individual BtuB proteins [(Kumar et al., 2017a)]. Imaging on top of vesicles is challenging because using too much force can displace the vesicles and the imaging is happening over a greater height range so the imaging parameter Z length cannot be reduced, resulting in a lower Z sensitivity.

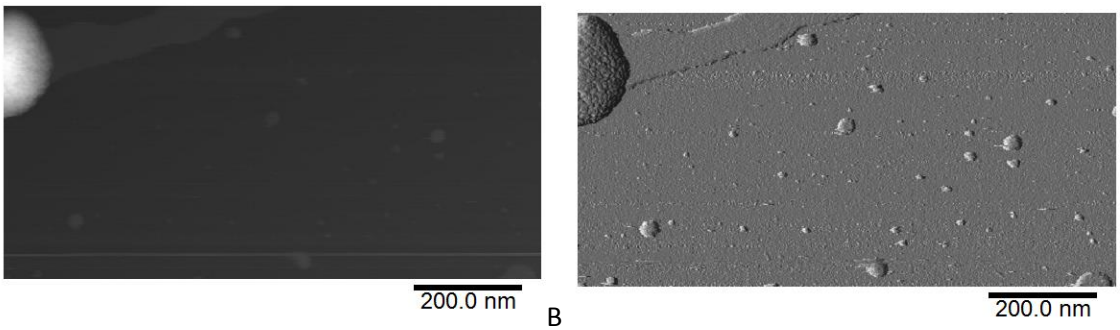

A B

Figure 8.8- Topography and amplitude images of a deflated vesicle on top of a strip of flat lipid. (A) has a Z scale (black to white) = 74 nm.

Figure 8.8 shows a vesicle in the top left hand corner of the vesicle which has been partially deflated, so it still has a curved surface but is not a sphere. Figure 8.8(B) is the amplitude image of the same scan and shows a trail of flat lipid to the right hand side of the deflated vesicle. This gives an indication of the difference in height of the vesicles compared with the flattened lipid which is important in the AFM imaging of the sample as the tip must climb the tall features during the scanning of the vesicle.

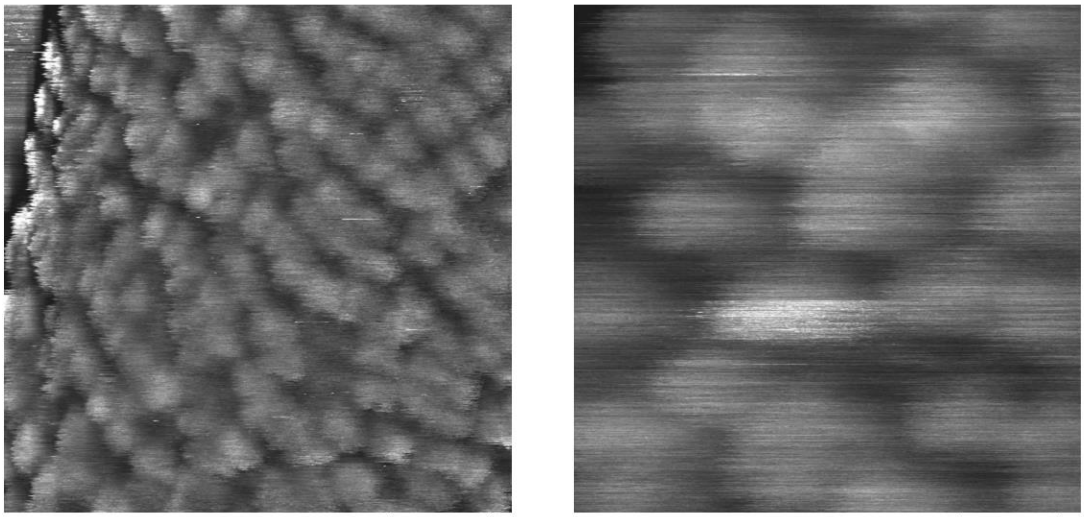

A B

Figure 8.9- Images of proteins taken on top of a deflated vesicle. (A) is a high pass filtered topography image with a Z scale (black to white) = 50 nm. (B) is a topography image with a Z scale (black to white) = 8 nm.

Zooming in to a smaller region on the top of the vesicle in Figure 8.9 shows that individual proteins can be resolved that have diameters of approximately the diameter of the BtuB protein.

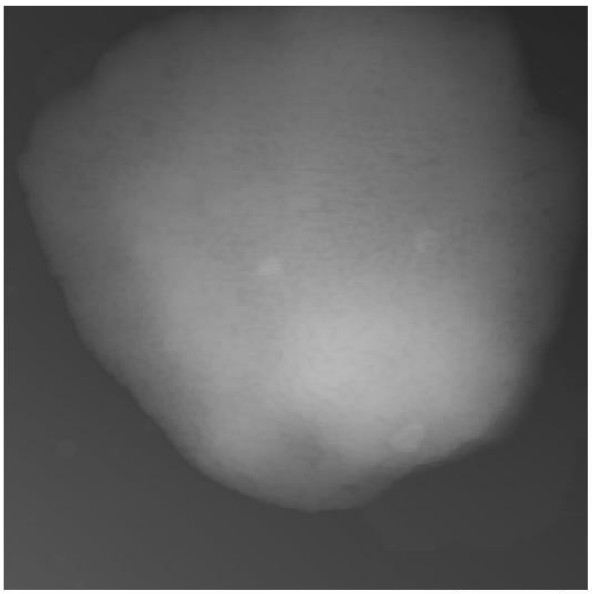

A

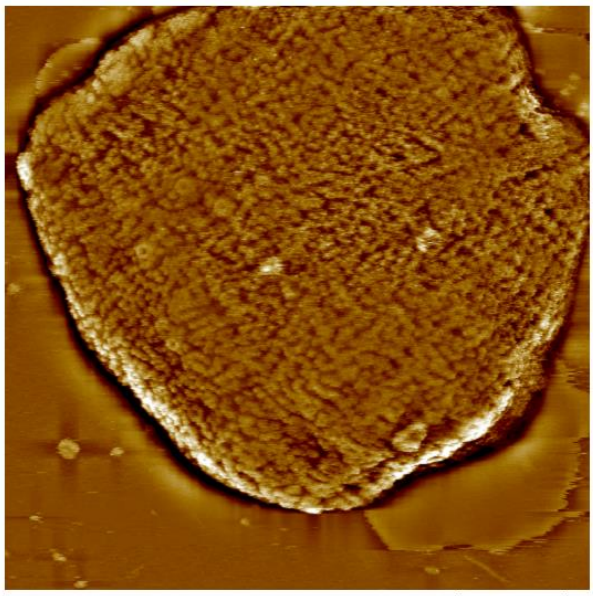

B

Figure 8.10- Images of a deflated vesicle showing thousands of proteins and some ring structures. (A) is a topography image with a Z scale (black to white) = 222 nm. (B) is a high pass filtered topography image with a filter size = 100 nm.

The larger collapsed vesicle in Figure 8.10 showed that as well as the bumps that were the on the smaller vesicle in Figure 8.9, there were some features that looked like rings. It shows that in the right conditions, individual proteins can be resolved in large scans. Imaging a smaller region of the same vesicle allowed the rings to be seen at higher resolution with a series of images in Figure 8.11 of the same area taken while adjusting the imaging settings with the aim of improving the resolution of the rings.

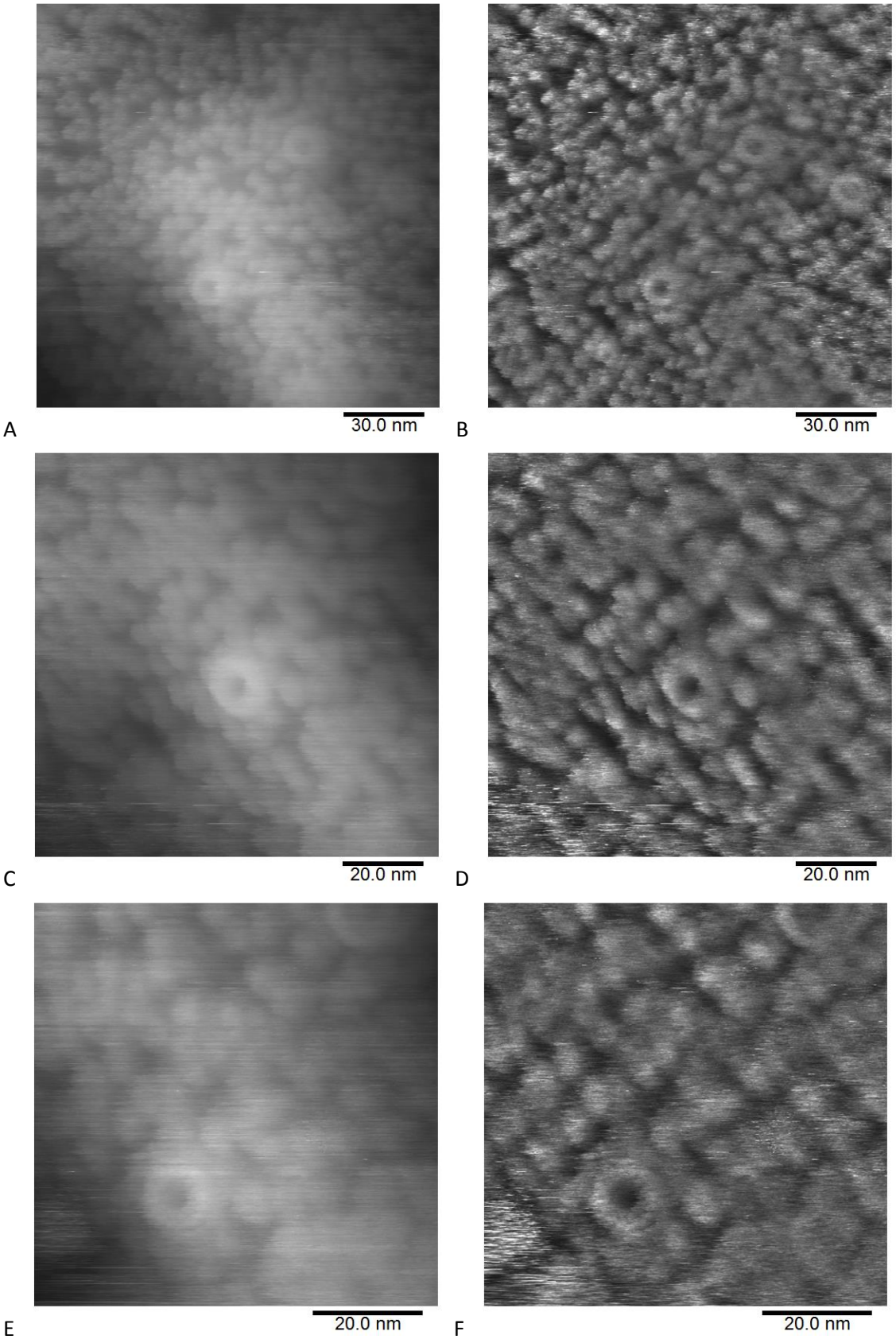

Figure 8.11- Topography and high pass filtered images of small scans of the deflated vesicle in Figure 8.10 that show the individual protein lumps and some ring shaped

structures. (A) is a topographic image with a Z scale (black to white) = 42 nm. (B) is a high pass filtered image with a filter size = 75 nm. (C) is a topographic image with a Z scale (black to white) = 33 nm. (D) is a high pass filtered image with a filter size = 50 nm. (E) is a topographic image with a Z scale (black to white) = 21 nm. (F) is a high pass filtered image with a filter size = 37 nm.

The series of images shows that the rings are spaced irregularly within the proteins and that over the course of the imaging, the rings do not move relative to the other proteins.

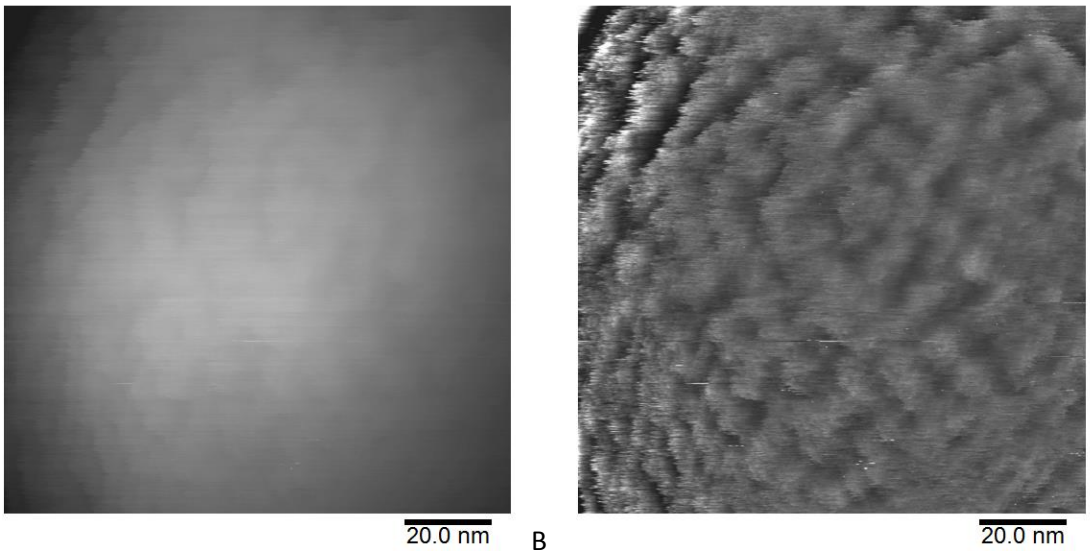

A B

Figure 8.12- Topographic and high pass filtered topography images of a deflated vesicle that shows proteins. (A) is a topographic image with a Z scale (black to white) = 98 nm. (B) is a high pass filtered topography image with a filter size = 58 nm.

The rings were seen on other collapsed vesicles within the background of individual proteins. The collapsed vesicles showed evidence of the proteins with them being resolvable in most cases. The proteins were measured to be on average 6 nm in diameter. This measurement could be increased due to tip convolution or the sides of the tip interacting with the surface before the end did causing an error in the diameter measurements.

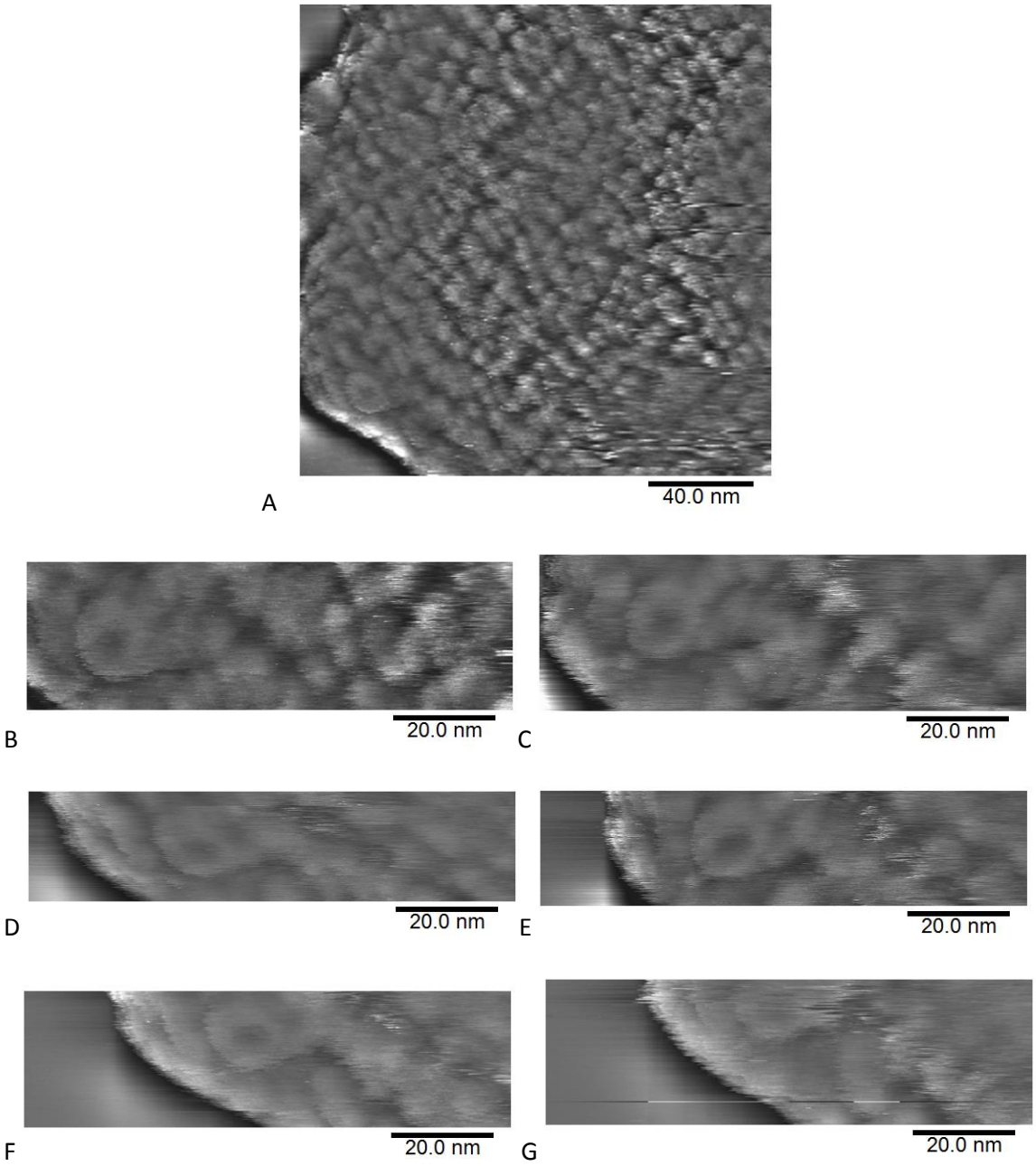

Figure 8.13- High pass filtered topography images of a deflated vesicle that shows individual proteins and a ring with zooms on the ring. (A) has a filter size = 50 nm. (B) has a filter size = 47 nm. (C) has a filter size = 48 nm. (D) has a filter size = 48 nm. (E) has a filter size = 48 nm. (F) has a filter size = 47 nm. (G) has a filter size = 47 nm.

A ring was imaged on another collapsed vesicle over multiple frames in Figure 8.13. The imaging parameters were changed between each image to try to optimise the resolution of the ring, with the aim of being able to resolve structure within the protein. The proteins do not seem to move relative to each other over time in this lipid vesicle configuration as there are no changes in the positions of the proteins from image to

image. The total diameter of the ring was measured to be ~15 nm with a pore opening at the centre of ~5 nm which is considerably larger than the X-ray data for BtuB indicates. Each BtuB unit should be ~4 nm in diameter in total meaning the rings are not BtuB rings although they may be assemblies of multiple BtuB proteins that have come together to form a ring [(Hickman et al., 2017)]. It is unclear as to why the rings form sporadically within a packed protein membrane.

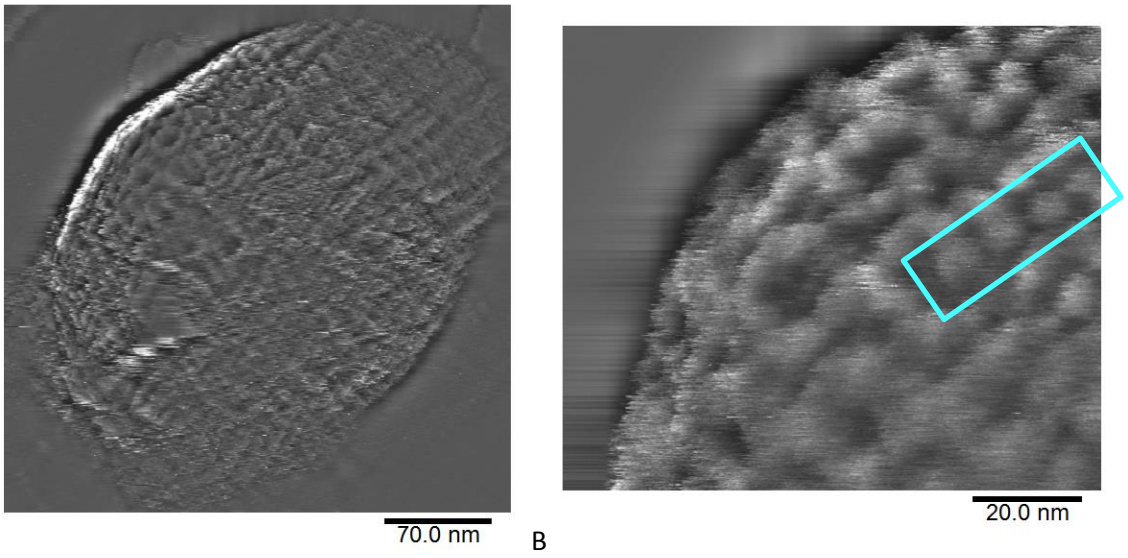

A B

Figure 8.14- High pass filtered topography images of a deflated vesicle that show individual proteins and large rings. (A) has a filter size = 50 nm. (B) has a filter size = 49 nm.

In a separate set of images shown in Figure 8.14 it was possible to see much larger rings made of proteins (~30 nm total diameter) within the collapsed vesicles. In Figure 8.14(A) the rings are seen at the top left hand region of the cell which is at a steep gradient. The tracking of the rings could be distorted due to the large gradient of the surface that is being measured as it is easier for the tip to track the surface when the height is not changing as dramatically. In Figure 4.14(B) there is a row of proteins (marked in a blue rectangle) in the top right corner of the image which were measured to have an average peak to peak distance, based on the 4 proteins of 10 nm. While the resolution on these rings is not as good as in the previous set of rings it is possible to see that the larger rings are not continuous raised ring but are made up of some of protein units.

The diameters of 30 proteins imaged in 3 different experiments on 4 different vesicles were measured with an average diameter of 6.1 ± 1.1 nm and an average height of ~1.3 nm above the membrane. This value corresponds with the value measured with X-ray

diffraction techniques of ~4 nm when accounting for the AFM not being able to perfectly track the surface of the proteins at this length scale. There could be some broadening of the features in the images due to tip broadening if the sharp tip cannot track down in the spaces between the proteins well.

A range of concentrations of sample were tried from 100 µg/ml to 500 µg/ml with a good coverage of the surface coming at a concentration of ~250 µg/ml. Buffer salt concentrations are an important factor in obtaining the best possible resolution images. The imaging buffer was altered during experiments with the concentration of KCl changing from 150 mM to 300 mM and the concentration of 10 mM $MgCl_2$ added on some experiments. It was found that the 300 mM concentration of KCl was a suitable buffer concentration that allowed for high resolution over a long time period. Divalent salts, like $MgCl_2$, have a greater charge screening effect at lower concentrations than monovalent ions but having higher charge screening can lead to faster tip fouling which causes a significant drop in the possible image resolution. Therefore, it was preferable to image using a buffer without $MgCl_2$ to keep the higher resolution over a longer period.

8.5- Discussion and conclusions

The experiments showed that it is possible to image and resolve individual proteins in the lipid membrane using high resolution tapping mode AFM where previous attempts by Hickman had not been able to distinguish individual BtuB proteins. When the positively charged end of phospholipid in the polar lipid vesicles interacts with the negatively charged mica surface they are expected to lyse and then lay flat due to the electrostatic attraction between the two. This should result in a mica surface that is coated in lipid with protein, however, in the course of these experiments it was difficult to find flat lipid full of protein while it was common to find flat empty lipid and deflated vesicles with protein on the surface. Unlike in the AFM study of other TBDTs [(Thoma et al., 2012)], it was not possible to get good resolution on proteins that were in a flattened out region of lipid on the mica surface, it was only possible to see individual proteins that were on the surface of deflated but still intact vesicles. The concentration of BtuB protein in the membrane in this study was higher than would naturally occur in a cell, as it needs to be overexpressed to give the best chance of finding proteins when imaging but this could lead to proteins being packed together with other BtuB proteins which is not likely in nature due to their low copy number of ~200 proteins per cell [(Di Masi et al., 1973), (Spector et al., 2010)]. The proteins were mostly found to have no overall order or

organisation but some seemed to have formed rings of proteins though the individual proteins in the ring were generally not resolvable.

Initial plans for the experiment involved progressing on to imaging a living *E. coli* cell with the BtuB overexpressed in the outer membrane but this did not happen due to the difficulty in trapping whole *E. coli* cells on a surface for AFM imaging. The grids that were developed in Chapter 7 were tested unsuccessfully with *E. coli. E. coli* cells are smaller than *B. subtilis* so were not as effectively trapped. Previously, whole *E. coli* cells have been immobilised on gelatine coated mica surfaces which could be used to trap the cells with overexpressed BtuB for AFM imaging [(Lonergan et al., 2013)]. Another difficulty with imaging whole cells with overexpressed proteins could be that it is difficult to know what features are BtuB as opposed to other outer membrane proteins. A combination of fluorescence techniques and AFM could be used to first localise the BtuB in the membrane then these areas could be imaged with AFM. An issue with this correlative approach is having the resolution in the fluorescence microscopy to localise individual proteins and also having the ability to accurately image the desired area with the AFM.

Future work could also include imaging of a crystalline version of the protein [(Fanucci et al., 2003)] to take try to resolve the individual domains within the protein. The ability to image at higher resolution would be expected due to the flatter and more robust sample surface which would aid with the resolution that can be achieved. This AFM work could provide direct measurement of the plug domains and could be compared to the crystal structure of the protein with the plug domain removed. Many of the previous AFM studies on *E. coli* outer membrane transport proteins have been performed on crystalline versions of the proteins [(Pfreundschuh et al., 2014)(Engel et al., 1997)(Bustamante and Keller, 1995)(Thoma et al., 2012)(Müller et al., 1999)].

Chapter 9- Conclusions and future work

An effective technique for imaging *S. aureus* cells in physiological conditions has been developed that allows for high resolution. Starting with the silicon hole immobilisation technique that had been successfully used previously [(Kailas et al., 2009)], the use of small amplitude tapping mode AFM in liquid has allowed for the cell wall architecture to be resolved at a molecular resolution on living cells for the first time. Small amplitude tapping mode using small cantilevers allows for greater force control and higher signal to noise ratio in measurements compared with traditional longer cantilevers. Other modes that were tested including liquid contact mode, liquid QI mode and liquid PeakForce mode did not allow for the architectural features to be imaged. Another important factor in achieving the best possible resolution has been buffer optimisation as ionic concentrations can affect the charge screening between the tip and the sample surface.

The cell wall architecture of *S. aureus* has previously been imaged using AFM and EM to determine the organisation of the peptidoglycan [(Touhami et al., 2004; Turner et al., 2014)]. There are two distinct architectures that have been seen that correspond to a nascent architecture and a mature architecture. From the previous experiments a model for each structure was built that stated the young architecture appears as rings, which are made during the formation of the septal plate. Some previous AFM data suggested that a remodelling and reorganisation process of the peptidoglycan transforms these rings into a disordered "knobbled" structure, however, there was also evidence of a mesh like architecture from contact mode imaging in liquid. In the images taken in this project a series of high resolution scans were taken of many cells in a range of imaging conditions including imaging the cells in their growth media at 37 °C. All conditions showed evidence of the ringed architecture that had been reported previously, while the mature architecture appeared to be in an organisation more similar to the mesh structure that had been seen rather than the "knobbled" structure. A series of experiments were performed that used different mutant bacterial strains or treatments of the cells that were used to systematically rule out other candidates that could form the cell wall structures seen in the images other than peptidoglycan. An experiment was also performed to test if the peptidoglycan maintains the same structure without a drying step which is part of the sample preparation procedure. The experiment showed evidence of rings and the porous structure so the drying does not cause a change in the peptidoglycan architecture.

Looking in closer detail at the ringed structure showed evidence of different densities of rings from densely packed rings to rings that were less dense with a more disordered structure in the gaps that had formed between the rings. Different cells showing varying degrees of degradation which was the first time AFM had been used to see stages of this gradual process. The pattern of the degradation in the rings suggests that there may be some selective remodelling or rather some of the rings that are not remodelled initially as some evenly spaced long rings were seen which could have some biological or structural significance.

High resolution scans of the rings provided the first images of individual glycan organisation in the cell wall to be seen. Using small amplitude tapping mode allowed for single molecules on a whole bacterial cell to be seen with peak to peak inter molecular distances of less than 3 nm measured. Features were also seen when scanning along a glycan strand that was measured to have a period of 4-5 nm which correlates well with these features being the side branches of the glycan chain that have previously been modelled to form in a given direction every 40 Å [(Kim et al., 2015)]. This level of resolution provides an insight into the peptidoglycan organisation that has not been achieved in previous studies.

Using these high resolution images a series of analyses were performed with the aim of better understanding and parameterising the ringed structure. A method of manually tracing the rings was developed that allowed bundles of glycans in the ringed structure to be plotted and then have a best fit circle from the traces. This analysis enabled a comparison to be made between the dense and less dense ringed cells. It was seen that the dense rings had some overlapping fibres, while the less dense rings did not. There is a central disordered region at the centre of the ringed structure on the cell. All of the centres of the rings, as calculated by the tracing analysis, fell within this central disordered region which gives an indication that the peptidoglycan synthesis and insertion proteins have some mechanism that revolves around this region. The images of this central disordered region showed no evidence of ringed structure and did not appear the same as the mature mesh structure. The diameter of the central disordered zones of 12 cells was measured and the average gave a value of 60 nm which is large enough that the AFM should be able to resolve the architecture of the region. If the theory that the rings only exist as a thin outer layer with the rest of the cell wall material being inserted in the disordered organisation is true, then the central plug may be

inserted in the same way, only without any ring cap, possibly due to there being a minimum radius that the strands can be inserted in.

The mature architecture was also studied in high resolution on whole cells. Using the small amplitude tapping mode technique a porous mesh like peptidoglycan organisation was seen. The mesh appeared to have large and sometime deep holes within the cell wall structure. To quantify the sizes and depths of these holes a bearing analysis technique was developed and performed on some of the high resolution mesh images. From the analysis the depth profile could be measured and all six of the images showed there were holes within the mesh that went down at least 20 nm into the cell wall peptidoglycan layer. The thickness of the cell wall in *S. aureus* has previously been measured to be 15–30 nm thick so the holes may be reaching most of, if not all, the way through the cell wall layer [(Vollmer et al., 2008a)]. This was not predicted by either model of the mature structure and raises questions about why the holes are formed.

A fibre width analysis was also performed on the mesh structures. The fibre diameters measured for every fibre in each image was measured to then be able to calculate an average fibre width and to be able to plot the distribution of the widths. These distributions show peaks from 6 nm to 9 nm and all have a long tail towards larger fibre diameters. Using the mean and median values for each distribution, a value for the maximum crosslinking percentage of the surface peptidoglycan can be calculated. The crosslinking percentages from the AFM data correlated with the NMR data that had been previously published which is significant as high crosslinking percentages are possible even in a loose mesh architecture made of fibres that are only 3 or 4 glycan strands across. The fibre width and hole size measurements will allow a model of the mesh structure to be made.

Images of cells undergoing division events revealed a common feature that had not been seen on the outside of *S. aureus* cells with AFM before. A raised band that is seen between two halves of the splitting cell on many of the dividing cells that were imaged in the project may be the pie crust. The pie crust architecture had been seen in isolated peptidoglycan sacculi on the inside of the cell wall and is formed as part of the division cycle [(Turner et al., 2010a)]. The pie crust was seen to appear in areas of ringed architecture that were undergoing division and splitting. The few cells that were dividing with mesh structure showed no evidence of the architectural feature. On dividing cells where both ringed and mesh structure were seen, the splitting process had developed further on the ringed region. This may signal a difference in the localisation of the

enzymes involved in splitting the two daughter cells apart or it could indicate a difference in the structure that makes the crack form through the rings first or for the crack to form more easily through the rings.

From all of the images of cells at different stages of the cell wall maturation process a timeline can be created that shows an approximate degradation process. Peptidoglycan is inserted mainly into the septum as the new septal plate is formed [(Lund, 2016)]. Imaging the emerging septal plate between the two halves of a dividing cell proved to be difficult with AFM due to the high gradient. The earliest time point that was imaged was of dense ringed structure. These rings are then remodelled with evidence of less dense rings and rings with regions of the mesh structure seen within a degrading set of rings. A mostly mesh structure will form with some evidence of some remnant ringed architecture before the final disordered mesh architecture is reached with no evidence of any orientation in the rings. This composite timeline shows how the degradation process most likely occurs but so far it has not been possible to image the process occurring on a single cell.

The resolution of the imaging has been pushed forward using small amplitude tapping mode AFM. For the first time individual molecules within a living cell have been imaged but there is still the possibility for greater resolution. It has not been possible to directly measure the length of individual glycans within the rings due to the inconsistent resolution during an image. By buffer optimisation and minimising factors that can cause thermal drift and other noise it is possible that individual strands could be mapped along their entire length. It is difficult to determine the resolution that has already been achieved in the mesh regions as the strands are not in an ordered organisation. It is possible that individual strands have already been seen. To prove single strand resolution has been taken within the mesh architecture, images that show the individual glycans within the peptidoglycan fibres would be needed. There is also scope for improving resolution on the disordered central region at the centre of the rings which has, so far, not been resolvable. There may be a different mechanism for the peptidoglycan insertion in this region but more information is needed to understand it.

One of the major aims of the project that was not achieved was to be able to image biological processes in *S. aureus* happening over time. The immobilisation method of using silicon has previously been used to image the division of a cell undergoing a division event but it was not possible to repeat this during this project [(Kailas et al., 2009)]. A series of experiments were performed to try to optimise the conditions to allow the cells

to grow including using different growth media, changing the size of the holes in silicon and making the substrate out of different materials. The cells were also imaged using different AFMs in various imaging modes without any signs of active division events. The large number of cells over the course of the project and the projects of other group members that have been imaged suggests that the lack of division events is not due to probability. Future work in the area should focus on solving the problem of getting the cells to undergo the division process during AFM imaging. One possible solution is using agar and agarose to make the holes out of. Soft gels have been difficult to image with AFM in the past but with small amplitude tapping mode it has been seen to be possible.

Having the ability to image dynamic processes in the bacteria would be a powerful tool in understanding the processes that the cells undergo during their lifetime. In this project a composite timeline of peptidoglycan degradation was made from molecular scale images. Imaging a single cell undergoing the degradation process would provide new information including how long remodelling takes. The resolution of AFM makes it one of the only techniques that could track a dynamic process at molecular resolution. By imaging a whole division process at this resolution a great amount of new information could emerge about how the splitting process occurs and how the cell expansion happens. These two dynamic processes could then be tracked for different mutants, similar to some of the experiments performed in Chapter 4. Seeing the degradation process of a SagB mutant cell, which lacks one of the key peptidoglycan hydrolases [(Wheeler et al., 2015)], would give great insight into the role of the hydrolases. One of the main goals within the field of antimicrobial resistance is to understand how antibiotics affect the normal cell processes. Performing the dynamic experiments in the presence of different antibiotics could reveal how they act on a molecular scale on a living cell. All of this information could be used to build a model of how the cell divides and the peptidoglycan matures in a normal cell and then a separate model for the same processes in the presence of antibiotics could be developed. This work could potentially be very important in the understanding of antibiotics and help in the fight against growing antibiotic resistance. There is potential for development of the automatic tracing program to be developed to then be able to map the action of individual molecules within the cell wall over the course of these dynamic processes.

A major objective during the project was to develop a method for immobilising rod shaped cells for imaging that is as effective as the one that has been used for high resolution imaging of *S. aureus.* A series of different designs of patterned silicon were

made and used to try to trap the rod shaped bacterium *B. subtilis.* Results when using these designs showed that some cells were able to be imaged using the grids but without the same yield of trapped cells or the same resolution that was possible with normal imaging techniques on *S. aureus.* Continued development of the physical trapping method for rod shaped cells could provide a new method for imaging a whole new range of different bacterial species enabling their cell wall structure to be studied. A wide survey of the peptidoglycan architecture of different bacteria could be performed which would feed into the creation of a comprehensive model of peptidoglycan structure. Materials other than silicon could be tested initially when designing a new trapping system for *B. subtilis* and other rod shaped bacteria. One of the experiments aimed to use the trapping technique that positions the cells with their poles facing up out of the surface [(Bisson-Filho et al., 2017)]. Adapting this technique could provide high resolution information on the polar architecture of the cells. If the method of immobilisation for rod shaped bacteria allows the cells to continue performing biological process, as discussed above for *S. aureus,* series of images could be taken of the division process in *B. subtilis* and other rod shaped bacteria as well as monitoring for changes in peptidoglycan structure as the cells elongate.

The *B. subtilis* cells were immobilised successfully with a protein trapping method, coating glass with Cell-Tak, which allowed for high resolution images to be taken using the small amplitude tapping mode technique. Previous data of the outer peptidoglycan cell wall architecture suggested a hydrolysed surface while the inner surface of the cell wall was shown to have a banded structure [(Hayhurst et al., 2008; Turner et al., 2014)]. Images of the outside of the cell wall that were taken during this project showed evidence of a mesh structure, like that seen in the mature regions of *S. aureus* cell wall. The mesh showed deep holes similar to those seen in *S. aureus* so the same bearing analysis technique was performed on the *B. subtilis* data which showed that some of the holes in the mesh were over 20 nm deep into the cell wall surface. Comparing the data for multiple *S. aureus* and *B. subtilis* showed a similar structure, total height and distribution of hole depths. The fibre width analysis was also performed on the *B. subtilis* architecture and compared to the analysis performed on the *S. aureus*. The distribution of the fibre widths were similar with some slightly narrower fibres seen in *S. aureus* which may just be due to improved resolution on those images.

The similarities between *S. aureus* and *B. subtilis* could indicate a trend in mature peptidoglycan architecture of Gram positive bacteria. The peptidoglycan in *B. subtilis* has

been shown to be inserted on the inside of the cell in bands and then the cell wall is slowly moved outwards as new material is added. By the time it is on the outer surface it appears to have this mesh structure. Since both *S. aureus* and *B. subtilis* have this mesh architecture there may be a physical or biological motivation or benefit to having this organisation like the structure being more resistant to tearing or ripping or for it providing benefits for transportation of nutrients and proteins into and out of the cell. A reduction in protein secretion was measured in the SagB mutant strain of S. aureus, suggesting the secretion of some proteins may require the long peptidoglycan chains in the young cell wall architecture to be broken into smaller chains and subsequent remodelling of the peptidoglycan architecture to allow for this protein transport [(Chan et al., 2016)]. It would be interesting to compare the architecture of different Gram positive bacteria and use the same methods of analysis to compare the results to the *S. aureus* and *B. subtilis* data.

A series of experiments involving the imaging of the *E. coli* outer membrane protein BtuB were performed with the aim of studying the organisation of proteins in lipid membranes. The proteins were inserted into lipid vesicles and adsorbed to a mica surface. Limited success was found in imaging the proteins in flat lipid membranes, however, proteins were seen in deflated vesicles that had partially collapsed. The proteins were seen to form small rings theorised made of multiple individual proteins. High resolution information like the plug domain in BtuB was not seen in the AFM imaging. Future work regarding the BtuB proteins could involve improving the adsorption of the vesicles to the mica so that flat membranes full of proteins could be imaged which could lead to better or more stable resolution images as the tip would not need to travel over as large a distance in Z during the scanning of the sample. One of the initial aims of imaging the proteins was to then move on to imaging the overexpressed protein in whole *E. coli* cells which would be trapped by the trapping method that was being developed for *B. subtilis*, which was not successful. Different trapping techniques or developing the technique that was initially developed for imaging of living rod shaped cells could allow *E. coli* cells with an overabundance of the protein to be imaged to see how the proteins are organised *in vivo*. An experiment could be performed where vitamin B12 is added into the imaging media to look for a conformational change in the protein such as the appearance of the transport channel opening up.

References

Al Aani, S., Gomez, V., Wright, C.J., and Hilal, N. (2017). Fabrication of antibacterial mixed matrix nanocomposite membranes using hybrid nanostructure of silver coated multi-walled carbon nanotubes. Chem. Eng. J. *326*, 721–736.

Adams, P.G., and Hunter, C.N. (2012). Adaptation of intracytoplasmic membranes to altered light intensity in Rhodobacter sphaeroides. Biochim. Biophys. Acta - Bioenerg. *1817*, 1616–1627.

Alberts, B. (2002). Molecular biology of the cell. (Garland science).

Alsteens, D., Verbelen, C., Dague, E., Raze, D., Baulard, A.R., and Dufrêne, Y.F. (2008). Organization of the mycobacterial cell wall: A nanoscale view. Pflugers Arch. Eur. J. Physiol. *456*, 117–125.

Alves, D., and Olívia Pereira, M. (2014). Mini-review: Antimicrobial peptides and enzymes as promising candidates to functionalize biomaterial surfaces. Biofouling *30*, 483–499.

Amako, K., Umeda, A., and Murata, K. (1982). Arrangement of peptidoglycan in the cell wall of Staphylococcus spp. J. Bacteriol. *150*, 844–850.

Aminov, R.I. (2010). A brief history of the antibiotic era: Lessons learned and challenges for the future. Front. Microbiol. *1*, 1–7.

Ando, T., Kodera, N., Naito, Y., Kinoshita, T., Furuta, K., and Toyoshima, Y.Y. (2003). A High-speed Atomic Force Microscope for Studying Biological Macromolecules in Action. ChemPhysChem *4*, 1196–1202.

Andre, G., Kulakauskas, S., Chapot-Chartier, M.-P., Navet, B., Deghorain, M., Bernard, E., Hols, P., and Dufrêne, Y.F. (2010). Imaging the nanoscale organization of peptidoglycan in living Lactococcus lactis cells. Nat. Commun. *1*, 27.

Andreu, J.M., Schaffner-Barbero, C., Huecas, S., Alonso, D., Lopez-Rodriguez, M.L., Ruiz-Avila, L.B., Núñez-Ramírez, R., Llorca, O., and Martín-Galiano, A.J. (2010). The antibacterial cell division inhibitor PC190723 is an FtsZ polymer-stabilizing agent that induces filament assembly and condensation. J. Biol. Chem. *285*, 14239–14246.

Appendini, P., and Hotchkiss, J.H. (2002). Review of antimicrobial food packaging. Innov. Food Sci. Emerg. Technol. *3*, 113–126.

Arciola, C.R., Campoccia, D., Speziale, P., Montanaro, L., and Costerton, J.W. (2012). Biofilm formation in Staphylococcus implant infections. A review of molecular mechanisms and implications for biofilm-resistant materials. Biomaterials *33*, 5967–5982.

Bailey, R. (2014). The Mechanical Properties of Bacteria through the Cell Cycle as Measured by Atomic Force Microscopy.

Bailey, R.G., Turner, R.D., Mullin, N., Clarke, N., Foster, S.J., and Hobbs, J.K. (2014). The Interplay between Cell Wall Mechanical Properties and the Cell Cycle in Staphylococcus aureus. Biophys. J. *107*, 2538–2545.

Barkan, D., Hedhli, D., Yan, H.G., Huygen, K., and Glickman, M.S. (2012). Mycobacterium tuberculosis lacking all mycolic acid cyclopropanation is viable but highly attenuated and hyperinflammatory in mice. Infect. Immun. *80*, 1958–1968.

Barth, C., Foster, A.S., Henry, C.R., and Shluger, A.L. (2011). Recent trends in surface characterization and chemistry with high-resolution scanning force methods. Adv. Mater. *23*, 477–501.

Beaussart, A., El-Kirat-Chatel, S., Herman, P., Alsteens, D., Mahillon, J., Hols, P., and Dufrêne, Y.F. (2013). Single-cell force spectroscopy of probiotic bacteria. Biophys. J. *104*, 1886–1892.

Beaussart, A., Péchoux, C., Trieu-Cuot, P., Hols, P., Mistou, M.-Y., and Dufrêne, Y.F. (2014). Molecular mapping of the cell wall polysaccharides of the human pathogen Streptococcus agalactiae. Nanoscale *6*, 14820–14827.

Beeby, M., Gumbart, J.C., Roux, B., and Jensen, G.J. (2013). Architecture and assembly of the Gram-positive cell wall. Mol. Microbiol. *88*, 664–672.

Ben-Yehuda, S., and Losick, R. (2002). Asymmetric cell division in B. subtilis involves a spiral-like intermediate of the cytokinetic protein FtsZ. Cell *109*, 257–266.

Binnig, G., Rohrer, H., Gerber, C., and Weibel, E. (1982). Surface Studies by Scanning Tunneling Microscopy. Phys. Rev. Lett. *49*, 57–61.

Bisson-Filho, A.W., Hsu, Y.-P., Squyres, G.R., Kuru, E., Wu, F., Jukes, C., Sun, Y., Dekker, C., Holden, S., VanNieuwenhze, M.S., et al. (2017). Treadmilling by FtsZ filaments drives peptidoglycan synthesis and bacterial cell division. Science (80-.). *355*, 739–743.

Blattner, F.R., Plunkett, G., Bloch, C.A., Perna, N.T., Burland, V., Riley, M., Collado-Vides, J., Glasner, J.D., Rode, C.K., Mayhew, G.F., et al. (1997). The complete genome sequence of Escherichia coli K-12. Science *277*, 1453–1462.

Boneca, I.G., Huang, Z., Gage, D.A., and Tomasz, A. (2000). Characterization of Staphylococcus aureus Cell Wall Glycan Strands , Evidence for a New ^{N_L} - N-Acetylglucosaminidase Activity *. *275*, 9910–9918.

Bottomley, A.L., Kabli, A.F., Hurd, A.F., Turner, R.D., Garcia-Lara, J., and Foster, S.J. (2014). Staphylococcus aureusDivIB is a peptidoglycan-binding protein that is required for a morphological checkpoint in cell division. Mol. Microbiol. *94*, 1041–1064.

Braun, V., Gnirke, H., Henning, U., and Rehn, K. (1973). Model for the structure of the shape-maintaining layer of the Escherichia coli cell envelope. J. Bacteriol. *114*, 1264–1270.

Brown, S., Santa Maria, J.P., and Walker, S. (2013). Wall Teichoic Acids of Gram-Positive Bacteria. Annu. Rev. Microbiol. *67*, 313–336.

Bruker (2017a). FastScan-D website.

Bruker (2017b). MLCT website.

Bruker (2017c). TESPA-V2 website.

Bullitt, E., and Makowski, L. (1998). Bacterial Adhesion Pili Are Heterologous Assemblies of Similar Subunits. *74*, 623–632.

Buss, J., Coltharp, C., Huang, T., Pohlmeyer, C., Wang, S.-C., Hatem, C., and Xiao, J. (2013). *In vivo* organization of the FtsZ-ring by ZapA and ZapB revealed by quantitative super-resolution microscopy. Mol. Microbiol. *89*, 1099–1120.

Bustamante, C., and Keller, D. (1995). Scanning Force Microscopy in Biology. Phys. Today *48*, 32–38.

Butt, H. (1992). Measuring local surface charge densities in electrolyte solutions with a scanning force microscope. Biophys. J. *63*, 578–582.

Butt, H.-J. (1991). Electrostatic interaction in atomic force microscopy. Biophys. J. *60*, 777–785.

Butt, H.-J., and Jaschke, M. (1995). Calculation of thermal noise in atomic force microscopy. Nanotechnology *6*, 1–7.

Butt, H.J., Downing, K.H., and Hansma, P.K. (1990). Imaging the membrane protein bacteriorhodopsin with the atomic force microscope. Biophys. J. *58*, 1473–1480.

Cappella, B., and Dietler, G. (1999). Force-distance curves by atomic force microscopy. Surf. Sci. Rep. *34*, 1–104.

Cartron, M.L., Olsen, J.D., Sener, M., Jackson, P.J., Brindley, A.A., Qian, P., Dickman, M.J., Leggett, G.J., Schulten, K., and Neil Hunter, C. (2014). Integration of energy and electron transfer processes in the photosynthetic membrane of Rhodobacter sphaeroides. Biochim. Biophys. Acta - Bioenerg. *1837*, 1769–1780.

Casuso, I., Khao, J., Chami, M., Paul-Gilloteaux, P., Husain, M., Duneau, J.-P., Stahlberg, H., Sturgis, J.N., and Scheuring, S. (2012). Characterization of the motion of membrane proteins using high-speed atomic force microscopy. Nat. Nanotechnol. *7*, 525–529.

Chan, Y.G.Y., Frankel, M.B., Missiakas, D., and Schneewind, O. (2016). SagB glucosaminidase is a determinant of *Staphylococcus aureus* glycan chain length, antibiotic susceptibility and protein secretion. J. Bacteriol. *198*, JB.00983-15.

Chimento, D.P., Kadner, R.J., and Wiener, M.C. (2003). The Escherichia coli outer membrane cobalamin transporter BtuB: Structural analysis of calcium and substrate binding, and identification of orthologous transporters by sequence/structure conservation. J. Mol. Biol. *332*, 999–1014.

Chimento, D.P., Kadner, R.J., and Wiener, M.C. (2005). Comparative structural analysis of TonB-dependent outer membrane transporters: implications for the transport cycle. Proteins *59*, 240–251.

Chopinet, L., Formosa, C., Rols, M.P., Duval, R.E., and Dague, E. (2013). Imaging living cells surface and quantifying its properties at high resolution using AFM in QI^{TM} mode. Micron *48*, 26–33.

Christner, B.C., Kvitko, B.H., and Reeve, J.N. (2003). Molecular identification of Bacteria and Eukarya inhabiting an Antarctic cryoconite hole. Extremophiles *7*, 177–183.

Corning (2014). Corning CellTak Adhesive Guide.

Cossart, P., and Jonquières, R. (2000). Sortase, a universal target for therapeutic agents against gram-positive bacteria? Proc. Natl. Acad. Sci. U. S. A. *97*, 5013–5015.

Coyette, J., and Van Der Ende, A. (2008). Peptidoglycan: The bacterial Achilles heel. FEMS Microbiol. Rev. *32*, 147–148.

Cruz, P., Mehretu, A.M., Buttner, M.P., Trice, T., and Howard, K.M. (2015). Development of

a polymerase chain reaction assay for the rapid detection of the oral pathogenic bacterium , Selenomonas noxia. BMC Oral Health 1–8.

Cunningham, K., and Wickner, W.T. (1989). Detergent disruption of bacterial inner membranes and recovery of protein translocation activity. Proc. Natl. Acad. Sci. *86*, 8673–8677.

D'Elia, M.A., Pereira, M.P., Chung, Y.S., Zhao, W., Chau, A., Kenney, T.J., Sulavik, M.C., Black, T.A., and Brown, E.D. (2006). Lesions in teichoic acid biosynthesis in Staphylococcus aureus lead to a lethal gain of function in the otherwise dispensable pathway. J. Bacteriol. *188*, 4183–4189.

Daniel, R. a, and Errington, J. (2003). Control of cell morphogenesis in bacteria: two distinct ways to make a rod-shaped cell. Cell *113*, 767–776.

Desmarais, S.M., De Pedro, M.A., Cava, F., and Huang, K.C. (2013). Peptidoglycan at its peaks: How chromatographic analyses can reveal bacterial cell wall structure and assembly. Mol. Microbiol. *89*, 1–13.

Dmitriev, B.A., Toukach, F. V, Schaper, K., Holst, O., Rietschel, E.T., and Ehlers, S. (2003). Tertiary Structure of Bacterial Murein : the Scaffold Model Tertiary Structure of Bacterial Murein : the Scaffold Model. *185*.

Doktycz, M.J., Sullivan, C.J., Hoyt, P.R., Pelletier, D.A., Wu, S., and Allison, D.P. (2003). AFM imaging of bacteria in liquid media immobilized on gelatin coated mica surfaces. Ultramicroscopy *97*, 209–216.

Dufrêne, Y.F. (2003). Recent progress in the application of atomic force microscopy imaging and force spectroscopy to microbiology. Curr. Opin. Microbiol. *6*, 317–323.

Dufrêne, Y.F. (2015). Sticky microbes: Forces in microbial cell adhesion. Trends Microbiol. *23*, 376–382.

Dupres, V., Alsteens, D., Pauwels, K., and Dufrêne, Y.F. (2009). *In vivo* imaging of S-layer nanoarrays on Corynebacterium glutamicum. Langmuir *25*, 9653–9655.

Engel, A., Schoenenberger, C.-A., and Müller, D.J. (1997). High resolution imaging of native biological sample surfaces using scanning probe microscopy. Curr. Opin. Struct. Biol. *7*, 279–284.

Fanucci, G.E., Lee, J.Y., and Cafiso, D.S. (2003). Spectroscopic Evidence that Osmolytes Used in Crystallization Buffers Inhibit a Conformation Change in a Membrane Protein. Biochemistry *42*, 13106–13112.

Farrance, O.E., Hann, E., Kaminska, R., Housden, N.G., Derrington, S.R., Kleanthous, C., Radford, S.E., and Brockwell, D.J. (2013). A force-activated trip switch triggers rapid dissociation of a colicin from its immunity protein. PLoS Biol. *11*, e1001489.

Farrance, O.E., Paci, E., Radford, S.E., and Brockwell, D.J. (2015). Extraction of accurate biomolecular parameters from single-molecule force spectroscopy experiments. ACS Nano *9*, 1315–1324.

Fischer, E., Günter, K., and Braun, V. (1989). Involvement of ExbB and TonB in transport across the outer membrane of Escherichia coli: phenotypic complementation of exb mutants by overexpressed tonB and physical stabilization of TonB by ExbB. J. Bacteriol.

171, 5127–5134.

Fleming, A. (1929). On the Antibacterial Action of Cultures of a Penicillium, with Special Reference to Their Use in the Isolation of B. influenzae. Br. J. Exp. Pathol. *10*, 226–236.

Formosa, C., Pillet, F., Schiavone, M., Duval, R.E., Ressier, L., and Dague, E. (2015). Generation of living cell arrays for atomic force microscopy studies. *10*, 199–204.

Francius, G., Domenech, O., Mingeot-Leclercq, M.P., and Dufrêne, Y.F. (2008). Direct observation of Staphylococcus aureus cell wall digestion by lysostaphin. J. Bacteriol. *190*, 7904–7909.

Frankel, B.A., Kruger, R.G., Robinson, D.E., Kelleher, N.L., and McCafferty, D.G. (2005). Staphylococcus aureus sortase transpeptidase SrtA: Insight into the kinetic mechanism and evidence for a reverse protonation catalytic mechanism. Biochemistry *44*, 11188–11200.

Friend, J., and Yeo, L. (2010). Fabrication of microfluidic devices using polydimethylsiloxane. Biomicrofluidics *4*, 1–5.

G Binnig, CF Quate, C.G. (1986). Atomic Force Microscope. Phys. Rev. Lett. 56, 930.

Giesbrecht, P., Kersten, T., Maidhof, H., and Wecke, J. (1998). Staphylococcal Cell Wall: Morphogenesis and Fatal Variations in the Presence of Penicillin. Microbiol. Mol. Biol. Rev. *62*, 1371–1414.

Gilbert, Y., Deghorain, M., Wang, L., Xu, B., Pollheimer, P.D., Gruber, H.J., Errington, J., Hallet, B., Haulot, X., Verbelen, C., et al. (2007). Single-molecule force spectroscopy and imaging of the vancomycin/D-Ala-D- Ala interaction. Nano Lett. *7*, 796–801.

González de Prado Salas, P., Hörger, I., Martín-García, F., Mendieta, J., Alonso, Á., Encinar, M., Gómez-Puertas, P., Vélez, M., and Tarazona, P. (2014). Torsion and curvature of FtsZ filaments. Soft Matter *10*, 1977–1986.

Grant, M.A.A., Wacław, B., Allen, R.J., and Cicuta, P. (2014). The role of mechanical forces in the planar-to-bulk transition in growing Escherichia coli microcolonies. J. R. Soc. Interface *11*, 20140400.

Gumbart, J., Wiener, M.C., and Tajkhorshid, E. (2007). Mechanics of force propagation in TonB-dependent outer membrane transport. Biophys. J. *93*, 496–504.

Harshey, R.M. (2003). Bacterial Motility on a Surface: Many Ways to a Common Goal. Annu. Rev. Microbiol. *57*, 249–273.

Hayhurst, E.J., Kailas, L., Hobbs, J.K., and Foster, S.J. (2008). Cell wall peptidoglycan architecture in Bacillus subtilis. Proc. Natl. Acad. Sci. U. S. A. *105*, 14603–14608.

Heidelberg, J.F., Eisen, J. a, Nelson, W.C., Clayton, R. a, Gwinn, M.L., Dodson, R.J., Haft, D.H., Tettelin, Â., Hickey, E.K., Peterson, J.D., et al. (2000). DNA sequence of both chromosomes of the cholera pathogen Vibrio cholerae. Nature *406*, 477–483.

Heu, C., Berquand, A., Elie-Caille, C., and Nicod, L. (2012). Glyphosate-induced stiffening of HaCaT keratinocytes, a Peak Force Tapping study on living cells. J. Struct. Biol. *178*, 1–7.

Hickman, S.J., Cooper, R.E.M., Bellucci, L., Paci, E., and Brockwell, D.J. (2017). Gating of TonB-dependent transporters by substrate-specific forced remodelling. Nat. Commun. *8*,

14804.

Hinterdorfer, P., and Dufrêne, Y.F. (2006). Detection and localization of single molecular recognition events using atomic force microscopy. Nat. Methods *3*, 347–355.

Hoffmann, T., Tych, K.M., Hughes, M.L., Brockwell, D.J., and Dougan, L. (2013). Towards design principles for determining the mechanical stability of proteins. Phys. Chem. Chem. Phys. *15*, 15767.

Holden, S.J., Pengo, T., Meibom, K.L., Fernandez Fernandez, C., Collier, J., and Manley, S. (2014). High throughput 3D super-resolution microscopy reveals Caulobacter crescentus *in vivo* Z-ring organization. Proc. Natl. Acad. Sci. U. S. A. *111*, 4566–4571.

Holland, L.M., Conlon, B., and O'Gara, J.P. (2011). Mutation of tagO reveals an essential role for wall teichoic acids in Staphylococcus epidermidis biofilm development. Microbiology *157*, 408–418.

Huang, C.-J., Lin, H., and Yang, X. (2012). Industrial production of recombinant therapeutics in Escherichia coli and its recent advancements. J. Ind. Microbiol. Biotechnol. *39*, 383–399.

Hugel, T., and Seitz, M. (2001). The study of molecular interactions by AFM force spectroscopy. Macromol. Rapid Commun. *22*, 989–1016.

Hutter, J.L., and Bechhoefer, J. (1993). Calibration of atomic-force microscope tips. Rev. Sci. Instrum. *64*, 1868–1873.

James, S.A., Powell, L.C., and Wright, C.J. (2016). Atomic Force Microscopy of Biofilms—Imaging, Interactions, and Mechanics. In Microbial Biofilms - Importance and Applications, (InTech), p.

Jana, B., Manning, M., and Postle, K. (2011). Mutations in the ExbB cytoplasmic carboxy terminus prevent energy-dependent interaction between the TonB and ExbD periplasmic domains. J. Bacteriol. *193*, 5649–5657.

Janganan, T.K., Mullin, N., Tzokov, S.B., Stringer, S., Fagan, R.P., Hobbs, J.K., Moir, A., and Bullough, P.A. (2016). Characterization of the spore surface and exosporium proteins of Clostridium sporogenes; implications for Clostridium botulinum group I strains. Food Microbiol. *59*, 205–212.

JPK Instruments (2011). QI^{TM} mode - Quantitative Imaging with the NanoWizard ® 3 AFM.

JPK Instruments (2012). JPK Instruments AG- NanoWizard3 User Manual. SPM Software Release 4.2.

Kaemmer, S.B. (2011). Application Note # 133 Introduction to Bruker ' s ScanAsyst and PeakForce Tapping AFM Technology.

Kailas, L., Ratcliffe, E.C., Hayhurst, E.J., Walker, M.G., Foster, S.J., and Hobbs, J.K. (2009). Immobilizing live bacteria for AFM imaging of cellular processes. Ultramicroscopy *109*, 775–780.

Kang, S., and Elimelech, M. (2009). Bioinspired single bacterial cell force spectroscopy. Langmuir *25*, 9656–9659.

Karami, N., Martner, A., Enne, V.I., Swerkersson, S., Adlerberth, I., and Wold, A.E. (2007).

Transfer of an ampicillin resistance gene between two Escherichia coli strains in the bowel microbiota of an infant treated with antibiotics. J. Antimicrob. Chemother. *60*, 1142–1145.

Kasas, S., and Ikai, A. (1995). A method for anchoring round shaped cells for atomic force microscope imaging. Biophys. J. *68*, 1678–1680.

Kasas, S., Longo, G., and Dietler, G. (2013). Mechanical properties of biological specimens explored by atomic force microscopy. J. Phys. D Appl. Phys. J. Phys. D Appl. Phys *46186*, 133001–133012.

Kaufman, Y., and Freger, V. (2011). Supported Biomimetic Membranes for Pressure-Driven Water Purification. In On Biomimetics, (InTech), p.

Kent, V. (2013). Cell wall architecutre and the role of teichoic acids in S. aureus.

Kim, S.J., Cegelski, L., Studelska, D.R., O'Connor, R.D., Mehta, A.K., and Schaefer, J. (2002). Rotational-echo double resonance characterization of vancomycin binding sites in Staphylococcus aureus. Biochemistry *41*, 6967–6977.

Kim, S.J., Chang, J., and Singh, M. (2015). Peptidoglycan architecture of Gram-positive bacteria by solid-state NMR. Biochim. Biophys. Acta - Biomembr. *1848*, 350–362.

Kohanski, M.A., Dwyer, D.J., and Collins, J.J. (2010). How antibiotics kill bacteria: from targets to networks. Nat. Rev. Microbiol. *8*, 423–435.

de Kraker, M.E.A., Stewardson, A.J., and Harbarth, S. (2016). Will 10 Million People Die a Year due to Antimicrobial Resistance by 2050? PLoS Med. *13*, 1–6.

Krewulak, K.D., and Vogel, H.J. (2011). TonB or not TonB: is that the question? Biochem. Cell Biol. *89*, 87–97.

Kumar, S., Cartron, M.L., Mullin, N., Qian, P., Leggett, G.J., Hunter, C.N., and Hobbs, J.K. (2017a). Direct Imaging of Protein Organization in an Intact Bacterial Organelle Using High-Resolution Atomic Force Microscopy. ACS Nano *11*, 126–133.

Kumar, S., Cartron, M.L., Mullin, N., Qian, P., Leggett, G.J., Hunter, C.N., and Hobbs, J.K. (2017b). Direct Imaging of Protein Organization in an Intact Bacterial Organelle Using High-Resolution Atomic Force Microscopy: Supporting Information. ACS Nano *11*, 126–133.

Kuyukina, M.S., Korshunova, I.O., Rubtsova, E. V., and Ivshina, I.B. (2013). Methods of microorganism immobilization for dynamic atomic-force studies (review). Appl. Biochem. Microbiol. *50*, 1–9.

Lathrop, J.T., Wei, B.Y., Touchie, G.A., and Kadner, R.J. (1995). Sequences of the Escherichia coli BtuB protein essential for its insertion and function in the outer membrane. J. Bacteriol. *177*, 6810–6819.

Le, D.T.L., Tran, T.L., Duviau, M.P., Meyrand, M., Guérardel, Y., Castelain, M., Loubière, P., Chapot-Chartier, M.P., Dague, E., and Mercier-Bonin, M. (2013). Unraveling the role of surface mucus-binding protein and pili in muco-adhesion of Lactococcus lactis. PLoS One *8*.

Lee, B.Y., Singh, A., David, M.Z., Bartsch, S.M., Slayton, R.B., Huang, S.S., Zimmer, S.M., Potter, M.A., Macal, C.M., Lauderdale, D.S., et al. (2013). The economic burden of community-associated methicillin-resistant Staphylococcus aureus (CA-MRSA). Clin.

Microbiol. Infect. *19*, 528–536.

Leung, C., Bestembayeva, A., Thorogate, R., Stinson, J., Pyne, A., Marcovich, C., Yang, J., Drechsler, U., Despont, M., Jankowski, T., et al. (2012). Atomic force microscopy with nanoscale cantilevers resolves different structural conformations of the DNA double helix. Nano Lett. *12*, 3846–3850.

Levin, P. a, Kurtser, I.G., and Grossman, a D. (1999). Identification and characterization of a negative regulator of FtsZ ring formation in Bacillus subtilis. Proc. Natl. Acad. Sci. U. S. A. *96*, 9642–9647.

Lewis, K. (2013). Platforms for antibiotic discovery. Nat. Rev. Drug Discov. *12*, 371–387.

Lim, D., and Strynadka, N.C.J. (2002). Structural basis for the beta lactam resistance of PBP2a from methicillin-resistant Staphylococcus aureus. Nat. Struct. Biol. *9*, 870–876.

Liu, B.Y., Zhang, G.M., Li, X.L., and Chen, H. (2012). Effect of glutaraldehyde fixation on bacterial cells observed by atomic force microscopy. Scanning *34*, 6–11.

Lonergan, N.E.E., Britt, L.D.D., and Sullivan, C.J.J. (2013). Immobilizing Live Escherichia coli for AFM Studies of Surface Dynamics. Ultramicroscopy *137*, 30–39.

Long, Z., Nugent, E., Javer, A., Cicuta, P., Sclavi, B., Cosentino Lagomarsino, M., and Dorfman, K.D. (2013). Microfluidic chemostat for measuring single cell dynamics in bacteria. Lab Chip *13*, 947–954.

Longo, G., Rio, L.M., Roduit, C., Trampuz, A., Bizzini, A., Dietler, G., and Kasas, S. (2012). Force volume and stiffness tomography investigation on the dynamics of stiff material under bacterial membranes. J. Mol. Recognit. *25*, 278–284.

Loose, M., and Mitchison, T.J. (2013). The bacterial cell division proteins FtsA and FtsZ self-organize into dynamic cytoskeletal patterns. Nat. Cell Biol. *16*, 38–46.

Louise Meyer, R., Zhou, X., Tang, L., Arpanaei, A., Kingshott, P., and Besenbacher, F. (2010). Immobilisation of living bacteria for AFM imaging under physiological conditions. Ultramicroscopy *110*, 1349–1357.

Lovering, A.L., Safadi, S.S., and Strynadka, N.C.J. (2012). Structural Perspective of Peptidoglycan Biosynthesis and Assembly. Annu. Rev. Biochem. *81*, 451–478.

Lund, V.A. (2016). Peptidoglycan Dynamics in Staphylococcus aureus using Super-Resolution Microscopy.

Marion, D. (2013). An introduction to biological NMR spectroscopy. Mol. Cell. Proteomics *12*, 3006–3025.

Martin, Y., Williams, C.C., and Wickramasinghe, H.K. (1987). Atomic force microscope-force mapping and profiling on a sub 100-Å scale. J. Appl. Phys. *61*, 4723–4729.

Di Masi, D.R., White, J.C., Schnaitman, C.A., and Bradbeer, C. (1973). Transport of vitamin B12 in Escherichia coli: common receptor sites for vitamin B12 and the E colicins on the outer membrane of the cell envelope. J. Bacteriol. *115*, 506–513.

Matias, V.R.F., and Beveridge, T.J. (2007). Cryo-electron microscopy of cell division in Staphylococcus aureus reveals a mid-zone between nascent cross walls. Mol. Microbiol. *64*, 195–206.

Mazmanian, S.K. (1999). Staphylococcus aureus Sortase, an Enzyme that Anchors Surface Proteins to the Cell Wall. Science (80-.). *285*, 760–763.

Mazmanian, S.K., Liu, G., Jensen, E.R., Lenoy, E., and Schneewind, O. (2000). Staphylococcus aureus sortase mutants defective in the display of surface proteins and in the pathogenesis of animal infections. Proc. Natl. Acad. Sci. *97*, 5510–5515.

Mazmanian, S.K., Ton-That, H., Su, K., and Schneewind, O. (2002). An iron-regulated sortase anchors a class of surface protein during Staphylococcus aureus pathogenesis. Proc. Natl. Acad. Sci. *99*, 2293–2298.

Merkel, R., Nassoy, P., Leung, A., Ritchie, K., and Evans, E. (1999). Energy landscapes of receptor–ligand bonds explored with dynamic force spectroscopy. Nature *397*, 50–53.

Meyer, G., and Amer, N.M. (1988). Novel optical approach to atomic force microscopy. Appl. Phys. Lett. *53*, 1045–1047.

Micic, M., Hu, D., Suh, Y.D., Newton, G., Romine, M., and Lu, H.P. (2004). Correlated atomic force microscopy and fluorescence lifetime imaging of live bacterial cells. Colloids Surfaces B Biointerfaces *34*, 205–212.

Miller, K.J., Zelt, S.C., and Bae, J.-H. (1991). Glycine betaine and proline are the principal compatible solutes ofStaphylococcus aureus. Curr. Microbiol. *23*, 131–137.

Mohammadi, T., van Dam, V., Sijbrandi, R., Vernet, T., Zapun, A., Bouhss, A., Diepeveen-de Bruin, M., Nguyen-Distèche, M., de Kruijff, B., and Breukink, E. (2011). Identification of FtsW as a transporter of lipid-linked cell wall precursors across the membrane. EMBO J. *30*, 1425–1432.

Monteiro, J.M., Fernandes, P.B., Vaz, F., Pereira, A.R., Tavares, A.C., Ferreira, M.T., Pereira, P.M., Veiga, H., Kuru, E., Vannieuwenhze, M.S., et al. (2015). Cell shape dynamics during the staphylococcal cell cycle. Nat. Commun. *6*, 1–12.

Müller, C., and Ziegler, C. (2013). The scanning force microscope in bacterial cell investigations. Phys. Status Solidi *210*, 846–852.

Müller, D.J., and Dufrêne, Y.F. (2008). Atomic force microscopy as a multifunctional molecular toolbox in nanobiotechnology. Nat. Nanotechnol. *3*, 261–269.

Müller, D.J., and Engel, A. (1997). The height of biomolecules measured with the atomic force microscope depends on electrostatic interactions. Biophys. J. *73*, 1633–1644.

Müller, D.J., Fotiadis, D., Scheuring, S., Müller, S. a, and Engel, A. (1999). Electrostatically balanced subnanometer imaging of biological specimens by atomic force microscope. Biophys. J. *76*, 1101–1111.

Mullin, N. (2009). Dynamic Imaging Methods for Scanning Probe Microscopy.

Mullin, N., and Hobbs, J. (2008). Torsional resonance atomic force microscopy in water. Appl. Phys. Lett. *92*, 53103.

Mullin, N., and Hobbs, J.K. (2011). Direct Imaging of Polyethylene Films at Single-Chain Resolution with Torsional Tapping Atomic Force Microscopy. Phys. Rev. Lett. *107*, 197801.

Mullin, N., Vasilev, C., Tucker, J.D., Hunter, C.N., Weber, C.H.M., and Hobbs, J.K. (2009). “Torsional tapping” atomic force microscopy using T-shaped cantilevers. Appl. Phys. Lett.

94, 173109.

Noinaj, N., Guillier, M., Barnard, T.J., and Buchanan, S.K. (2010). TonB-Dependent Transporters: Regulation, Structure, and Function. Annu. Rev. Microbiol. *64*, 43–60.

Oesterhelt, F. (2000). Unfolding Pathways of Individual Bacteriorhodopsins. Science (80-.). *288*, 143–146.

Oestreicher, Z., Taoka, A., and Fukumori, Y. (2015). A comparison of the surface nanostructure from two different types of gram-negative cells: Escherichia coli and Rhodobacter sphaeroides. Micron *72*, 8–14.

Office of National Statistics UK (2013). Statistical Bulletin Deaths Involving MRSA : England and Wales , 2008 to 2012. 1–19.

Ojkic, N., López-Garrido, J., Pogliano, K., and Endres, R.G. (2016). Cell-wall remodeling drives engulfment during Bacillus subtilis sporulation. Elife *5*, 1–30.

Page, K., Wilson, M., and Parkin, I. (2009). Antimicrobial surfaces and their potential in reducing the role of the inanimate environment in the incidence of hospital-acquired infections. J. Mater. Chem. *19*, 3819–3831.

Paulo, Á., and García, R. (2001). Tip-surface forces, amplitude, and energy dissipation in amplitude-modulation (tapping mode) force microscopy. Phys. Rev. B *64*, 1–4.

Pen, Y., Zhang, Z.J., Morales-García, A.L., Mears, M., Tarmey, D.S., Edyvean, R.G., Banwart, S.A., and Geoghegan, M. (2015). Effect of extracellular polymeric substances on the mechanical properties of Rhodococcus. Biochim. Biophys. Acta - Biomembr. *1848*, 518–526.

Pereira, S.F.F., Henriques, A.O., Pinho, M.G., de Lencastre, H., and Tomasz, A. (2009). Evidence for a dual role of PBP1 in the cell division and cell separation of Staphylococcus aureus. Mol. Microbiol. *72*, 895–904.

Pfreundschuh, M., Martinez-martin, D., Mulvihill, E., Wegmann, S., and Muller, D.J. (2014). Multiparametric high-resolution imaging of native proteins by force-distance curve – based AFM. Nat. Protoc. *9*, 1113–1130.

Pinho, M.G., and Errington, J. (2005). Recruitment of penicillin-binding protein PBP2 to the division site of Staphylococcus aureus is dependent on its transpeptidation substrates. Mol. Microbiol. *55*, 799–807.

Plomp, M., Leighton, T.J., Wheeler, K.E., Hill, H.D., and Malkin, A.J. (2007). *In vitro* high-resolution structural dynamics of single germinating bacterial spores. Proc. Natl. Acad. Sci. U. S. A. *104*, 9644–9649.

Radotić, K., Roduit, C., Simonović, J., Hornitschek, P., Fankhauser, C., Mutavdžić, D., Steinbach, G., Dietler, G., and Kasas, S. (2012). Atomic force microscopy stiffness tomography on living arabidopsis thaliana cells reveals the mechanical properties of surface and deep cell-wall layers during growth. Biophys. J. *103*, 386–394.

Reed, P., Atilano, M.L., Alves, R., Hoiczyk, E., Sher, X., Reichmann, N.T., Pereira, P.M., Roemer, T., Filipe, S.R., Pereira-Leal, J.B., et al. (2015). Staphylococcus aureus Survives with a Minimal Peptidoglycan Synthesis Machine but Sacrifices Virulence and Antibiotic Resistance. PLoS Pathog. *11*, 1–19.

Rief, M., Oesterhelt, F., and Gaub, H.E. (1997). Single Molecule Force Spectroscopy on Polysaccharides by Atomic Force Microscopy. Science (80-.). *275*, 1295–1297.

Rodríguez, T.R., and García, R. (2002). Tip motion in amplitude modulation (tapping-mode) atomic-force microscopy: Comparison between continuous and point-mass models. Appl. Phys. Lett. *80*, 1646–1648.

Rodríguez, T.R., and García, R. (2003). Theory of Q control in atomic force microscopy. Appl. Phys. Lett. *82*, 4821–4823.

Roduit, C., Sekatski, S., Dietler, G., Catsicas, S., Lafont, F., and Kasas, S. (2009). Stiffness tomography by atomic force microscopy. Biophys. J. *97*, 674–677.

Rothschild, L.J., and Mancinelli, R.L. (2001). Life in extreme environments (nature).PDF. Nature *409*, 1092–1101.

Ruiz, N. (2015). Lipid flippases for bacterial peptidoglycan biosynthesis. Lipid Insights *2015*, 21–31.

Sader, J.E., Larson, I., Mulvaney, P., and White, L.R. (1995). Method for the calibration of atomic force microscope cantilevers. Rev. Sci. Instrum. *66*, 3789–3798.

Sader, J.E., Chon, J.W.M., and Mulvaney, P. (1999). Calibration of rectangular atomic force microscope cantilevers. Rev. Sci. Instrum. *70*, 3967–3969.

Sauvage, E., Kerff, F., Terrak, M., Ayala, J.A., and Charlier, P. (2008). The penicillin-binding proteins: Structure and role in peptidoglycan biosynthesis. FEMS Microbiol. Rev. *32*, 234–258.

Scheffers, D., and Pinho, M.G. (2005). Bacterial Cell Wall Synthesis: New Insights from Localization Studies. Microbiol. Mol. Biol. Rev. *69*, 585–607.

Schindler, C.A., and Schuhardt, V.T. (1964). Lysostaphin: A New Bacteriolytic Agent for the *Staphylococcus*. Proc. Natl. Acad. Sci. U. S. A. *51*, 414–421.

Schleifer, K.H., and Kandler, O. (1972). Peptidoglycan types of bacterial cell walls and their taxonomic implications. Bacteriol. Rev. *36*, 407–477.

Sengupta, S., Chattopadhyay, M.K., and Grossart, H.P. (2013). The multifaceted roles of antibiotics and antibiotic resistance in nature. Front. Microbiol. *4*, 1–13.

Sharif, S., Kim, S.J., Labischinski, H., and Schaefer, J. (2009a). Characterization of Peptidoglycan in Fem -Deletion Mutants of Methicillin-Resistant Staphylococcus aureus by Solid-State NMR. Biochemistry 3100–3108.

Sharif, S., Singh, M., Kim, S.J., and Schaefer, J. (2009b). *Staphylococcus aureus* Peptidoglycan Tertiary Structure from Carbon-13 Spin Diffusion. J. Am. Chem. Soc. *131*, 7023–7030.

Sharif, S., Kim, S.J., Labischinski, H., Chen, J., and Schaefer, J. (2013). Uniformity of glycyl bridge lengths in the mature cell walls of fem mutants of methicillin-resistant Staphylococcus aureus. J. Bacteriol. *195*, 1421–1427.

Shibata, M., Yamashita, H., Uchihashi, T., Kandori, H., and Ando, T. (2010). High-speed atomic force microscopy shows dynamic molecular processes in photoactivated bacteriorhodopsin. Nat. Nanotechnol. *5*, 208–212.

Shibata, M., Uchihashi, T., Yamashita, H., Kandori, H., and Ando, T. (2011). Structural changes in bacteriorhodopsin in response to alternate illumination observed by high-speed atomic force microscopy. Angew. Chemie - Int. Ed. *50*, 4410–4413.

Shultis, D.D., Purdy, M.D., Banchs, C.N., and Wiener, M.C. (2006). Outer Membrane Active Transport: Structure of the BtuB:TonB Complex. Science (80-.). *312*, 1396–1399.

Silhavy, T., Kahne, D., and Walker, S. (2010). The bacterial cell envelope. Cold Spring Harb. Perspect. Biol. *2*, 1–16.

Silver, L.L. (2011). Challenges of Antibacterial Discovery. Clin. Microbiol. Rev. *24*, 71–109.

Smith, I. (2003). *Mycobacterium tuberculosis* pathogenesis and molecular determinants of virulence. Clin. Microbiol. Rev. *16*, 463–496.

Del Sol, R., Armstrong, I., Wright, C., and Dyson, P. (2007). Characterization of changes to the cell surface during the life cycle of Streptomyces coelicolor. Atomic force microscopy of living cells. J. Bacteriol. *189*, 2219–2225.

Spector, J., Zakharov, S., Lill, Y., Sharma, O., Cramer, W.A., and Ritchie, K. (2010). Mobility of BtuB and OmpF in the Escherichia coli outer membrane: Implications for dynamic formation of a translocon complex. Biophys. J. *99*, 3880–3886.

Steele, V.R., Bottomley, A.L., Garcia-Lara, J., Kasturiarachchi, J., and Foster, S.J. (2011). Multiple essential roles for EzrA in cell division of Staphylococcus aureus. Mol. Microbiol. *80*, 542–555.

Strauss, M.P., Liew, A.T.F., Turnbull, L., Whitchurch, C.B., Monahan, L.G., and Harry, E.J. (2012). 3D-SIM Super Resolution Microscopy Reveals a Bead-Like Arrangement for FtsZ and the Division Machinery: Implications for Triggering Cytokinesis. PLoS Biol. *10*.

Swoboda, J.G., Campbell, J., Meredith, T.C., and Walker, S. (2010). NIH Public Access. Chembiochem. *11*, 35–45.

Takami, H., Inoue, A., Fuji, F., and Horikoshi, K. (1997). Microbial flora in the deepest sea mud of the Mariana trench. FEMS Microbiol. Lett. *152*, 279–285.

Tamayo, J., and Garcia, R. (1996). Deformation, Contact Time, and Phase Contrast in Tapping Mode Scanning Force Microscopy - Langmuir (ACS Publications). Langmuir *7463*, 4430–4435.

Thoma, J., Bosshart, P., Pfreundschuh, M., and Müller, D.J. (2012). Out but not in: the large transmembrane β-barrel protein FhuA unfolds but cannot refold via β-hairpins. Structure *20*, 2185–2190.

Tiyanont, K., Doan, T., Lazarus, M.B., Fang, X., Rudner, D.Z., and Walker, S. (2006). Imaging peptidoglycan biosynthesis in Bacillus subtilis with fluorescent antibiotics. Proc. Natl. Acad. Sci. U. S. A. *103*, 11033–11038.

Toole, G.O., Kaplan, H.B., and Kolter, R. (2000). B f m d. 49–79.

Touhami, A., Jericho, M.H., and Beveridge, T.J. (2004). Atomic Force Microscopy of Cell Growth and Division in Staphylococcus aureus Atomic Force Microscopy of Cell Growth and Division in Staphylococcus aureus. *186*.

Trtik, P., Kaufmann, J., and Volz, U. (2012). On the use of peak-force tapping atomic force

microscopy for quantification of the local elastic modulus in hardened cement paste. Cem. Concr. Res. *42*, 215–221.

Turner, R.D., Kirkham, J., Devine, D., and Thomson, N.H. (2009). Second harmonic atomic force microscopy of living Staphylococcus aureus bacteria. Appl. Phys. Lett. *94*, 43901.

Turner, R.D., Ratcliffe, E.C., Wheeler, R., Golestanian, R., Hobbs, J.K., and Foster, S.J. (2010a). Peptidoglycan architecture can specify division planes in Staphylococcus aureus. Nat. Commun. *1*, 26.

Turner, R.D., Thomson, N.H., Kirkham, J., and Devine, D. (2010b). Improvement of the pore trapping method to immobilize vital coccoid bacteria for high-resolution AFM: A study of Staphylococcus aureus. J. Microsc. *238*, 102–110.

Turner, R.D., Vollmer, W., and Foster, S.J. (2014). Different walls for rods and balls: The diversity of peptidoglycan. Mol. Microbiol. *44*, 1–24.

Typas, A., Banzhaf, M., Gross, C.A., and Vollmer, W. (2011). From the regulation of peptidoglycan synthesis to bacterial growth and morphology. Nat. Rev. Microbiol. *23*, 923–934.

Varbel, A., and Leilani, M. (2000). Dimension TM 3100 Manual Dimension 3100 Manual Table of Contents. *0*, 4–320.

Velegol, S.B., Pardi, S., Li, X., Velegol, D., and Logan, B.E. (2003). AFM imaging artifacts due to bacterial cell height and AFM tip geometry. Langmuir *19*, 851–857.

Ventola, C.L. (2015). The antibiotic resistance crisis: part 1: causes and threats. P T A Peer-Reviewed J. Formul. Manag. *40*, 277–283.

Vergara-Irigaray, M., Maira-Litran, T., Merino, N., Pier, G.B., Penades, J.R., and Lasa, I. (2008). Wall teichoic acids are dispensable for anchoring the PNAG exopolysaccharide to the Staphylococcus aureus cell surface. Microbiology *154*, 865–877.

Verwer, R.W.H., and Nanninga, N. (1976). Electron Micrsocopy of isolated cell walls of *Bacillus subtilis* var. *niger*. Arch. Microbiol. *109*, 195–197.

Viani, M.B., Schäffer, T.E., Chand, A., Rief, M., Gaub, H.E., and Hansma, P.K. (1999). Small cantilevers for force spectroscopy of single molecules. J. Appl. Phys. *86*, 2258–2262.

Vollmer, W. (2006). The prokaryotic cytoskeleton: A putative target for inhibitors and antibiotics? Appl. Microbiol. Biotechnol. *73*, 37–47.

Vollmer, W., and Seligman, S.J. (2010). Architecture of peptidoglycan: more data and more models. Trends Microbiol. *18*, 59–66.

Vollmer, W., Höltje, J., and Ho, J. (2004). The Architecture of the Murein (Peptidoglycan) in Gram-Negative Bacteria : Vertical Scaffold or Horizontal Layer (s)? MINIREVIEW The Architecture of the Murein (Peptidoglycan) in Gram-Negative Bacteria : Vertical Scaffold or Horizontal Layer (s)?†. *186*, 5978–5987.

Vollmer, W., Blanot, D., and de Pedro, M. a (2008a). Peptidoglycan structure and architecture. FEMS Microbiol. Rev. *32*, 149–167.

Vollmer, W., Joris, B., Charlier, P., and Foster, S. (2008b). Bacterial peptidoglycan (murein) hydrolases. FEMS Microbiol. Rev. *32*, 259–286.

Walters, D.A., Cleveland, J.P., Thomson, N.H., Hansma, P.K., Wendman, M.A., Gurley, G., and Elings, V. (1996). Short cantilevers for atomic force microscopy. Rev. Sci. Instrum. *67*, 3583–3590.

Wang, P., Robert, L., Pelletier, J., Dang, W.L., Taddei, F., Wright, A., and Jun, S. (2010). Robust growth of escherichia coli. Curr. Biol. *20*, 1099–1103.

Weisenhorn, A.L., Hansma, P.K., Albrecht, T.R., and Quate, C.F. (1989). Forces in atomic force microscopy in air and water. Appl. Phys. Lett. *54*, 2651–2653.

Wheeler, R. (2012). Peptidoglycan architecture and dynamics in Gram-positive bacteria.

Wheeler, R., Turner, R.D., Bailey, R.G., Salamaga, B., Mesnage, S., Mohamad, S.A.S., Hayhurst, E.J., Horsburgh, M., Hobbs, J.K., and Foster, S.J. (2015). Bacterial Cell Enlargement Requires Control of Cell Wall Stiffness Mediated by Peptidoglycan Hydrolases. *6*, 1–10.

Whitehead, K.A., Rogers, D., Colligon, J., Wright, C., and Verran, J. (2006). Use of the atomic force microscope to determine the effect of substratum surface topography on the ease of bacterial removal. Colloids Surfaces B Biointerfaces *51*, 44–53.

Wu, L.J., and Errington, J. (2012). Nucleoid occlusion and bacterial cell division. Nat Rev Microbiol *10*, 8–12.

Wu, J. a, Wu, J. a, Kusuma, C., Kusuma, C., Mond, J.J., Mond, J.J., Kokai-kun, J.F., and Kokai-kun, J.F. (2003). Lysostaphin Disrupts Staphylococcus aureus and Staphylococcus epidermidis Bio lms on Arti cial Surfaces. Society *47*, 3407–3414.

Xia, G., Maier, L., Sanchez-Carballo, P., Li, M., Otto, M., Holst, O., and Peschel, A. (2010). Glycosylation of wall teichoic acid in Staphylococcus aureus by TarM. J. Biol. Chem. *285*, 13405–13415.

Yamada, S., Sugai, M., Komatsuzawa, H., Nakashima, S., Oshida, T., Matsumoto, a, and Suginaka, H. (1996). An autolysin ring associated with cell separation of Staphylococcus aureus. J. Bacteriol. *178*, 1565–1571.

Yamashita, H., Taoka, A., Uchihashi, T., Asano, T., Ando, T., and Fukumori, Y. (2012). Single-molecule imaging on living bacterial cell surface by high-speed AFM. J. Mol. Biol. *422*, 300–309.

Ythier, M., Resch, G., Waridel, P., Panchaud, A., Gfeller, A., Majcherczyk, P., Quadroni, M., and Moreillon, P. (2012). Proteomic and Transcriptomic Profiling of *Staphylococcus aureus* Surface LPXTG-proteins: Correlation with *agr* Genotypes and Adherence Phenotypes. Mol. Cell. Proteomics *11*, 1123–1139.

Zapun, A., Contreras-Martel, C., and Vernet, T. (2008). Penicillin-binding proteins and β-lactam resistance. FEMS Microbiol. Rev. *32*, 361–385.

Zhong, Q., Inniss, D., Kjoller, K., and Elings, V.B. (1993). Fractured polymer/silica fiber surface studied by tapping mode atomic force microscopy. Surf. Sci. *290*, L688–L692.

Zhou, X., Halladin, D.K., Rojas, E.R., Koslover, E.F., Lee, T.K., Huang, K.C., and Theriot, J.A. (2015). Mechanical crack propagation drives millisecond daughter cell separation in Staphylococcus aureus. *348*.